University of Nebraska - Lincoln
DigitalCommons@University of Nebraska - Lincoln

Theses, Dissertations, and Student Research: Department of Physics and Astronomy
Physics and Astronomy, Department of

8-2022

Nanoscale Studies of the Ferroelectric and Electromechanical Properties of Hafnia-based Capacitors

Pratyush Buragohain
University of Nebraska–Lincoln, pratyush.pb@huskers.unl.edu

Follow this and additional works at: https://digitalcommons.unl.edu/physicsdiss

Part of the Condensed Matter Physics Commons

Buragohain, Pratyush, "Nanoscale Studies of the Ferroelectric and Electromechanical Properties of Hafnia-based Capacitors" (2022). *Theses, Dissertations, and Student Research: Department of Physics and Astronomy*. 58.
https://digitalcommons.unl.edu/physicsdiss/58

This Article is brought to you for free and open access by the Physics and Astronomy, Department of at DigitalCommons@University of Nebraska - Lincoln. It has been accepted for inclusion in Theses, Dissertations, and Student Research: Department of Physics and Astronomy by an authorized administrator of DigitalCommons@University of Nebraska - Lincoln.

NANOSCALE STUDIES OF THE FERROELECTRIC AND ELECTROMECHANICAL PROPERTIES OF HAFNIA-BASED CAPACITORS

by

Pratyush Prabhab Buragohain

A DISSERTATION

Presented to the Faculty of

The Graduate College at the University of Nebraska

In Partial Fulfilment of Requirements

For the Degree of Doctor of Philosophy

Major: Physics and Astronomy

Under the Supervision of Professor Alexei Gruverman

Lincoln, Nebraska

August 2022

NANOSCALE STUDIES OF THE FERROELECTRIC AND ELECTROMECHANICAL PROPERTIES OF HAFNIA-BASED CAPACITORS

Pratyush Prabhab Buragohain, Ph.D.

University of Nebraska, 2022

Adviser: Alexei Gruverman

The work presented in this dissertation aims to provide nanoscopic insights into the electrical and electromechanical behavior of the recently discovered ferroelectric HfO_2 or hafnia-based capacitors. Hafnia-based ferroelectrics are highly promising for technological applications due to compatibility with the existing Si technology. To realize the full potential of hafnia, however, requires comprehensive understanding of its properties. In this regard, this dissertation hopes to bridge a gap between an understanding of the nanoscopic and macroscopic properties of hafnia by performing combined high-resolution piezoresponse force microscopy (PFM) and pulse switching studies.

More specifically, the dynamics of domain nucleation and wall motion during polarization reversal in hafnia was investigated. Polarization reversal was found to occur mainly via nucleation of new domains, albeit with limited expansion and sluggish domain wall motion, following the nucleation limited switching (NLS) model at low fields. At high fields, close to the thermodynamic activation fields, a convergence of the NLS and the Kolmogorov-Avrami-Ishibashi switching models was observed, signifying a uniform domain-less polarization reversal process.

Furthermore, negative d_{33} was demonstrated for the first time in hafnia after careful calibration of the PFM phase signal, providing confirmation of a theoretically predicted negative d_{33}. However, the sign was found to be strongly sample dependent.

Depending on the film thickness, electrode materials, deposition method used, or state of the capacitors (pristine vs field-cycled), hafnia-based capacitors exhibited either a uniformly negative or positive d_{33} response or a mixture of both positive and negative d_{33} responses.

In addition, a unique imprint behavior was identified in hafnia that was found to strongly depend on the switching pre-history. Our measurements highlight the critical role played by injected charges and mobile charges/defects in the imprint behavior of hafnia-based devices.

Finally, application of PFM spectroscopy to ZrO_2-based capacitors revealed dramatically different PFM amplitude response compared to hafnia that could be attributed to the divergence of dielectric susceptibility during field-induced antiferroelectric $\leftrightarrow$ ferroelectric phase transitions, providing a microscopic confirmation of antiferroelectricity in ZrO_2.

ACKNOWLEDGMENTS

I would like to express my sincere gratitude to the multitude of people whose support, help and guidance during my journey as a doctoral student made this dissertation possible.

First of all, I would like to thank my advisor Prof. Alexei Gruverman for his invaluable support and guidance during the course of my doctoral research. His insights into tackling and navigating complex research problems and coming up with new ideas have helped me develop as a researcher and will serve as an inspiration in the years to come. Through very many discussions with him, I have learned to put research problems into perspective and look at it from the bigger picture which has had a profound influence on my thinking and I am grateful to him for that.

I am indebted to Dr. Haidong Lu, who has mentored me over the years regarding the nitty-gritties of using our beloved PFM systems and helping me develop a deeper understanding of the complex PFM results. I am grateful to him for patiently answering all of my innumerable (and sometimes silly!) questions and will cherish our discussions on many-a-different topic over the years.

I would like to thank my supervisory committee members, Prof. Evgeny Tsymbal, Prof. Stephen Ducharme, Prof. Xiaoshan Xu and Prof. Alexander Sinitskii for their help and guidance during this research and reading this dissertation.

This work would not have been possible without the support of our many wonderful collaborators who have provided us with excellent samples and theoretical inputs. I would like to sincerely thank Dr. Uwe Schroeder, Dr. Tony Schenk and Dr. Patrick Lomenzo from NaMLab, Prof. Hiroshi Funakubo and his group at Tokyo Institute of Technology, Dr. Anastasia Chouprik and Prof. Andrei Zenkevich at Moscow Institute of Physics and Technology, Prof. Jorge Iniguez and his group

at Luxembourg Institute of Science and Technology, Dr. Yingfen Wei, and Prof. Beatriz Noheda at University of Groningen, Prof. Pavan Nukala at Indian Institute of Science, and Prof. Xu's group here at UNL. A special thanks to Dr. Yu Yun from Prof. Xu's group, with who I would often have long and intense discussions as we tried to figure out the myriad mysteries of hafnia and improper ferroelectrics.

I am grateful to my current and former group members, Dr. Haidong Lu, Dr. Tao Li, Ohheum Bak, Pradeep Chaudhary, Adam Erickson and Anarta Roy, for all the help and discussions and for making my stay in the lab a memorable one.

I have been very fortunate to have met some wonderful fellow Physics graduate students - Harin, Joaquin, Alex, Karl, Zahra, Kyle, Peter, Kishan, Anil R., Shashi, Colton, Andrew, Dan, Giovanni, Ming, Rafeeq, many of who have become my close friends here in Lincoln. In particular, Joaquin and Harin are dearly acknowledged here for all those road, biking and hiking trips and also our trips to have moharra whenever we got the chance; Alex for those impromptu, improvised and inspired dinners, and khichdi; Karl for some great Hanabi sessions, movie nights, chili times and concerts. In addition, I would like to thank Adam (Hootie) for being a great friend and a lot of fun times both in the lab and outside; Emily for being a super cool neighbor and friend, for all the late night cemetery walks and our conversations on everything from rolly-polly to politics and for introducing me to poetry reading sessions; Shyamaly for some really fun times; and Jessie for being my go-to friend here in Lincoln. Pallav da and Dola ba are heartily acknowledged for all the help and support and making my initial adjustment to life in Lincoln a very pleasant one. And a special thanks to Jerry for all the margs, fossil hunts and introducing me to gardening.

I am grateful to my professors from undergraduate - Prof. Kannan Ramaswamy, Dr. Swarnali Bandopadhyay and Prof. Aravinda Raghavan - for mentoring me during

my undergraduate days, and encouraging me to pursue a PhD in physics. A big shout-out to Dr. Vineeth Parakkat and Dr. Arnab Roy for introducing me to the delights of building and performing experiments from scratch during my wonderful stay at the Indian Institute of Science that ultimately led me to pursuing a PhD in experimental physics.

Last but not the least, I want to express my deepest gratitude to Oosa, Astha (Kiddo), Iyer, Vakul, Soham and Noopur, who have been my closest friends since undergrad and have been my most solid support system over the past 14 years. Thanks for being there through the good, the bad and the best.

Finally, I would like to thank my parents for having my back!

PREFACE

The present shift towards increasingly data-centric computation requires the availability of large amounts of data to be able to be accessed at the shortest possible times. In addition, as the number of transistors continue to increase as per Moore's prediction there is an increasing need for low power devices to reduce overall energy consumption. In the current landscape of commercial available memory technologies, there are several orders of magnitude difference between the access times for volatile dynamic random access memories (DRAM) and the non-volatile hard disk drives used for long term information storage. Although flash memories have bridged this gap partially, they are still slow compared to DRAM with access times in the order of μs as compared to the tens of ns access times in DRAM [1]. Flash memories also suffer from limited endurance and higher energy consumption. In this regard, the fast read and write speeds ($\sim$ 10 ns) which are comparable to the state of the art dynamic random access memories (DRAM), coupled with non-volatility, lower energy consumption and high endurance make ferroelectric-based memories (FRAM) highly promising candidates for non-volatile random access memories (NV-RAM).

The current commercially available FRAMs are fabricated using perovskite ferroelectrics and due to processing and scaling challenges, the perovskite-based FRAMs are limited to the 130 nm technology node which is more than a decade behind the state of the art 7-10 nm technology nodes used in the current technology [1]. Due to the processing challenges, FRAMs are expensive compared to DRAM and remained as a niche product [2].

In this regard, the report of ferroelectricity in hafnium oxide-based thin films in 2011 [3] was a significant breakthrough towards the commercial realization of

ferroelectric memories. Hafnium oxide (HfO_2) has been in use as the current state-of-the-art gate dielectric since 2007 as part of Intel's 'high-k solution' that allowed the continued miniaturization of transistors [4]. Inherent advantages of ferroelectric hafnium oxide (HfO_2) over conventional perovskite films include compatibility with existing complementary metal oxide semiconductor (CMOS) technology, thickness scalability, and they are lead-free ferroelectrics [5].

However, realization of the full potential of the HfO_2-based ferroelectrics requires comprehensive studies to understand its properties. In this regard, scanning probe microscopy techniques such as piezoresponse force microscopy (PFM) allows the visualization of domain structures and together with local quantitative PFM spectroscopy it can provide nanoscopic insights into the local switching behavior and electromechanical response. The broad motivation of this dissertation is to combine high resolution PFM with pulse switching techniques to gain a deeper insight into the electrical and electromechanical behavior in HfO_2-based ferroelectrics. More specifically, the main goals of this dissertation include PFM-based investigations of: (i) polarization switching behavior and comparison of the effects of film microstructure on the switching properties, (ii) mechanism of the wake-up process, (iii) piezoelectric properties with a focus on identifying the sign of the longitudinal piezoelectric coefficient, d_{33}, and intriguing variations based on electrical and mechanical boundary conditions, and (iv) mechanism of imprint in HfO_2-based ferroelectric capacitors. In addition, field induced reversible antiferroelectric $\leftrightarrow$ ferroelectric phase transitions were also investigated in ZrO_2-based capacitors.

A general outline of this dissertation is presented below:

Chapter 1 briefly describes the basics of ferroelectricity and gives an introduction to perovskite and HfO_2-based ferroelectrics.

Chapter 2 gives an overview of the experimental methods used in this dissertation.

Specifically, scanning probe microscopy based methods are discussed with a special focus on piezoresponse force microscopy. Finally, various pulse switching methods are discussed.

Chapter 3 provides a nanoscopic insight into the wake-up process and the mechanism of polarization reversal in La:HfO_2based capacitors through the visualization of the domain structures. The results presented in this chapter have been published in ***P. Buragohain***, *C. Richter, T. Schenk, H. Lu, T. Mikolajick, U. Schroeder, and A. Gruverman, Appl. Phys. Lett.* ***112****, 222901 (2018).* Used with permission (license numbers - 5278340057445 and 5278331291138, AIP Publishing).

Chapter 4 compares the effect of film microstructure on the domain nucleation process by comparing polycrystalline and epitaxial Y:HfO_2-based capacitors. In addition, the physical conditions under which homogeneous domain-less switching in the Y:HfO_2-based capacitors can be realized are discussed. The results presented in this chapter have been published in ***P. Buragohain****, A. Erickson, T. Mimura, T. Shimizu, H. Funakubo, and A. Gruverman, Adv. Funct. Mater.* ***32****, 2108876 (2022).* Used with permission (license number - 5296261202322, John Wiley and Sons).

Chapter 5 first outlines two different methodologies used to quantify the PFM phase signal. These methodologies are then extended to La:HfO_2 capacitors to experimentally demonstrate a negative longitudinal piezoelectric coefficient, d_{33}, in La:HfO_2. However, under the same measurement protocols a variation in the sign of the d_{33} was observed depending on the electrical and mechanical boundary conditions. The results presented in this chapter will be included in a manuscript that is currently under preparation.

Chapter 6 provides a nanoscale investigation of the antiferroelectric $\leftrightarrow$

ferroelectric phase transitions using piezoresponse force microscopy in $PbZrO_3$ and ZrO_2 capacitors. The results presented in this chapter have been published in *H. Lu, S. Glinsek, **P. Buragohain**, E. Defay, J. Iñiguez, and A. Gruverman, Adv. Funct. Mater. **30**, 2003622 (2020)* and in *P. D. Lomenzo, M. Materano, T. Mittmann, **P. Buragohain**, A. Gruverman, T. Kiguchi, T. Mikolajick, and U. Schroeder, Adv. Electron. Mater. **8**, 2100556 (2022).* Used with permission (license numbers - 5278340445242 and 5296261091573, John Wiley and Sons).

Chapter 7 identifies a unique imprint behavior in La:HfO_2-based capacitors that has been termed as a fluid imprint and discuss the conditions that lead to the unique fluid imprint as well as a conventional time-dependent imprint. The results presented in this chapter have been published in ***P. Buragohain**, A. Erickson, P. Kariuki, T. Mittmann, C. Richter, P. D. Lomenzo, H. Lu, T. Schenk, T. Mikolajick, U. Schroeder, and A. Gruverman, ACS Appl. Mater. Interfaces **11**, 38, 35115 (2019).* Adapted with permission from Buragohain et al., ACS Appl. Mater. Interfaces **11**, 38, 35115 (2019). Copyright 2019 American Chemical Society.

Chapter 8 summarizes the results presented in this dissertation and gives an outlook for future studies.

References

[1] T. Schenk, M. Pešić, S. Slesazeck, U. Schroeder, and T. Mikolajick, Rep. Prog. Phys. **83**, 086501 (2020).

[2] T. Mikolajick, U. Schroeder, and S. Slesazeck, IEEE Transactions on Electron Devices **67**, 4, 1434 (2020).

[3] T. S. Boescke, J. Mueller, D. Braeuhaus, U. Schroeder, and U. Boetgger, Appl. Phys. Lett. **99**, 102903 (2011).

[4] M. T. Bohr, R. S. Chau, T. Ghani, and K. Mistry, IEEE Spectrum **44**, 10, 29 (2007).

[5] M. H. Park, Y. H. Lee, H. J. Kim, Y. J. Kim, T. Moon, K. D. Kim, J. Müller, A. Kersch, U. Schroeder, T. Mikolajick, and C. S. Hwang, Adv. Mater. **27**, 1811 (2015).

Table of Contents

1 Fundamentals of ferroelectricity **1**

1.1 Introduction 1

1.1.1 Application perspectives 6

1.2 Ferroelectric phase transitions 8

1.3 Polarization switching behavior 14

1.4 Piezoelectric behavior 19

1.5 Perovskite ferroelectrics 22

1.6 Hafnium oxide-based ferroelectrics 23

References **28**

2 Experimental methods **37**

2.1 Scanning probe microscopy 37

2.1.1 Atomic force microscopy 38

2.1.2 Piezoresponse force microscopy 41

2.1.2.1 Resonance enhanced PFM 46

2.1.2.2 PFM spectroscopy 48

2.1.2.3 Stroboscopic PFM 50

2.2 Electrical characterization 51

2.2.1 Measurement setup 51

2.2.2 Types of electrical measurements 54

2.2.2.1 Hysteresis measurements 55

2.2.2.2 Pulse switching measurements 58

2.3 Typical experimental conditions used in this dissertation 61

2.3.1 PFM measurements 61

2.3.2 Quasi-static strain loop measurements 62

2.3.3 Electrical characterization 62

References **64**

3 Nanoscopic studies of domain structure dynamics in ferroelectric La:HfO_2 capacitors **68**

3.1 Introduction 68

3.2 Materials and Methods 69

3.3 Results and Discussion 70

3.3.1 Wake-up effect 70

3.3.2 Domain dynamics 75

3.4 Conclusion 78

References **80**

4 Effect of film microstructure on domain nucleation and intrinsic switching in ferroelectric Y:HfO_2 thin film capacitors **83**

4.1 Introduction 83

4.2 Materials and methods 85

4.3 Macroscopic electrical characterization 86

4.4 Time dependent evolution of domain structure 88

4.5 Voltage dependent evolution of domain structure 93

4.6 Intrinsic switching 94
4.7 Conclusion 98

References 100

5 Quantification of the electromechanical measurements by piezoresponse force microscopy 103

5.1 Introduction 103
5.2 Materials and methods 105
5.3 Quantification of the PFM phase signal 106
5.3.1 Identification of parasitic phase offset using a reference sample 107
5.3.2 Identification of the parasitic phase offset from the electrostatic effect 112
5.4 PFM testing of hafnia-based thin film capacitors 115
5.4.1 Thickness effect on the d_{33} sign in La:HfO_2 capacitors 115
5.4.2 Electrical tuning of the sign of d_{33} in polycrystalline Y:HfO_2 thin-film capacitors 117
5.4.3 Coexistence of positive and negative d_{33} regions in IrO_x/La:HfO_2/IrO_x capacitors 120
5.5 Conclusion 122

References 124

6 Nanoscale probing of antiferroelectric-ferroelectric phase transitions 129

6.1 Introduction 129
6.2 Materials and methods 131
6.3 PFM spectroscopy measurements in antiferroelectrics 131
6.4 Theoretical description of the piezoelectric response in antiferroelectrics 134

6.5 Field induced AFE ↔ FE phase transitions in ZrO_2 137
6.6 Conclusion 139

References 141

7 Fluid imprint and inertial switching in ferroelectric HfO_2-based capacitors 143
7.1 Introduction 143
7.2 Materials and methods 144
7.3 Wake-up effect 145
7.4 Fluid and time-dependent imprint 147
7.5 Inertial switching 157
7.6 Conclusion 160

References 161

8 Summary and future directions 164
8.1 Summary 164
8.2 Future directions 166

References 167

Appendix A Supplementary Information for Chapter 4 168

Appendix B Supplementary Information for Chapter 5 172

Appendix C Supplementary Information for Chapter 7 185

List of Figures

1.1 Features of second order phase transition 10
1.2 Features of first order phase transition 12
1.3 Correlation of P-E hysteresis loop and double well potential configuration 13
1.4 Schematic of different stages of the polarization switching process in ferroelectrics. 14
1.5 Strain-field loop in an ideal ferroelectric with positive and negative longitudinal piezoelectric coefficients 20
1.6 Crystal structure of perovskites in paraelectric cubic phase and polar tetragonal phase 23
1.7 P-E loops demonstrating ferroelectricity in pure and doped-HfO_2 24
1.8 Structural polymorphs in hafnia. 25

2.1 Schematic of a typical AFM setup 38
2.2 Interatomic force regimes as a function of tip-sample separation distance 40
2.3 Schematic of the origin of the 180° PFM phase contrast 43
2.4 Example of PFM amplitude and phase images 44
2.5 Schematic of DART PFM setup 48
2.6 PFM spectroscopy waveform and typical PFM amplitude and phase hysteresis loops 49
2.7 Sawyer-Tower and shunt resistor methods for electrical characterization . 52

2.8 Circuit schematic of shunt resistor method integrated with AFM setup . 53
2.9 Waveforms used for P-V hysteresis measurements 56
2.10 PUND waveform and estimation of switching current 59
2.11 Waveform to determine polarization switching mechanism 60
2.12 Waveform to test polarization retention 61
2.13 Optical microscopy image of cantilever and external probe for PFM measurements in capacitor geometry 62

3.1 Electrical characterization and pristine PFM images in La:HfO_2 capacitors 70
3.2 Comparison of capacitor switchability in the pristine state and after the wake-up process 72
3.3 Local PFM spectroscopy loops that exhibit domain pinning 74
3.4 Comparison of 2d imprint maps before and after wake-up obtained by PFM switching spectroscopy 75
3.5 PFM visualization of domain dynamics and comparison with the KAI and NLS models 76

4.1 Comparison of switching speeds and activation fields in 27-nm-thick epitaxial and polycrystalline Y:HfO_2 capacitors 86
4.2 Comparison of switching speeds and activation fields in 23-nm-thick epitaxial and 24-nm-thick polycrystalline Y:HfO_2 capacitors 87
4.3 Stroboscopic PFM images of domain evolution and estimation of nucleation rate in the 27-nm-thick epitaxial and polycrystalline Y:HfO_2 capacitors 89
4.4 Comparison of topography and PFM images 90
4.5 High resolution stroboscopic PFM images in the 27-nm-thick polycrystalline Y:HfO_2 capacitors 91

4.6 Voltage dependent evolution of domain structures in the 27-nm-thick epitaxial and polycrystalline Y:HfO_2 capacitors 93
4.7 Determination of polarization switching mechanism using pulse-switching in the 27-nm-thick epitaxial and polycrystalline Y:HfO_2 capacitors 95

5.1 Identification of parasitic phase offset using a reference sample 108
5.2 Phase and amplitude spectrum near resonance with calibrated initial phase offsets 111
5.3 Identification of parasitic phase offset from electrostatics 115
5.4 Negative d_{33} in TiN/La:HfO_2/TiN capacitors for film thicknesses up to 30 nm 116
5.5 Structure of hafnia in cubic paraelectric and polar orthorhombic phase . 117
5.6 Positive d_{33} in 45-nm and 100-nm-thick Pt/La:HfO_2/Pt capacitors 118
5.7 Electrical tuning of the sign of d_{33} in polycrystalline Y:HfO_2 thin-film capacitors 119
5.8 Coexistence of positive and negative d_{33} regions in IrO_x/La:HfO_2/IrO_x capacitors 121

6.1 Comparison of P-V loops and PFM hysteresis loops in prototypical ferroelectrics and anti-ferroelectrics 132
6.2 P-V loops and PFM hysteresis loops in TiN/ZrO_2/TiN capacitors with different ZrO_2 thicknesses 137
6.3 Evolution of the PFM amplitude and PFM phase images as a function of constant DC bias in TiN/ZrO_2/TiN capacitors 139

7.1 Comparison of P-V and PFM images before and after wake-up in IrO_x/La:HfO_2 (20 nm)/IrO_x capacitors 146

7.2 Time-dependent imprint in IrO_x/La:HfO_2 (20 nm)/IrO_x capacitors . . . 148

7.3 Demonstration of erasure of imprint by field cycling 149

7.4 Depolarization fields in representative HfO_2 and PZT capacitors 152

7.5 Investigation and elucidation of mechanism of time-dependent and fluid imprint 154

7.6 Simplified band diagram illustrating mechanisms of fluid and conventional imprint. 156

7.7 Observation of inertial switching behavior in IrO_x/La:HfO_2 (20 nm)/IrO_x capacitors 158

B.1 Principle of PFM phase contrast in positive and negative d_{33} materials . 172

B.2 Procedure for adjustment of initial phase offsets using reference samples . 174

B.3 Comparison of arbitrary and properly adjusted initial phase offsets in PFM phase loops 175

B.4 Quantification of the PFM phase loops in single frequency PFM mode . 177

B.5 Effect of cantilever stiffness on electrostatics 178

B.6 PFM phase images with calibrated initial phase offsets 180

B.7 Comparison of topography and PFM images, and transient switching currents in IrO_x/La:HfO_2/IrO_x capacitors 181

B.8 Schematic of PFM phase loops for hysteretic and anti-hysteretic behavior. 183

C.1 Effect of the set pulse amplitude on conventional time-dependent imprint 185

C.2 Comparison of wake-up process and imprint behavior in La:HfO_2 capacitors with IrO_x and TiN electrodes 186

C.3 Correlation of split-up in I-V peaks and domain configuration 187

C.4 Inertial switching to P_{down} state in IrO_x/La:HfO_2 (20 nm)/IrO_x capacitors 189

C.5 Inertial switching in TiN/$Hf_{0.5}Zr_{0.5}O_2$ (10 nm)/TiN capacitors 190

Chapter 1

Fundamentals of ferroelectricity

1.1 Introduction

Ferroelectric materials are a class of ferroic materials, which are characterized by an order parameter, spontaneous polarization, that emerges spontaneously below a transition temperature. The spontaneous polarization can be switched between two or more energetically equivalent states by an electric field. The word 'ferroelectric' ("ferroelektrisch" in German) was coined by Schrodinger in 1912 in analogy with ferromagnets when he predicted the existence of liquids that can spontaneously polarize upon solidification [1]. The phenomenon was first discovered in Rochelle salt ($KNaC_4H_4O_6.4H_2O$) in 1920 by Valasek, a PhD student at the time, while investigating the dielectric properties of Rochelle salt [2]. This was followed by the discovery of ferroelectricity in potassium dihydrogen phosphate (KDP) salts (KH_2PO_4) in 1935 [3]. However, as both Rochelle salt and KDP were fragile and water soluble, it was difficult to utilize their ferroelectric properties in applications and ferroelectrics remained mostly an academic curiosity. The situation changed dramatically with the discovery of ferroelectricity in the inorganic perovskite $BaTiO_3$ (BTO) by independent groups in the US, USSR and Japan during the second world war [4, 5, 6, 7]. The relatively simple structure and high dielectric constant of BTO made it highly suitable for applications such as high energy density capacitors, sonars, transducers, etc. This discovery spurred worldwide experimental and theoretical interest in ferroelectrics from both fundamental and

application point of view and since then ferroelectrics have become one of the most widely used and well studied class of materials. In the following subsections, the major developments in the field of ferroelectrics since the discovery of BTO is divided into separate epochs. Although the development of the entire field is too vast a subject matter to cover here, the important developments that have a direct bearing on this dissertation are highlighted and provide a historical context for the motivation of this dissertation.

Late 1940's to 1970's: Concerted theoretical and experimental efforts to understand the physics of ferroelectrics began soon after the discovery of ferroelectric BTO. In the theoretical front, Ginzburg first extended Landau's phenomenological theory of phase transitions to BTO [8], which was further refined by Devonshire [9] to develop the full phenomenological theory of phase transitions in ferroelectrics - commonly referred to as the Landau-Ginzburg-Devonshire (LGD) theory. This model still forms the basis for the thermodynamic description of ferroelectrics and will be described in detail in Section 1.2. An important milestone in terms of understanding the microscopic mechanism of structural phase transitions in ferroelectrics was the soft mode concept put forward independently by Cochran [10] and Anderson [11]. The soft mode concept suggests the presence of an optical phonon mode in the high temperature paraelectric phase whose vibration frequency becomes zero or condenses at the transition temperature (T_c) leading to a structure of lower symmetry below T_c, which leads to the appearance of a spontaneous polarization.

In the decades following the discovery of BTO, ferroelectricity was discovered not only in more perovskite-based compounds such as $PbTiO_3$ (PTO), $Pb(Zr_x, Ti_{1-x})O_3$ (PZT) etc. [12] but also in non-perovskite compounds such as

lithium niobate $LiNbO_3$ (LNO) [13], triglycine sulphate (TGS) [14], boracites ($M_3B_7O_{13}X$, where M is a divalent metal and X is a halogen) [15] and polymers, such as polyvinylidene difluoride (PVDF) [16], to highlight a few. In addition to the material discovery aspects, several studies were conducted to understand the physics of polarization switching behavior in ferroelectrics. In this regard, the pioneering experimental works by Merz on BTO single crystals [17] and the phenomenological description of the switching process by Ishibashi [18] laid the foundations towards the understanding of the polarization switching process. The switching of polarization from one state to the other will be explored in detail in Section 1.3.

The majority of applications of ferroelectrics during this period utilized their piezoelectric and dielectric properties to make high density capacitors, transducers, etc. Interestingly, the possibility of the bi-stable polarization states in BTO to encode binary information for computer memory applications was quickly recognized and the concept of a ferroelectric-based memory (ferroelectric random access memory or FRAM) was proposed as early as 1952 by Buck [19]. Soon after, Bell labs produced a 256-bit memory in 1955, but the development of FRAM was beset with manufacturing challenges and was surpassed by dynamic random access memory (DRAM) and static random access memory (SRAM) in the late 1960's and 1970's. Finally we would like to point out that the majority of the studies during this period were focused on bulk single crystals or on ceramics.

mid-1980's up to 2010: This period saw a resurgence of interest in ferroelectric memories enabled by advances in thin film growth processes. Although development of ferroelectric thin films had started in the late 1960's [20, 21], it was not until the mid-1980's when advances in thin film processing techniques [22, 23] enabled the first demonstration of a ferroelectric thin film memory device integrated with silicon

[24]. This led to a flurry of research activities and the first commercial FRAMs became available by the early 1990's [25]. However, these perovskite-based FRAMs still suffered from issues related to compatibility with the complementary metal oxide semiconductor (CMOS) technology, such as severe degradation of the ferroelectric properties during forming gas annealing [26, 27, 28, 29], etching [30, 31], etc. Additionally, scaling limitations prevented the miniaturization of these devices beyond the 130-nm technology node [32]. Due to these issues, FRAMs were expensive compared to DRAM or SRAM and remained as a niche product [33], with progress stalling in the mid-2000's [34].

Nevertheless, with further advances in the processing of thin films, very high quality epitaxial thin films down to thicknesses of a few unit cells could be grown, which opened up avenues for the exploration of newer ferroelectric functionalities. One such important functionality is tunneling electroresistance, or the polarization dependent change in the electrical resistance [35]. This represents an alternative resistive-switching based non-volatile memory approach where the binary information can be encoded based on the high or low resistance states of the device.

In terms of experimental techniques, the inception of piezoresponse force microscopy (PFM) during the 1990's proved to be a major milestone in the nanoscale probing of ferroelectric properties [36, 37, 38, 39]. This non-destructive technique allowed the visualization and manipulation of domain structures with a lateral resolution of 25-30 nm, and along with quantitative PFM spectroscopic techniques led to profound insights on the local switching behavior. In this regard, the work done by Gruverman and co-workers on ferroelectric capacitor structures is particularly important in the context of ferroelectric memory applications [40, 41, 42, 43]. This technique heralded the exploration of nanoferroic phenomena and was instrumental in the discovery and demonstration of ferroelectric

functionalities such as tunneling electroresistance [44, 45], domain wall conductivity [46], nanoscale flexoelectricity [47] and so on [48]. This technique forms the basis of the majority of the studies done in this dissertation and will be described in detail in Chapter 2.1.2.

2010's to present: The discovery of ferroelectricity in the fluorite-structure doped hafnium oxide (HfO_2) thin films in 2011 [49] was a significant breakthrough towards the realization of commercial non-volatile ferroelectric memories due to its compatibility with the existing CMOS technology [50, 51]. The order of magnitude higher coercive fields in comparison to perovskite-based ferroelectrics, coupled with robust ferroelectricity down to thicknesses of 10 nm or lower, high remanent polarization values of 15-35 $\mu C/cm^2$ and high scalability makes HfO_2-based devices very promising for memory applications [?]. Already, ferroelectric field effect transistors in the 28-nm technology node were demonstrated in 2012 [52]. Going beyond the current von-Neumann computing architecture, logic in-memory HfO_2-based devices have also been demonstrated in the 28-nm and 22-nm fully depleted Si on insulator technology [53]. This is already a great starting point for further exploration and miniaturization for the HfO_2-based devices.

Finally, we would like to conclude this section by highlighting several other highly exciting research areas in ferroelectricity that have emerged over the past decade or so - nanoscale flexoelectricity, which provides a voltage-free approach towards polarization switching [47], the very nascent field of ferroelectricity in two-dimensional layered van der Waals materials such as $CuInP_2S_6$ (CIPS) [54], In_2Se_3 [55, 56] etc., which are promising for miniature functional devices, topological features such as vortex structures [57, 58, 59] and polar skyrmions [60], ferroelectric negative capacitance [61, 62] and so on.

1.1.1 Application perspectives

Since the discovery of BTO during the second world war, ferroelectrics have found wide scale applications in several different areas such as transducers, actuators, medical ultrasound, capacitors, computer memory applications and so on. Here, we highlight a few of the possible applications with a focus on electronic devices for memory applications.

Ferroelectric memories: Currently, there is a nearly five order of magnitude difference in the access times between dynamic random access memories (DRAM) (which is volatile) and non-volatile hard disk drives. Although flash memories have partially bridged this gap, they are still slow compared to DRAM with access times in the order of μs as compared to the tens of ns access times in DRAM. In addition, flash memories suffer from limited endurance and higher energy consumption. The fast read and write speeds ($\sim$ 10 ns) which are comparable to the state of the art dynamic random access memories (DRAM), coupled with non-volatility, lower energy consumption and high endurance make ferroelectric-based memories highly promising candidates for non-volatile random access memories (NV-RAM) [34]. The applicability of ferroelectrics in such memory applications originates from the electrically switchable bi-stable remanent polarization states, which can be used to encode digital information.

Ferroelectric tunnel junctions: Another class of promising candidates towards the realization of NV-RAM is based on the resistive switching (RS) phenomenon, in which the resistance state of the device can be changed by an external electric or magnetic field. In this regard, ferroelectric tunnel junctions (FTJ) are a type of RS device that exhibit tunneling electroresistance (TER) effect which is a polarization dependent change in the electrical resistance of the device [35]. In an FTJ, two

metal electrodes are separated by a sufficiently thin ferroelectric layer through which tunneling can take place. Reversal of polarization in the ferroelectric layer by an electric field leads to changes in the tunneling barrier potential profile giving rise to nonvolatile switching of the junction conductance. FTJ's have the advantages of high scalability, fast read and write access times, low energy consumption, non-destructive readout and non-volatility [63].

Neuromorphic computing: The ever increasing shift towards data-centric computing has led to the development of efficient artificial intelligence (AI)-based computing approaches such as artificial neural networks (ANN). ANN algorithms provide faster computations by mimicking the neural network of the human brain [64]. However, at the hardware level, such algorithms are implemented using the traditional von Neumann architecture in which there is data transfer between the logic and memory units leading to processing bottlenecks and increased power consumption [65]. Hence, there is an increasing push towards the hardware realization of beyond von Neumann architectures such as low power-consuming neuromorphic computing approaches that are based on emulating the neurons and synapses of the human brain. The realization of neuromorphic computing at the hardware level requires electronic devices that can act as artificial synapses and neurons. In this regard, ferroelectric-based devices with memristive functionality can emulate the biological synapses through the continuous tuning of their electrical resistance states. An example of a ferroelectric memristor is the ferroelectric tunnel junction (FTJ) described above, in which the resistance of the device depends on the volume fraction of domains with polarization pointing upwards or downwards [66]. Hence, a voltage-dependent tuning of the volume fraction of domains results in multiple resistance states [66].

Ferroelectrics are, thus, a very important class of ferroic materials with significant importance from both fundamental as well as functional device application perspectives. In the following sections, we look at some of the physical properties of ferroelectrics.

1.2 Ferroelectric phase transitions

The thermodynamic description of ferroelectrics is given by the phenomenological Landau-Ginzburg-Devonshire (LGD) theory of phase transitions. According to this theory, phase transition in ferroelectrics can be described in terms of a physical order parameter called the spontaneous polarization, P, which is zero above the paraelectric-ferroelectric phase transition temperature, T_0, and becomes finite below T_0. This is accompanied by a lowering of the symmetry from the high temperature symmetric phase to a lower symmetry phase below T_0. In this formalism, the Gibbs free energy density, ϕ, can be represented by a series expansion of the order parameter in the presence of an external electric field, E:

$$\phi = \phi_0 + \frac{1}{2}\alpha P^2 + \frac{1}{4}\beta P^4 + \frac{1}{6}\gamma P^6 - EP \tag{1.1}$$

where ϕ_0 is the polarization independent part of the free energy density, α, β and γ are expansion coefficients. The sign of β determines whether the phase transition is first ($\beta < 0$) or second ($\beta > 0$) order in nature, while γ is positive. Both β and γ are temperature independent coefficients. On the other hand, α is a temperature dependent coefficient which changes sign as a function of temperature upon crossing T_0 and is given by:

$$\alpha = \alpha_0(T - T_0), \;\; \alpha_0 > 0 \tag{1.2}$$

The ground state configuration can be obtained from the minimum of the free energy density (Eq. 1.1), referred to as the equation of state:

$$\frac{\partial \phi}{\partial P} = 0 \tag{1.3}$$

For a second order phase transition, $\beta > 0$ and $\gamma = 0$ such that the free energy density is reduced to

$$\phi = \phi_0 + \frac{1}{2}\alpha P^2 + \frac{1}{4}\beta P^4 - EP \tag{1.4}$$

and the equation of state (Eq. 1.3) correlates E and P as

$$E = \alpha P + \beta P^3 \tag{1.5}$$

When $E = 0$, the solution to Eq. 1.5 describes the appearance of spontaneous polarization below T_0 since $P = 0$ for $T > T_0$ and only for $T < T_0$, P becomes finite with the following two values:

$$P = \pm P_s = \pm(\alpha_0(T_0 - T)/\beta)^{1/2}, \;\; T < T_0 \tag{1.6}$$

Both of these values give the same free energy density, and hence they are degenerate in energy and represent the ground state of the system. Upon cooling below T_0, there is an equal probability of the polarization taking either of these two values unless there is an external perturbation. Fig. 1.1 (a) shows the variation of the free energy density as a function of temperature.

The dielectric susceptibility, $\chi(= \partial P/\partial E)$, is given by

$$\chi = \frac{1}{\alpha_0(T - T_0)} \equiv \frac{\epsilon_0 C}{T - T_0}, \;\; T > T_0 \tag{1.7}$$

$$\chi = \frac{\epsilon_0 C/2}{T_0 - T}, \ \ T < T_0 \tag{1.8}$$

where C is the Curie-Weiss constant and Eq. 1.7 is the well-known Curie-Weiss behavior for $T > T_0$. The susceptibility diverges at the transition temperature, T_0.

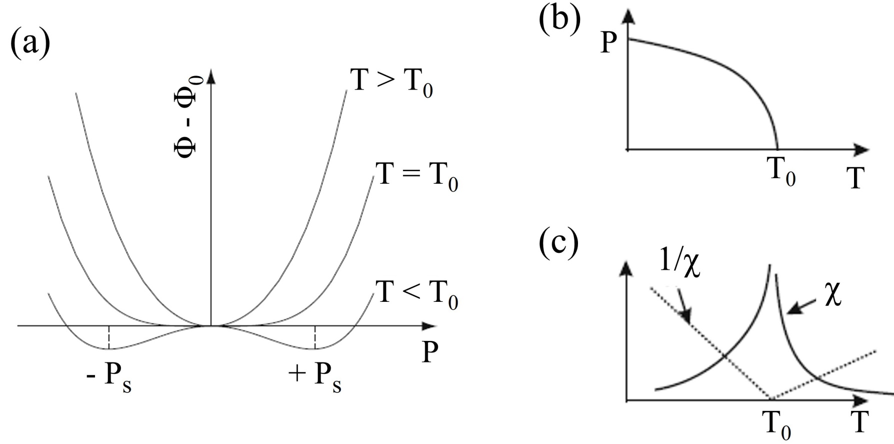

Figure 1.1. Features of second order phase transition. (a) Free energy density as a function of temperature for $T > T_0$, $T = T_0$, and $T < T_0$. (b) Variation of polarization with temperature showing a continuous transition. (c) Variation of the dielectric susceptibility (solid lines) and the inverse dielectric susceptibility (dotted lines) with temperature. Figure (a) adapted from [67]. Figures (b,c) adapted from [68].

One of the hallmarks of the second order phase transition is the continuous variation of the order parameter, P, with temperature (Fig. 1.1 (b)) while the dielectric susceptibility, χ, diverges at T_0 (Fig. 1.1 (c)). Another feature is that the paraelectric-ferroelectric phase transition temperature (T_0) is equal to the Curie temperature (T_C) in second order phase transitions.

On the other hand, there is a discontinuous variation of the order parameter, P, in a first order phase transition. Using the conditions $\beta < 0$ and $\gamma > 0$ in the free energy density given by Eq. 1.1, the equation of state obtained from Eq. 1.3 is:

$$E = \alpha P + \beta P^3 + \gamma P^5 \tag{1.9}$$

In the absence of an electric field, the solutions to Eq. 1.9 are:

$$P = 0, \tag{1.10}$$

$$P = \pm P_s = \pm\sqrt{\frac{\sqrt{\beta^2 - 4\alpha\gamma} - \beta}{2\gamma}} \tag{1.11}$$

In a first order phase transition, both of the above solutions with $P = 0$ and $P = \pm P_s$, corresponding to the paraelectric and ferroelectric states, respectively, can coexist between temperatures T_0 and T_1 with one of the solutions being metastable. The $P = \pm P_s$ solutions become the most stable states below the temperature T_0 and hence the system will exist only in the ferroelectric state below T_0. As the temperature is increased above T_0, both $P = 0$ and $P = \pm P_s$ states can coexist, with the $P = \pm P_s$ states lower in energy than the paraelectric state. With a further increase in temperature, the $P = 0$ and the $P = \pm P_s$ states become equal in energy at the Curie temperature, T_c, which is given by

$$T_c = T_0 + \frac{3\beta^2}{16\alpha_0\gamma} \tag{1.12}$$

Increasing the temperature beyond T_c results in the paraelectric state becoming more stable in energy and the paraelectric state becomes the only stable state above T_1 which is given by

$$T_1 = T_0 + \frac{\beta^2}{4\alpha_0\gamma} \tag{1.13}$$

Fig. 1.2 (a) shows the free energy density as a function of temperature, where the variation of the free energy density with respect to T_0, T_c and T_1 can be clearly observed. An important feature of the first order phase transition is the discontinuous jump of the polarization between the $P = 0$ and $P = \pm P_s$ solutions as shown in Fig. 1.2 (b).

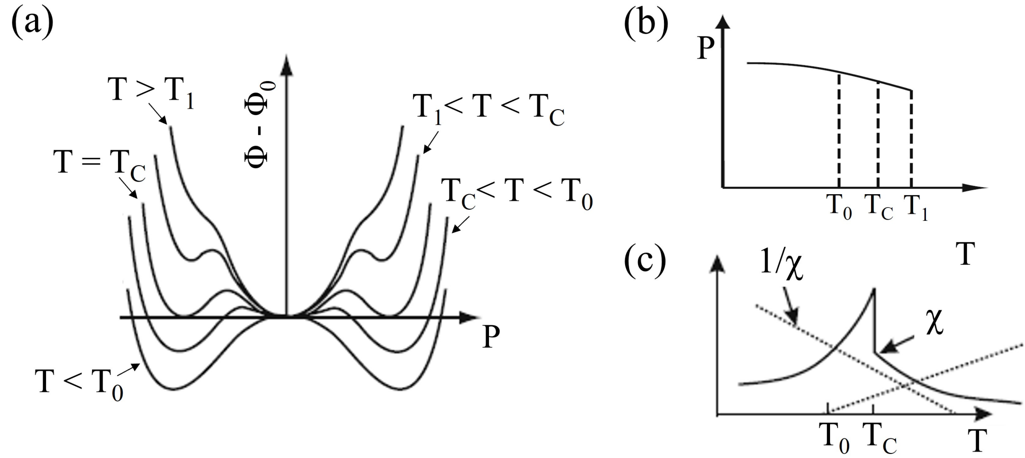

Figure 1.2. Features of first order phase transition. (a) Free energy density as a function of temperature for $T > T_0$, $T = T_0$, and $T < T_0$. (b) Variation of polarization with temperature showing a continuous transition. (c) Variation of the dielectric susceptibility (solid lines) and the inverse dielectric susceptibility (dotted lines) with temperature. Figures (a,b) adapted from [67] and (c) adapted from [68].

In the previous discussion it was seen that in both first and second order phase transitions, the order parameter vanishes above the transition temperature. Based upon the nature of the thermal motion of the atoms involved in the phase transition that gives rise to the spontaneous polarization, ferroelectrics can be very broadly generalized into two categories: (i) *displacive ferroelectrics*: The energy barrier between the two minima in the double well potential vanishes as the temperature is raised and the atoms responsible for the symmetry change at the phase transition perform small harmonic oscillations about their mean positions, and (ii)

order-disorder ferroelectrics: The double-well potential is temperature independent but due to the increase in temperature the atoms controlling the symmetry change oscillate between the minima in the double-well potential such that the average polarization is zero. Examples of ferroelectrics that exhibit displacive transitions are perovskite-based ferroelectrics such as BTO, PZT, etc.; while sodium nitrite ($NaNO_2$) is an example of an order-disorder ferroelectric [67].

Finally, we would like to conclude this section by analyzing the behavior of the double-well potential in the ferroelectric state under an applied electric field. In the presence of an electric field, the degeneracy of the two minima gets lifted and one polarization state becomes more energetically favorable over the other. At a sufficiently large electric field, called the coercive field, the polarization will switch to the energetically favorable state. After the field is removed, the polarization will continue to remain in this state because of the energy barrier between the two states. Such a behavior results in a hysteresis loop as shown in Fig. 1.3, and it is a characteristic feature of ferroelectrics.

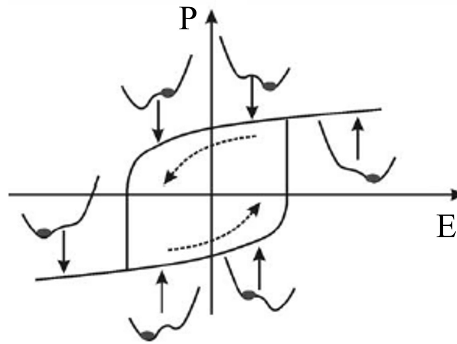

Figure 1.3. Polarization-electric field (P-E) hysteresis loop showing the correlation of the different configurations of the double well potential under an applied field with the different stages of the hysteresis loop. Figure adapted from [68].

The mechanism by which the polarization switches from one minima to the other in the presence of an electric field is discussed in the next section.

1.3 Polarization switching behavior

In ferroelectrics, the switching of polarization from one state to the other in presence of an electric field occurs in a three step process: (i) *nucleation* - domains of opposite polarization state (in the direction of the applied electric field) first nucleate at the ferroelectric-electrode interface, (ii) *forward growth*: nucleated domains grow in the forward direction till they reach the bottom electrode, and (iii) *lateral growth*: domain walls expand laterally or sidewise resulting in the expansion of the switched domains. This process was first identified by Merz [17, 69] and is schematically illustrated here in Fig. 1.4.

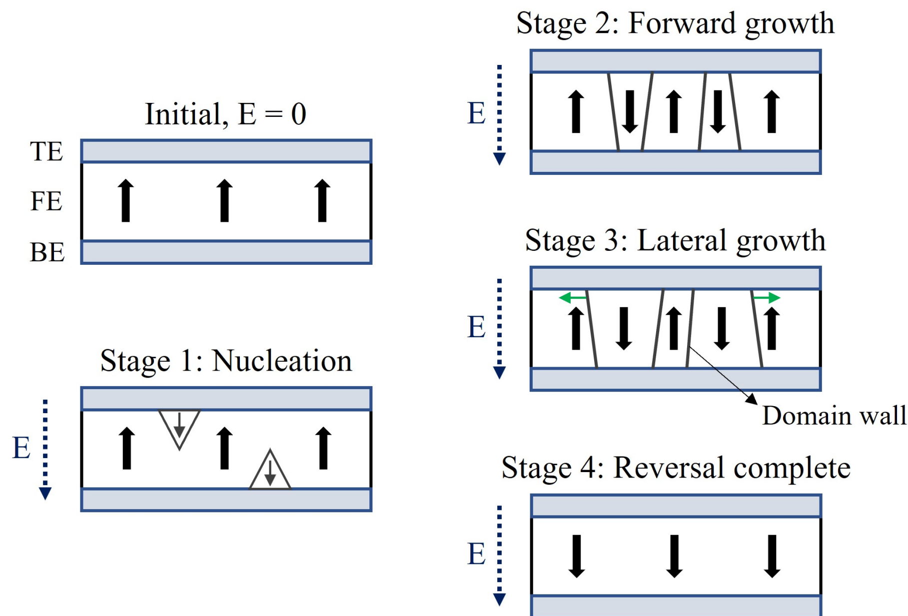

Figure 1.4. Schematic of the different stages of the polarization switching process in ferroelectrics. TE - Top electrode, FE - Ferroelectric, BE - Bottom electrode. The dotted arrows indicate the direction of the applied field, the solid arrows indicate the polarization direction in the ferroelectric layer, and the green arrows indicate the direction of lateral growth of the domain walls. Figure adapted from Ref. [70].

To understand the mechanism of polarization reversal in BTO single crystals, Merz

performed pulse switching measurements and observed an exponential dependence of the switching current, i_{max}, and the switching time, t_{sw}, with the applied electric field, E, encapsulated in the following empirical expressions

$$i_{max} = i_0 exp(-\alpha/E) \tag{1.14}$$

$$t_{sw} = t_0 exp(\alpha/E) \tag{1.15}$$

where α is a temperature dependent activation field which is related to the critical field required for the generation and growth of anti-parallel nuclei [17, 69]. In the BTO single crystals, the switching time was found to strongly depend on nucleation of new domains at low fields, while at high fields the switching time was found to be primarily dependent on the domain wall velocity. Theoretically, polarization switching models can be broadly divided into two classes depending on whether the rate-limiting parameter for switching is domain wall velocity or nucleation limited. These two models are discussed below.

Domain wall velocity is the rate-limiting factor: The Kolmogorov-Avrami-Ishibashi (KAI) model is based on a statistical theory of nucleation and domain growth in an infinite homogeneous medium with deterministic nucleation centers [18]. According to this model, polarization switching occurs by the expansion of nucleated domains via domain wall (DW) motion, and hence the DW velocity is the rate limiting factor. The nucleated domains can expand unrestricted till neighboring domains coalesce. The basic assumptions of this model are that the DW velocity depends only on the magnitude of the applied field and that the nucleation rate is either constant during the entire switching process or all the nuclei appear at the beginning of the

switching process. Under these assumptions, the fraction of switched polarization as a function of time, $\Delta P(t)$, was found to be

$$\Delta P(t) = 2P_s[1 - exp(-(t/t_0)^n)] \quad (1.16)$$

where P_s is the spontaneous polarization, t_0 is the characteristic switching time, and n is the effective dimension of domain growth.

The previous expression for fraction of switched polarization (Eq. 1.16) is valid when the electric field is time-independent (eg. for pulses with sufficiently short rise times). When using a time-varying electrical stimulus such as triangular pulses, the polarization switching mechanism can be found from the frequency dependence of the coercive field, E_c. In the context of DW velocity being the rate-limiting parameter, Ishibashi and Orihara extended the KAI model to obtain a power law, $E_c \sim f^\beta$, where f is the measurement frequency [71]. The exponent β is related to the dimension of domain growth, n, as $\beta = n/\alpha$, where $\alpha\,(\sim 6)$ [72] originates from the functional form of the applied waveform [71]. The value of β in the literature has been reported to be ~ 0.08 in multiferroic LiCuVO4 [73], ~ 0.1 in h-ErMnO3 single crystals [74], and ~ 0.23 in tryglycine sulphate [71] for pure domain wall motion.

The KAI model was found to be able to describe the polarization switching process in single crystals and epitaxial thin films [75, 76, 77], although the dimensionality of domain growth, n, often deviates from the integral values predicted by the theory [78]. The deviation of n from the integral values can occur because of the expansion of domains in multiple dimensions, e.g., in both forward ($n = 1$) as well as lateral dimensions ($n = 2$). Additionally, this model fails to capture the polarization switching behavior in highly disordered medium such as poly-crystalline films, where the nucleation limited mechanism (discussed below) is

found to be better suited.

Nucleation time is the rate-limiting factor: Du and Chen first put forward an alternate model in which the nucleation time for new domains is the limiting factor in the sense that the waiting time for a domain to nucleate is much longer than the time it takes for the domain wall to pass by that region [79]. In a disordered medium, pinning centers such as defects can act as an attractive potential well that can restrict the movement of domain walls at low fields. The nucleating domain needs to reach a critical size which can overcome the attractive potential well. In addition, the time required for the nucleating domain to reach the critical size and escape the potential well, τ, has an activation field type dependence on the applied electric field and the temperature given by [80] :

$$\tau = \tau_0 exp\left[\frac{1}{kT}\left(\frac{4\pi\gamma_b^2\gamma}{(\Delta P)^2}\right)\frac{1}{E^2}\right] \tag{1.17}$$

where γ is the domain wall energy, γ_b is the binding energy between the defects and the wall, ΔP is the polarization change due to the passing of the domain wall, T is the temperature, k is the Boltzmann constant and τ_0 is the cutoff time below which the nucleated domain cannot escape the attractive potential well. The coercive field is essentially the lowest field at which the nucleated domain can escape the potential well in a given time. With increasing field, the time required to escape reduces till it reaches the cutoff time τ_0. At a certain high frequency, f_0, the nucleated domain will not get enough time to escape the potential well and consequently there will be no polarization switching irrespective of the magnitude of the applied field. Hence, in this model there is a cutoff frequency, f_0, at which the coercive field is expected to diverge. The frequency dependence of the coercive field in the Du and Chen model has the following form:

$$\ln f = \ln f_0 - \frac{1}{kT}\left(\frac{4\pi\gamma_b^2\gamma}{(\Delta P)^2}\right)\frac{1}{E_c^2} = \ln f_0 - \frac{\alpha}{E_c^2} \tag{1.18}$$

It is important to note here that the Du-Chen model has an intrinsic temperature dependence. In situations where there is an ambiguity regarding the validity of the Du-Chen model over the KAI model in describing the polarization dynamics, performing temperature dependent measurements of the frequency dependence of the coercive field can help resolve the ambiguities [80].

Tagantsev and co-workers also developed a nucleation limited switching (NLS) model in which they considered a defect-rich film to be composed of an ensemble of microscopic regions switching independently of each other [81]. In this situation, there is a broad distribution of the nucleation waiting time in each of these regions and the waiting time is much longer than the time it takes to switch the region after the nucleation event. Hence, the nucleation time becomes the limiting parameter in this model and the time dependence of the switched polarization is given by the following expression [81]:

$$\Delta P(t) = 2P_s \int_{\infty}^{\infty} [1 - exp(-(t/t_0)^n)].F(logt_0).d(logt_0) \tag{1.19}$$

where P_s is the spontaneous polarization, $F(log(t_0))$ is a distribution function of the characteristic switching times, t_0 , and n is the effective dimension of domain growth. The distribution function is a Lorentzian function [82]:

$$F(logt_0) = \frac{A}{\pi}[\frac{w}{(logt_0 - logt_1)^2 + w^2}] \tag{1.20}$$

where A is a normalization constant, $2w$ is the full-width at half-maximum (FWHM) and $logt_1$ is the center of the distribution.

The nucleation limited mechanism successfully described the polarization switching behavior in polycrystalline PZT thin films [81, 82], $Ba_{0.5}Sr_{0.5}TiO_3$ (BST) thin films [80], polycrystalline HfO_2-based thin films [83, 84, 85], to give a few examples.

1.4 Piezoelectric behavior

Ferroelectrics are a subgroup of piezoelectric materials, and hence all ferroelectrics are piezoelectric. Piezoelectricity is a linear electromechanical coupling between the electrical and mechanical states of the system and occurs in non-centrosymmetric crystal structures. There are two kinds of piezoelectric effects:

(i) *Direct piezoelectric effect*: The polarization, P, induced in a piezoelectric material in response to an applied stress, σ, is proportional to the stress. Mathematically, it can be represented as:

$$P_i = d_{ijk}\sigma_{jk} \tag{1.21}$$

where d_{ijk} is the proportionality coefficient and is known as the piezoelectric tensor.

(ii) *Converse piezoelectric effect*: It refers to the mechanical deformation that a piezoelectric material undergoes in response to an applied electric field. Physically, the strain, η, developed is proportional to the applied electric field, E, and can be represented as:

$$\eta_{jk} = d_{ijk}E_i \tag{1.22}$$

where d_{ijk} is the same piezoelectric tensor that appears in the direct piezoelectric

effect. Although d_{ijk} is a third rank tensor with 27 components, it is symmetrical in j and k and the number of independent components reduce to 18. Taking advantage of the reduced number of independent components, the piezoelectric tensor is commonly represented in a two-dimensional matrix form (referred to as Voigt notation), d_{ij}

$$d_{ij} = \begin{pmatrix} d_{11} & d_{12} & d_{13} & d_{14} & d_{15} & d_{16} \\ d_{21} & d_{22} & d_{23} & d_{24} & d_{25} & d_{26} \\ d_{31} & d_{32} & d_{33} & d_{34} & d_{35} & d_{36} \end{pmatrix} \tag{1.23}$$

Depending on the symmetry of the particular piezoelectric crystal, the number of components can reduce further. In general, the piezoelectric coefficient in the direction of the applied electric field is known as the longitudinal piezoelectric coefficient and perpendicular to the electric field is known as the transverse coefficient. The other coefficients are referred to as the shear coefficients. It is worth pointing out here that the piezoelectric coefficients can be either positive or negative.

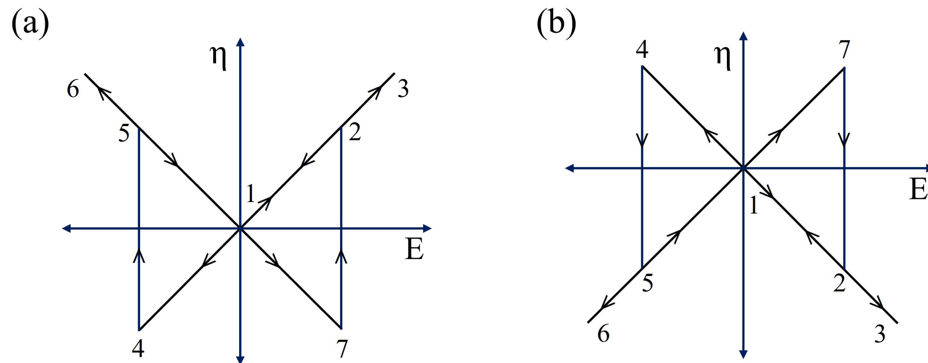

Figure 1.5. Strain-field ($\eta - E$) loop in an ideal ferroelectric with a positive (a) and negative (b) longitudinal piezoelectric coefficient.

A characteristic electromechanical feature of ferroelectrics with a positive longitudinal piezoelectric coefficient is the 'butterfly-shaped' strain-field ($\eta - E$)

loop as shown in Fig. 1.5 (a). The underlying principle is the converse piezoelectric effect (CPE) and the hysteresis arises due to polarization switching in the ferroelectric material. According to CPE, in a ferroelectric material with a
(i) *positive* longitudinal piezoelectric coefficient, the sample will expand (contract) when the polarization and electric field are oriented parallel (anti-parallel) to each other
(ii) *negative* longitudinal piezoelectric coefficient, the sample will contract (expand) when the polarization and electric field are oriented parallel (anti-parallel) to each other.

Let us first examine the shape of the $\eta - E$ loop for a positive longitudinal piezoelectric coefficient (Fig. 1.5 (a)). Starting from point 1, if the polarization was already in the downward direction then increasing the positive field will expand the ferroelectric and correspondingly the strain will increase linearly along the branch 1-2-3. Upon reducing the field, the strain decreases linearly along the branch 3-2-1 and then becomes negative along the branch 1-4. Negative strain reflects the contraction of the sample since the direction of the electric field and the polarization direction are anti-parallel. At point 4, due to the polarization switching the strain suddenly jumps to point 5 and becomes positive since the polarization and the field are now parallel to each other. Further increase of the field in the negative polarity leads to a linear increase along the branch 5-6. When the magnitude of the field is reduced, the strain reduces linearly along the branch 6-1. Similar to the branch 1-4, the strain is negative for the branch 1-7 and then suddenly jumps to a positive value at 2 due to the polarization switching. The points where the strain loop crosses the horizontal axis are the coercive field values. The shape of the $\eta - E$ loop in (Fig. 1.5 (b)) can be understood from a simple extension of the CPE principle for a negative longitudinal piezoelectric coefficient mentioned above. The particular

shape of the $\eta - E$ loops (Fig. 1.5 (a) vs. (b)) can be used to identify the sign of the longitudinal piezoelectric coefficients.

The piezoelectric property of ferroelectrics find a wide range of electromechanical applications such as nanopositioning systems, medical ultrasound transducers, sonars, high precision accelerometers and so on [86]. The majority of these applications are based on perovskite ferroelectrics, which are briefly described in the next section.

1.5 Perovskite ferroelectrics

A perovskite is a material that has the same ABO_3-type structure as the mineral called perovskite (calcium titanate) with the chemical formula ($CaTiO_3$). The 'A' cations typically comprise of large ions such as Ba^{2+}, Pb^{2+} and the 'B' cations are smaller transition metal ions such as Zr^{4+}, Ti^{4+}, etc. In the high symmetry cubic phase, the A^{2+} cations sit at the eight corners of the cube; while the B^{4+} cations are at the body center and forms an octahedron with the six O^{2-} anions at the face centers of the cube (Fig. 1.6 (a)). In the specific case of perovskite ferroelectrics, the cubic symmetry gets lowered below the transition temperature to a tetragonal phase, accompanied by a displacement of the B^{4+} cations with respect to the center of the octahedron which results in a net dipole moment in this lower symmetry phase ((Fig. 1.6 (b))).

Perovskite ferroelectrics are one of the most widely studied classes of ferroelectrics and as mentioned previously, was the material of choice in the FRAM technology. However, due to challenges related to Si compatibility and scaling, the perovskite-based FRAM technology is at least a decade behind the current state of the art DRAM and flash memory technology [34]. In this regard, the newly-discovered hafnia-based ferroelectrics might be a game changer due to inherent advantages compared

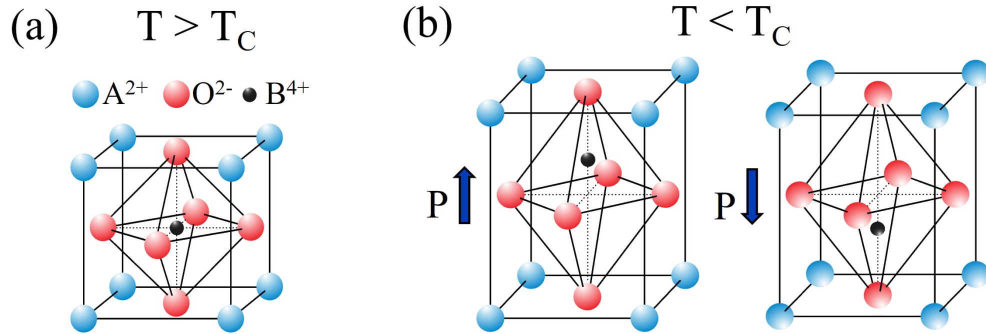

Figure 1.6. Crystal structure of perovskites in the high symmetric cubic phase (a) and in the lower symmetry tetragonal phase (b). In (b), displacement of the B^{4+} cations above or below the oxygen octahedron leads to a spontaneous polarization pointing upwards or downwards, respectively. T_c represents the transition temperature and the arrows denote the polarization directions. Figure adapted from [87].

to perovskites. In the next section, we look in detail the properties of ferroelectric hafnium oxide.

1.6 Hafnium oxide-based ferroelectrics

Ferroelectricity was first reported in Si-doped hafnium oxide ($Si : HfO_2$) thin films in 2011 [49]. Since then ferroelectricity has been demonstrated in HfO_2 or hafnia doped with Y [89], Zr [90], Al [91], Gd [92], La [93], Sr [94] as well as in pure HfO_2 [95] as shown in Fig. 1.7. Inherent advantages of ferroelectric HfO_2 over conventional perovskite films include compatibility with existing CMOS technology [50], thickness scalability [52], large bandgap (> 5 eV), which makes them resilient against leakage current and electrical breakdown, and they are lead-free. In addition, robust polarization and high switching endurance make them highly promising candidates for ferroelectric memory and logic devices [51, 96, 97]. This application potential has been emphasized by the development of functional HfO_2-based ferroelectric field effect transistors [52], demonstration of

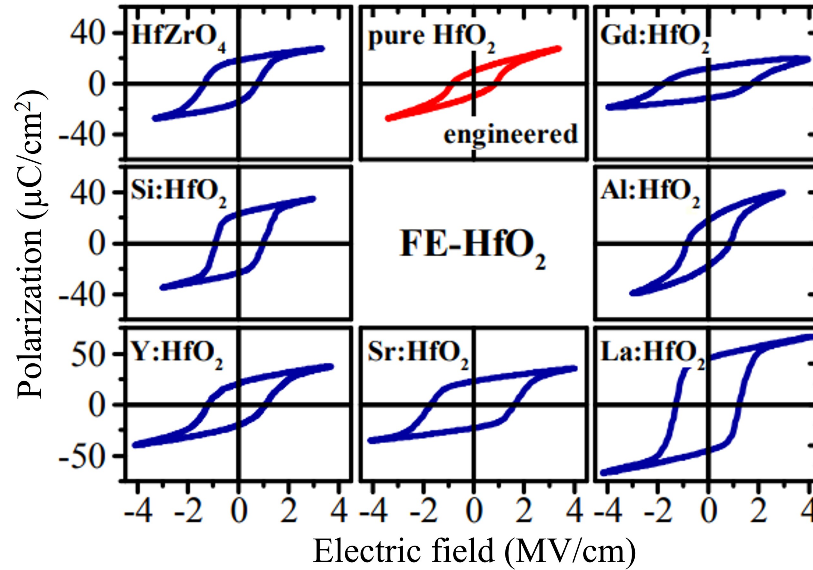

Figure 1.7. P-E loops demonstrating ferroelectricity in pure and doped-HfO_2. Figure adapted from [88].

polarization-controlled tunneling electroresistance effect in ultrathin HfO_2-based tunnel junctions [98, 99, 100, 101, 102, 103], memristors [104, 105], negative capacitance-based devices [106, 107, 108, 109], neuromorphic computing applications [110, 111, 112] etc.

Not only does ferroelectric hafnia have certain advantages, there are remarkable atypical intriguing features that set hafnia apart from traditional perovskite-based ferroelectrics. For instance, ferroelectricity gets enhanced (remanent polarization increases) as the hafnia film thickness reduces, with the best ferroelectric properties occurring below 20-30 nm depending on the dopant and the processing conditions [113, 114, 95, 115, 116, 117]. (It was only recently that ferroelectricity has been demonstrated in thick films ($>$ 100 nm) [118, 119] and in bulk hafnia crystals [120].) This is in sharp contrast to perovskite ferroelectrics where strong depolarization field effects at reduced thicknesses can suppress the ferroelectricity [121, 122]. The

resilience to depolarizing field effects at reduced dimensions might stem from the unique two dimensional nature of the polar layers in hafnia, which has a much smaller electrostatic energy cost in comparison to perovskite ferroelectrics, as a recent theoretical report suggested [123, 124]. Another fundamental question is with regards to the nature of the ferroelectricity itself in hafnia, with theoretical reports suggesting that the ferroelectricity is improper [123]. Moreover, there are conflicting reports regarding the sign of the longitudinal piezoelectric coefficient, d_{33}, in hafnia with theoretical predictions of a negative d_{33} [125, 126, 127] and most experimental results showing a positive d_{33} [49, 128, 129, 130]. It was only recently, and during the course of this dissertation, that a negative d_{33} was experimentally demonstrated [127]. This further highlights the uniqueness of hafnia-based ferroelectrics in comparison to other well-known perovskite-based ferroelectrics.

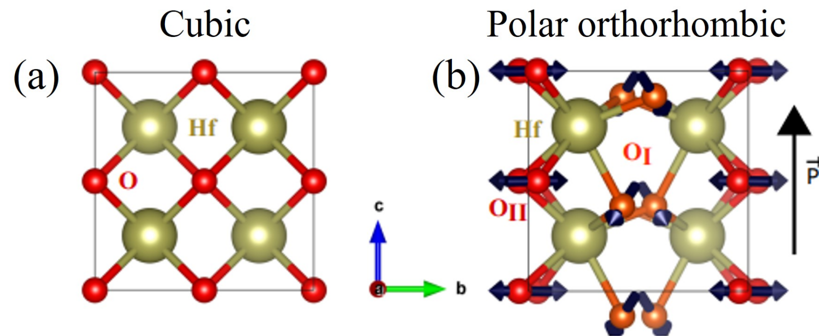

Figure 1.8. Structural polymorphs in hafnia. (a) Paraelectric cubic $Fm3m$ phase. (b) Polar orthorhombic $Pca2_1$ phase. Due to the downward shift of the O_I atoms, there is a net spontaneous polarization in the upward direction. Figure adapted from [127].

Ferroelectricity in hafnia is generally attributed to a polar orthorhombic phase (o-phase) of space group $Pca2_1$ [49, 131, 132], although there have been reports of another polar rhombohedral phase with $R3m$ symmetry [116]. The polar orthorhombic phase is not the ground state, however, and is unstable under ambient

temperature and pressure. Under ambient conditions, HfO_2 exists in a monoclinic phase (m-phase) with a space group $P2_1/c$. It undergoes a phase transition to a higher symmetric tetragonal phase (t-phase) of space group $P4_2/nmc$ above 1973 K and finally to a cubic $Fm3m$ phase above 2773 K under atmospheric pressure [133]. All of the above stable polymorphs of hafnia are centrosymmetric and, hence, are not ferroelectric. The polar o-phase emerges as an intermediate stage between the t-phase and the m-phases under compressive hydrostatic stress [134]. The ferroelectric phase can be stabilized via doping [90, 135], stress [114], controlling film thickness which becomes especially critical when using atomic layer deposition (ALD) [95, 113, 114], top electrode confinement [49], and surface energy considerations [136, 137]. Fig. 1.8 shows the structure of the cubic paraelectric and the polar orthorhombic phases. The spontaneous polarization in the $Pca2_1$ phase arises due to the shift of the O_I atoms as indicated in Fig. 1.8 (b).

On the other hand, thin-film ZrO_2, which is a sister compound of HfO_2 and is the state of the art gate dielectric in the DRAM industry [138], stabilizes in the t-phase [90]. Energetically, the total energy of the non-polar t-phase is lower than the polar o-phase by only $\sim$ 1 meV per formula unit with a barrier of $\sim$ 35 meV per formula unit separating the two phases [135]. The low energy barrier can be easily overcome by the application of a sufficiently large electric field such that there is a reversible field-induced phase transition between the non-polar t-phase and the polar o-phase, which makes ZrO_2 an antiferroelectric material.

Finally, we note that in this relatively new material it was important to understand the polarization switching process (especially with respect to the film microstructure), piezoelectric behavior and other technologically important properties such as imprint, switching speeds, and so on. Hence, the main motivation of this dissertation was to perform nanoscale investigations of the electrical and electromechanical behavior in

HfO_2 and ZrO_2-based thin film capacitors using a combination of high resolution PFM and pulse switching techniques.

References

[1] E. W. Schrödinger, Aus sen Sitzungsberichten der Kaiserl. Akademie der Wissenschaften in Wien. Mathem.-Naturw. Klasse. Bd. CXXI, Abt. Iia (1912).

[2] J. Valasek, Phys. Rev. **15**, 537 (1920); **17**, 475 (1920).

[3] G. Busch, and P. Scherrer, Naturwiss **23**, 737 (1935).

[4] H. Thurnaurer, and J. Deaderick, U.S. Patent No. 2, 429, 588, 1947; filed (1941).

[5] B. Wul, and J. M. Goldman, C.R. Acad. Sci. URSS **46**, 139 (1945).

[6] A. Von Hippel, R. G. Breckenridge, F. G. Chesley, and L. Tisza, Ind. Eng. Chem. **38**, 1097 (1946).

[7] T. Ogawa, and S. Waku (discovered 1944); T. Ogawa, Busseiron, Kenkyu **6**, 1 (1947).

[8] V. L. Ginzburg, Zh. Eksp. Teor. Fiz. **15**, 739 (1945); V. L. Ginzburg, J. Phys. USSR **10**, 107 (1946).

[9] A. F. Devonshire, Philos. Mag. **40**, 1040 (1949); A. F. Devonshire, Philos. Mag. **42**, 1065 (1951).

[10] W. Cochran, Phys. Rev. Lett. **3**, 8, 412 (1959); W. Cochran, Adv. Phys. **9**, 4, 387 (1960).

[11] P. W. Anderson, Fizika Dielektrikov, Moscow: Akad. Nauk SSSR, Fiz. Institute im. Lebedeva P.N..(1960).

[12] G. Shirane, and A. Takeda, J. Phys. Soc. Japan **7**, 1, 5 (1952); G. Shirane, K. Suzuki, and A. Takeda, J. Phys. Soc. Japan **7**, 1 (1952).

[13] B. T. Matthias, and J. Remeika, Phys. Rev. **76**, 12, 1886 (1949).

[14] B. T. Matthias, C. E. Miller, and J. Remeika, Phys. Rev. **104**, 3, 849 (1956).

[15] V. LeCorre, J. Phys. Radium **18**, 629 (1957).

[16] H. Kawai, Jpn. J. Appl. Phys. **8**, 975 (1969); R. G. Kepler, and R. A. Anderson, J. Appl. Phys. **49**, 1232 (1978).

[17] W. J. Merz, Phys. Rev. **95**, 690 (1954).

[18] A. N. Kolmogorov, Izv. Akad. Nauk SSSR Ser. Mater. **3**, 355 (1937); M.J. Avrami, Chem. Phys. **7**, 1103 (1939); Y. Ishibashi, and Y. J. Takagi, Phys. Soc. Jpn. **31**, 506 (1971).

[19] D. A. Buck, Ferroelectrics for digital information storage and switching, Master's thesis, MIT (1952).

[20] D. W. Chapman, J. Appl. Phys. **40**, 2381 (1969).

[21] B. S. Sharma, S. F. Vogel, and P. I. Prentky, Ferroelectrics **5**, 69 (1973).

[22] T. Nakagawa, J. Phys. Soc. Jpn. **18**, 897 (1979).

[23] K. D. Budd, S. K. Dey, and D. A. Payne, Proc. Br. Ceram. Soc. **36**, 107 (1985); S. K. Dey, K. D. Budd, and D. A. Payne, IEEE Transactions on Ultrasonics, Ferroelectrics, and Frequency Control **35**, 1, 80 (1988).

[24] G. A. Rohrer, and L. D. McMillan, U. S. Patent **4**, 707, 897 (1987).; L. McMillan, C. Araujo, and G. A. Rohrer, U. S. Patent **4**, 713, 157 (1987).

[25] D. Bondurant, Ferroelectrics **112**, 1, 273 (1990).

[26] K. Kushida-Abdelghafar, H. Miki, K. Torii, and Y. Fujisaki, Appl. Phys. Lett. **69**, 3188 (1996).

[27] Y. Shimamoto, K. Kushida-Abdelghafar, H. Miki, and Y. Fujisaki, Appl. Phys. Lett. **70**, 3096 (1997).

[28] J.-P. Han, and T. P. Ma, Appl. Phys. Lett. **71**, 1267 (1997).

[29] S. Aggarwal, S. R. Perusse, C. W. Tipton, R. Ramesh, H. D. Drew, T. Venkatesan, D. B. Romero, V. B. Podobedov, and A. Weber, Appl. Phys. Lett. **73**, 1973 (1998).

[30] W. Pan, C. L. Thio, S. B. Desu, and C. Chung, MRS Online Proceedings Library **361**, 93 (1994).

[31] C. Soyer, E. Cattan, D. Rèmiens, and M. Guilloux-Viry, J. Appl. Phys. **92**, 1048 (2002).

[32] J. Rodriguez, K. Remack, K. Boku, K.R. Udayakumar, S. Aggarwal, S. Summerfelt, T. Moise, H. McAdams, I. McPherson, R. Bailey, M. Depner, and G. Fox, IEEE International Reliability Physics Symposium. Proceedings, 200 (2004).

[33] T. Mikolajick, U. Schroeder, and S. Slesazeck, IEEE Transactions on Electron Devices **67**, 4, 1434 (2020).

[34] T. Schenk, M. Pešić, S. Slesazeck, U. Schroeder, and T. Mikolajick, Rep. Prog. Phys. **83**, 086501 (2020).

[35] E. Y. Tsymbal, and H. Kohlstedt, Science **313**, 5784, 181 (2006).

[36] P. Guthner, and K. Dransfeld, Appl. Phys. Lett. **61**, 1137 (1992).

[37] O. Kolosov, A. Gruverman, J. Hatano, K. Takahashi, and H. Tokumoto, Phys. Rev. Lett. **74**, 4309 (1995).

[38] A. Gruverman, O. Auciello, and H. Tokumoto, J. Vac. Sci. Technol. B **14**, 602 (1996).

[39] A. Gruverman, O. Auciello, and H. Tokumoto, Annu. Rev. Mater. Sci. **28**, 101, (1998).

[40] A. Gruverman, O. Auciello, and H. Tokumoto, Appl. Phys. Lett. **69**, 3191 (1996).

[41] A. Gruverman, B. J. Rodriguez, A. I. Kingon, R. J. Nemanich, A. K. Tagantsev, J. S. Cross, and M. Tsukada, Appl. Phys. Lett. **83**, 728 (2003).

[42] A. Gruverman, B. J Rodriguez, C. Dehoff, J. D. Waldrep, A. I. Kingon, R. J. Nemanich, and J. S. Cross, Appl. Phys. Lett. **87**, 082902 (2005).

[43] A. Gruverman, D. Wu, and J. F. Scott, Phys. Rev. Lett. **100**, 097601 (2008).

[44] V. Garcia, S. Fusil, K. Bouzehouane, S. Enouz-Vedrenne, N. D. Mathur, A. Barthélémy, and M. Bibes, Nature **460**, 81 (2009).

[45] A. Gruverman, D. Wu, H. Lu, Y. Wang, H. W. Jang, C. M. Folkman, M. Ye. Zhuravlev, D. Felker, M. Rzchowski, C.-B. Eom, and E. Y. Tsymbal, Nano Lett. **9**, 10, (2009).

[46] J. Seidel, L. W. Martin, Q. He, Q. Zhan, Y.-H. Chu, A. Rother, M. E. Hawkridge, P. Maksymovych, P. Yu, M. Gajek, N. Balke, S. V. Kalinin, S. Gemming, F. Wang, G. Catalan, J. F. Scott, N. A. Spaldin, J. Orenstein, and R. Ramesh, Nat. Mater. **8**, 229 (2009).

[47] H. Lu, C.-W. Bark, D. Esque de los Ojos, J. Alcala, C. B. Eom, G. Catalan, and A. Gruverman, Science **336**, 6077, 59 (2012).

[48] A. Gruverman, M. Alexe, and D. Meier, Nat. Commun. **10**, 1661 (2019).

[49] T. S. Boescke, J. Mueller, D. Braeuhaus, U. Schroeder, and U. Boetgger, Appl. Phys. Lett. **99**, 102903 (2011).

[50] M. T. Bohr, R. S. Chau, T. Ghani, and K. Mistry, IEEE Spectrum **44**, 10, 29 (2007).

[51] M. H. Park, Y. H. Lee, H. J. Kim, Y. J. Kim, T. Moon, K. D. Kim, J. Müller, A. Kersch, U. Schroeder, T. Mikolajick, and C. S. Hwang, Adv. Mater. **27**, 1811 (2015).

[52] J. Müller, E. Yurchuk, T. Schlösser, J. Paul, R. Hoffmann, S. Müller, D. Martin, S. Slesazeck, P. Polakowski, J. Sundqvist, M. Czernohorsky, K. Seidel, P. Kücher, R. Boschke, M. Trentzsch, K. Gebauer, U. Schröder, and T. Mikolajick, 2012 Symposium on VLSI Technology (VLSIT), 25 (2012).

[53] E. T. Breyer, H. Mulaosmanovic, T. Mikolajick, and S. Slesazeck, 2017 IEEE International Electron Devices Meeting (IEDM), 28.5.1 (2017).

[54] F. Liu, L. You, K. Seyler, X. Li, P. Yu, J. Lin, X. Wang, J. Zhou, H. Wang, H. He, S. Pantelides, W. Zhou, P. Sharma, X. Xu, P. Ajayan, J. Wang, and Z. Liu, Nat. Commun. **7**, 12357 (2016).

[55] C. Zheng, L. Yu, L. Zhu, J. L. Collins, D. Kim, Y. Lou, C. Xu, M. Li, Z. Wei, Y. Zhang, M. T. Edmonds, S. Li, J. Seidel, Y. Zhu, J. Z. Liu, W.-X. Tang, and M. S. Fuhre, Sci. Adv. **4**:eaar772 (2018).

[56] C. Cui, W.-J. Hu, X. Yan, C. Addiego, W. Gao, Y. Wang, Z. Wang, L. Li, Y. Cheng, P. Li, X. Zhang, H. N. Alshareef, T. Wu, W. Zhu, X. Pan, and L.-J. Li, Nano Lett. **18**, 1253 (2018).

[57] T. Choi, Y. Horibe, H. T. Yi, Y. J. Choi, W. Wu, and S. -W. Cheong, Nat. Mater. **9**, 423 (2010).

[58] T. Jungk, Á. Hoffmann, M. Fiebig, and E. Soergel, Appl. Phys. Lett. **97**, 012904 (2010).

[59] D. Meier, J. Seidel, A. Cano, K. Delaney, Y. Kumagai, M. Mostovoy, N. A. Spaldin, R. Ramesh, and M. Fiebig, Nature Mater. **11**, 284 (2012).

[60] S. Das, Y. L. Tang, Z. Hong, M. A. P. Gonçalves, M. R. McCarter, C. Klewe, K. X. Nguyen, F. Gómez-Ortiz, P. Shafer, E. Arenholz, V. A. Stoica, S.-L. Hsu, B. Wang, C. Ophus, J. F. Liu, C. T. Nelson, S. Saremi, B. Prasad, A. B. Mei, D. G. Schlom, J. Íñiguez, P. García-Fernández, D. A. Muller, L. Q. Chen, J. Junquera, L. W. Martin, and R. Ramesh, Nature **568**, 368 (2019).

[61] J. Íñiguez, P. Zubko, I. Luk'yanchuk, and A. Cano, Nat. Rev. Mater. **4**, 243 (2019).

[62] M. Hoffmann, S. Slesazeck, and T. Mikolajick, APL Mater. **9**, 020902 (2021).

[63] Z. Wen, and D. Wu, Adv. Mater. **32**, 1904123 (2020).

[64] C. Mead, Proceedings of the IEEE **78**, 10, 1629 (1990).

[65] V. K. Sangwan, and M. C. Hersam, Nat. Nanotechnol. **15**, 517 (2020).

[66] A. Chanthbouala, V. Garcia, R. O. Cherifi, K. Bouzehouane, S. Fusil, X. Moya, S. Xavier, H. Yamada, C. Deranlot, N. D. Mathur, M. Bibes, A. Barthélémy, and J. Grollier, Nature Mater. **11**, 860 (2012).

[67] A. K. Tagantsev, L. E. Cross, and J. Fousek, *Domains in Ferroic Crystals and Thin Films* (Springer-Verlag, New York 2010).

[68] K. Rabe, Ch. H. Ahn, and J.-M. Triscone, (Eds.) Physics of Ferroelectrics: A Modern Perspective (Springer-Verlag, Berlin Heidelberg 2007).

[69] W. J. Merz, J. Appl. Phys. **27**, 8 (1956).

[70] M. Dawber, K. M. Rabe, and J. F. Scott, Rev. Mod. Phys. **77**, 4, (2005).

[71] Y. Ishibashi, and H. Orihara, Integr. Ferroelectr. **9**, 1, 57 (1995).

[72] J. F. Scott, Integr. Ferroelectr. **12**, 2, 71 (1996).

[73] A. Ruff, A. Loidl, and S. Krohns, Materials **10**, 1318 (2017).

[74] A. Ruff, Z. Li, A. Loidl, J. Schaab, M. Fiebig, A. Cano, Z. Yan, E. Bourret, J. Glaum, D. Meier, and S. Krohns, Appl. Phys. Lett. **112**, 182908 (2018).

[75] Y. Ishibashi, and Y. J. Takagi, Phys. Soc. Jpn. **31**, 506 (1971).

[76] Y. W. So, D. J. Kim, T. W. Noh, J.-G. Yoon, and T. K. Song, Appl. Phys. Lett. **86**, 092905 (2005).

[77] D. Wu, I. Vrejoiu, M. Alexe, and A. Gruverman, Appl. Phys. Lett. **96**, 112903 (2010).

[78] V. Shur, E. Rumyantsev, and S. Makarov, J. Appl. Phys. **84**, 445 (1998).

[79] X. Du, and I.-W. Chen, MRS Online Proc. Libr. **493**, 311 (1997).

[80] D. J. Jung, M. Dawber, J. F. Scott, L. J. Sinnamon, and J. M. Gregg, Integr. Ferroelectr. **48**, 1, 59 (2002).

[81] A. K. Tagantsev, I. Stolichnov, N. Setter, J. S Cross, and M. Tsukada, Phys. Rev. B **66**, 214109 (2002).

[82] J. Y. Jo, H. S. Han, J.-G Yoon, T. K. Song, S. H. Kim, and T. W. Noh, Phys. Rev. Lett. **99**, 267602 (2007).

[83] H. Mulaosmanovic, J. Ocker, S. Müller, U. Schroeder, J. Müller, P. Polakowski, S. Flachowsky, R. van Bentum, T. Mikolajick, and S. Slesazeck, ACS Appl. Mater. Interfaces **9**, 3792 (2017).

[84] P. Buragohain, C. Richter, T. Schenk, H. Lu, T. Mikolajick, U. Schroeder, and A. Gruverman, Appl. Phys. Lett. **112**, 222901 (2018).

[85] M. Materano, P. D. Lomenzo, H. Mulaosmanovic, M. Hoffmann, A. Toriumi, T. Mikolajick, and U. Schroeder, Appl. Phys. Lett. **117**, 262904 (2020).

[86] S. T.-McKinstry, Am. Cer. Soc. Bull. **99**, 1 (2020).

[87] From Wikipedia, by Pinin - Own work, Public Domain
`(https://commons.wikimedia.org/w/index.php?curid=11103109)`

[88] J. Müller, P. Polakowski, S. Riedel, S. Mueller, E. Yurchuk, and T. Mikolajick, 14th Annual Non-Volatile Memory Technology Symposium (NVMTS), 1 (2014).

[89] J. Müller, U. Schröder, T. S. Böscke, I. Müller, U. Böttger, L. Wilde, J. Sundqvist, M. Lemberger, P. Kücher, T. Mikolajick, and L. Frey, J. Appl. Phys. **110**, 114113 (2011).

[90] J. Müller, T. S. Böscke, U. Schröder, S. Mueller, D. Bräuhaus, U. Böttger, L. Frey, and T. Mikolajick, Nano Lett. **12**, 8, 4318 (2012).

[91] S. Mueller, J. Mueller, A. Singh, S. Riedel, J. Sundqvist, U. Schroeder, and T. Mikolajick, Adv. Funct. Mater. **22**, 2412 (2012).

[92] S. Mueller, C. Adelmann, A. Singh, S. Van Elshocht, U. Schroeder, and T. Mikolajick, ECS J. Solid State Sci. Technol. **1**, N123 (2012).

[93] J. Müller, T.S. Böscke, S. Müller, E. Yurchuk, P. Polakowski, J. Paul, D. Martin, T. Schenk, K. Khullar, A. Kersch, W. Weinreich, S. Riedel, K. Seidel, A. Kumar, T.M. Arruda, S.V. Kalinin, T. Schlösser, R. Boschke, R. van Bentum, U. Schröder, and T. Mikolajick, 2013 IEEE International Electron Devices Meeting, 10.8.1-10.8.4 (2013).

[94] T. Schenk, S. Mueller, U. Schroeder, R. Materlik, A. Kersch, M. Popovici, C. Adelmann, S. Van Elshocht, and T. Mikolajick, 2013 Proceedings of the European Solid-State Device Research Conference (ESSDERC), 260-263 (2013).

[95] P. Polakowski, and J. Müller, Appl. Phys. Lett. **106**, 232905 (2015).

[96] J. F. Scott, *Ferroelectric Memories* (Springer, Berlin, 2000).

[97] See "International Technology Roadmap for Semiconductors - 2013 Emerging Research Devices" @ http://www.itrs2.net/itrs-reports.html.

[98] F. Ambriz-Vargas, G. Kolhatkar, M. Broyer, A. Hadj-Youssef, R. Nouar, A. Sarkissian, R. Thomas, C. Gomez-Yáñez, M. A. Gauthier, and A. Ruediger, ACS Appl. Mater. Interfaces **9**, 13262 (2017).

[99] A. Chouprik, A. Chernikova, A. Markeev, V. Mikheev, D. Negrov, M. Spiridonov, S. Zarubin, and A. Zenkevich, Microelectron. Eng. **178**, 250 (2017).

[100] H. Y. Yoong, H. Wu, J. Zhao, H. Wang, R. Guo, J. Xiao, B. Zhang, P. Yang, S. J. Pennycook, N. Deng, X. Yan, and J. Chen, Adv. Funct. Mater. **28**, 1806037 (2018).

[101] L. Chen, T.-Y. Wang, Y.-W. Dai, M.-Y. Cha, H. Zhu, Q.-Q. Sun, S.-J. Ding, P. Zhou, L. Chua, and D. W. Zhang, Nanoscale **10**, 15826 (2018).

[102] J. Yoon, S. Hong, Y. W. Song, J.-H. Ahn, and S.-E. Ahn, Appl. Phys. Lett. **115**, 153502 (2019).

[103] P. Chaudhary, P. Buragohain, M. Kozodaev, S. Zarubin, V. Mikheev, A. Chouprik, A. Lipatov, A. Sinitskii, A. Zenkevich, and A. Gruverman, Appl. Phys. Lett. **118**, 083106 (2021).

[104] V. Mikheev, A. Chouprik, Y. Lebedinskii, S. Zarubin, Y. Matveyev, E. Kondratyuk, M. G. Kozodaev, A. M. Markeev, A. Zenkevich, and D. Negrov, ACS Appl. Mater. Interfaces **11**, 32108 (2019).

[105] V. Mikheev, A. Chouprik, Y. Lebedinskii, S. Zarubin, A. M. Markeev, A. V. Zenkevich, and D. Negrov, Nanotechnology **31**, 215205 (2020).

[106] M. Hoffmann, M. Pešić, K. Chatterjee, A. I. Khan, S. Salahuddin, S. Slesazeck, U. Schroeder, and T. Mikolajick, Adv. Funct. Mater. **26**, 8643 (2016).

[107] F. A McGuire, Y.-C. Lin, K. Price, G. B. Rayner, S. Khandelwal, S. Salahuddin, and A. D. Franklin, Nano Lett. **17**, 8, 4801 (2017).

[108] M. Si, C.-J. Su, C. Jiang, N. J. Conrad, H. Zhou, K. D. Maize, G. Qiu, C.-T. Wu, A. Shakouri, M. A. Alam, and P. D. Ye, Nat. Nanotech. **13**, 24 (2018).

[109] M. Hoffmann, F. P. G. Fengler, M. Herzig, T. Mittmann, B. Max, U. Schroeder, R. Negrea, P. Lucian, S. Slesazec, and T. Mikolajick, Nature **565**, 464 (2019).

[110] H. Ryu, H. Wu, F. Rao, and W. Zhu, Scientific Reports **9**, 20383 (2019).

[111] S. Oh, H. Hwang, and I. K. Yoo, APL Materials **7**, 091109 (2019).

[112] B. Max, M. Hoffmann, H. Mulaosmanovic, S. Slesazeck, and T. Mikolajick, ACS Appl. Electron. Mater. **2**, 12, 4023 (2020).

[113] E. Yurchuk, J. Müller, S. Knebel, J. Sundqvist, A. P. Graham, T. Melde, U. Schröder, and T. Mikolajick, Thin Solid Films **533**, 88 (2013).

[114] M. H. Park, H. J. Kim, Y. J. Kim, T. Moon, and C. S. Hwang, Appl. Phys. Lett. **104**, 072901 (2014).

[115] U. Schroeder, C. Richter, M. H. Park, T. Schenk, M. Pešić, M. Hoffmann, F. P. G. Fengler, D. Pohl, B. Rellinghaus, C. Zhou, C.-C. Chung, J. L. Jones, and T. Mikolajick, Inorg. Chem. **57**, 5, 2752 (2018).

[116] Y. Wei, P. Nukala, M. Salverda, S. Matzen, H. J. Zhao, J. Momand, A. S. Everhardt, G. Agnus, G. R. Blake, P. Lecoeur, B. J. Kooi, J. Íñiguez, B. Dkhil, and B. Noheda, Nature Mater. **17**, 1095 (2018).

[117] T. Song, R. Bachelet, G. Saint-Girons, N. Dix, I. Fina, and F. Sánchez, J. Mater. Chem. C **9**, 12224 (2021).

[118] T. Mimura, T. Shimizu, and H. Funakubo, Appl. Phys. Lett. **115**, 032901 (2019).

[119] T. Schenk, N. Godard, A. Mahjoub, S. Girod, A. Matavz, V. Bobnar, E. Defay, and S. Glinsek, Phys. Status Solidi RRL **14**, 1900626 (2020).

[120] X. Xu, F.-T. Huang, Y. Qi, S. Singh, K. M. Rabe, D. Obeysekera, J. Yang, M.-W. Chu, and S.-W. Cheong, Nature Mater. **20**, 826 (2021).

[121] J. Junquera, and P. Ghosez, Nature **422**, 506 (2003).

[122] D. J. Kim, J. Y. Jo, Y. S. Kim, Y. J. Chang, J. S. Lee, Jong-Gul Yoon, T. K. Song, and T. W. Noh, Phys. Rev. Lett. **95**, 237602 (2005).

[123] H.-J. Lee, M. Lee, K. Lee, J. Jo, H. Yang, Y. Kim, A. C. Chae, U. Waghmare, and J. H. Lee, Science **369**, 6509, 1343 (2020).

[124] B. Noheda, and J. Íñiguez, Science **369**, 1300 (2020).

[125] J. Liu, S. Liu, L. H. Liu, B. Hanrahan, and S. T. Pantelides, Phys. Rev. Appl. **12**, 034032 (2019).

[126] J. Liu, S. Liu, J.-Y. Yang, and L. Liu, Phys. Rev. Lett. **125**, 197601 (2020).

[127] S. Dutta, P. Buragohain, S. Glinsek, C. Richter, H. Aramberri, H. Lu, U. Schroeder, E. Defay, A. Gruverman, and J. Íñiguez, Nat. Commun. **12**, 7301 (2021).

[128] T. Schenk, N. Godard, A. Mahjoub, S. Girod, A. Matavz, V. Bobnar, E. Defay, and S. Glinsek, Phys. Status Solidi RRL **14**, 1900626 (2020).

[129] R. Shimura, T. Mimura, A. Tateyama, T. Shimizu, T. Yamada, Y. Tanaka, Y. Inoue, and H. Funakubo, Jpn. J. Appl. Phys. **60**, 031009 (2021).

[130] J. Muller, P. Polakowski, S. Mueller, and T. Mikolajick, ECS J. Solid State Sci. Technol. **4**, N30 (2015).

[131] X. Sang, E. D. Grimley, T. Schenk, U. Schroeder, and J. M. LeBeau, Appl. Phys. Lett. **106**, 162905 (2015).

[132] E. D. Grimley, T. Schenk, X. Sang, M. Pešić, U. Schroeder, T. Mikolajick, and J. M. LeBeau, Adv. Electron. Mater. **2**, 1600173 (2016).

[133] O. Ohtaka, H. Fukui, T. Kunisada, T. Fujisawa, K. Funakoshi, W. Utsumi, T. Irifune, K. Kuroda, and T. Kikegawa, J. Am. Ceram. Soc., **84**, 6, 1369 (2001).

[134] E. H. Kisi, J. Am. Ceram. Soc. **81**, 3, 741 (1998).

[135] S. E. Reyes-Lillo, K. F. Garrity, and K. M. Rabe, Phys. Rev. B. **90**, 140103(R) (2014).

[136] R. Materlik, C. Kunneth, and A. Kersch, J. Appl. Phys. **117**, 134109 (2015).

[137] M. H. Park, Y. H. Lee, H. J. Kim, T. Schenk, W. Lee, K. Do Kim, F. P. Fengler, T. Mikolajick, U. Schroeder, and C. S. Hwang, Nanoscale **9**, 28, 9973 (2017).

[138] D.-S. Kil, H.-S. Song, K.-J. Lee, K. Hong, J.-H. Kim, K.-S. Park, S.-J. Yeom, J.-S. Roh, N.-J. Kwak, H.-C. Sohn, J.-W. Kim, and S.-W. Park, 2006 Symposium on VLSI Technology, 2006. Digest of Technical Papers, 38–39 (2006).

Chapter 2

Experimental methods

The bulk of the work presented in this dissertation has been performed using scanning probe microscopy-based techniques such as piezoresponse force microscopy (PFM) in conjunction with pulse switching measurements. In scanning probe microscopy, a nanoscopic probe rasters over a sample surface to detect a specific surface property depending on the type of probe-sample interaction being measured. On the other hand, pulse switching measurements involve the application of DC voltages with different waveforms to measure various parameters related to the polarization switching process in ferroelectric materials. In this chapter, a brief summary of the experimental methods used in this dissertation is presented.

2.1 Scanning probe microscopy

Richard Feynman, in his talk "There is plenty of room at the bottom" given at Caltech in 1959, first suggested the enormous potential of exploring nanoscale features [1]. It was not until the invention of the scanning tunneling microscope (STM) in 1981 by Binnig and Rohrer that made the visualization and manipulation of atomic features of surfaces down to the nanoscale an experimental reality [2], for which they won the Nobel prize in Physics in 1986. STM is based on the quantum tunneling effect, whereby the tunneling current between an atomically sharp metallic tip and a conducting or semiconducting sample is used to profile the sample surface. Since the tunneling current depends on the tip-sample separation distance,

maintaining a constant tunneling current using a feedback loop while the tip scans over the sample surface generates a two-dimensional surface topography image with atomic resolution. The invention of the atomic force microscope (AFM) in 1986 by Binnig, Quate and Gerber [3] extended the possibility of nanoscale imaging of surfaces to insulators through the detection of the tip-sample interatomic forces instead of the tunneling current which had limited the applicability of STM to conductors or semiconductors. The invention of STM and AFM, which are types of scanning probe microscopes (SPMs), have been crucial to the development of the field of nanoscience and nanotechnology [4]. Since then, different SPM-based techniques have expanded the applicability of SPM to investigate electrical, magnetic, optical and mechanical properties down to the level of several tens of nanometres thereby opening a pathway for the understanding and exploration of nanoscale functionalities.

2.1.1 Atomic force microscopy

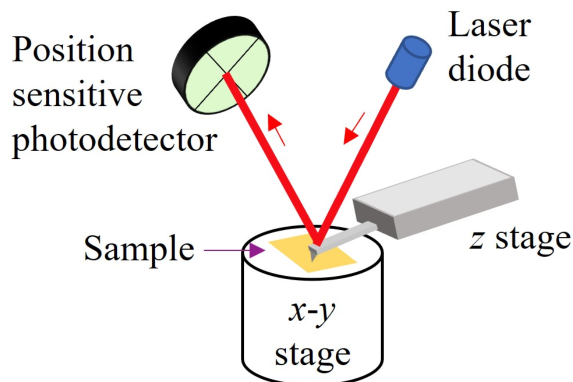

Figure 2.1. Schematic of a typical AFM setup. An optical beam is reflected off of the back of the cantilever and is collected on the four segment position sensitive photodetector (PSD). The sample is mounted on an $x - y$ piezoelectric stage and the cantilever is mounted on to a z piezoelectric stage.

In AFM, the tip-sample interatomic forces are used as a feedback control to determine the tip-sample separation distance. The tip is mounted on the end of a cantilever that can detect forces such as van der Waals force, electrostatic force, magnetic force, etc. down to the pN range [3]. A typical AFM setup is shown in Fig. 2.1. Most AFM setups are based on the optical beam deflection (OBD) method [5] in which a light beam reflected off the back of the cantilever is collected on a four-segment position-sensitive photodetector (PSD). The cantilever deflection is monitored as a change in the position of the reflected beam spot in the PSD. A feedback loop maintains a constant tip-sample force by adjusting the tip-sample separation distance or the z-position. In one configuration, the sample is mounted on a piezoelectric actuator that adjusts the z-position to maintain a constant tip-sample force; while in another configuration, the tip is attached to a piezoelectric actuator to adjust the z-position. The scanning in the x and y directions is performed through additional piezoelectric actuators by either moving the sample with respect to the tip or vice-versa. For the specific case of the Asylum Research MFP3D AFM system used in this dissertation, the sample is mounted on an $x-y$ piezoelectric stage, while the cantilever is mounted on a z-piezoelectric actuator.

One of the key principles towards understanding the AFM operation is the tip-sample force-distance curve that ultimately determines the AFM operating mode (Fig. 2.2). Depending on the tip-sample separation distance, the tip can experience either short-range repulsive forces due to the overlap of electronic orbitals or long-range attractive forces such as van der Waals or electrostatic forces. When the tip-sample separation distance is very small, the short-range forces dominate and the resolution approaches the atomic scale. As the separation distance increases, the long range forces start to dominate and the interaction between the tip apex and the surface atoms gets smeared out over multiple atoms resulting in a reduced resolution.

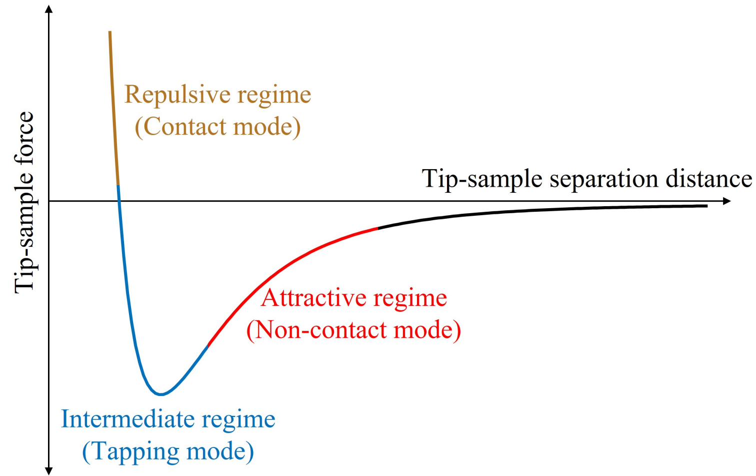

Figure 2.2. Different force regimes as a function of the tip-sample separation distance. The different operating modes of AFM are also indicated.

The operating modes of AFM can be broadly divided into static and dynamic modes depending on whether the static or dynamic deflection of the cantilever are measured, respectively. These modes can be further subdivided depending on the force regime - *contact* (static) mode operated in the repulsive force regime, *non-contact* (dynamic) mode operated in the attractive force regime and an intermediate *tapping* (dynamic) mode that experiences both attractive and repulsive forces intermittently (Fig. 2.2).

In the *contact* mode, the tip is in mechanical contact with the sample surface and the tip-sample separation distance is maintained by keeping the cantilever deflection constant (i.e., constant tip-sample force) during scanning. Since the cantilever deflection is kept constant, the contact mode is an example of a static mode.

In the *dynamic* mode, the tip is maintained at a small distance above the sample surface and is oscillated mechanically by a piezoelectric actuator at or near the cantilever resonance frequency. From the changes in the corresponding oscillation amplitude, phase and resonance frequency due to the tip-sample interaction forces,

different sample surface properties can be mapped out. If the changes in the amplitude are monitored, then the dynamic mode is referred to as *amplitude-modulation* (AM-AFM), while in the *frequency-modulation* (FM-AFM) mode the changes in the resonance frequency are monitored. In the FM-AFM mode, the cantilever is oscillated with a fixed amplitude at its resonance frequency and the changes in the resonance frequency are used as the feedback signal to adjust the tip-sample separation distance. In the AM-AFM mode, the cantilever is oscillated near its resonance frequency and the changes in the amplitude signal are used as the feedback to adjust the tip-sample separation distance. Depending on the force regime, there can be two modes of dynamic AFM - *non-contact* mode and *tapping* mode. The *non-contact* mode is operated in the attractive force regime and either AM-AFM or FM-AFM modes can be used to image the sample surface in this regime. The *tapping* mode works in an intermediate force range where the tip can experience both attractive and repulsive forces intermittently. It is typically operated in the AM-AFM mode and is the most widely used operational mode of AFM due to higher resolution compared to the *non-contact* mode and can preserve the sharpness of the tip and is more gentle on the surface than the *contact* mode.

2.1.2 Piezoresponse force microscopy

Piezoresponse force microscopy (PFM) is a voltage modulated mode of AFM which can be used to detect a local electromechanical response in piezoelectrically active materials such as ferroelectrics. It is operated in the contact AFM mode where an oscillating electric field applied via a conductive tip in contact with the sample leads to periodic sample deformation due to the converse piezoelectric effect (see Section 1.4 in Chapter 1). According to the converse piezoelectric effect, the mechanical strain, η, generated due to an applied electric field, E, is given by:

$$\eta_{ij} = d_{ij} E_i \tag{2.1}$$

where d_{ij} are the piezoelectric coefficients in matrix notation. The piezoelectric coefficients are related to the dielectric constant, ϵ_{ij}, electrostriction coefficients, Q_{ijk}, and the spontaneous polarization, P_i, in a ferroelectric as [6]:

$$d_{ij} = 2\epsilon_{im} Q_{jmk} P_k \tag{2.2}$$

Due to the linear coupling between the piezoelectric coefficients and the spontaneous polarization, the sample will either expand or contract depending on the mutual direction of the applied field and the direction of polarization, which gives information regarding the domain polarity. However, the small value of the piezoelectric coefficient (typically around tens of pm/V) makes it very difficult to detect the static expansion or contraction of the sample. To overcome this limitation, an AC modulation field is applied to excite the electromechanical response from the sample, and this AC response is then detected and amplified using lock-in amplifiers. More specifically, the AC modulation voltage applied to the tip

$$V_{tip} = V_{ac} cos(\omega t) \tag{2.3}$$

results in a sample deformation, z, due to the converse piezoelectric effect, given by

$$z = A_{1\omega} cos(\omega t + \phi) \tag{2.4}$$

where $A_{1\omega}$ is the first harmonic oscillation amplitude and ϕ is the phase shift with respect to the applied voltage. The PFM amplitude, $A_{1\omega}$, and the PFM phase, ϕ, are

related to the magnitude and sign of the piezoelectric coefficients. We illustrate this by taking the example of a sample with an out-of-plane polarization direction, P_3. In this situation, the relevant piezoelectric coefficient is d_{33} and the PFM amplitude, $A_{1\omega}$, is given by

$$A_{1\omega} = d_{33,eff}V_{ac} \tag{2.5}$$

Please note that, in practice, other coefficients of the piezoelectric tensor can also make a contribution to the out-of-plane signal such that an effective longitudinal piezoelectric coefficient, $d_{33,eff}$, is measured.

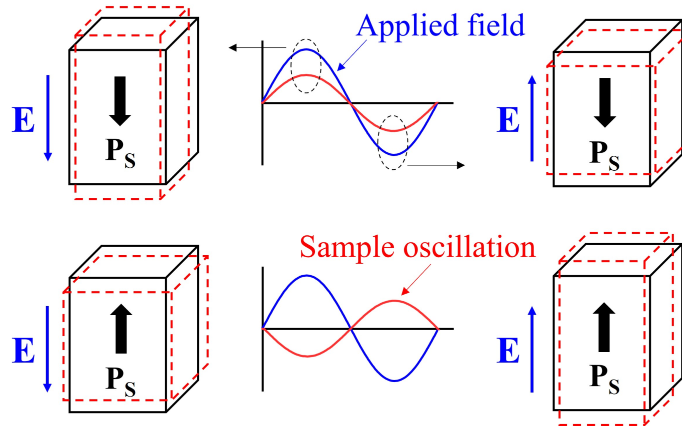

Figure 2.3. Schematic of the origin of the 180° PFM phase contrast for the domains with opposite polarity in a material with positive d_{33}.

The phase signal, on the other hand, is related to the sign of the longitudinal piezoelectric coefficient, d_{33}, and gives information on the domain polarity. For a material with a positive d_{33}, when the polarization is oriented downwards the sample will expand (contract) during the positive (negative) half cycle. The net result is that the sample deformation and the applied field are in phase (top row in Fig. 2.3). For the upward polarization state, the sample will contract (expand) during the positive (negative) half cycles resulting in a 180° out-of-phase signal (bottom row in Fig. 2.3).

The situation will be reversed in a material with a negative d_{33} such that the PFM phase signal will be in-phase when the polarization is oriented upwards and 180° out-of-phase when the polarization is oriented downwards. From this working principle, information on the ferroelectric domain polarity as well as the sign of the piezoelectric coefficient can be determined.

In addition to the out-of-plane (z-direction) polarization component, PFM can also detect the in-plane (x and y-direction) polarization component. The out-of-plane polarization component is detected via the vertical cantilever deflection, and this mode of PFM is referred to as vertical PFM (VPFM). On the other hand, the in-plane polarization component is detected via the torsional motion of the cantilever induced by the shear strains and this mode is commonly referred to as lateral PFM (LPFM). A combination of VPFM to image the z-direction polarization component and LPFM imaging in both x and y-directions can generate the three dimensional polarization orientation, an approach known as vector PFM [7].

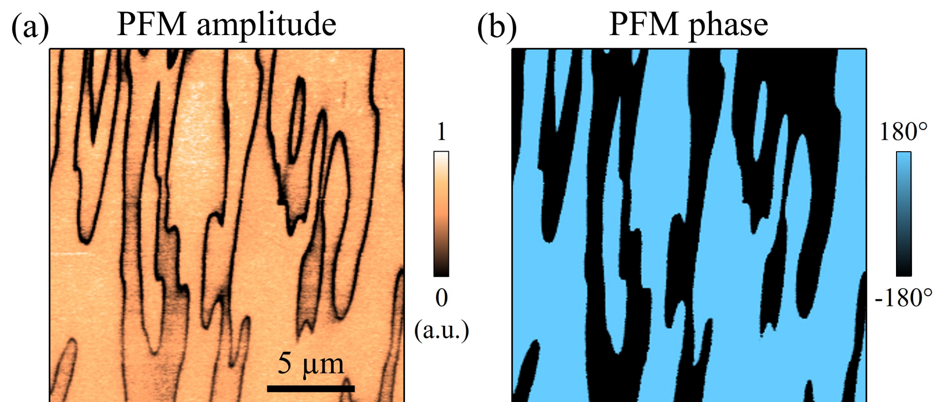

Figure 2.4. Representative PFM amplitude (a) and PFM phase (b) images obtained on a $Pb_5Ge_3O_{11}$ (PGO) single crystal.

Fig. 2.4 shows representative PFM amplitude and PFM phase images of a polydomain configuration observed on a $Pb_5Ge_3O_{11}$ (PGO) single crystal. In PFM

amplitude images, regions with finite amplitude correspond to domains while the amplitude vanishes at the domain walls. At the domain walls, there is a corresponding flipping of the phase signal resulting in the nearly 180° phase contrast observed in the PFM phase images for domains with opposite polarity.

The PFM measurements can be performed in two different configurations - (i) *local* excitation: measurements are done on the bare ferroelectric surface, and (ii) *integral* excitation: measurements are done through the top electrode in a metal/ferroelectric/metal capacitor geometry. The *local* excitation method allows very high lateral resolution (of the order of a few tens of nm depending on the sharpness of the tip) and local control of the ferroelectric domains. Using this approach, nanoscale insights on the domain wall creep process [8], local disorder potential [9], energetics of domain wall formation [10], etc. can be obtained. However, in this approach the applied electric field is highly inhomogeneous [11] and the PFM signal can suffer from non-ferroelectric contributions [12, 13] which can make the interpretation of the results highly challenging. Some of these issues can be alleviated in the *integral* excitation approach, where the PFM measurements are done through the top electrode. In this approach, the electric field is homogeneous between the top and bottom electrodes and extrinsic electrostatic contributions to the PFM signal can be significantly reduced [11]. Please note that the PFM response is still detected locally from the region underneath the tip, although the spatial resolution in this geometry becomes a function of the top electrode thickness [14]. This approach allows the determination of the polarization switching mechanism [15], imprint [16], etc. which are important from the technological viewpoint. We would like to highlight here that the majority of the work done in this dissertation has been performed in the *integral* excitation mode.

The first visualization of ferroelectric domain structure using PFM was

demonstrated by Güthner and Dransfeld in 1992, who used this technique to visualize locally written domains in a ferroelectric vinylidene-fluoride trifluoroethylene (VDF-TrFE) copolymer film [17]. Since then, PFM has now become an ubiquitous tool in the exploration of nanoferroic phenomena. It is a powerful non-destructive technique that has led to profound insights into the local polarization switching behavior in inorganic and organic ferroelectric films, polymers, single crystals and capacitors [15, 17, 18, 19, 20, 21, 22, 23, 24, 25, 26], exploration of the magnetoelectric coupling [27, 28, 29], etc.. A combination of PFM with other scanning probe techniques has been very successful in exploring a variety of the functional properties in ferroic material such as domain wall conductivity [30, 31, 32, 33], tunneling electroresistance phenomena [34, 35], etc. In the next few sub-sections, we briefly describe some of the advanced modes of PFM.

2.1.2.1 Resonance enhanced PFM

In the conventional implementation of PFM, the measurements are performed at a single frequency and this mode is referred to as single frequency PFM. When the single frequency PFM measurements are performed far away from the tip-sample contact resonance, there can be a frequency-dependent arbitrary reduction of the amplitude signal and flipping of the phase signal due to coupling of cantilever dynamics to the PFM signal, which can mask the true electromechanical response [36]. In addition, for samples with weak piezoelectric response due to a small piezoelectric coefficient, very large voltages are required to obtain a meaningful signal-to-noise ratio (SNR). This, however, becomes an issue if the applied voltages are larger than the coercive voltage or leads to dielectric breakdown. To circumvent the issue of low SNR, many researchers work at the first tip sample contact resonance frequency to take advantage of the natural signal boost arising from the quality factor, Q, of the resonance. In

this situation, Eq. 2.5 gets modified to

$$A_{1\omega} = d_{33,eff} V_{ac} Q \tag{2.6}$$

Since typical values of the Q-factor are around 10-100 [37], working at resonance can lead to at least an order of magnitude amplification of the PFM signal. The single frequency resonance enhanced PFM mode is beset with its own issues, however. Spatial variations in the tip-sample contact resonance due to changes in the tip-sample contact stiffness can cause arbitrary jumps in the phase signal unrelated to the local polarization direction which can lead to misinterpretation of the measured PFM signal [38]. To overcome such issues, multi-frequency resonance enhanced methods such as dual ac resonance tracking (DART) [39] and band-excitation (BE) [40] have been developed. In this dissertation, since the measurements have been performed in the DART mode we will briefly discuss only the DART PFM method.

A schematic of the DART PFM mode is presented in Fig. 2.5. In this method, two driving voltages are applied simultaneously - one with a frequency, f_1, below the contact resonance frequency, f_0, and the other with a frequency, f_2, above the contact resonance frequency. The corresponding electromechanical response is detected by two lock-in amplifiers and decoupled into two amplitude signals, A_1 and A_2, and two phase signals, ϕ_1 and ϕ_2, corresponding to f_1 and f_2, respectively, in both cases. By tracking the difference in the amplitude signals, $A_1 - A_2$, using a feedback loop, the resonance frequency is tracked constantly. This method alleviates the problems associated with the arbitrary phase jumps and provides significant signal amplification since the measurements are done very close to the resonance frequency. This technique can be particularly helpful when doing PFM measurements on samples with a small piezoelectric coefficient, e.g., in the HfO_2-based ferroelectrics where the $d_{33,eff}$ has

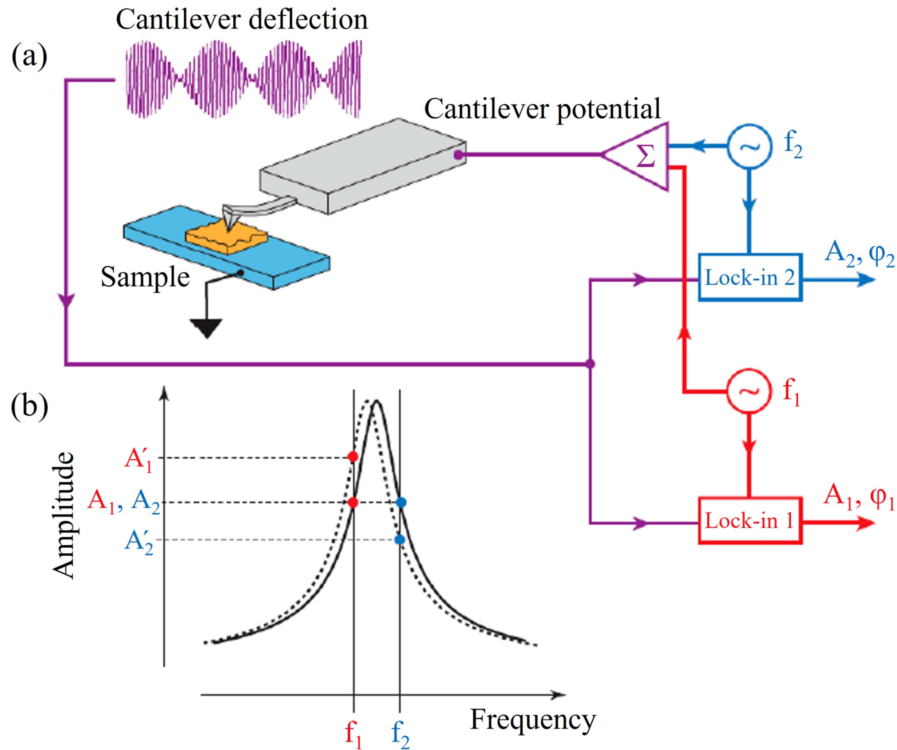

Figure 2.5. (a) Schematic of DART experimental setup. (b) Principle of tracking the resonance frequency using the difference in the amplitude signals, $A_1 - A_2$, at frequencies f_1 and f_2. Figure adapted from Ref. [39].

been reported to be around 2-5 pm/V [41], which is nearly an order of magnitude smaller than the $\sim$ 50 pm/V reported in Pb(Zr,Ti)O_3 (PZT)-based ferroelectrics [6].

2.1.2.2 PFM spectroscopy

In addition to the visualization of the domain structure, quantitative information about the local switching behavior can be obtained by acquiring a local hysteresis loop in the PFM spectroscopic mode [42]. The PFM spectroscopy measurements are performed by sweeping a DC waveform along with the simultaneous acquisition of the local electromechanical response. Typically, a pulsed DC waveform is used in the measurements - where a small signal AC probing voltage, V_{ac}, is superimposed on to

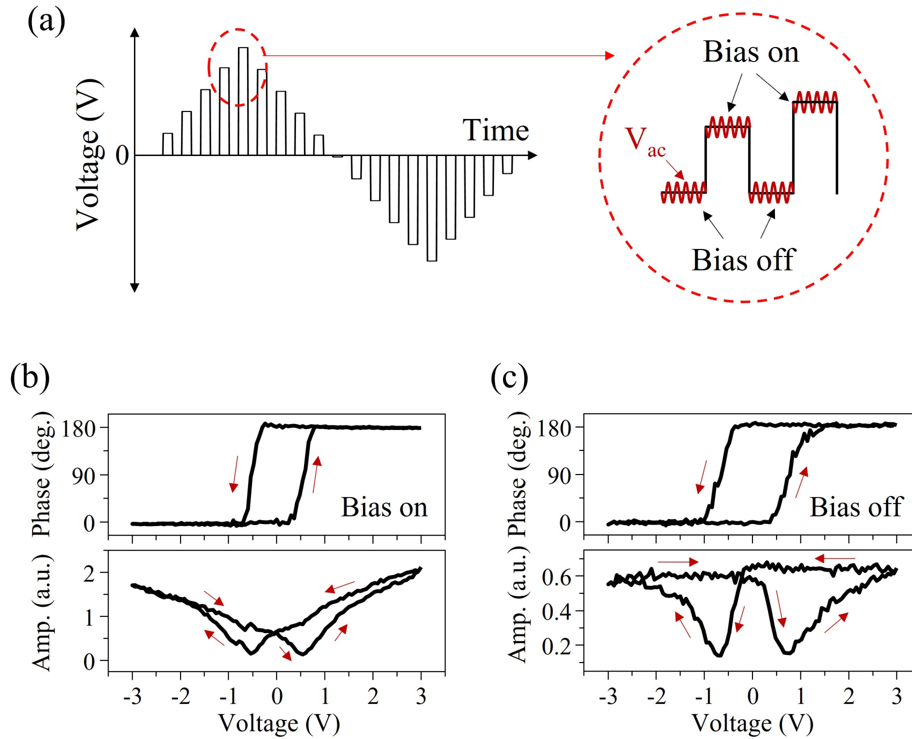

Figure 2.6. (a) Schematic of pulsed DC mode waveform used in PFM spectroscopy. (b,c) PFM hysteresis loops in the bias ON (b) and bias OFF (c) modes. The hysteresis loops were acquired on a Pt/Ti/TiN/La:HfO_2 (10 nm)/TiN capacitor. The arrows indicate the direction in which the loops are traversed.

DC pulses, V_{dc} (Fig. 2.6 (a)). The V_{ac} is used to detect the electromechanical response while the V_{dc} is applied to induce polarization switching. When the electromechanical response is measured in presence (absence) of the V_{dc}, the obtained loops are said to be in the bias on (bias off) mode. An example of a PFM amplitude and PFM phase hysteresis loop obtained on a Pt/Ti/TiN/La:HfO_2 (10 nm)/TiN capacitor is shown in Figs. 2.6 (b,c). To understand the physical origin of the specific shape of the loops, we first describe the butterfly-shaped PFM amplitude loops. Due to the finite remanent polarization in ferroelectrics, there is a finite PFM amplitude signal at zero bias. Increase in the DC voltage induces polarization switching, which is manifested in the gradual reduction of the amplitude signal till it reaches a minima

corresponding to the presence of an equal fraction of oppositely oriented domains underneath the tip. The voltage at which the minima occurs is referred to as the local coercive voltage. As the DC voltage is increased further, the fraction of the switched polarization becomes larger, resulting in an increase in the PFM amplitude till the amplitude saturates due to completion of the polarization switching process. If there is no relaxation of the polarization, the amplitude will remain constant as the DC voltage is reduced from the maximum to zero. In the PFM phase loops, the 180° phase difference between the far positive and the far negative DC voltages indicate the oppositely oriented domain states, with the phase reversal coinciding with the minima in the PFM amplitude. It is worth pointing out here that there is an additional linear contribution in the bias on amplitude loops as observed in Fig. 2.6 (b) due to extrinsic electrostatic artifacts. Such extrinsic contributions are minimized in the bias-off loops, from which the genuine electromechanical response can be obtained (Fig. 2.6 (c)).

By collecting the local hysteresis loops in an $M \times N$ array of points, a two-dimensional (2-D) map of the spatial variations in the local coercive voltages, imprint, etc. can be obtained. This approach, known as switching spectroscopy PFM (SS-PFM) map, reveals quantitative insights into the spatial variations of the local switching behavior.

2.1.2.3 Stroboscopic PFM

The typical image acquisition time in PFM is of the order of minutes. However, in many ferroelectrics the polarization switching can occur below 100 ns. This issue of low time resolution in PFM can be circumvented by using the so-called stroboscopic PFM approach [15]. In this approach, a series of pulses of fixed amplitude and incrementally increasing duration, τ_i, are applied such that $\tau_1 < \tau_2 < \tau_3 ... < \tau_n$

($\tau_{i=1,2,..n-1} < \tau_n$ where τ_n is the total switching time) to induce partial polarization switching. PFM imaging of the resulting domain configuration after each pulse allows visualization of the instantaneous domain configuration during the polarization reversal process. However, the applicability of this approach relies on the stability of the instantaneous domain configurations, which should be independently verified.

2.2 Electrical characterization

Electrical characterization refers to the measurement of current or charge response from a sample under study when it is subjected to an external stimuli. Since ferroelectrics are also pyroelectric and piezoelectric, the external stimuli can be purely electrical, thermal or mechanical or a combination of them. In this section, we consider the current or charge response from the sample when it is subjected to a voltage excitation, i.e., a purely electronic stimulus. Such electrical characterization of the ferroelectric materials are particularly relevant for ferroelectric memory applications as it allows the determination of the remanent charge, the polarization switching speeds, device failure mechanisms and so on.

2.2.1 Measurement setup

Schematics of the circuit configurations used in this dissertation for the electrical characterization of ferroelectric capacitors are shown in Fig. 2.7. There were two methods used - the Sawyer-Tower method (Fig. 2.7 (a)) [43], and the shunt resistor method (Fig. 2.7 (b)) [44], which are described in more detail below.

Sawyer-Tower method: This is a charge measurement method in which a reference capacitor, C_{ref}, is placed in series with the ferroelectric capacitor, C_{FE}, to

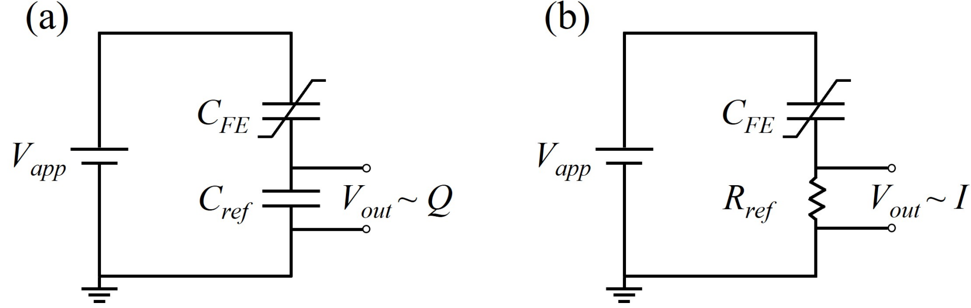

Figure 2.7. Schematic circuit diagrams of the Sawyer-Tower (a) and shunt resistor (b) methods. C_{FE} and C_{ref} are the ferroelectric and reference capacitors, respectively. R_{ref} is the reference resistor. V_{app} is the applied voltage, and V_{out} is the voltage drop measured across C_{ref} or R_{ref}.

be tested (Fig. 2.7 (a)). The polarization charge of the ferroelectric capacitor is measured as a voltage drop across the reference capacitor given by $V_{out} = Q/C_{ref}$, where Q is the polarization charge. Dividing Q by the capacitor area gives the polarization, P, in units of charge/area, and a plot of P vs V_{app} generates the polarization-voltage hysteresis loops. In addition, this method can be used to obtain ferroelectric capacitance-voltage $(C_{FE} - V)$ plots in which a small probing voltage (much smaller than the coercive voltage) is superimposed on to a step-wise triangular DC waveform. From the $C - V$ plots, a variation of the dielectric constant, κ, with the applied voltage can also be obtained using the relation $\kappa = C_{FE}d/\epsilon_0 A$, where d is the thickness of the ferroelectric layer, A is the area of C_{FE} and ϵ_0 is the vacuum permittivity.

Shunt resistor method: In this current measurement method, the reference capacitor of the Sawyer-Tower method is replaced by a reference resistor, R_{ref}, in series with C_{FE} (Fig. 2.7 (b)). The polarization-related current, I, is measured as a voltage drop across the R_{ref} as $V_{out} = R_{ref}I$, which can then be numerically integrated to obtain the polarization, P, using $P = (\int Idt)/A$. The majority of the

electrical measurements presented in this dissertation have been performed using the shunt resistor method, which was implemented using a custom built setup.

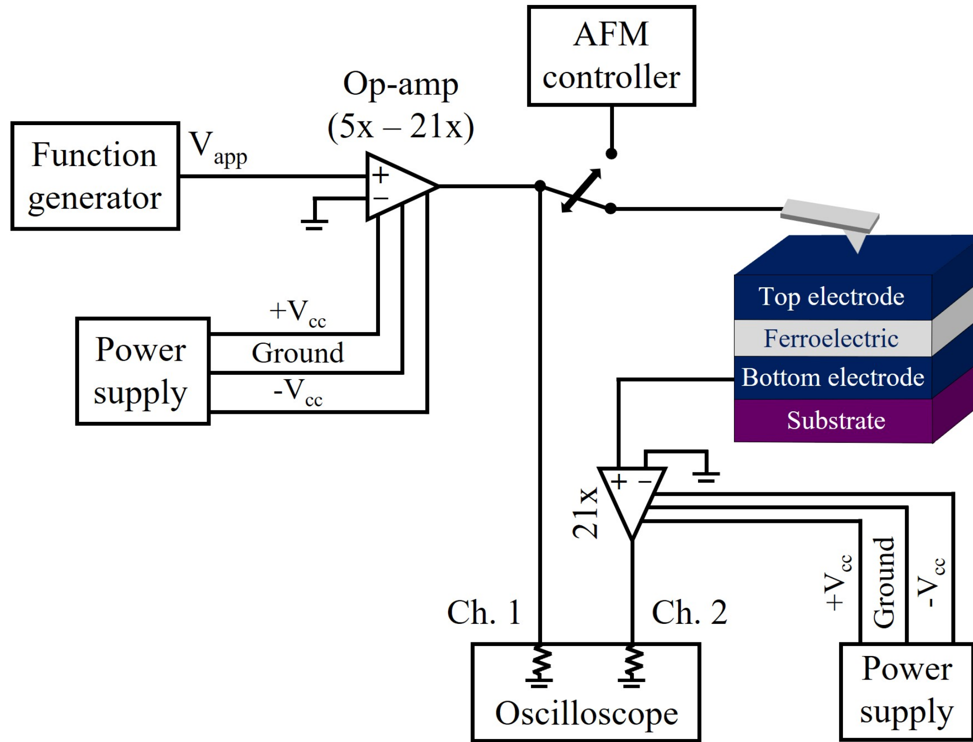

Figure 2.8. Schematic of implementation of shunt resistor method integrated with AFM setup. The 5x and 21x refers to the voltage amplification factor of the op-amp. Ch.1 and Ch.2 refers to channels 1 and 2, respectively, of the oscilloscope.

To correlate PFM imaging of domain evolution during the polarization reversal process with the macroscopic polarization switching, the shunt resistor method was integrated directly with the AFM setup [45]. Another advantage of the AFM-based setup is that it allows the characterization of very small capacitors, including capacitors with sub-micron dimensions, which otherwise cannot be contacted directly using an external probe. A schematic of this setup is shown in Fig. 2.8. An arbitrary waveform function generator generates the voltage waveform, V_{app}, which is split into two equal signals - one signal is recorded in channel 1 of the oscilloscope

as a reference and the other signal goes to the conductive AFM tip in contact with the top electrode to apply the voltage waveform to the capacitor. An operational amplifier (op-amp) can be placed between the output of the function generator and the signal split for two reasons: (i) when voltages larger than the 5 V maximum amplitude that can be supplied by the function generator are required to obtain complete polarization switching, and (ii) to act as a power amplifier when measurements are performed on large capacitors (lateral area $> 900\ \mu m^2$) to obtain fast rise times of less than 15 ns. The corresponding transient currents are collected through the bottom electrode and recorded in channel 2 of the oscilloscope, whose input impedance acts as the shunt resistor. When small capacitors (lateral area $< 25\ \mu m^2$) are used, an op-amp can be placed between the bottom electrode and the oscilloscope input to amplify the very small transient currents. The whole setup is software controlled using LabVIEW, which allows great flexibility in creating different types of waveforms in the arbitrary waveform mode of the function generator. For PFM mode operation in this setup, the source of the input signal to the cantilever has to be be changed to the AFM controller and the bottom electrode has to be grounded.

2.2.2 Types of electrical measurements

The types of electrical measurements performed can be broadly divided into two types depending on the waveform used - (i) hysteresis measurements using triangular waveforms, and (ii) pulse switching measurements using square pulses. These two types of measurements are discussed in more detail below.

2.2.2.1 Hysteresis measurements

The polarization-voltage (P-V) hysteresis loops are obtained by measuring the polarization in response to an applied triangular voltage waveform. As mentioned in the previous section, the polarization switching charge, Q, can be obtained directly using the Sawyer-Tower method from which the polarization, P, can be obtained using the relation $P = Q/A$. On the other hand, using the shunt resistor method the $P - V$ loops can be constructed by integrating the transient switching currents ($P = (\int I dt)/A$).

In the most commonly used bipolar triangular waveform used for P-V measurements, where a positive half cycle is followed by a negative half cycle (Fig. 2.9 (a)), there can be additional non-ferroelectric contributions to the P-V loop due to dielectric, I_{diel}, as well as leakage, I_{leak}, contributions. An example of a P-V loop obtained using this waveform is shown in Fig. 2.9 (b), where the continuous increase of the polarization with increasing voltage can be attributed to the linear dielectric contribution. In the presence of leakage, the loops become more rounded.

The non-ferroelectric contributions to the P-V loop can be removed by using the so-called PUND-type triangular waveform, where P,U,N,D stands for positive, up, negative, down, respectively, that refers to the polarity of the voltage pulses applied (Fig. 2.9 (c)). In this waveform, the transient current, I_P, due to 'P' pulse contains the switching current due to polarization reversal from the upward to the downward polarization state, $I_{sw,down}$, as well as the non-ferroelectric contributions, I_{diel} and I_{leak}:

$$I_P = I_{sw,down} + I_{diel} + I_{leak} \tag{2.7}$$

Application of the 'U' pulse (with exactly the same parameters as the 'P' pulse)

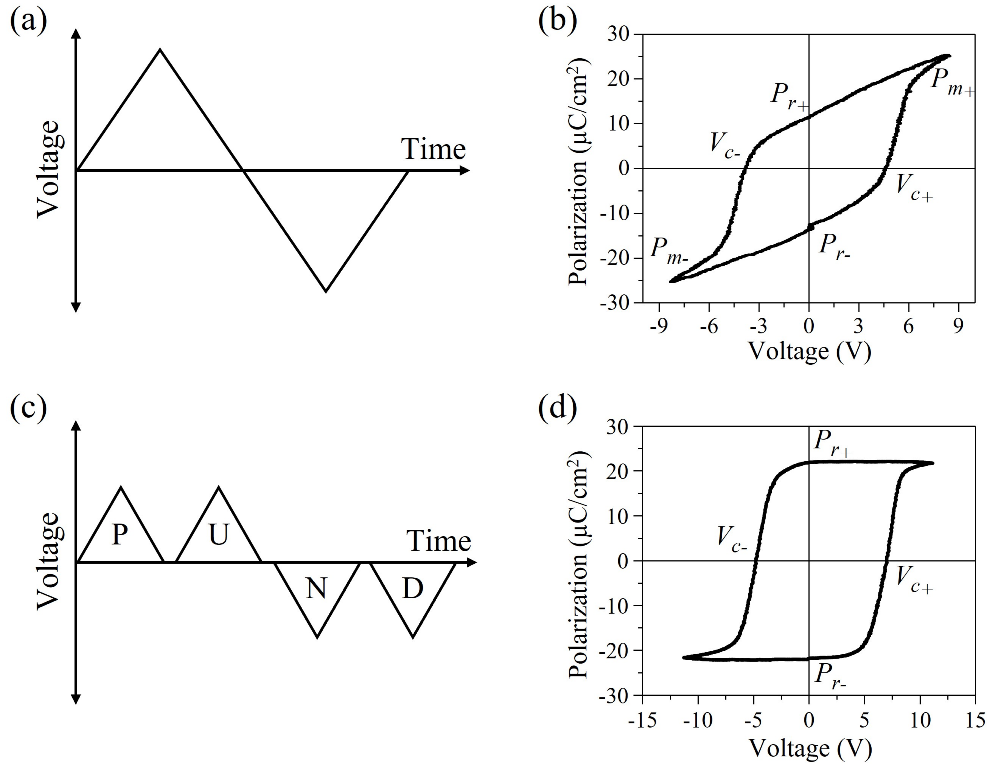

Figure 2.9. (a) Typical bipolar waveform used to measure P-V hysteresis loops. (b) Representative P-V loop obtained using the waveform in (a). (c) PUND-type triangular waveform used to measure the remanent polarization. (d) Representative remanent P-V hysteresis loop obtained using the waveform in (c). P_{r+} and P_{r-} represent the remanent polarization for the downward and the upward polarization states, respectively. V_{c+} and V_{c-} are the positive and negative coercive voltages, respectively. P_{m+} and P_{m-} are the maximum polarization values at the maximum applied positive and negative voltages, respectively.

results in a transient current, I_U, that contains only the non-ferroelectric contributions assuming there was no polarization relaxation between the two pulses:

$$I_U = I_{diel} + I_{leak} \tag{2.8}$$

It is then straightforward to observe that the subtraction of the transient currents due to the 'U' pulse from the 'P' pulse will give the switching current:

$$I_P - I_U = I_{sw,down} \tag{2.9}$$

Following the same logic, subtraction of the transient currents due to the 'D' pulse from the 'N' pulse will lead to the transient switching current due to polarization reversal from downward to upward polarization state, $I_{sw,up}$:

$$I_N - I_D = I_{sw,up} \tag{2.10}$$

The P-V loops constructed using $I_{sw,down}$ and $I_{sw,up}$ contain contributions only from the ferroelectric polarization and are commonly referred to as remanent hysteresis loops. An example of a remanent hysteresis loop is shown in Fig. 2.9 (d).

Some of the important parameters that can be obtained from the P-V loop measurements include:

$P_{r+,-}$ The remanent polarization corresponding to the downward and the upward polarization states. The higher the value of the remanent polarization, the higher is the readout charge for non-volatile memory (NVM) applications. A high P_r enables miniaturization of devices since the high readout charge can be easily detected.

$V_{c+,-}$ The coercive voltages for positive and negative polarities. For NVM applications, the coercive voltages should be high enough to ensure stability of the polarization states against thermal fluctuations but low enough so that polarization switching does not require a lot of energy. In addition, the presence of an internal field due to asymmetric boundary conditions at the top and bottom interfaces can result in asymmetric coercive voltages. This asymmetry is commonly referred to as imprint and is manifested by a shift

of the P-V loops along the voltage axis [46]. The magnitude of imprint, V_{shift}, can be calculated as $V_{shift} = (V_{c+} + V_{c-})/2$. An example of an imprinted remanent P-V loop is shown in Fig. 2.9 (d).

$P_{m+,-}$ The maximum polarization value at the maximum applied positive and negative voltages. Please note that the P_m is larger than P_r in the typical P-V loops due to the presence of the linear dielectric contributions (Fig. 2.9 (b)). However, in the remanent P-V loops such as that shown in Fig. 2.9 (d), $P_r = P_m$ since the linear dielectric contribution was removed.

2.2.2.2 Pulse switching measurements

Pulse switching measurements allow testing of the ferroelectric devices for FRAM applications under real world measurement conditions where square read and write voltage pulses are used to read and write information [47]. Various parameters relevant to FRAM applications such as switching speeds, switching mechanism and polarization retention can be obtained from pulse switching measurements. These are described in detail below.

Estimation of polarization switching speed: The determination of the fastest polarization switching speeds gives an estimate of the access time of an FRAM device. A typical waveform used to estimate the switching speeds is the PUND waveform [48], which consists of five pulses as shown in Fig. 2.10 (a). The description of these pulses are similar to the PUND-type triangular waveform discussed in the previous section. The preset pulse switches or sets the polarization to one particular state. Fig. 2.10 (b) shows a representative voltage pulse (blue curve) along with the experimentally measured transient currents from which the switching current can be obtained. The black curve in Fig. 2.10 (b) represents the typical transient current due to either pulse

P or N and contains both switching and non-switching contributions, while the green curve in Fig. 2.10 (b) represents the typical transient current due to either pulse U or D and contains only the non-switching contributions. The polarization switching current can be obtained by subtracting the green curve from the black curve, and is represented by the red curve in Fig. 2.10 (b). The switching time, t_{sw}, is defined as the time taken from the onset of switching to when the switching current becomes 90% from its maximum value [49]. From a technical viewpoint, t_{sw} is strongly dependent on the magnitude of the applied field, capacitor area as well as the rise time of the applied pulses.

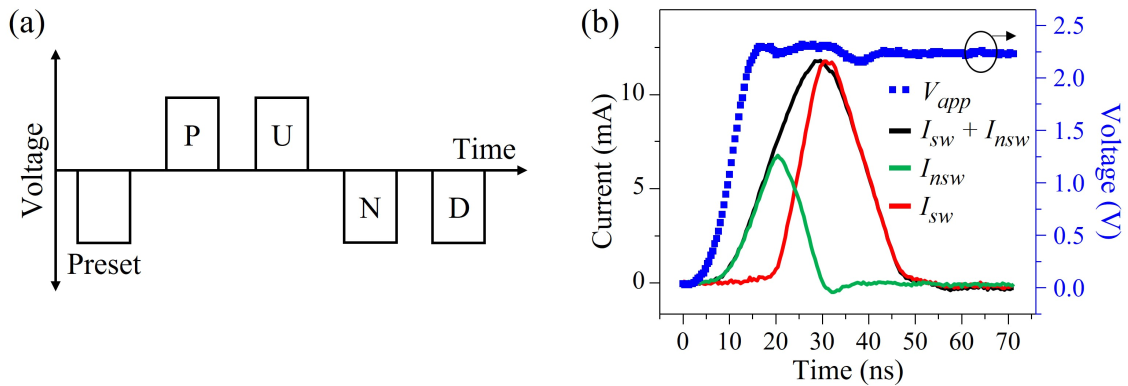

Figure 2.10. (a) Typical PUND square pulse waveform. (b) The black and the green curves are representative experimentally measured transient currents containing both the switching and non-switching contributions ($I_{sw} + I_{nsw}$) and only non-switching contributions (I_{nsw}), respectively. The red curve corresponds to the switching current and was obtained by subtracting the green curve from the black curve. The blue curve represents the initial part of a typical voltage pulse used in these measurements.

Delineation of polarization switching mechanism: The polarization switching mechanism can be determined by using a pulse waveform such as that shown in Fig. 2.11 (a). The capacitors are first subjected to field-cycling to remove any previous imprint. The set pulse, P1, of a sufficiently high amplitude and duration sets the polarization to a particular state. P1 is followed by pulse P2 whose magnitude, V,

and duration, τ, can be varied. The fraction of polarization switched due to P2 will be included in the total current obtained from pulse P3. The switching current in P3 is extracted by subtracting the purely dielectric current contribution obtained via pulse P4 from the total current in P3. Finally, integration of the switching current gives the switched polarization which is plotted with respect to τ as shown in Fig. 2.11 (b). The time dependent variation of the fraction of switched polarization can be then fit by the Kolmogorov-Avrami-Ishibashi (KAI) [50] or the nucleation limited switching (NLS) [51] models as discussed in section 1.3 in Chapter 1 to determine the switching mechanism that best describes the polarization switching process. An example of the fitting by the KAI and the NLS models is shown in Fig. 2.11 (b) from which it can be inferred that the NLS model gives the best fit to describe the polarization switching process.

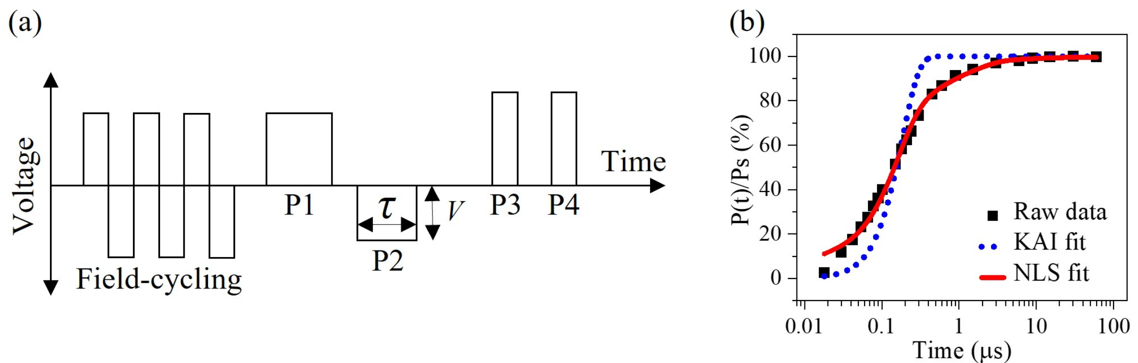

Figure 2.11. (a) Waveform to determine the polarization switching mechanism. A description of the pulses is provided in the main text. (b) Plot of ratio of the fraction of switched polarization as a function of time, $P(t)$, to the total polarization, P_s, vs duration of pulse P2. The black squares represent the raw data, while the solid line is the fit using the NLS model and the dotted line is the fit using the KAI model.

Polarization retention: Polarization retention is the ability of a ferroelectric device to maintain a particular polarization state. In the context of FRAM applications, the retention should be of the order of 10 years [52]. The retention can be measured

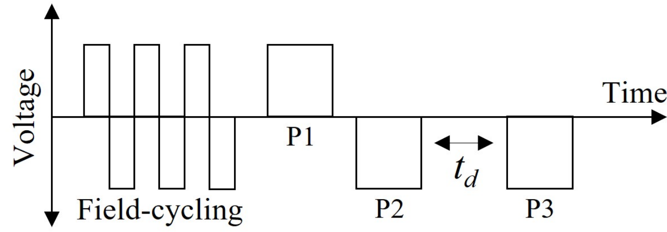

Figure 2.12. Waveform to determine polarization retention by varying the delay time, t_d, between pulses P2 and P3.

using a pulse waveform such as that shown in Fig. 2.12, where the stability of the polarization state can be determined by increasing the time delay, t_d, between pulses P2 and P3. The capacitors can be first subject to field cycling to remove any previous imprint and then set to a particular polarization state by applying the set pulse P1.

2.3 Typical experimental conditions used in this dissertation

2.3.1 PFM measurements

The PFM measurements have been carried out using a commercial AFM system (MFP-3D, Asylum Research) in the resonance enhanced DART mode. The experiments in the capacitor geometry have been carried out using non-conductive single crystalline diamond tips (D80, K-Tek Nanotechnology) with a force constant of $\sim$ 3-4 N/m, employing a $\sim$ 350 kHz AC modulation bias with amplitude varying from 0.075 – 1 V depending on the sample tested. The bias was applied to the top electrode using a microscopic external probe, while the PFM cantilevers were used to detect the local electromechanical response of the samples. This approach allows alleviation of the problem associated with the quick deterioration of the tip-sample contact resistance as well as with the strong electrostatic effect on the measured PFM signal. An optical microscopy photo of the cantilever and the microscopic

external probe is shown in Fig. 2.13. In all measurements, the bottom electrode was grounded.

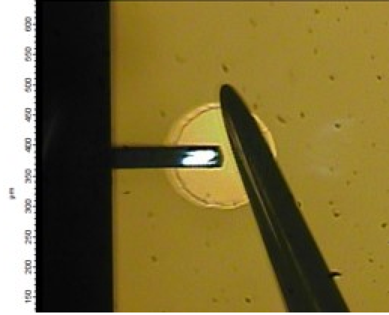

Figure 2.13. Representative optical microscopy image of cantilever and external probe for PFM measurements in capacitor geometry.

The PFM measurements on the bare surface have been performed in the DART mode using conductive Pt-coated Si probes (HQ:DPE-XSC11, MikroMasch), with a force constant of $\sim$ 6 N/m and employing a $\sim$ 700 kHz AC drive signal. The bias was applied to the conductive tip and the bottom electrode was grounded.

2.3.2 Quasi-static strain loop measurements

The quasi-static strain loop measurements were obtained using the same AFM system by detecting the static cantilever deflection while sweeping a triangular DC bias at 1 Hz. The deflection signal was converted to the actual displacement of the sample by calibrating the cantilever optical lever sensitivity. The strain values were obtained by dividing the measured displacement by the sample thickness.

2.3.3 Electrical characterization

The voltage pulses were applied using a Keithley 33621A arbitrary waveform generator via a microscopic external probe in contact with the top electrode, while the transient switching currents through the bottom electrode were recorded using a

Tektronix TDS 3014B oscilloscope. Either an Analog Devices ADA4870ARR-EBZ or a Texas Instruments THS4021EVM high speed evaluation module board was used as a power amplifier to achieve short rise times for the applied pulses. The higher bandwidth of the THS4021EVM resulted in shortest rise times of $\sim$ 9 ns, while the shortest rise time that could be achieved with the ADA4870ARR-EBZ was $\sim$ 12 ns.

References

[1] R. P. Feynman, *There's Plenty of Room at the Bottom.* Engineering and Science **23**, 5, 22 (1960).

[2] G. Binnig, H. Rohrer, Ch. Gerber, and E. Weibel, App. Phys. Lett. **40**, 178 (1982).

[3] G. Binnig, C. F. Quate, and Ch. Gerber, Phys. Rev. Lett. **56**, 930 (1986).

[4] C. Gerber and H. P. Lang, Nat. Nanotechnol. **1**, 3 (2006).

[5] G. Meyer, and N. M. Amer, Appl. Phys. Lett. **53**, 1045 (1988).

[6] A. Kholkin, E. K. Akdogan, A. Safari, P.-F. Chauvy, and N. Setter, J. Appl. Phys. **89**, 8066 (2001).

[7] S. V. Kalinin, B. J. Rodriguez, S. Jesse, J. Shin, A. P. Baddorf, P. Gupta, H. Jain, D. B. Williams, and A. Gruverman, Microsc Microanal. **12**, 206 (2006).

[8] T. Tybell, P. Paruch, T. Giamarchi, and J.-M. Triscone, Phys. Rev. Lett. **89**, 097601 (2002).

[9] S. Jesse, B. Rodriguez, S. Choudhury, A. P. Baddorf, I. Vrejoiu, D. Hesse, M. Alexe, E. A. Eliseev, A. N. Morozovska, J. Zhang, L.-Q. Chen, and S. V. Kalinin Nature Mater **7**, 209 (2008).

[10] H. Lu, T. Li, S. Poddar, O. Goit, A. Lipatov, A. Sinitskii, S. Ducharme, and A. Gruverman, Adv. Mater. **27**, 7832 (2015).

[11] A. L. Kholkin, S. V. Kalinin, A. Roelofs, and A. Gruverman, Chapter I.6 in *Scanning Probe Microscopy: Electrical and Electromechanical Phenomena at the Nanoscale*, S. Kalinin and A. Gruverman, Eds., (Springer Science+Business Media, 2007).

[12] N. Balke, P. Maksymovych, S. Jesse, A. Herklotz, A. Tselev, C.-B. Eom, I. I. Kravchenko, P. Yu, and S. V. Kalinin, ACS Nano **9**, 6, 6484 (2015).

[13] R. K. Vasudevan, N. Balke, P. Maksymovych, S. Jesse, and S. V. Kalinin, Appl. Phys. Rev. **4**, 021302 (2017).

[14] S. V. Kalinin, B. J. Rodriguez, S.-H. Kim, S.-K. Hong, A. Gruverman, and E. A. Eliseev, Appl. Phys. Lett. **92**, 152906 (2008).

[15] A. Gruverman, D. Wu, and J. F. Scott, Phys. Rev. Lett. **100**, 097601 (2008).

[16] A. Gruverman, B. J. Rodriguez, A. I. Kingon, R. J. Nemanich, A. K. Tagantsev, J. S. Cross and M. Tsukada, Appl. Phys. Lett. **83**, 728 (2003).

[17] P. Guthner and K. Dransfeld, Appl. Phys. Lett. **61**, 1137 (1992).

[18] A. Gruverman, O. Auciello, and H. Tokumoto, J. Vac. Sci. Technol. B **14**, 602–605 (1996).

[19] T. Tybell, C.H. Ahn, and J.-M. Triscone, Appl. Phys. Lett. **75**, 856 (1999).

[20] B. J. Rodriguez, R. J. Nemanich, A. Kingon, A. Gruverman, S.V. Kalinin, K. Terabe, X. Y. Liu, and K. Kitamura, Appl. Phys. Lett. **86**, 012906 (2005).

[21] P. Paruch, T. Tybell, and J.-M. Triscone, Appl. Phys. Lett. **79**, 530 (2001).

[22] P. Sharma, T. J. Reece, S. Ducharme, and A. Gruverman, Nano Lett. **11**, 5, 1970 (2011).

[23] H. Lu, T. Li, S. Poddar, O. Goit, A. Lipatov, A. Sinitskii, S. Ducharme, and A. Gruverman, Adv. Mater. **27**, 7832 (2015).

[24] O. Bak, T. S. Holstad, Y. Tan, H. Lu, D. M. Evans, K. A. Hunnestad, B. Wang, J. P. V. McConville, P. Becker, L. Bohatý, I. Lukyanchuk, V. M. Vinokur, A. T. J. van Helvoort, J. M. Gregg, L.-Q. Chen, D. Meier, and A. Gruverman, Adv. Funct. Mater. **30**, 2000284 (2020).

[25] J. Y. Jo, H. S. Han, J.-G. Yoon, T. K. Song, S.-H. Kim, and T. W. Noh, Phys. Rev. Lett. **99**, 267602 (2007).

[26] D. J. Kim, J. Y. Jo, T. H. Kim, S. M. Yang, B. Chen, Y. S. Kim, and T. W. Noh, Appl. Phys. Lett. **91**, 132903 (2007).

[27] T. Zhao, A. Scholl, F. Zavaliche, K. Lee, M. Barry, A. Doran, M. P. Cruz, Y. H. Chu, C. Ederer, N. A. Spaldin, R. R. Das, D. M. Kim, S. H. Baek, C. B. Eom, and R. Ramesh, Nat. Mater. **5**, 823 (2006).

[28] Y.-H. Chu, L. W. Martin, M. B. Holcomb, M. Gajek, S.-J. Han, Q. He, N. Balke, C.-H. Yang, D. Lee, W. Hu, Q. Zhan, P.-L. Yang, A. F.-Rodríguez, A. Scholl, S. X. Wang, and R. Ramesh, Nat. Mater. **7**, 478 (2008).

[29] Y. Geng, H. Das, A. L. Wysocki, X. Wang, S.-W. Cheong, M. Mostovoy, C. J. Fennie, and W. Wu, Nat. Mater. **13**, 163 (2014).

[30] J. Seidel, L. W. Martin, Q. He, Q. Zhan, Y.-H. Chu, A. Rother, M. E. Hawkridge, P. Maksymovych, P. Yu, M. Gajek, N. Balke, S. V. Kalinin, S. Gemming, F. Wang, G. Catalan, J. F. Scott, N. A. Spaldin, J. Orenstein, and R. Ramesh, Nat. Mater. **8**, 3, 229 (2009).

[31] G. Catalan, J. Seidel, R. Ramesh, and J. F. Scott, Rev. Mod. Phys. **84**, 119 (2012).

[32] P. Sharma, Q. Zhang, D. Sando, C. H. Lei, Y. Liu, J. Li, V. Nagarajan, and J. Seidel, Sci. Adv. **3**, 6, e170051 (2017).

[33] H. Lu, Y. Tan, J. P. V. McConville, Z. Ahmadi, B. Wang, M. Conroy, K. Moore, U. Bangert, J. E. Shield, L.-Q. Chen, J. M. Gregg, and A. Gruverman, Adv. Mater. **31**, 1902890 (2019).

[34] V. Garcia, S. Fusil, K. Bouzehouane, S. Enouz-Vedrenne, N. D. Mathur, A. Barthélémy, and M. Bibes, Nature **460**, 81 (2009).

[35] A. Gruverman, D. Wu, H. Lu, Y. Wang, H. W. Jang, C. M. Folkman, M. Y. Zhuravlev, D. Felker, M. Rzchowski, C.-B. Eom, and E. Y. Tsymbal, Nano Lett. **9**, 10, 3539 (2009).

[36] R. Proksch, J. Appl. Phys. **118**, 072011 (2015).

[37] S. Jesse, S. Guo, A. Kumar, B. J. Rodriguez, R. Proksch and S. V. Kalinin, Nanotechnology **21**, 405703 (2010).

[38] B.J. Rodriguez, S. Jesse, K. Seal, N. Balke, S.V. Kalinin, and R. Proksch, Chapter 17 in *Scanning Probe Microscopy of Functional Materials: Nanoscale Imaging and Spectroscopy*, S. V. Kalinin and A. Gruverman, Eds., (Springer Science+Business Media, 2010).

[39] B. J. Rodriguez, C. Callahan, S. V. Kalinin, and R. Proksch, Nanotechnology **18**, 475504, (2007).

[40] S. Jesse, R. K. Vasudevan, L. Collins, E. Strelcov, M. B. Okatan, A. Belianinov, A. P. Baddorf, R. Proksch, and S. V. Kalinin, Annual Review of Physical Chemistry **65**, 1, 519 (2014).

[41] L. Collins, and U. Celano, ACS Appl. Mater. Interfaces **12**, 37, 41659 (2020).

[42] S. Jesse, A. P. Baddorf, and S. V. Kalinin, Appl. Phys. Lett. **88**, 062908 (2006).

[43] C. B. Sawyer, and C. H. Tower, Physical Review **35**, 269 (1930).

[44] S. Tiedke, and T. Schmitz, Chapter 3 in *Nanoscale Characterisation of Ferroelectric Materials*, M. Alexe, and A. Gruverman, Eds., (NanoScience and Technology. Springer, Berlin, Heidelberg (2004).)

[45] C. Dehoff, B. J. Rodriguez, A. I. Kingon, R. J. Nemanich, A. Gruverman, and J. S. Cross, Rev. Sci. Instrum. **76**, 023708 (2005).

[46] W. L. Warren, D. Dimos, G. E. Pike, B. A. Tuttle, M. V. Raymond, R. Ramesh, and J. T. Evans, Appl. Phys. Lett. **67**, 866 (1995).

[47] S. Bernacki, L. Jack, Y. Kisler, S. Collins, S. D. Bernstein, R. Hallock, B. Armstrong, J. Shaw, J. Evans, B. Tuttle, B. Hammetter, S. Rogers, B. Nasby, J. Henderson, J. Benedetto, R. Moore, Cpt. R. Pugh, and A. Fennelly, Int. Ferro. **3**, 97 (1993).

[48] D. Bondurant, Ferroelectrics **112**, 273 (1990).

[49] J. Li, B. Nagaraj, H. Liang, W. Cao, C. H. Lee, and R. Ramesh, Appl. Phys. Lett. **84**, 7 (2004).

[50] A. N. Kolmogorov, Izv. Akad. Nauk SSSR Ser. Mater. **3**, 355 (1937); M.J. Avrami, Chem. Phys. **7**, 1103 (1939); Y. Ishibashi, and Y. J. Takagi, Phys. Soc. Jpn. **31**, 506 (1971).

[51] A. K. Tagantsev, I. Stolichnov, N. Setter, J. S Cross, and M. Tsukada, Phys. Rev. B **66**, 214109 (2002).

[52] T. Schenk, M. Pešić, S. Slesazeck, U. Schroeder, and T. Mikolajick, Rep. Prog. Phys. **83**, 086501 (2020).

Chapter 3

Nanoscopic studies of domain structure dynamics in ferroelectric La:HfO_2 capacitors

3.1 Introduction

The discovery of ferroelectricity (FE) in hafnium oxide (HfO_2) or hafnia-based thin films [1] opens a possibility of overcoming significant problems associated with application of perovskite ferroelectrics in electronic devices, such as poor complementary metal oxide semiconductor (CMOS) compatibility, small bandgap and low resistance to hydrogen [2]. However, realization of the full potential of the HfO_2-based films requires comprehensive studies to understand the properties of hafnia as well as to understand the mechanism of polarization reversal from a nanoscopic perspective.

One of the characteristic features of hafnia is the so-called "wake-up" effect [3, 4, 5, 6] (also termed as AC training [7]), in which a polarization hysteresis loop, initially constricted, opens up upon AC field cycling exhibiting a significantly increased remanent polarization. Although several groups have reported that the underlying cause for this effect might be a redistribution of mobile ions [8] and oxygen vacancies [9, 10, 11] or a phase transition from a non-FE to a FE phase [12, 13] most of the measurements were performed using integral methods with information on the local spatial variability missing. In addition, in spite of active studies by means of integral electrical methods, such as polarization hysteresis and

transient current measurements [14], there is dearth of information on the kinetics of domain nucleation and wall motion during polarization reversal in HfO_2-based films.

In this chapter, a combination of high-resolution domain imaging and local switching spectroscopy by piezoresponse force microscopy (PFM) was used in conjunction with pulse switching measurements to get a nanoscopic insight into the mechanism of the wake-up phenomenon and switching behavior of polycrystalline La-doped HfO_2 (La:HfO_2) ferroelectric capacitors. We find that AC field cycling leads to de-pinning of domains, resulting in an increase in the remanent polarization. It is also shown that polarization reversal behavior is consistent with the nucleation-limited switching (NLS) model [15].

The results presented in this chapter have been published in Ref. [16].

3.2 Materials and Methods

Experiments have been carried out using 125x110 μm^2 capacitors fabricated on Si substrates by atomic layer deposition (ALD) [17]. A stack of 10-nm-thick La:HfO_2 film sandwiched between TiN electrodes has been annealed in N_2 atmosphere at 800 °C for 20 s. Subsequently, 10-nm-thick Ti and 25-nm-thick Pt layers were evaporated on TiN and patterned into top electrode pads [17].

The PFM measurements have been performed in the capacitor geometry using a ~0.5 V AC modulation bias. Details of the PFM measurement configuration are discussed in section 2.3.1 in Chapter 2. The details of the pulse switching measurements are discussed in section 2.3.3 in Chapter 2.

3.3 Results and Discussion

3.3.1 Wake-up effect

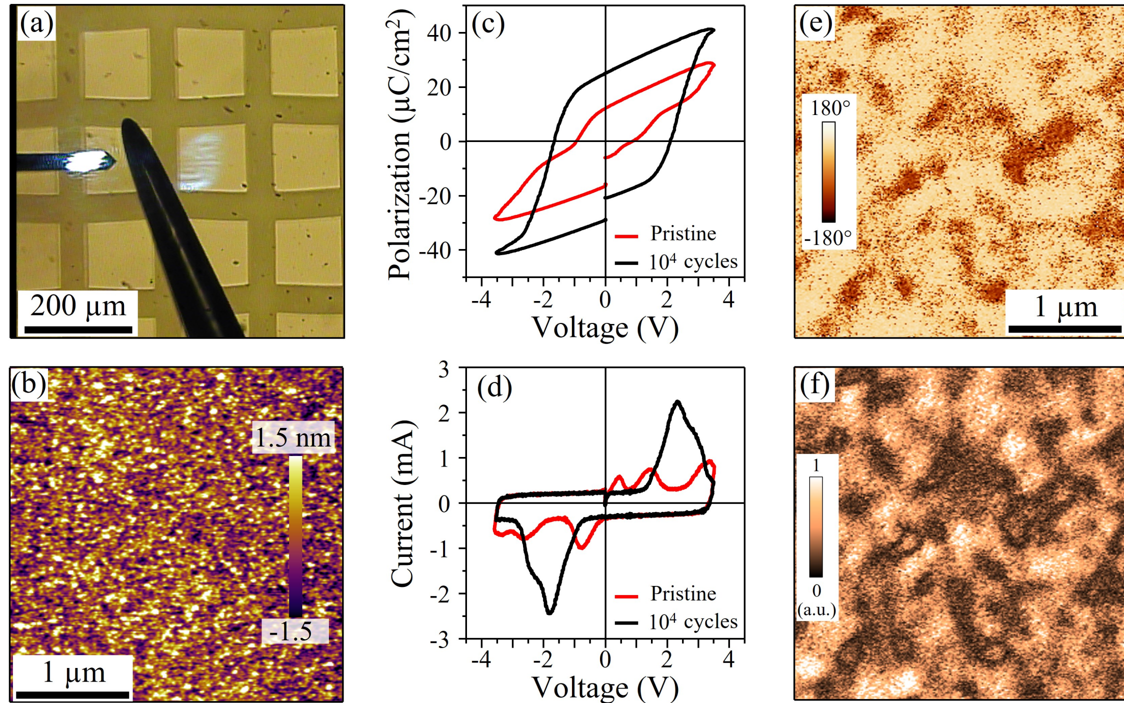

Figure 3.1. (a) Optical microscopy photo of the 125x110 μm^2 La:HfO_2 capacitors array showing the cantilever and an external microprobe on top of one of the capacitors. (b) Topographic image of the TiN top electrode using atomic force microscopy (AFM). (c) P-V hysteresis loops and (d) I-V loops acquired from the La:HfO_2 capacitor in the pristine state (red) and after 10^4 cycles of AC training (black). (e-f) PFM phase (e) and amplitude (f) of a pristine capacitor. Figure adapted from Ref. [16].

The pristine state of the La:HfO_2 capacitors is characterized by a pinched polarization-voltage (P-V) hysteresis loop with a low value of remanent polarization (Fig. 3.1 (c), red curve), which is consistent with the earlier reported results [5, 8, 9, 17]. Multiple switching peaks in the corresponding current-voltage (I-V) curve (Fig. 3.1 (d), red curve) can be attributed to a wide variability of the local

pinning potential. PFM imaging of the pristine La:HfO_2 capacitors reveals a polydomain structure with an average domain size of several hundred nanometers (Figs. 3.1 (e) and 3.1 (f)) and no correlation with any topographic features. To induce the wake-up process, the capacitors were subjected to 10^4 cycles of AC training using rectangular voltage pulses of ±3.5 V amplitude and 25 μs duration. As a result of this cyclic switching, the remanent polarization increased to about 25 μC/cm^2 (Fig. 3.1 (c), black curve) while the transient current peaks merged into single switching peaks (Fig. 3.1 (d), black curve) suggesting significant changes in the switching potential landscape.

To understand the underlying mechanism of the wake-up effect, the nanoscopic domain structure and its response to the applied electrical bias have been investigated by means of the PFM technique. Figs. 3.2 (a) and 3.2 (b) show that application of ±3.0 V, 1 ms voltage pulses to the pristine capacitors results in a minimal change in the domain configuration suggesting strong pinning of domains, which is consistent with the low remanent polarization value detected from the P-V loop measurements. The switchability of the capacitors dramatically changes after they were subjected to 10^4 cycles of AC training as is illustrated by the PFM images in Figs. 3.2 (c) and 3.2 (d). It can be seen that the domain structure changes completely in response to the application of the ±3.0 V, 1 ms poling pulses indicating increased switchability of domains as a result of the wake-up process. This result, in conjunction with X-ray diffraction results indicating a FE phase volume fraction of almost 90 % in the studied films [17], suggests that the increase in the remanent polarization upon AC cycling is mostly due to domain de-pinning, even though some contribution from the field-induced phase transformation cannot be ruled out [13, 17]. Note, that the de-pinning process is not symmetric: some of the domains with the downward polarization were still pinned after AC cycling as they could not be switched upward by application

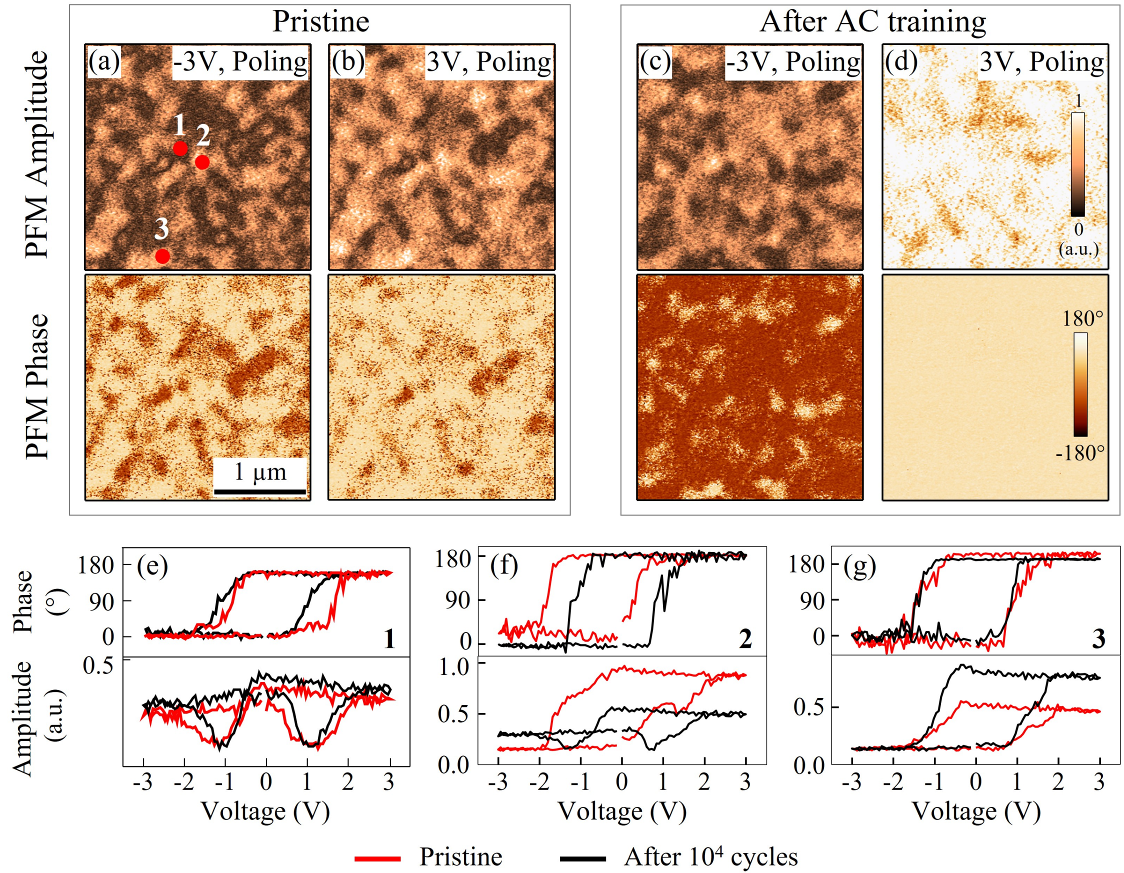

Figure 3.2. (a-d) Comparison of capacitor switchability in the pristine state and after the wake-up process. PFM amplitude (top) and phase (bottom) images of a La:HfO_2 capacitor after application of a ±3 V, 1 ms pulse in pristine state (a-b) and after application of 10^4 cycles of AC training (c-d). Bright (dark) color in the phase images corresponds to downward (upward) polarization. (e-g) Local PFM hysteresis loops acquired in location 1 (e), 2 (f) and 3 (g) marked with red dots in (a) for pristine (red) and after the wake-up process (black). Figure adapted from Ref. [16].

of a -3 V pulse (Fig. 3.2 (c)), while switching to the downward direction by a 3 V pulse was complete (Fig. 3.2 (d)). It can be assumed that this asymmetry is a result of the asymmetric boundary conditions at the top and bottom interfaces due to the fabrication route. The bottom electrode is subject to oxidizing species during the ALD process, which is not the case for the top electrode, and a Ti-O(-N) layer has been shown to form under similar conditions also due to the thermal energy

imposed by the crystallization anneal [19, 20, 21]. Another feature worth mentioning is strong spatial variability of the local switching parameters at the nanoscale level likely caused by structural imperfections associated with polycrystalline nature of the La:HfO_2 capacitors.

Analysis of the PFM images in Figs. 3.2 (a) and 3.2 (b) allows us to select different representative regions to illustrate this point. Shown in Figs. 3.2 (e-g) are the local PFM hysteresis loops for the pristine state (red curves) and after AC cycling (black curves) for the three locations marked in Fig. 3.2 (a). Location 1 exhibits symmetric coercive voltages and good switchability before and after the wake-up process (Fig. 3.2 (e)), which is consistent with the switching behavior revealed by the PFM imaging in Figs. 3.2 (a-d). Location 2, however, shows strong negative imprint in the pristine state (Fig. 3.2 (f)) consistent with the pinned downward polarization state. This imprint disappears after AC cycling suggesting domain de-pinning, which can be also seen in the PFM phase image (Fig. 3.2 (d)). In location 3, no evidence of the ferroelectric behavior can be observed even after the wake-up process (Fig. 3.2 (g)), which could be a signature of a residual non-ferroelectric phase. Both findings, an initial local imprint that disappears during AC cycling and the existence of non-FE phase fractions are consistent with earlier reports based on first-order reversal curves [8] and Rietveld refinement [17].

Interestingly, careful observation of the pristine PFM amplitude loop in regions with strong pinning such as location 2 reveals abrupt jumps in the amplitude levels (Fig. 3.2 (f), red curve). Such a behavior was found in multiple locations across several different capacitors in the pristine state and a representative loop is shown in the red curve in Fig. 3.3 (a). To better illustrate the abrupt jumps in the amplitude levels, the corresponding piezoresponse loop (obtained from the convolution of the amplitude and the cosine of the PFM phase signal) is shown in the red curve in Fig.

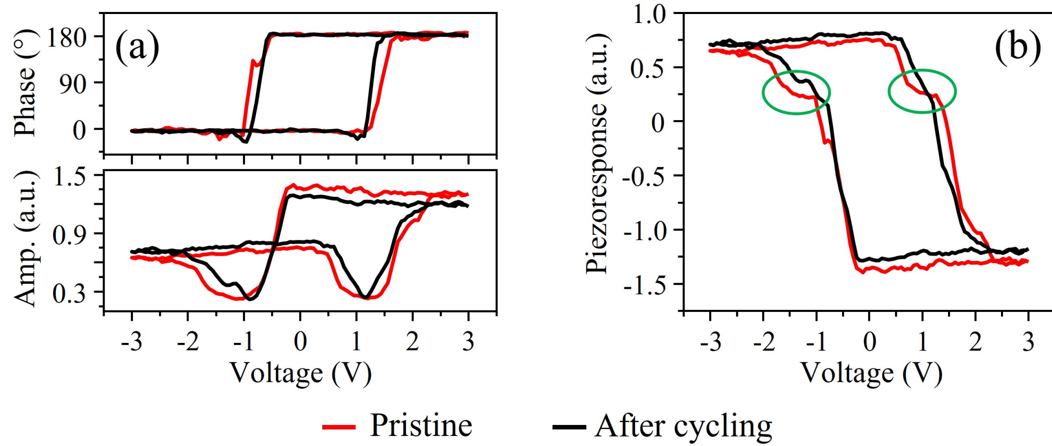

Figure 3.3. Representative Local PFM hysteresis loops (a) and corresponding piezoresponse loops (b) in the pristine state (red) and after AC training (black). Abrupt jumps in the PFM amplitude loops are highlighted by the green ovals.

3.3 (b) with the green ovals highlighting the abrupt jumps. This effect can be attributed to domain wall pinning by local defects, which gives rise to several discreet levels in the piezoresponse amplitude signal due to abrupt switching steps at different voltages [22]. Such jumps are consistent with the multiple switching peaks observed in the pristine integral switching current measurements (Fig. 3.1 (d), red curve). Upon field cycling, the abrupt jumps nearly disappeared in the locations tested (black curves in Figs. 3.3 (b,d)) similar to what was observed in the integral switching current measurements (Fig. 3.1 (d), black curve).

The switching spectroscopy PFM (SS-PFM) approach [23] provides further insight into the spatial variability of the local switching parameters. Two-dimensional maps of the local imprint bias have been generated by acquiring local hysteresis loops at each point while rastering the 500 x 500 nm^2 region on the top electrode surface of the capacitors in the pristine state (Fig. 3.4 (a)) and after the wake-up process (Fig. 3.4 (b)). Histogram analysis of the acquired maps reveals the reduction in the

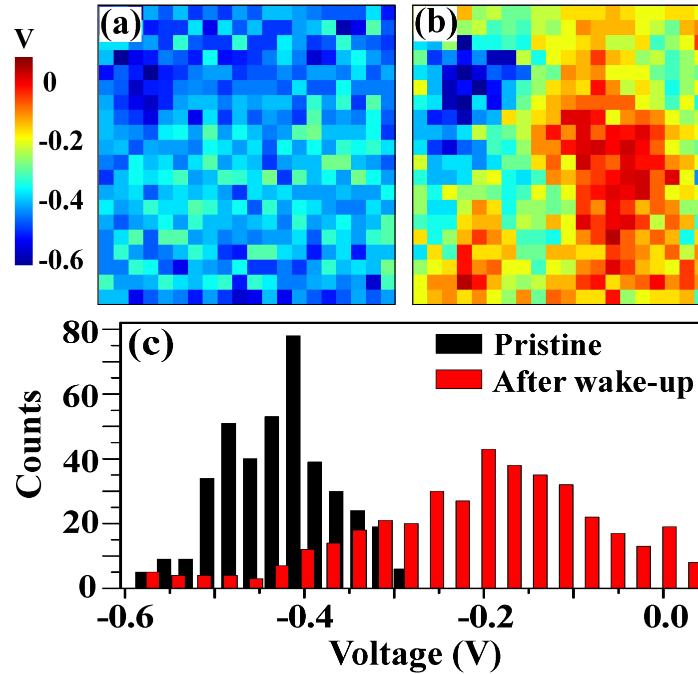

Figure 3.4. (a, b) 500 x 500 nm^2 imprint maps obtained by PFM switching spectroscopy using a 20 x 20 grid for the pristine state (a) and after wake-up (b). (c) Comparison of histograms of the imprint maps in (a) and (b) illustrating a change in the overall imprint bias after the wake-up process. Figure taken from Ref. [16].

magnitude of imprint upon AC field cycling (Fig. 3.4 (c)), even though about 90% of the imaged area still exhibits some negative imprint after the wake-up process. The SS-PFM maps and the corresponding histograms further corroborate the switching behavior seen in the PFM poling data (Fig. 3.2).

3.3.2 Domain dynamics

The spatial variations of the imprint and coercive bias give a sense of the expected domain kinetics in the La:HfO_2 capacitors during polarization reversal, which has been investigated by means of the stroboscopic PFM approach [24]. In this approach, a sequence of input voltage pulses of incrementally increasing duration (each one shorter than the total switching time) is applied to a capacitor inducing

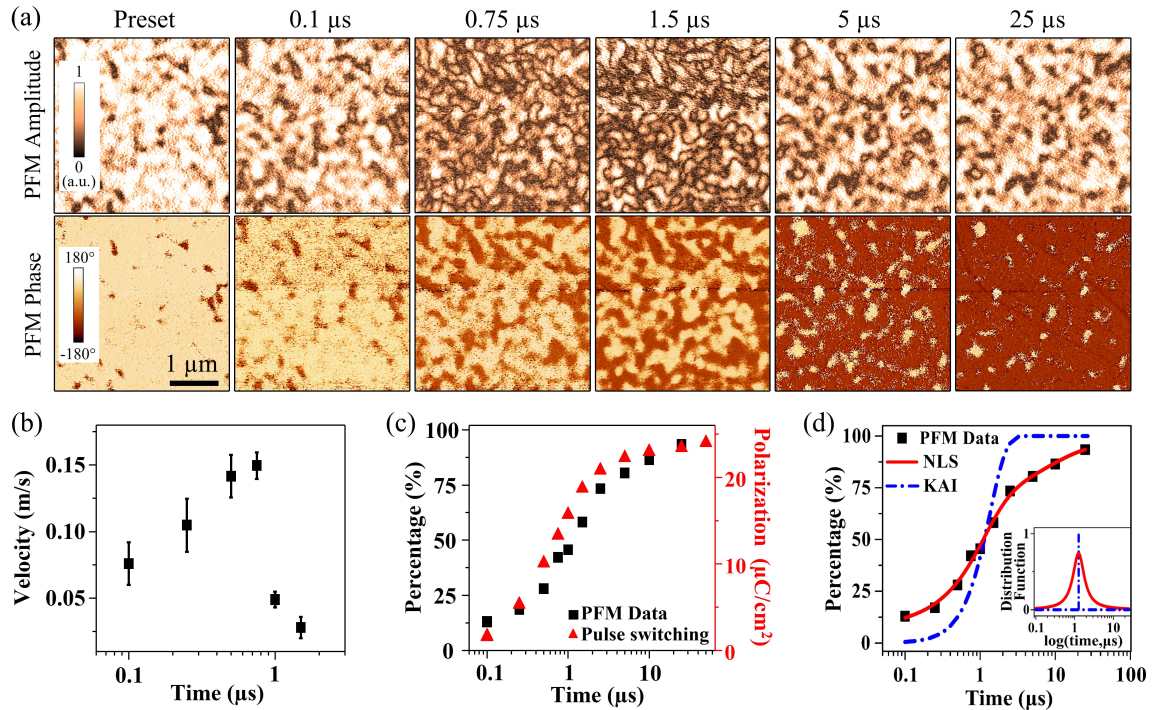

Figure 3.5. (a) PFM amplitude (top panels) and PFM phase images (bottom panels) of instantaneous domain configurations developing at different stages of polarization reversal under application of 4.0 V pulses of increasing duration. (b) Time-dependent variations in domain wall velocity obtained by analyzing images in (a). (c) Comparison of experimental PFM data showing switched capacitor area as a function of time with the polarization obtained from pulse switching measurements. (d) Fitting of the PFM switching data by the KAI and NLS models. The inset shows the distribution functions for the corresponding models. Figure adapted from Ref. [16].

partial polarization switching. PFM imaging of the resulting domain pattern representing a certain stage of polarization reversal is performed after each pulse. Figure 3.5 (a) shows PFM images of instantaneous domain configurations developing in the previously AC-trained La:HfO_2 capacitors at different stages of polarization reversal process induced by 4 V switching pulses. It can be seen that, switching occurs through the sidewise expansion of the residual (pinned) domains of the corresponding polarity that have not been removed during the wake-up process

as well as via nucleation and growth of new domains. By analyzing the space-time dependence of the domain expansion in the PFM snapshots, we were able to estimate the lateral domain wall (DW) velocity. It was found that the DW velocity varied depending on the azimuthal direction and was not constant throughout the switching process suggesting a strong impact of structural defects, such as grain boundaries. This hypothesis is supported by the fact that the size of the growing domains reaches values of up to 300 nm, which is larger than the average grain size (30-50 nm), implying that the DWs move across several grain boundaries before annihilation by domain coalescence. Figure 3.5 (b) shows a representative plot of the variations in the DW velocity as a function of time. The maximum velocity measured is about 0.15 m/s, which is two orders of magnitude slower than the velocities observed in $Pb(Zr,Ti)O_3$ capacitors for the same ratio of the applied field to the coercive field [24, 25]. This low DW velocity seems to be consistent with recent reports on a small value of the Rayleigh constant measured in HfO_2-based films [26].

To quantify the domain switching kinetics, a time dependence of the switched capacitor volume fraction has been obtained by image analysis of the PFM data and plotting the obtained results as a function of the pulse duration. In addition, we performed pulse switching measurements using a four pulse waveform [15] to estimate the switched polarization as a function of the pulse duration to compare it with the PFM stroboscopic data. We found that the switched capacitor fraction with polarization along the direction of the applied field detected by PFM is proportional to the switched charge obtained by integration of current induced by pulse switching (Fig. 3.5 (c)). This allows us to treat the time-dependent PFM switching data, shown in Fig. 3.5 (d), the same way as the switched polarization data and fit them with the well-known NLS model [15]:

$$\triangle P(t) = 2P_s \int_{\infty}^{\infty} [1 - exp(-(t/t_0)^n)].F(logt_0).d(logt_0) \tag{3.1}$$

where P_s is the spontaneous polarization, $F(logt_0)$ is a distribution function of the characteristic switching time, t_0, and n is the effective dimension of domain growth (n=2 in this case). The term in the square brackets in Eq. (4.2) represents the Kolmogorov-Avrami-Ishibashi (KAI) switching model [27, 28, 29], which does not consider spatial inhomogeneities in the film structure. To account for the polycrystalline nature of the La:HfO_2 films and non-uniform internal potential landscape manifested in the imprint map (Fig. 3.4 (b)), a Lorentzian distribution of the local switching times [30] is used in the NLS fitting:

$$F(logt_0) = \frac{A}{\pi}[\frac{w}{(logt_0 - logt_1)^2 + w^2}] \tag{3.2}$$

where A is a normalization constant, w is the half-width at half-maximum and $logt_1$ is the center of the distribution. When w approaches zero, $F(x)$ becomes a delta function and we obtain the KAI model. Fig. 3.5 (d) shows that the NLS model provides a better fit to the experimental data than the KAI model, in agreement with previous reports that involved only pulse switching measurements [14, 31].

3.4 Conclusion

In conclusion, a combination of PFM imaging and macroscopic polarization switching measurements provides direct evidence that the increase in the remanent polarization upon AC cycling in the La:HfO_2 capacitors is mainly a result of electrically-induced domain de-pinning although some contribution from the field-induced phase transformation cannot be ruled out. PFM poling experiments

and switching spectroscopy reveal a broad variation in the local switching parameters likely caused by the asymmetry in the boundary conditions at the capacitors top and bottom interfaces and by the polycrystalline nature of the La:HfO_2 films. The remanent (pinned) domains serve as the nucleation centers during polarization reversal and contribute to the switching behavior that is best described by the NLS model. The nanoscopic visualization of domain structure evolution during the wake-up process as well as during polarization reversal will allow optimization of the switching behavior of the La:HfO_2-based ferroelectric devices.

References

[1] T. S. Boescke, J. Mueller, D. Braeuhaus, U. Schroeder, and U. Boetgger, Appl. Phys. Lett. **99**, 102903 (2011).

[2] M. H. Park, Y. H. Lee, H. J. Kim, Y. J. Kim, T. Moon, K. D. Kim, J. Müller, A. Kersch, U. Schroeder, T. Mikolajick, and C. S. Hwang, Adv. Mater. **27**, 1811 (2015).

[3] D. Zhou, J. Xu, Q. Li, Y. Guan, F. Cao, X. Dong, J. Müller, T. Schenk, and U. Schroeder, Appl. Phys. Lett. **103**, 192904 (2013).

[4] S. Müller, C. Adelmann, A. Singh, S. Van Elshocht, U. Schroeder, and T. Mikolajick, ECS J. Solid State Sci. Technol. **1**, N123 (2012).

[5] T. Schenk, U. Schroeder, M. Pešic, M. Popovici, Y. V. Pershin, and T. Mikolajick, ACS Appl. Mater. Interfaces **6**, 19744 (2014).

[6] M. H. Park, H. J. Kim, Y. J. Kim, Y. H. Lee, T. Moon, K. D. Kim, S. D. Hyun, F. Fengler, U. Schroeder, and C. S. Hwang, ACS Appl. Mater. Interfaces **8**, 15466 (2016).

[7] M. Kohli, P. Muralt, and N. Setter, Appl. Phys. Lett. **72**, 3217 (1998).

[8] T. Schenk, M. Hoffmann, J. Ocker, M. Pešic, T. Mikolajick, and U. Schroeder, ACS Appl. Mater. Interfaces **7**, 20224 (2015).

[9] S. Starschich, S. Menzel, and U. Böttger, Appl. Phys. Let. **108**, 032903 (2016).

[10] M. Pešic, F. P. G. Fengler, L. Larcher, A. Padovani, T. Schenk, E. D. Grimley, X. Sang, J. M. LeBeau, S. Slesazeck, U. Schroeder, and T. Mikolajick, Adv. Funct. Mater. **26**, 4601 (2016).

[11] F. P. G. Fengler, M. Pešic, S. Starschich, T. Schneller, C. Künneth, U. Böttger, H. Mulaosmanovic, T. Schenk, M. H. Park, R. Nigon, P. Muralt, T. Mikolajick, and U. Schroeder, Adv. Electron. Mater. **3**, 1600505 (2017).

[12] M. H. Park, H. J. Kim, Y. J. Kim, Y. H. Lee, T. Moon, K. D. Kim, S. D. Hyun, and C. S. Hwang, Appl. Phys. Lett. **107**, 192907 (2015).

[13] E. D. Grimley, T. Schenk, X. Sang, M. Pešic, U. Schroeder, T. Mikolajick, and J. M. LeBeau, Adv. Electron. Mater. **2**, 1600173 (2016).

[14] H. Mulaosmanovic, J. Ocker, S. Müller, U. Schroeder, J. Müller, P. Polakowski, S. Flachowsky, R. van Bentum, T. Mikolajick, and S. Slesazeck, ACS Appl. Mater. Interfaces **9**, 3792 (2017).

[15] A. K. Tagantsev, I. Stolichnov, N. Setter, J. S Cross, and M. Tsukada, Phys. Rev. B **66**, 214109 (2002).

[16] P. Buragohain, C. Richter, T. Schenk, H. Lu, T. Mikolajick, U. Schroeder, and A. Gruverman, Appl. Phys. Lett. **112**, 222901 (2018).

[17] U. Schroeder, C. Richter, M. H. Park, T. Schenk, M. Pešić, M. Hoffmann, F. Fengler, D. Pohl, B. Rellinghaus, C. Zhou, C.-C. Chung, J. Jones, and T. Mikolajick, Inorg. Chem. **57**(5), 2752 (2018).

[18] S. V. Kalinin, and D. A. Bonnell, Phys. Rev. B **65**, 125408 (2002).

[19] U. Schroeder, W. Weinreich, E. Erben, J. Mueller, L. Wilde, J. Heitmann, R. Agaiby, D. Zhou, G. Jegert, and A. Kersch, ECS Trans. **25** (4), 357 (2009).

[20] W. Weinreich, R. Reiche, M. Lemberger, G. Jegert, J. Müller, L. Wilde, S. Teichert, J. Heitmann, E. Erben, L. Oberbeck, U. Schröder, A. J. Bauer, and H. Ryssel, Microelectron. Eng. **86**, 1826 (2009).

[21] W. Weinreich, T. Tauchnitz, P. Polakowski, M. Drescher, S. Riedel, J. Sundqvist, K. Seidel, M. Shirazi, S. D. Elliott, S. Ohsiek, E. Erben, and B. Trui, J. Vac. Sci. Techn. A **31**, 01A123 (2013).

[22] S. V. Kalinin, S. Jesse, B. J. Rodriguez, Y. H. Chu, R. Ramesh, E. A. Eliseev, and A. N. Morozovska, Phys. Rev. Lett. **100**, 155703 (2008).

[23] P. Bintachitt, S. Trolier-McKinstry, K. Seal, S. Jesse, and S. V. Kalinin, Appl. Phys. Lett. **94**, 042906 (2009).

[24] A. Gruverman, D. Wu, and J. F. Scott, Phys. Rev. Lett. **100**, 097601 (2008).

[25] A. Grigoriev, D.-H. Do, D. M. Kim, C.-B. Eom, B. Adams, E. M. Dufresne, and P. G. Evans, Phys. Rev. Lett. **96**, 187601 (2006).

[26] Y. Guan, D. Zhou, J. Xu, X. Liu, F. Cao, X. Dong, J. Müller, T. Schenk, and U. Schroeder, Phys. Status Solidi RRL **9**, 589 (2015).

[27] A. N. Kolmogorov, Izv. Akad. Nauk USSR, Ser. Math. **3**, 355 (1937).

[28] M. Avrami, J. Chem. Phys. **7**, 1103 (1939).

[29] Y. Ishibashi, and Y. Takagi, J. Phys. Soc. Jpn. **31**, 506 (1971).

[30] J. Y. Jo, H. S. Han, J.-G Yoon, T. K. Song, S. H. Kim, and T. W. Noh, Phys. Rev. Lett. **99**, 267602 (2007).

[31] S. Mueller, S. R. Summerfelt, J. Müller, U. Schroeder, and T. Mikolajick, IEEE Elec. Device Lett. **33**, 1300 (2012).

Chapter 4

Effect of film microstructure on domain nucleation and intrinsic switching in ferroelectric Y:HfO_2 thin film capacitors

4.1 Introduction

One of the general features of ferroelectric systems is a complex nature of polarization reversal, which involves domain nucleation and motion of domain walls. Since functionality of the ferroelectric-based devices in most cases depends on the electrical switching of the spontaneous polarization, increasing application of the HfO_2-based ferroelectric (FE) films especially in negative-capacitance-based devices [1, 2, 3, 4] calls for a better understanding of the mechanism of polarization reversal in these materials, which is far from being understood [5, 6, 7, 8]. For example, hysteresis-free negative capacitance can only occur if the polarization switches intrinsically, i.e., without domain nucleation and growth [9, 10]. Does it mean that the 'S'-shaped polarization-electric field (P-E) curve - a signature of the negative capacitance effect - experimentally demonstrated in the $Hf_{0.5}Zr_{0.5}O_2$ (HZO) heterostructures [4] is also an indicator of the intrinsic switching? A possibility of the intrinsic switching in the HZO structures was recently deduced from a similarity between the coercive fields obtained from the macroscopic P-E hysteresis and piezoresponse force microscopy (PFM) spectroscopic measurements [7]. On the

other hand, it is widely accepted that polarization reversal in real ferroelectrics is of extrinsic nature, i.e. it is driven by heterogeneous nucleation caused by the local defects, which results in a significant difference between the experimentally measured coercive field and the so-called intrinsic coercive value, predicted theoretically [11, 12, 13]. It has been surmised, however, that the intrinsic switching can be, in principle, realized if domain nucleation is suppressed by using a very strong (much larger than the coercive value) electric field with fast (faster than the nucleation time) ramping or by using materials with low defect concentration [14]. This latter condition is generally difficult to fulfill but it could be bypassed by using well-textured epitaxial films with a grain density comparable with the domain nucleation density. In this case, assuming a narrow distribution function of the nucleation times, polarization switching could be considered homogeneous, resembling intrinsic switching.

Currently, there are very few reports on investigation of the domain switching behavior in the HfO_2-based thin films. Most of them are focused on the switching of the polycrystalline films where polarization reversal is extrinsic, i.e., occurs via domain formation [15, 16, 17, 18, 19, 20], as was discussed in the previous chapter. In this regard, investigation of the domain switching dynamics in the epitaxial as opposed to the polycrystalline HfO_2-based thin films would provide an important insight into correlation between the film microstructure and mechanism of electrical response of these materials. In this chapter, we have performed a comparative study of the polarization switching behavior in the epitaxial and polycrystalline yttrium-doped HfO_2 ($Y{:}HfO_2$) thin films using a combination of the stroboscopic PFM [21, 22] and pulse switching techniques. Visualization of the instantaneous domain configurations arising during the polarization switching process allowed measurement of the domain nucleation rate, nucleation density as well as evaluation

of the domain wall velocity. It has been found that the epitaxial films switch noticeably slower compared to the polycrystalline films. Switching in the epitaxial films occurs mainly via nucleation while both nucleation and lateral domain expansion contribute to the polarization reversal in the polycrystalline films. Most importantly, it has been observed that when the applied field was close to the activation field, the switching kinetics could be described equally well by the nucleation limited switching (NLS) [23] and the Kolmogorov-Avrami-Ishibashi (KAI) [24] models. This signifies convergence of two different mechanisms at high fields implying that the polarization reversal is approaching the intrinsic switching limit.

The results presented in this chapter have been published in Ref. [25].

4.2 Materials and methods

The experiments have been carried out on ~86-μm-diameter capacitor structures made of 0.07YO1.5-0.93HfO_2 (Y:HfO_2) films prepared by pulsed laser deposition (PLD) using a KrF excimer laser (λ = 246 nm and a fluence of 3 J cm^{-2}) [26, 27]. These films were deposited at room temperature on ITO// (111)YSZ and Pt/ TiO_x/ SiO_2/ Si substrates for the preparation of epitaxial and polycrystalline films, respectively. The atmosphere was maintained at 10 mTorr O_2. The ferroelectric orthorhombic phase was obtained by the following heat treatment at 1000 °C for 10 s under N_2 flow. The film thickness was confirmed by scanning X-ray reflectivity (XRR) measurements (X'Pert-MRD, Philips). The crystal structures of these films were investigated by X-ray diffraction (XRD) $2\theta - \psi$ mapping (D8 DISCOVER, Bruker). XRD pole figure measurements were performed for the (111)-oriented epitaxial films to clarify the in-plane orientations. All films were covered with

Pt-top electrodes through metal mask by electron beam evaporation at room temperature to measure electrical properties. The typical grain size in these films is around 110 nm and less than 35 nm for the polycrystalline and the epitaxial films, respectively [28]. The majority of the experiments were performed on 27-nm-thick epitaxial and polycrystalline films. In addition, 23-nm-thick epitaxial and 24-nm-thick polycrystalline films were also used for one set of measurements.

The PFM measurements have been carried out as described in section 2.3.1 in Chapter 2, using a ∼1 V AC modulation bias in the capacitor geometry with 20-nm-thick top electrodes in both the polycrystalline and epitaxial films. Details of the macroscopic electrical characterization are given in 2.3.3 in Chapter 2. All polarization-voltage (P-V) loop measurements have been carried out at 10 kHz.

4.3 Macroscopic electrical characterization

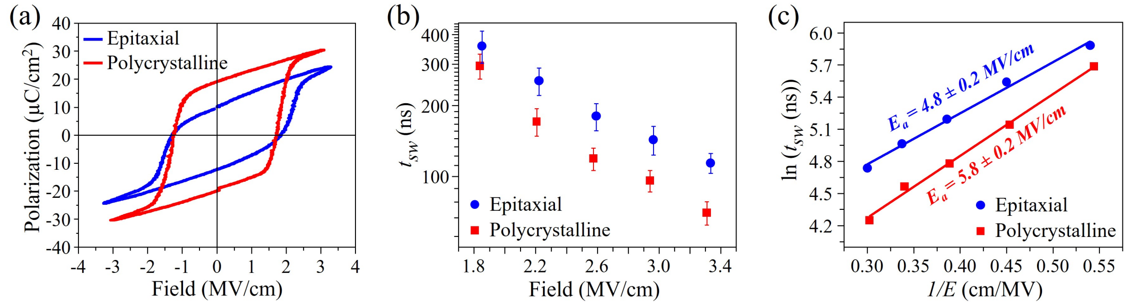

Figure 4.1. (a) P-E hysteresis loops measured in the 27-nm-thick epitaxial and polycrystalline Y:HfO_2 thin film capacitors. (b) Comparison of the switching times (t_{sw}) in the same epitaxial and polycrystalline Y:HfO_2 capacitors. The error bars represent the standard deviation of the switching times from at least three different capacitors for each film type. (c) Calculation of the activation field (E_a) from the field dependence of the switching times in the epitaxial and polycrystalline Y:HfO_2 capacitors. Figure adapted from Ref. [25].

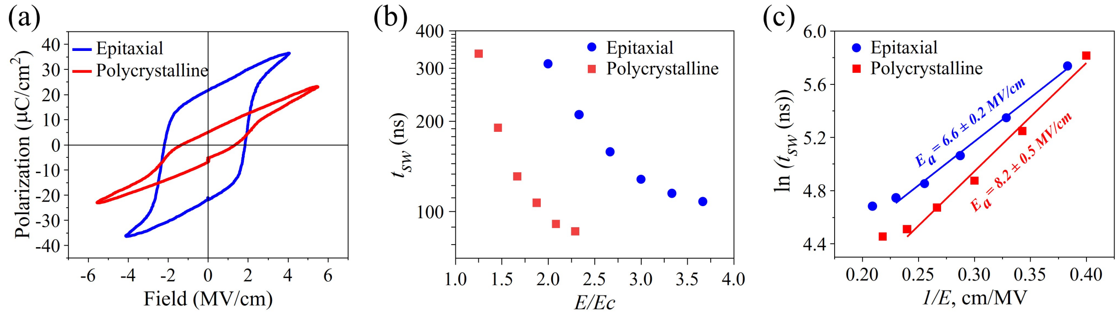

Figure 4.2. (a) Polarization-Field (P-E) loops after wake-up in the 23-nm-thick epitaxial and 24-nm-thick polycrystalline Y:HfO_2 capacitors. (b) Comparison of switching times between the epitaxial and the polycrystalline Y:HfO_2 capacitors. Here, E represents the applied electric field and E_c represents the coercive field. To normalize the different coercive fields for the two films, the switching times were plotted with respect to the ratio of the applied electric field (E) to the coercive field (E_c) (c) Calculation of the activation field (E_a) from the field dependence of the switching times in the epitaxial and polycrystalline Y:HfO_2 capacitors. Figure adapted from Ref. [25].

Preliminary macroscopic electrical testing of the ferroelectric properties of the Y:HfO_2 samples has been carried out by measuring the P-E hysteresis loops on the capacitors with nearly identical dimension (∼86-μm in diameter) (Fig. 4.1 (a)). The loops were obtained after the wake-up procedure [29], which involved electrical cycling of the capacitors for ∼50,000 cycles using pulses with an amplitude of 8 V and a duration of 10 μs. Investigation of the field dependence of the switching times (t_{sw}) revealed that the epitaxial films switched more slowly compared to the polycrystalline films (Fig. 4.1 (b)). This trend was reproducible from capacitor to capacitor and was observed for both polarities of the applied voltage. To make sure that the observed differences in the switching time between the 27-nm-thick epitaxial and polycrystalline films shown in Fig. 4.1 (b) was not an isolated instance, the switching times were also measured on capacitors with the 23-nm-thick epitaxial and 24-nm-thick polycrystalline Y:HfO_2 films. The epitaxial capacitors

were again found to have switched more slowly compared to the polycrystalline films in these thinner films as shown in Fig. 4.2 (b), highlighting that the observed differences in the switching speeds are due to the underlying differences in the film microstructure. The switching dynamics could be described by Merz's empirical equation [30]:

$$t_{sw} = t_0 exp(E_a/E) \tag{4.1}$$

where t_0 is the field independent switching time factor, E is the applied electric field and E_a is the activation field (Fig. 4.1 (c)). The epitaxial films were found to have a lower E_a of 4.8 MV/cm in comparison to 5.8 MV/cm for the polycrystalline films. These values are at least four times larger than those reported previously in other HfO_2-based thin films [20, 31].

4.4 Time dependent evolution of domain structure

To gain a nanoscale insight into the mechanism of the polarization switching behavior and its dependence on microstructure, the stroboscopic PFM measurements [21] have been carried out in the $Y:HfO_2$ capacitors. Instantaneous domain configurations were visualized through the top electrode at various stages of the polarization reversal process. Fig. 4.3 shows the domain snapshots illustrating time-dependent evolution of the polarization in the epitaxial (Fig. 4.3 (a)) and polycrystalline (Fig. 4.3 (b)) films. Comparison of the top electrode surface morphology with the observed features in the PFM images (Fig. 4.4) showed no correlation confirming the authenticity of the PFM-imaged domain configurations. The time dependence of the switched charge (Fig. 4.3 (c)) obtained by numerical integration of the switching current correlates well with the time dependence of the switched capacitor volume determined from

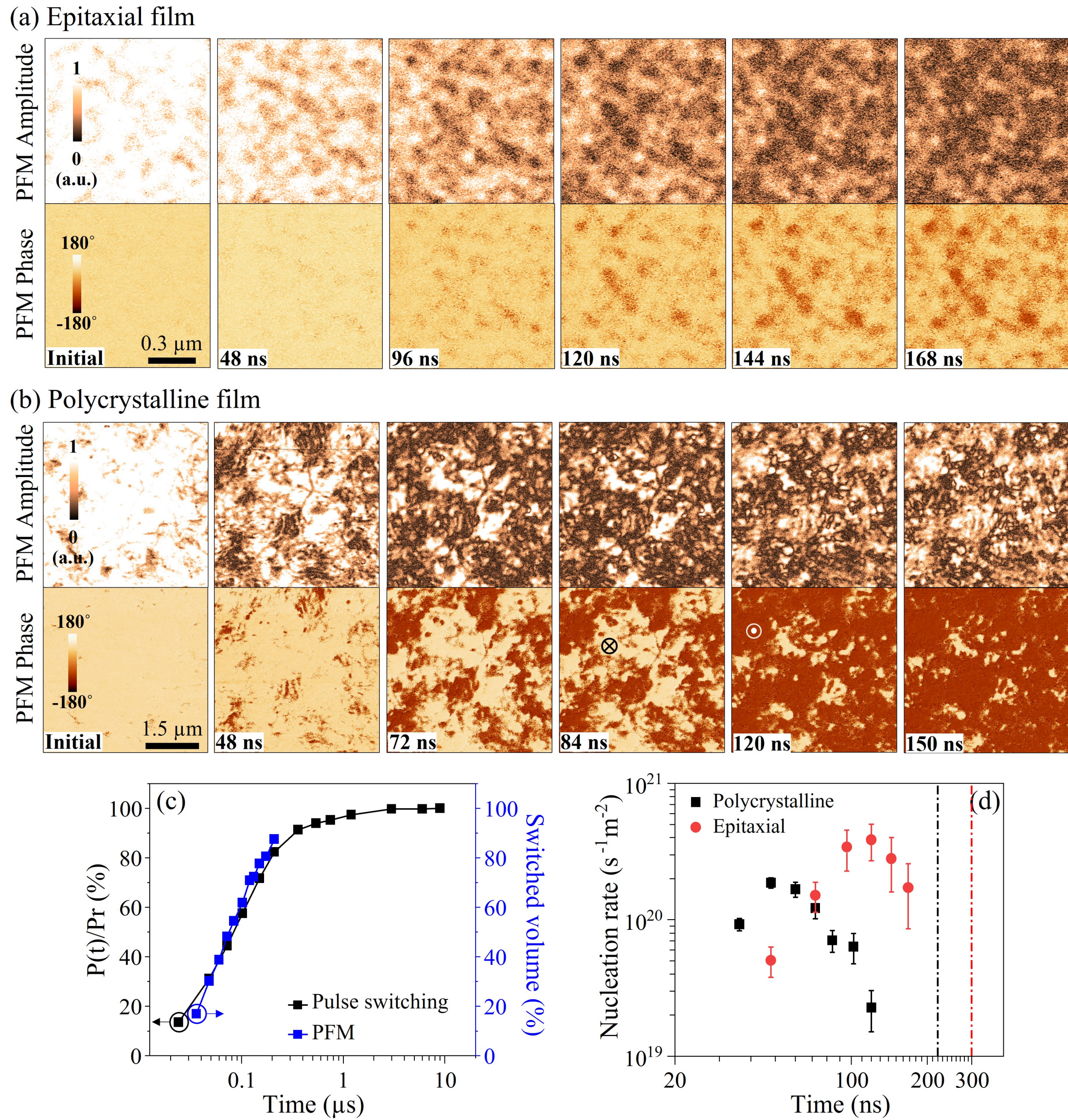

Figure 4.3. PFM amplitude (top row) and phase (bottom row) images of the instantaneous domain configurations in epitaxial (a) and in polycrystalline (b) 27-nm-thick Y:HfO_2 capacitors at different stages of polarization reversal under an applied electric field of -2 MV/cm. (c) Comparison of the fraction of switched volume obtained from the analysis of the PFM images with the pulse switching measurements in the polycrystalline Y:HfO_2 capacitors. (d) Nucleation rate as a function of the switching pulse duration for an applied electric field of -2 MV/cm. At this field, the switching times were around 220 ns and 300 ns for the polycrystalline and epitaxial capacitors, respectively, as indicated by the dashed lines. Figure adapted from Ref. [25].

PFM data in Figs. 4.3 (a,b). This confirms good correlation between the electrically measured integral switching current and domain switching kinetics detected by PFM.

It can be seen that polarization reversal in the epitaxial films occurs mainly via nucleation of new domains (Fig. 4.3 (a)). In comparison, switching in the polycrystalline films occurs via nucleation and lateral expansion of the nucleated domains (Fig. 4.3 (b) and Fig. 4.5). It could be argued that since grain boundaries significantly restrict (although probably do not completely stop) domain wall motion [32, 33], in the epitaxial films with grains of less than 35 nm in size only negligible lateral domain growth could be observed. In comparison, the nucleated domains can grow laterally in the polycrystalline films where the average grain size is above 100 nm [28].

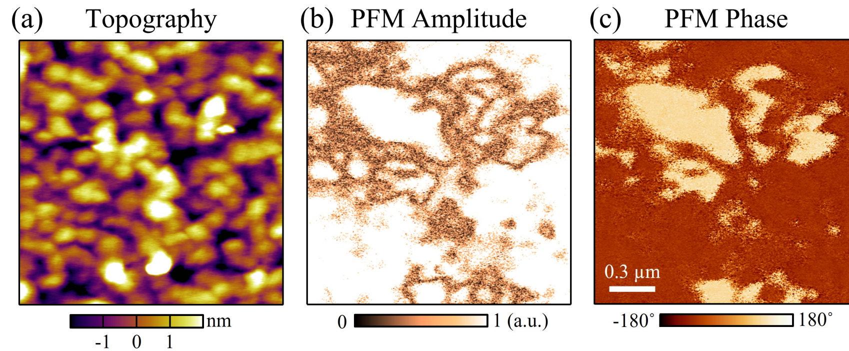

Figure 4.4. Topography (a), PFM amplitude (b) and PFM phase (c) images obtained through the top electrode in the 27-nm-thick polycrystalline Y:HfO_2 capacitor. No correlation was observed between the surface morphology and the observed features in PFM images. Figure adapted from Ref. [25].

Visualization of the instantaneous domain configurations during the step-by-step switching process allowed us to directly measure the domain nucleation rate as well as lateral domain wall velocity. As shown in Fig. 4.3 (d), the nucleation rate was found to be non-steady during the switching process in both types of the films. In the polycrystalline films, after reaching a peak value of 1.9×10^{20} $s^{-1}m^{-2}$ shortly

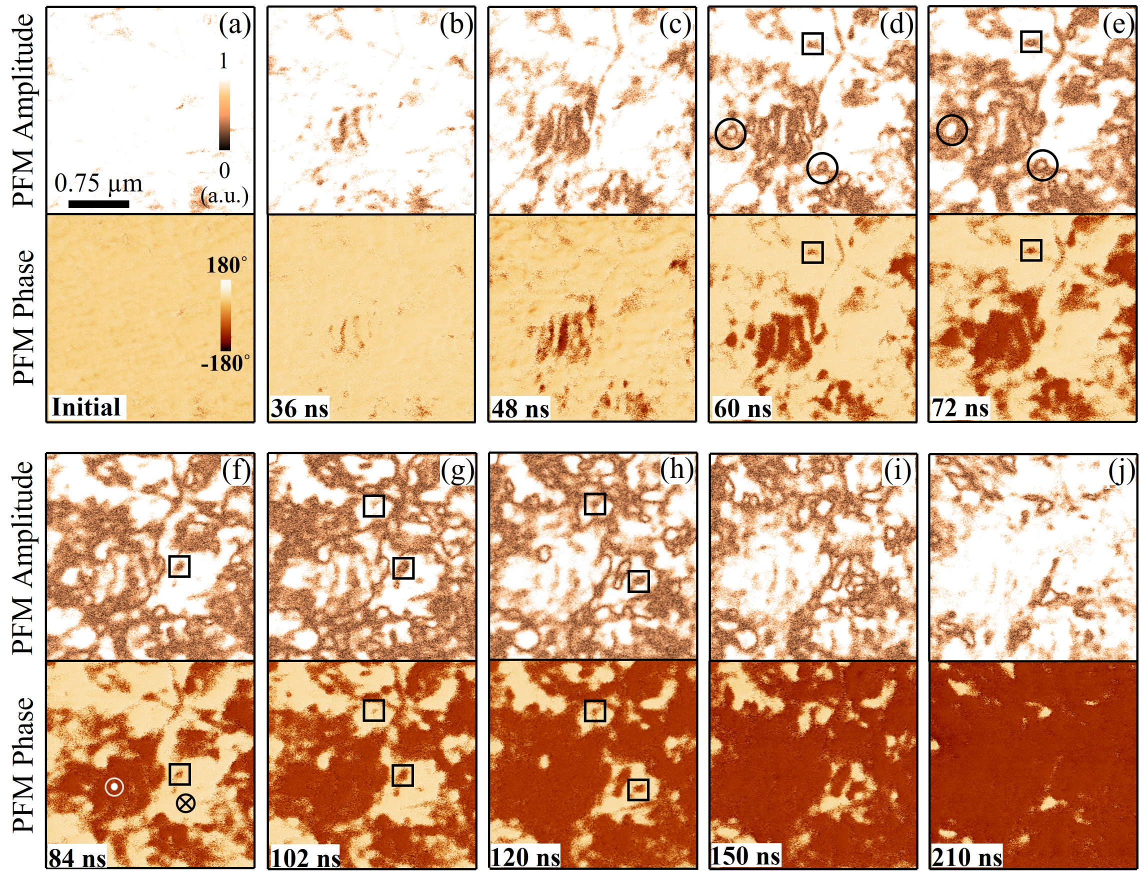

Figure 4.5. Sequence of high-resolution PFM amplitude (top) and phase (bottom) images in the 27-nm-thick polycrystalline Y:HfO_2 capacitors illustrating a time-dependent evolution of the domain structure under the external field of -2 MV/cm. The black squares indicate representative nucleation events and their subsequent growth. The black circles indicate nearly circular domains that were used to estimate the lateral domain wall velocity. Figure adapted from Ref. [25].

after the start of the switching, by the middle of this process the nucleation rate drops by almost an order of magnitude. This suggests a transition from the nucleation-dominated regime to the predominantly lateral domain wall motion regime. In contrast, in the epitaxial films, the peak nucleation rate is twice as high at 3.8×10^{20} $s^{-1}m^{-2}$ and is achieved much later than in the polycrystalline films (at the time of the peak nucleation rate, about 50% of the capacitor volume is

switched). After that, only a gradual insignificant decrease in the nucleation rate is observed. A possible reason for the peak nucleation rate to occur more quickly in the polycrystalline film might be the presence of latent nuclei (residual domains), from which domains can start growing almost immediately upon application of the switching pulse. Moreover, a higher disorder in the polycrystalline films can reduce a local energy barrier for polarization reversal facilitating faster nucleation. Parenthetically, we note that the peak nucleation rates in both the epitaxial and the polycrystalline Y:HfO_2 capacitors are an order of magnitude larger than those reported in polycrystalline PZT-based capacitors when compared for the same E/E_c ratio [21].

Domain wall velocity in the polycrystalline films was measured by analyzing the growing domains of less than 100 nm in size whose shapes could be approximated as a circle (highlighted by black circles in Fig. 4.5) (typically, growing domains are of irregular shape due to high non-uniformity of the wall velocity in azimuthal directions, which is an indication of nonuniform internal potential associated with microstructural defects). It was shown previously [16, 19] that the lateral domain wall velocity was not steady throughout the switching process, which was also observed in this study. Maximum lateral velocity was found to be in the range from 1.6 m/s to 3.2 m/s, which is nearly an order of magnitude higher than the previously reported values for the polycrystalline La:HfO_2 and Si:HfO_2 capacitors [16, 19]. The significant increase in the lateral wall velocity clearly illustrates the strong dependence of the wall velocity on interactions with grain boundaries [32, 33] given that the grain sizes in the polycrystalline Y:HfO_2 capacitors studied here are ~110 nm as opposed to the grains of ~50 nm or less in the previously reported La:HfO_2 and Si:HfO_2 capacitors [19, 34]. Similar observation of strong azimuthal variations in the lateral wall velocity was previously reported for the Pb(Zr,Ti)O_3 capacitors [35, 36].

4.5 Voltage dependent evolution of domain structure

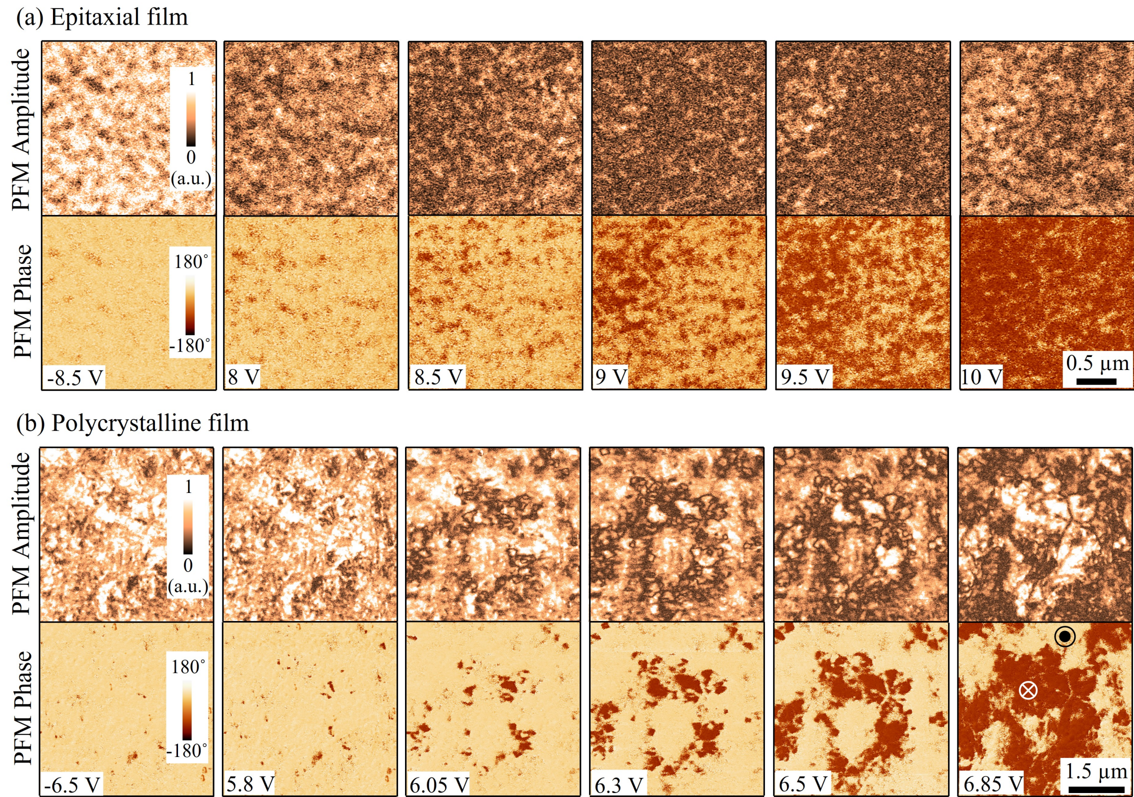

Figure 4.6. PFM amplitude (top row) and phase (bottom row) images of the voltage dependent switching behavior in the 27-nm-thick epitaxial (a) and in polycrystalline (b) Y:HfO_2 capacitors. The pulse duration was 0.1 ms for the epitaxial and 1 ms for the polycrystalline capacitors. Figure adapted from Ref. [25].

The voltage-dependent evolution of the domain structure in the epitaxial and polycrystalline Y:HfO_2 capacitors has been performed by acquiring series of PFM images after application of voltage pulses of incrementally increasing amplitude and fixed duration (Figs. 4.6 (a,b)). Similar to the time-dependent behavior, under an increasing voltage, the switching of the epitaxial samples proceeds mainly via domain nucleation while the polycrystalline samples switch via a combination of nucleation and the lateral domain expansion. A nucleation density is increasing

with the voltage amplitude with the maximum value of 1.2×10^{13} m^{-2} for the epitaxial capacitors. A maximum nucleation density observed in the polycrystalline capacitors was significantly lower: 7.8×10^{11} m^{-2}. Note, that the estimated nucleation densities are likely much lower than the actual values since the PFM spatial resolution limit for domain imaging through the top electrode (~30 nm) precludes detection of nucleation events that occur at the distances smaller than this limit.

4.6 Intrinsic switching

Intrinsic switching is said to take place when polarization is reversed homogeneously over the whole sample volume without any domain formation. The PFM data, presented here, reveal that the switching proceeds extrinsically via nucleation and formation of domains. Our previous studies of the polycrystalline La:HfO_2 capacitors [16] also found distinct region-by-region switching, which was described within the framework of the NLS model. The region-by-region switching essentially entails a statistical ensemble of regions characterized by a distribution of switching times due to the randomly distributed internal potential. It can be argued that under a sufficiently large (i.e., close to the thermodynamic activation field E_a value) electric field, the local potential variations would get "smoothed out" and the statistical distribution of the nucleation times would collapse to a delta function. As a result, in this high field limit both the KAI and the NLS models will converge. For a high nucleation site density this would be equivalent to the homogeneous, domain-less switching.

To test this hypothesis, we have performed pulse switching measurements of the macroscopic polarization in the epitaxial and polycrystalline capacitors as a

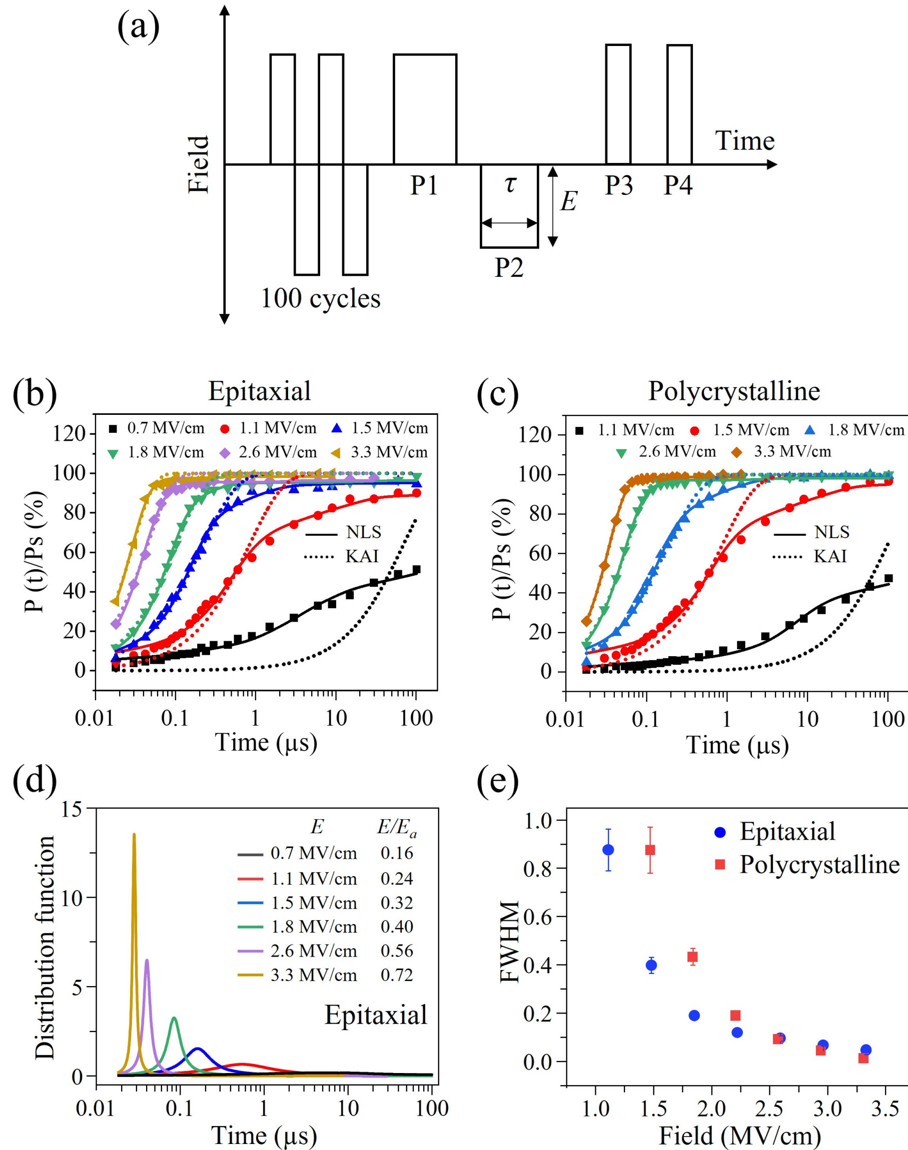

Figure 4.7. (a) Pulse sequence used to determine the switching mechanism. P1 is the set pulse; P2 is the switching pulse of varying amplitude, E, and duration, τ; P3 and P4 are the switching pulse and non-switching pulse, respectively, used to obtain the fraction of polarization switched due to pulse P2. The time delays between all pulses are 480 ns and 420 ns for the epitaxial and the polycrystalline capacitors, respectively.(b,c) Switched polarization measured at different applied electric fields as a function of the pulse duration in epitaxial (a) and poly-crystalline (b) films. The solid lines are fit by the NLS model while the dotted lines are fits by the KAI model. (d) Lorentzian distribution functions for different external fields used in the fitting by the NLS model for the epitaxial capacitors. (e) Field dependence of the full width at half maximum of the Lorentzian distribution function used in the fitting for the NLS model. Figure adapted from Ref. [25].

function of the switching pulse duration and amplitude using a pulse train sequence shown in Fig. 4.7 (a). To nullify the time dependent imprint, the capacitors were first subjected to 100 AC cycles before each measurement. Then, a set pulse, P1, of sufficiently high amplitude and duration was applied to set the polarization to one state. P1 was followed by pulse P2 of opposite polarity whose amplitude and duration were varied. The fraction of polarization switched due to P2 will be included in the total current obtained from pulse P3. The switching current in P3 is extracted by subtracting the purely dielectric current contribution obtained via pulse P4 from the total current in P3. Finally, integration of the switching current gives the switched polarization. The parameters of the pulse sequence are given in Tables 4.1 and 4.2 for the epitaxial and the polycrystalline capacitors, respectively.

Table 4.1. Epitaxial capacitors

Pulse type	Duration	Amplitude
Cycling pulses	6 μs	2.78 MV/cm
Pulse P1	30 μs	2.78 MV/cm
Pulse P2	Variable	Variable
Pulse P3, P4	900 ns	3.15 MV/cm

It is worth noting that the coercive fields and the activation fields (see Figs. 4.1(a,c)) in our Y:HfO_2 films are of the same order of magnitude, which allows us to perform measurements in the high field range close to E_a. Figs. 4.7 (b,c) show the plots of the switched polarization fraction as a function of time (the switching pulse duration) for different voltages. The time dependence of the switched polarization was fit by the following equation [23]:

Table 4.2. Polycrystalline capacitors

Pulse type	Duration	Amplitude
Cycling pulses	6 μs	2.78 MV/cm
Pulse P1	30 μs	2.78 MV/cm
Pulse P2	Variable	Variable
Pulse P3, P4	900 ns	2.96 MV/cm

$$\Delta P(t) = 2P_s \int_{\infty}^{\infty} [1 - exp(-(t/t_0)^n)].F(logt_0).d(logt_0) \quad (4.2)$$

where P_s is the spontaneous polarization, $F(log(t_0))$ is a distribution function of the characteristic switching times, t_0, and n is the effective dimension of domain growth ($n = 2$ for thin films). For the KAI model, the distribution function is a Dirac delta function while for the NLS model it is a Lorentzian function [37]:

$$F(logt_0) = \frac{A}{\pi}[\frac{w}{(logt_0 - logt_1)^2 + w^2}] \quad (4.3)$$

where A is a normalization constant, $2w$ is the full-width at half-maximum (FWHM) and $logt_1$ is the center of the distribution. Fig. 4.7 (d) shows the Lorentzian distribution functions as a function of the applied field for the epitaxial capacitors. In the low field range (defined as $E/E_a < 0.5$), a broad distribution of the local switching times is indicative of the heterogeneous region-by-region switching via domain formation consistent with the PFM switching data. (The time dependent domain evolution for this field range is shown in Fig. 4.3 where E/E_a is 0.42 and 0.34 for the epitaxial and polycrystalline capacitors, respectively.) As the external field increases, $2w$ decreases to nearly 0 at high fields (Fig. 4.7 (e)). With

$2w$ approaching zero, $F(x)$ transforms into a delta function suggesting nearly homogeneous switching, which results in convergence of the NLS and KAI switching models. Indeed, plots in Fig. (4.7 (a,b)) show that in the low field range, only the NLS model provides a good fit for the switching kinetics of both types of capacitors. However, for the external fields approaching the thermodynamic activation field E_a, the switching kinetics could be described equally well both by both the NLS and KAI models illustrating that in this field range, irrespective of the film microstructure, polarization reversal is driven by the same mechanism of homogeneous thermally-activated nucleation [38, 39]. Parenthetically, we note that the intrinsic coercive fields, $E_{c,i}$, calculated from the depolarization fields [40] are 7.5 MV/cm and 4.5 MV/cm for the polycrystalline and the epitaxial films, respectively. This suggests that the activation fields and the intrinsic coercive fields are remarkably close to each other with $E_{c,i}/E_a$ ratios of 1.3 and $\sim$1 for the polycrystalline and the epitaxial films, respectively (see Appendix A.1). In fact, the intrinsic coercive fields for the epitaxial films overlap within the experimental errors. Thus, the obtained results suggest that even for the disordered samples such as polycrystalline Y:HfO_2 thin films with a high concentration of grain boundaries, homogeneous switching resembling the intrinsic polarization reversal can be realized by using the electric fields closing in on the thermodynamic activation field value.

4.7 Conclusion

In conclusion, we have used a combination of time-resolved nanoscale domain imaging with macroscopic switching current measurements to investigate the effect of film microstructure on the polarization reversal in the ferroelectric Y:HfO_2 capacitors. It has been found that a rate-limiting mechanism is nucleation, which

causes slower switching of the epitaxial capacitors in comparison to their polycrystalline counterparts. Most importantly, for the applied fields close to the activation field value, we have observed convergence of the NLS and KAI models describing the polarization reversal dynamics in both types of capacitors. This observation implies that in the high field range the polarization reversal process becomes unaffected by the film microstructure and is no longer driven by the defect-mediated inhomogeneous nucleation. Instead, it should be concluded that switching is governed by homogeneous nucleation characterized by narrow distribution function of the nucleation times. For a high nucleation site density this would be equivalent to the uniform domain-less polarization reversal resembling intrinsic switching. The obtained results indicate that, at least from the viewpoint of their dynamic characteristics, the microstructure of the HfO_2-based films is of less importance when the devices are operated in the high field range close to the activation field value. The obtained results are of fundamental importance as they provide direct experimental evidence of the intrinsic switching in the $Y:HfO_2$ capacitors supporting feasibility of the ferroelectric devices employing this effect.

References

[1] M. Hoffmann, M. Pešić, K. Chatterjee, A. I. Khan, S. Salahuddin, S. Slesazeck, U. Schroeder, and T. Mikolajick, Adv. Funct. Mater. **26**, 8643 (2016).

[2] F. A McGuire, Y.-C. Lin, K. Price, G. B. Rayner, S. Khandelwal, S. Salahuddin, and A. D. Franklin, Nano Lett. **17**, 8, 4801 (2017).

[3] M. Si, C.-J. Su, C. Jiang, N. J. Conrad, H. Zhou, K. D. Maize, G. Qiu, C.-T. Wu, A. Shakouri, M. A. Alam, and P. D. Ye, Nat. Nanotech. **13**, 24 (2018).

[4] M. Hoffmann, F. P. G. Fengler, M. Herzig, T. Mittmann, B. Max, U. Schroeder, R. Negrea, P. Lucian, S. Slesazec, and T. Mikolajick, Nature **565**, 464 (2019).

[5] H.-J. Lee, M. Lee, K. Lee, J. Jo, H. Yang, Y. Kim, S. C. Chae, U. Waghmare, and J. H. Lee, Science **369**, 6509, 1343 (2020).

[6] P. Nukala, M. Ahmadi, Y. Wei, S. D. Graaf, E. Stylianidis, T. Chakrabortty, S. Matzen, H. W. Zandbergen, A. Björling, D. Mannix, D. Carbone, B. Kooi, and B. Noheda, Science **372**, 6542, 630 (2021).

[7] I. Stolichnov, M. Cavalieri, Gastaldi, M. Hoffmann, U. Schroeder, T. Mikolajick, and A. M. Ionescu, Appl. Phys. Lett. **117**, 172902 (2020).

[8] C. Gastaldi, M. Cavalieri, A. Saeidi, E. O'Connor, S. Kamaei, T. Rosca, I. Stolichnov, and A. M. Ionescu, Appl. Phys. Lett. **118**, 192904 (2021).

[9] J. Íñiguez, P. Zubko, I. Luk'yanchuk, and A. Cano, Nat. Rev. Mater. **4**, 243 (2019).

[10] M. Hoffmann, A. I. Khan, C. Serrao, Z. Lu, S. Salahuddin, M. Pešić, S. Slesazeck, U. Schroeder, and T. Mikolajick, J. App. Phys. **123**, 184101 (2018).

[11] R. Landauer, J. Appl. Phys. **28**, 227 (1957).

[12] V. L. Ginzburg, Zh. Eksp. Teor. Fiz. **19**, 36 (1949).

[13] V. L. Ginzburg, Phys.-Usp. **44**, 1037 (2001).

[14] J. F. Scott, Adv. Mater. **22**, 5315 (2010).

[15] H. Mulaosmanovic, J. Ocker, S. Müller, U. Schroeder, J. Müller, P. Polakowski, S. Flachowsky, R. van Bentum, T. Mikolajick, and S. Slesazeck, ACS Appl. Mater. Interfaces **9**, 3792 (2017).

[16] P. Buragohain, C. Richter, T. Schenk, H. Lu, T. Mikolajick, U. Schroeder, and A. Gruverman, Appl. Phys. Lett. **112**, 222901 (2018).

[17] S. D. Hyun, H. W. Park, Y. J. Kim, M. H. Park, Y. H. Lee, H. J. Kim, Y. J. Kwon, T. Moon, K. Do Kim, Y. Bin Lee, B. S. Kim, and C. S. Hwang, ACS Appl. Mater. Interfaces **10**, 35374 (2018).

[18] K. Lee, H.-J. Lee, T. Y. Lee, H. H. Lim, M. S. Song, H. K. Yoo, D. I. Suh, J. G. Lee, Z. Zhu, A. Yoon, M. R. MacDonald, X. Lei, K. Park, J. Park, J. H. Lee, and S. C. Chae, ACS Appl. Mater. Interfaces **11**, 38929 (2019).

[19] S. Y. Lim, M. S. Park, A. Kim, and S. M. Yang, Appl. Phys. Lett. **118**, 102902 (2021).

[20] M. Materano, P. D. Lomenzo, H. Mulaosmanovic, M. Hoffmann, A. Toriumi, T. Mikolajick, and U. Schroeder, Appl. Phys. Lett. **117**, 262904 (2020).

[21] A. Gruverman, D. Wu, and J. F. Scott, Phys. Rev. Lett. **100**, 097601 (2008).

[22] A. Gruverman, M. Alexe, and D. Meier, Nat Commun **10**, 1661 (2019).

[23] A. K. Tagantsev, I. Stolichnov, N. Setter, J. S Cross, and M. Tsukada, Phys. Rev. B **66**, 214109 (2002).

[24] A. N. Kolmogorov, Izv. Akad. Nauk SSSR Ser. Mater. **3**, 355 (1937); M.J. Avrami, Chem. Phys. **7**, 1103 (1939); Y. Ishibashi, Y. J. Takagi, Phys. Soc. Jpn. **31**, 506 (1971).

[25] P. Buragohain, A. Erickson, T. Mimura, T. Shimizu, H. Funakubo, and A. Gruverman, Adv. Funct. Mater. **32**, 2108876 (2022).

[26] T. Mimura, K. Katayama, T. Shimizu, H. Uchida, T. Kiguchi, A. Akama, T. J. Konno, O. Sakata, and H. Funakubo, Appl. Phys. Lett. **109**, 052903 (2016).

[27] T. Mimura, T. Shimizu, H. Uchida, and H. Funakubo, Appl. Phys. Lett. **115**, 032901 (2019).

[28] T. Mimura, T. Shimizu, H. Uchida, O. Sakata, and H. Funakubo, Appl. Phys. Lett. **113**, 102901 (2018).

[29] T. Schenk, U. Schroeder, M. Pešic, M. Popovici, Y. V. Pershin, and T. Mikolajick, ACS Appl. Mater. Interfaces **6**, 19744 (2014).

[30] W. Merz, Phys. Rev. **95**, 3 (1954).

[31] S.-N. Choi, S.-E. Moon, and S.-M. Yoon, Ceramics International **45**, 22642 (2019).

[32] A. Gruverman, B. J. Rodriguez, C. Dehoff, J. D. Waldrep, A. I. Kingon, R. J. Nemanich, and J. S. Cross, Appl. Phys. Lett. **87**, 082902 (2005).

[33] N. Setter, D. Damjanovic, L. Eng, G. Fox, S. Gevorgian, S. Hong, A. Kingon, H. Kohlstedt, N. Y. Park, G. B. Stephenson, I. Stolitchnov, A. K. Taganstev, D. V. Taylor, T. Yamada, and S. Streiffer, J. Appl. Phys. **100**, 051606 (2006).

[34] U. Schroeder, C. Richter, M. H. Park, T. Schenk, M. Pešić, M. Hoffmann, F. P. G. Fengler, D. Pohl, B. Rellinghaus, C. Zhou, C.-C. Chung, J. L. Jones, and T. Mikolajick, Inorg. Chem. **57**, 2752 (2018).

[35] D. Wu, I. Vrejoiu, M. Alexe, and A. Gruverman, Appl. Phys. Lett. **96**, 112903 (2010).

[36] D. J. Kim, J. Y. Jo, Y. S. Kim, and T. K. Song, J. Phys. D: Appl. Phys. **43**, 395403 (2010).

[37] J. Y. Jo, H. S. Han, J.-G Yoon, T. K. Song, S. H. Kim, and T. W. Noh, Phys. Rev. Lett. **99**, 267602 (2007).

[38] J.Y. Jo, D. J. Kim, Y. S. Kim, S.-B. Choe, T. K. Song, J.-G. Yoon, and T.W. Noh, Phys. Rev. Lett. **97**, 247602 (2006).

[39] M. J. Highland, T. T. Fister, M.-I. Richard, D. D. Fong, P. H. Fuoss, C. Thompson, J. A. Eastman, S. K. Streiffer, and G. B. Stephenson, Phys. Rev. Lett. **105**, 167601 (2010).

[40] E. Paramonova, V. Bystrov , X. Meng, H. Shen, J. Wang, and V. Fridkin, Nanomaterials **10**, 1841 (2020).

Chapter 5

Quantification of the electromechanical measurements by piezoresponse force microscopy

5.1 Introduction

Piezoresponse force microscopy (PFM) has become a ubiquitous tool in the exploration of a wide-ranging variety of nanoscale phenomena in ferroelectrics, multiferroics and other polar materials in the past couple of decades [1, 2, 3, 4]. The underlying principle of PFM is the converse piezoelectric effect in which a piezoelectrically active material undergoes deformation upon the application of an electric field. In the conventional PFM configuration, an oscillating electric field applied via a conductive nanoscopic atomic force microscopy (AFM) probe in contact with the sample leads to periodic sample deformation, transferred to the cantilever oscillation, which is detected via a quadrant photodetector using lock-in techniques [5]. When applied to ferroelectrics, the PFM amplitude contains information on the magnitude of the piezocoefficient, while the PFM phase allows delineation of the polarization direction. Although the physical principle of PFM might seem straightforward, the interpretation of the PFM signal requires very careful analysis since the PFM signal can be beset with several artifacts such as electrostatics [6], electrochemical reactions due to ionic motion [7, 8, 9], thermal effects due to Joule heating, which can be particularly problematic for leaky samples [10] and complex cantilever dynamics [11, 12]. The extrinsic contributions to the

PFM signal have been extensively discussed in literature [13, 14]. Currently, the majority of PFM-based reports on quantitative estimation of physical parameters such as local coercive fields [15], imprint [15], domain wall roughness [16], domain wall velocity [17, 18] or polarization switching mechanism [18, 19] are derived using uncalibrated raw PFM signals. Quantification of the PFM signal – both amplitude and phase – has been an ongoing challenge owing to the complex interplay of the various factors mentioned above [20]. Hence, most publications report results based on uncalibrated measurements. This can cause confusion when comparing different reports on similar materials. For instance, the vertical PFM phase signal is related to the sign of the longitudinal piezoelectric coefficient, d_{33}, but, with the uncalibrated PFM results it might be difficult to ascertain the sign of the d_{33} even for the well-studied ferroelectrics [21, 22, 23, 24, 25, 26, 27]. On the other hand, a properly calibrated PFM phase signal [28] can be particularly useful when exploring the piezoelectric properties of the emerging ferroelectrics. For instance, recent theoretical studies predicted a negative d_{33} in a wide variety of low-dimensional layered ferroelectrics [29]. To verify the true sign of d_{33} in these materials and explore its possible dependence on the mechanical and electrical boundary conditions or chemical composition it is necessary to provide reliable, artifact-free measurements of the PFM phase signal [30, 31].

In this chapter, we focus on quantification of the PFM phase signal (approaches to quantification of the amplitude signal can be found elsewhere [20, 32]) using two different approaches, which are then extended to investigate the intriguing variations in the sign of the longitudinal piezoelectric coefficient, d_{33}, in the recently discovered technologically relevant family of hafnium oxide (HfO_2) or hafnia-based ferroelectrics [33]. The developed methods provide confirmation of a theoretically predicted negative sign of the d_{33} coefficient [34, 35, 36]. Furthermore, it has been

found that the sign of the d_{33} could change depending on the state of the capacitors tested (pristine vs ac field-cycled), or their thickness and a deposition method used. In addition, coexistence of the positive and negative d_{33} regions within the same device was observed.

5.2 Materials and methods

The methodology for the quantification of the PFM phase signal have been tested using standard reference ferroelectric samples with a known sign of the d_{33}: Pb(Zr,Ti)O_3 (PZT) capacitors and $PbTiO_3$ (PTO) thin films, both of which have a positive d_{33} [37, 38] and poly(vinylidene fluoride) (PVDF) thin films with a negative d_{33} [39]. Measurements on HfO_2 samples have been carried out on atomic layer deposition (ALD) grown TiN/La:HfO_2/TiN capacitors with La:HfO_2 (LHO) thicknesses of 10 nm, 20 nm and 30 nm [40], ALD grown IrO_x/LHO (20 nm)/IrO_x capacitors [41], chemical solution deposited (CSD) grown Pt/LHO (100 nm)/Pt capacitors [47], and pulsed laser deposition (PLD) grown Pt/Y:HfO_2 (24 nm)/Pt capacitors [42].

Table 5.1. List of HfO_2-based thin film capacitors that were used to investigate the sign of d_{33}

Capacitor geometry	HfO_2 film thickness (nm)	Deposition method
Ti/Pt/TiN/La:HfO_2/TiN	10, 20, 30	Atomic layer deposition
IrO_x/La:HfO_2/IrO_x	20	Atomic layer deposition
Pt/La:HfO_2/Pt	45, 100	Chemical solution deposition
Pt/Y:HfO_2/Pt	24	Pulsed laser deposition

The PFM measurements, strain loop measurements and the electrical characterizations have been carried out as described in sections 2.3.1, 2.3.2 and 2.3.3, respectively, in Chapter 2.

5.3 Quantification of the PFM phase signal

The vertical PFM amplitude and phase signals are related to the magnitude and the sign of the longitudinal piezoelectric coefficient, d_{33}, respectively (see Appendix B, section B.1.). Before delving deeper into the quantification of the PFM phase signal, it is worthwhile to first have a closer look at some of the instrumental and measurement challenges associated with the quantification of the PFM signal and possible ways to overcome such challenges. In the majority of conventional atomic force microscope (AFM) setups, PFM measurements are implemented using the optical beam detection (OBD) method [43] where the cantilever arm, the tip-sample contact, and the sample form a coupled oscillator system driven by the mechanical oscillation of the sample, and this oscillation is transferred with a phase lag to the cantilever bending angle detected by the optical laser system [44]. More importantly, there can be a strong effect of the cantilever dynamics on the measured PFM signal resulting in an arbitrary shifting of the phase signal, which can mask the true electromechanical response [12]. Even more challenging are the measurements in the resonance-enhanced mode developed to circumvent the issue of low signal-to-noise ratio in materials with a weak piezoelectric response, where the cantilever is driven near its contact resonance, in which case the phase response would strongly depend on the driving frequency relative to the resonance. Spatial variations in the local tip-sample contact resonance during scanning or during local spectroscopic measurements can cause arbitrary changes or even 180° reversal of the

phase signal unrelated to the local polarization direction, leading to misinterpretation of the measured phase signal. In addition, instrument related phase offsets may also be present in the measured raw PFM data [28]. Hence, PFM-based investigations of the sign of the piezoelectric coefficient requires proper calibration of the PFM phase signal and careful selection of the measurement conditions. This is particularly relevant when investigating the sign of the longitudinal piezoelectric coefficient, d_{33}, in the HfO_2 or hafnia-based ferroelectrics, which have been the subject of significant controversy: while theoretical modeling predicts and some experimental studies observe a negative d_{33} coefficient [34, 35, 36, 45], majority of the experimental works report a positive d_{33} [46, 47, 48, 49]. To ascertain the true sign of d_{33} and explore possible variations of the sign depending on different mechanical or electrical boundary conditions in hafnia then requires that the afore-mentioned artifacts to the PFM raw phase signal are properly addressed.

To address these issues, we have adopted two approaches to correct the parasitic phase offset typically present in the cantilever displacement measurements by the OBD method: The first approach uses a reference sample with a known d_{33} sign, and the second approach involves the detection of the cantilever-sample electrostatic interactions to determine the parasitic phase offset. In the following sections, general methodologies to quantify the PFM phase signal are outlined. Although these results were obtained in the resonance-enhanced PFM mode, they can be extended to single frequency PFM as well.

5.3.1 Identification of parasitic phase offset using a reference sample

In this approach, the choice of PFM cantilever is important, as the cantilever and the tip-sample contact form a coupled oscillator, while different samples may show

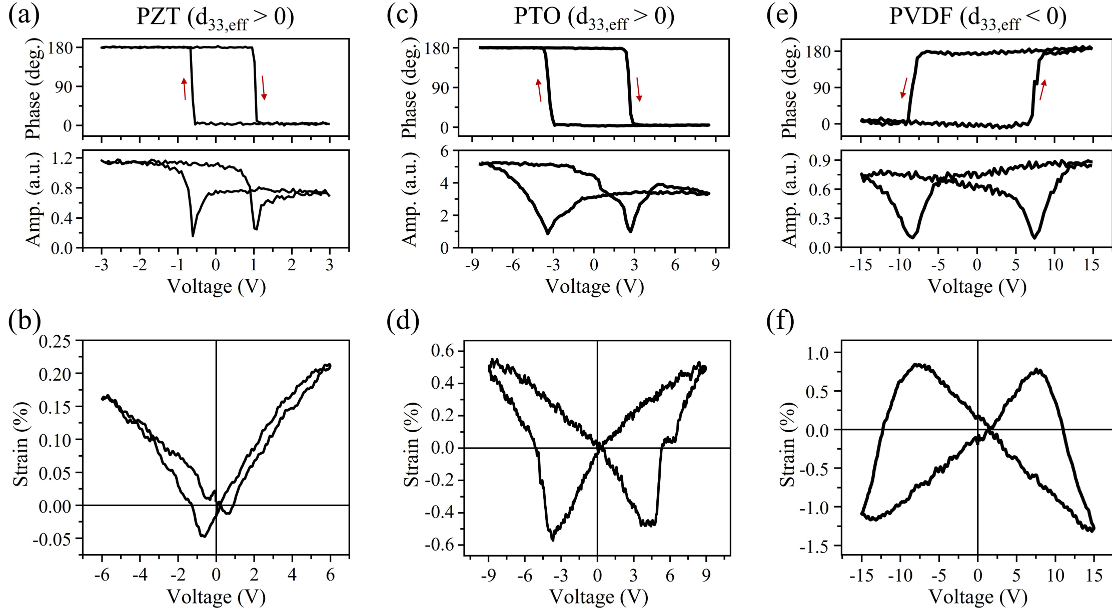

Figure 5.1. (a,c,e) PFM phase (top panel) and amplitude (bottom panel) and (b,d,f) quasi-static strain loops in IrO_2/PZT/Pt capacitors (a,b), PTO/$SrRuO_3$ (SRO)/$KTaO_3$ (KTO) thin film (c,d) and PVDF thin film (e,f). The strain loops show that the d_{33} is positive for PZT and PTO and negative for PVDF. A clear correlation between the sense of rotation of the phase signal and the sign of the d_{33} can be observed here. The PFM hysteresis loops were acquired in the bias-off mode below the resonance frequency and the phase loops had the same initial phase offsets for all three samples.

very different elastic properties that significantly affect the tip-sample effective contact stiffness. Note that typical elasticity for the inorganic ferroelectrics are in the order of tens of GPa [50, 51, 52, 53], and a quick estimation of the tip-sample effective contact stiffness yields a value in the order of 10^2 N/m, assuming typical PFM parameters of tip radius ∼25 nm and a contact force ∼100 nN (the effective stiffness of the tip-sample contact can be obtained from the Hertzian contact model by $k_{eff} = (6RF_cE^{*2})^{1/3}$ [54], where R is the tip radius, F_c the applied contact force, and E^* the effective tip-sample modulus). A choice of PFM cantilevers with a spring constant much smaller than the effective tip-sample contact stiffness ensures that the effective phase shift of the

cantilever-sample system is mainly governed by the cantilever. Hence, the use of the same cantilever offers the same cantilever dynamics which is essential for the determination of the phase shift.

In the resonance-enhanced PFM mode commonly used for weak piezoelectric materials, a proper tracking of the resonance with a feedback loop is realized by the dual ac resonance tracking (DART) PFM technique [55]. The DART technique helps eliminate the frequency-dependent phase variations introduced by cantilever dynamics. This is essential in stabilizing the PFM phase signal when there are variations in the contact resonance during the measurements.

The raw PFM phase signal, θ, with an additional parasitic phase offset, $\Delta\theta$, related to an instrument, cables and a cantilever [10, 28], can obscure the true information related to the sign of the d_{33}. This parasitic phase offset can be obtained from the PFM measurements of a reference sample with a known d_{33} sign, and can be either compensated by adjusting the initial phase offsets of the lock-in amplifiers, or subtracted from the raw PFM phase signal manually, i.e., the adjusted phase, $\theta - \Delta\theta$, should be in phase (180° out of phase) when the polarization is pointing downwards (upwards) in a material with positive d_{33}. Fig. 5.1 (a) shows a local PFM spectroscopy loop after phase adjustment, $\theta - \Delta\theta$, measured using the DART mode in the PZT capacitor. Details of the phase adjustment procedure are given in Appendix B, section B.2. The $\Delta\theta$ obtained from this procedure is then kept the same and is used in all subsequent measurements for the same cantilever under the same measurement conditions. To make sure that there were no 'local surprises', we also acquired the local quasi-static strain loops in the same locations where the PFM spectroscopic loops were collected. The strain loop shown in Fig. 5.1 (b) confirms that the sign of d_{33} is indeed positive [37].

Next, we acquired the PFM spectroscopic loops for PTO (positive d_{33} [38]) (Fig.

5.1 (c)) and PVDF (negative d_{33} [39]) (Fig. 5.1 (e)) thin films, with $\Delta\theta$ adjusted from the previous step. The corresponding strain loops verifying the signs of the d_{33} are shown in Fig. 5.1 (d) and Fig. 5.1 (f). We found that when using the correct initial phase offset, the sense of rotation of the phase signal was always consistent with the sign of d_{33} across all the reference samples – clockwise for positive d_{33} (top panels in Figs. 5.1 (a,c)) and counter-clockwise for negative d_{33} (top panel in Fig. 5.1 (e)).

Additionally, since these results were obtained in the DART PFM mode, it was important to test the frequency response of the phase and amplitude near the resonance. Fig. 5.2 shows the PFM phase response near the resonance for the same initial phase offsets identified previously. It was found that the typical quality factor of the cantilever used in our measurements was in the order of 100, which makes it possible to perform the DART measurements within 5 kHz below and above the resonance frequency with significant signal enhancement. With the calibrated phase offsets identified previously, the phase responses at 1% or ~3 kHz below the resonance (our typical measurement condition) for the upward and downward polarization states were found to be in agreement with the expected phase values from the strain-field relationship, i.e., a high (low) phase value was observed for the upward (downward) polarization state in a material with positive d_{33} and vice-versa in a material with negative d_{33}. This scenario is highlighted in the phase spectrum for the PTO films (Fig. 5.2 (a)), PVDF films (Fig. 5.2 (b)) and for the PZT capacitors (Fig. 5.2 (c)). On the other hand, a ~180° phase shift was obtained ~3 kHz above the resonance, while the phase response very close to the resonance (within about 1%) had significant frequency-dependent variations that should be avoided during the PFM measurements. Also, the phase difference between polarization up and down states started to reduce far away from the resonance (~20% away in Fig. 5.2) due to the reduced signal-to-noise ratio of the raw PFM

data. It is clear that a proper tracking of the resonance is essential for recording the correct phase signal in the resonance-enhanced PFM measurements. Extending this methodology to the 20-nm-thick La:HfO_2-based capacitors revealed that the phase response was similar to PVDF suggesting that the sign of the d_{33} is negative. This will be discussed in more detail in section 5.4.

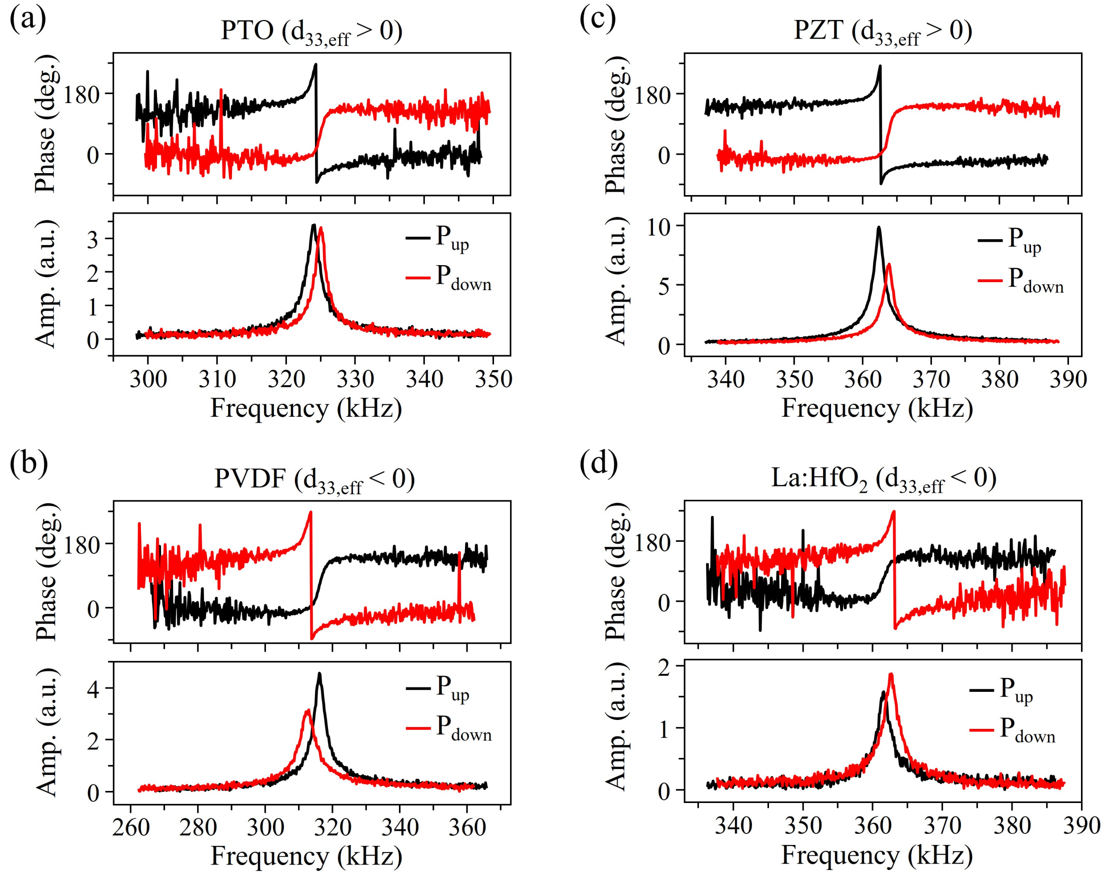

Figure 5.2. Phase and amplitude spectrum near resonance obtained after adjusting the initial phase offsets to correct for the arbitrary instrumental phase offset in PTO/$SrRuO_3$/$KTaO_3$ thin film (a), PVDF thin film (b), IrO_2/PZT/Pt capacitors (c) and TiN/La:HfO_2 (20 nm)/TiN capacitor (d). All the plots were obtained with the same initial phase offsets and the plots correspond to the first lock-in amplifier which tracks the frequency below resonance in the DART PFM mode.

We would like to point out here that in the vast majority of the publications,

the PFM measurements are performed with arbitrary initial phase offsets thereby showing opposite sense of rotation of the PFM phase loops for the same material [21, 22, 23, 24, 25, 26, 27], potentially causing confusion regarding the sign of its piezoelectric coefficient. Figs. B.3 (b,c) in the Appendix B, section B.3 illustrate the effect of the arbitrary initial phase offsets in the PFM measurements of the PZT capacitor, which result in the mirror inverted loops. However, upon using the correct initial phase offsets, consistent results can be reproducibly obtained as shown in Figs. B.3 (e,f), highlighting the importance of calibrating the initial phase offsets. Extension of the calibration procedure discussed above to the single-frequency PFM measurements is discussed in the Appendix B, section B.4.

5.3.2 Identification of the parasitic phase offset from the electrostatic effect

During PFM spectroscopic measurements in the pulsed DC mode, a sinusoidal AC driving voltage, V_{ac}, is superimposed onto DC pulses, V_{dc}, to detect the local electromechanical response while the V_{dc} is applied to induce polarization switching underneath the tip [59]. When the electromechanical response is measured in the presence (absence) of the V_{dc}, the obtained loops are said to be obtained in the bias-on (bias-off) mode. In such spectroscopic measurements, the total first harmonic piezoresponse signal, $PR_{1\omega}$, (obtained by the convolution of the amplitude with the cosine of the phase signal) is given by the following equation:

$$PR_{1\omega} = d_{33,eff} V_{ac} + \frac{1}{k}\frac{dC}{dz} V_{ac}(V_{dc} - V_{sp}) \tag{5.1}$$

where k is the cantilever spring constant, $\frac{dC}{dz}$ is the cantilever-sample capacitance gradient and V_{sp} is the surface potential. The first term on the right contains only the

piezoelectric response and gives rise to the signal in the bias-off mode. The second term is the electrostatic term, which adds a linear signal with a negative slope to the measured piezoresponse as a function of the applied V_{dc} due to the capacitive coupling. In the bias-on mode which includes both terms in Eq. 5.1, the raw piezoresponse signal can be split into the PFM amplitude and PFM phase response as:

$$PR_{1\omega,on} = PR_{1\omega,off} + \frac{1}{k}\frac{dC}{dz}V_{ac}(V_{dc} - V_{sp}) = A_{on}cos(\theta_{on} - \Delta\theta) \tag{5.2}$$

where A_{on} is the bias-on amplitude, θ_{on} is the phase signal due to the true piezoelectric response and $\Delta\theta$ is an unknown parasitic phase offset. When using cantilevers with medium stiffness (k $\sim$ 3 N/m) or lower, there is usually a strong electrostatic coupling between the cantilever arm and the sample that results in a linear contribution to the bias-on signal. This electrostatic coupling will also exist in capacitor structures if a sizeable fraction of the cantilever arm extends over the sample surface, due to surface potential mismatch between the cantilever arm and the sample surface. The linear contribution can be clearly obtained by taking the differential piezoresponse signal ($PR_{1\omega,on} - PR_{1\omega,off}$), which can be used to identify the correct phase offset, $\Delta\theta$. The $\Delta\theta$ should be adjusted such that $\theta_{on} - \Delta\theta = 0$, or $\theta_{on} - \Delta\theta = 180°$ on the far negative V_{dc} side of the hysteresis loop, whichever leads to a negative linear slope in the differential piezoresponse signal. Note that since the initial phase offsets will be the same for both bias-on and bias-off loops, the same $\Delta\theta$ should be subtracted from the bias-off loops during the construction of the differential piezoresponse signal.

This scenario is highlighted in Fig. 5.3. The obtained PFM phase loops are mirror reflected for the frequencies below and above resonance (compare Figs. 5.3 (a,b) and Figs. 5.3 (d,e)). For the frequency below (above) resonance, the differential

piezoresponse gives a linear contribution with a positive (negative) slope (Figs. 5.3 (c,f)). It is then straightforward to ascribe the correct phase signal to the frequency above resonance since it leads to a differential piezoresponse signal with a negative slope (Fig. 5.3 (f)). The correct raw phase signal for the frequency below resonance can be obtained by subtracting $\Delta\theta$ such that $\theta_{on} - \Delta\theta = 0$ on the far negative V_{dc} side of the hysteresis loop so that the differential piezoresponse signal will have a negative slope. This method can be used to identify the correct sense of rotation of the phase signal when using arbitrary initial phase offsets and in the presence of a noticeable electrostatic contribution.

Parenthetically, we note that in some commercial AFM systems the spectroscopic loops are not performed in the pulsed mode but using a triangular waveform, i.e, in the bias-on mode only. As follows from Eq. 5.1, such PFM signals can contain significant electrostatic contribution unless very stiff cantilevers (k $>$ 10 N/m) are used (however, soft materials preclude the use of stiffer cantilevers). In the presence of the parasitic electrostatic contribution, determination of the true ferroelectric parameters out of the measured PFM loops, such as a coercive field, becomes problematic. A possible way to still extract the true electromechanical response in that case will be to construct the piezoresponse loops and then subtract the linear contribution to reveal the true electromechanical response. Depending on the sense of rotation of such deconstructed piezoresponse loops, the sign of d_{33} as well as other parameters can be obtained. Fig. B.5 (d) in Appendix B, section B.5, shows the overlap of the bias-on and bias-off PFM loops after subtracting the linear contribution validating the applicability of this approach.

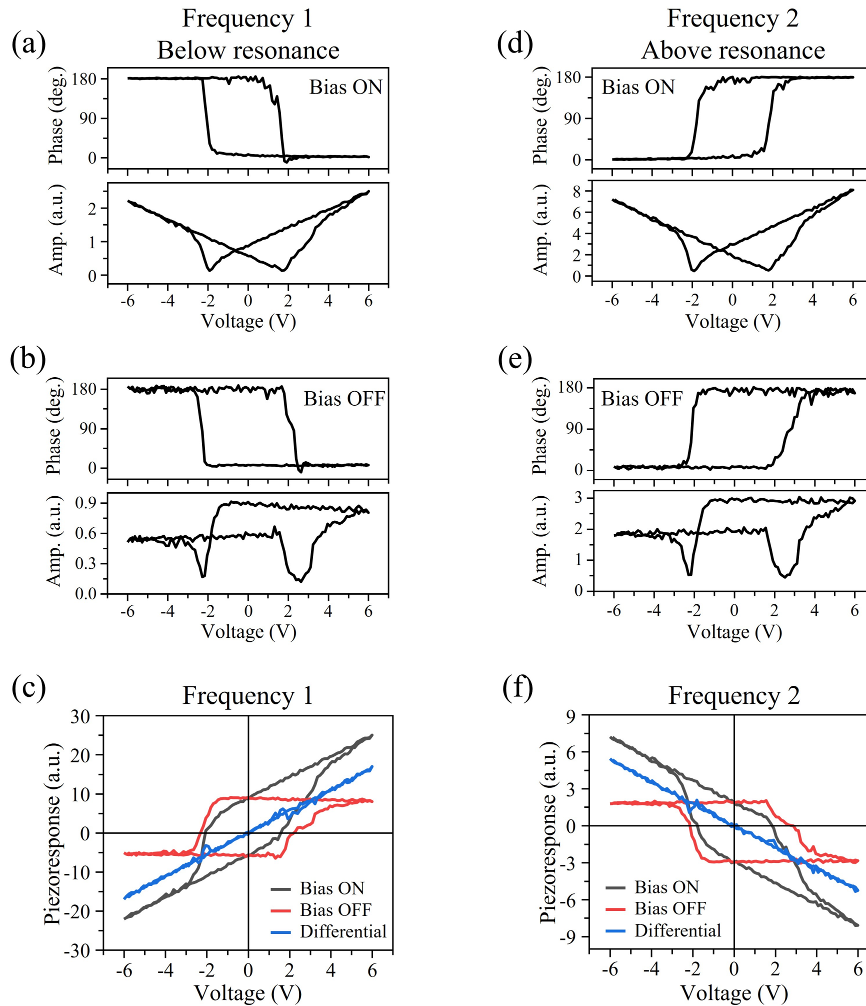

Figure 5.3. PFM spectroscopic loops in Ti/Pt/TiN/La:HfO_2 (20 nm)/TiN capacitors measured using a ∼ 3 N/m tip. (a,b) Bias-on (a) and bias-off (b) loops measured at the frequency below resonance. (d,e) Bias-on (d) and bias-off (e) loops measured at the frequency above resonance. (c,f) Bias-on, bias-off and differential piezoresponse signals for frequency 1 (below resonance) (c) and frequency 2 (above resonance) (f). The differential signal for frequency 1 in (c) gives a positive slope, which means that the phase for frequency 1 is not correct and must be inverted. When this phase is inverted, such as that for frequency 2, then we obtain a differential signal with a negative slope signifying that this is the correct phase.

5.4 PFM testing of hafnia-based thin film capacitors

5.4.1 Thickness effect on the d_{33} sign in La:HfO_2 capacitors

Recently, it has been predicted theoretically that the sign of the longitudinal piezoelectric coefficient in hafnia-based ferroelectrics should be negative [34, 35, 36].

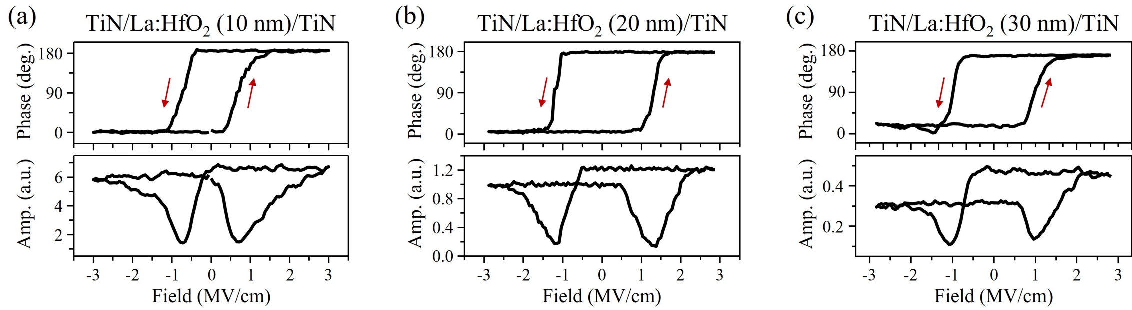

Figure 5.4. Negative d_{33} in La:HfO_2 thin film-based capacitors for La:HfO_2 thicknesses of 10 nm (a), 20 nm (b) and 30 nm (c). In all three cases, the La:HfO_2 films were sandwiched between TiN top and bottom electrodes. The top TiN layer was covered with additional Ti/Pt layers. All measurements were performed after wake-up.

Application of the methodologies outlined above to the ALD grown TiN/La:HfO_2/TiN capacitors with the relatively thin HfO_2 layer (thickness of less than 30 nm) showed that their calibrated PFM phase loops had a counter-clockwise rotation (Fig. 5.4), thus confirming that the sign of the d_{33} was indeed negative (see Sec. 5.3.1). The agreement of the PFM phase signal from both the above-mentioned methodologies can be observed from the comparison of the phase loops in Fig. 5.4 (b), which was obtained after calibrating the phase offset using PZT as a reference, and Fig. 5.3 (e), where the correct sense of rotation of the phase signal was determined based on the cantilever-sample electrostatic interaction. The negative sign was consistently observed in the hafnia films with a thickness of up to 30 nm. The density functional theory (DFT) calculations in Ref. [36] show that the d_{33} sign is negative due to the peculiar chemical environment of the oxygen atoms that are responsible for the appearance of the polar $Pca2_1$ phase in hafnia (O_I atoms in Fig. 5.5 (b)). Application of a tensile strain in the vertical direction results in a shift of the O_I oxygen atom upwards and a downward shift of the Hf atoms to try and maintain the optimal bond length that go against (reduce) the polarization of the

unperturbed material, resulting in the negative d_{33}. The DFT calculations also indicate a possibility of a tunable piezoresponse, i.e. the d_{33} sign could be reversed by changing the local chemical environment of the O_I oxygen atoms [36].

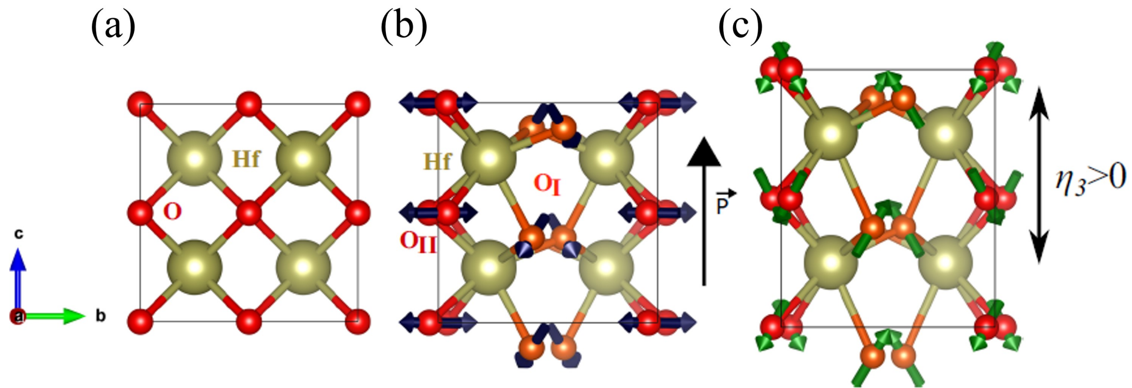

Figure 5.5. Structure of HfO_2 in the cubic paraelectric phase (a) and the orthorhombic ferroelectric phases in the absence (b) and in the presence (c) of a tensile strain, η_3. P represents the spontaneous polarization, whose direction is given by the single headed arrow in (b). Figure adapted from Ref. [36].

On the other hand, application of the same measurement protocols as above to much thicker CSD-grown La:HfO_2 capacitors with Pt electrodes yields a positive d_{33} as shown in Fig. 5.6. The opposite sign of d_{33} is unclear and might arise due to the differences in the mechanical and electrical boundary conditions between the ALD and the CSD grown films. This is an open question that requires further experimental work to identify the different parameters that can lead to this intriguing variation in the sign of the d_{33}.

5.4.2 Electrical tuning of the sign of d_{33} in polycrystalline Y:HfO_2 thin-film capacitors

In the course of this study, it was observed that the sign of the d_{33} in Pt/Y:HfO_2/Pt capacitors strongly depends on the state of the capacitor, i.e. pristine vs field-cycled

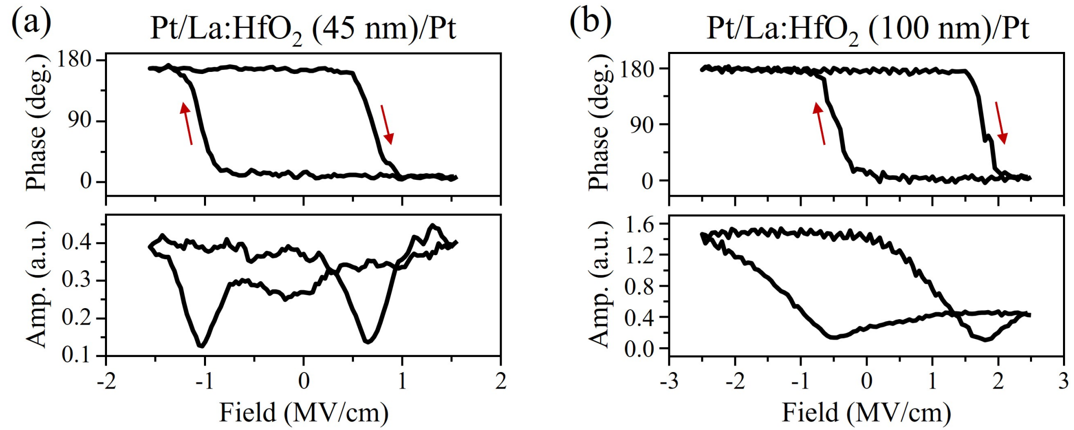

Figure 5.6. (a, b) PFM phase (top panel) and amplitude (bottom panel) loops obtained on Pt/La:HfO2/Pt capacitors with La:HfO_2 film thickness of 45 nm (a) and 100 nm (b). The clockwise rotation of the phase signal shows that the d_{33} is positive in these samples. The loops shown in (a) were obtained after wake-up, while the loops in (b) were obtained in the pristine state.

(Fig. 5.7). A common phenomenon observed in the HfO_2-based capacitors is a low remanent polarization and/or pinched hysteresis loops in the as-grown pristine state. Subjecting the capacitors to electrical field-cycling leads to an increase in the remanent polarization along with de-pinching of the hysteresis loops, a process known as wake-up cycling [60, 61, 62]. PFM spectroscopic loops measured on the same location in the pristine state and after field-cycling in the Pt/Y:HfO_2/Pt capacitors showed dramatically different features. In the pristine state, the phase signal had a clockwise rotation implying a positive d_{33} (top panel in Fig. 5.7 (b)) along with highly unconventional bias-on amplitude loops (bottom panel in Fig. 5.7 (a)) which resulted in a non-linear differential piezoresponse loop as shown in Fig. 5.7 (c). After wake-up, the sign of d_{33} changed to negative which can be inferred from the counterclockwise rotation (top panel in Fig. 5.7 (e)) and the bias-on amplitude loops acquired a more conventional shape (bottom panel in Fig. 5.7 (d)), resulting in a linear differential piezoresponse loop (Fig. 5.7 (f)). The non-linear differential loops

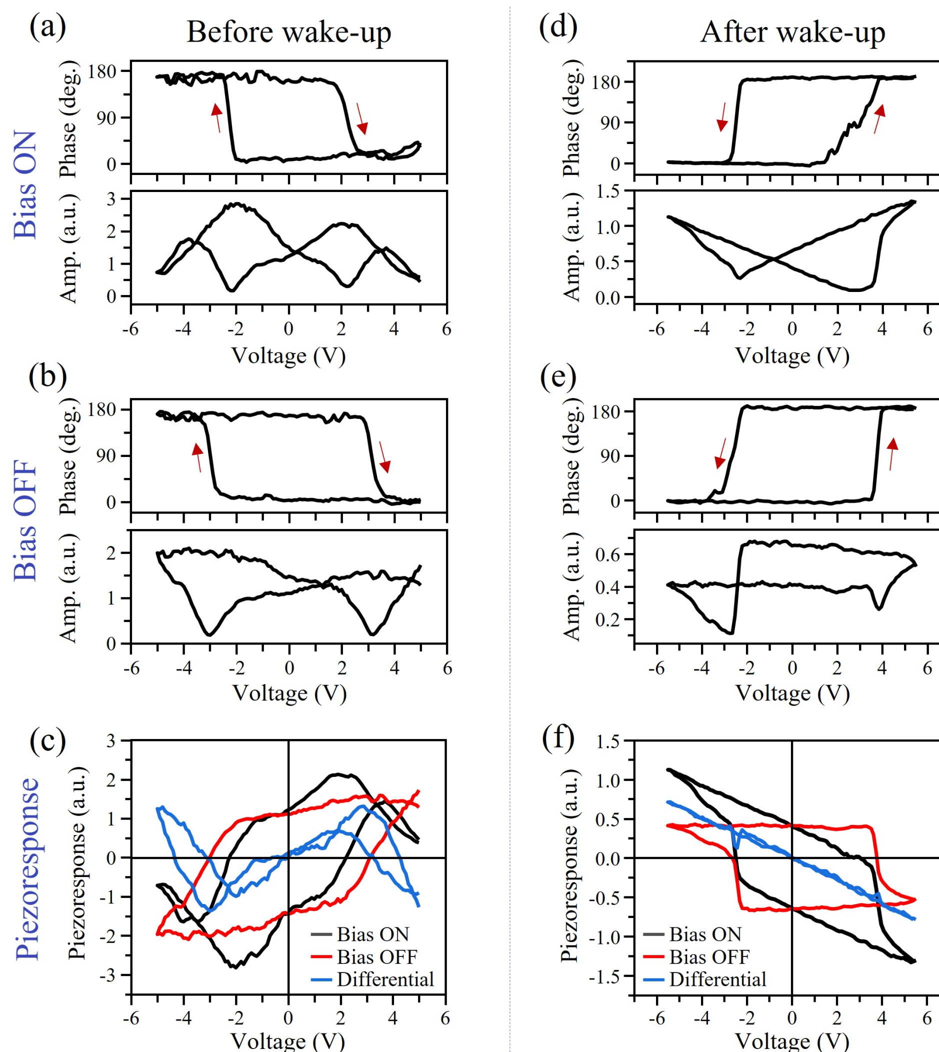

Figure 5.7. Effect of cycling on the sign of the piezoelectric coefficient in PLD grown polycrystalline Pt/Y:HfO_2/Pt capacitors. (a-c) Bias-on (a), bias-off (b) and piezoresponse loops (c) in the pristine state. The highly non-linear differential loop in (c) suggests extrinsic contributions to the bias-on response. (d-f) Bias-on (d), bias-off (e) and piezoresponse loops (f) after wake-up. The differential loops become linear after wake-up.

might arise due to the presence of extrinsic contributions to the measured bias-on signal such as charge injection [10]. This might be due to the presence of non-polar phases such as the defect rich tetragonal phase in the pristine state, which can undergo a field-induced phase transformation to the polar orthorhombic phase after wake-up

[63]. While the origin of the extrinsic contributions to the bias-on PFM signal can be speculative at best and requires complementary structural investigations such as transmission electron microscopy (TEM), it is worth reiterating that the adopted methodology unambiguously confirms the fact that the sign of the d_{33} in hafnia can change depending on the state of the capacitors.

5.4.3 Coexistence of positive and negative d_{33} regions in IrO_x/La:HfO_2/IrO_x capacitors

Finally, we would like to report a very interesting observation in IrO_x/La:HfO_2/IrO_x capacitors after wake-up. A polydomain configuration was observed during PFM imaging after application of switching pulses of opposite polarity in these capacitors (Figs. 5.8 (a,b)). Careful analysis of these polydomain configuration revealed the presence of regions with opposite phase contrast in comparison to the surrounding matrix. For clarity, in Fig. 5.8 (a) we label the surrounding matrix as L1 and a region with opposite switching behavior as L2, which is also highlighted by a black frame in Figs. 5.8 (a,b). Application of the switching pulses led to polarization reversal in both the L1 and L2 regions, but they always exhibit opposite phase contrast after switching.

Using the methodologies outlined above, we have measured the local PFM loops in L1 matrix and in L2 region. It has been found that L1 regions exhibit a negative d_{33} (Fig. 5.8 (c)), while the L2 region shows positive d_{33} (Fig. 5.8 (d)). From the histogram analysis of the differential PFM phase images, 70% of the regions were found to exhibit negative d_{33}, while 10% of the regions showed positive d_{33} and 20% of the regions were pinned (no change in PFM contrast after pulse application). The reason for coexistence of the regions with opposite d_{33} requires further investigation.

Coexistence of regions with opposite phase contrast and their opposite switching

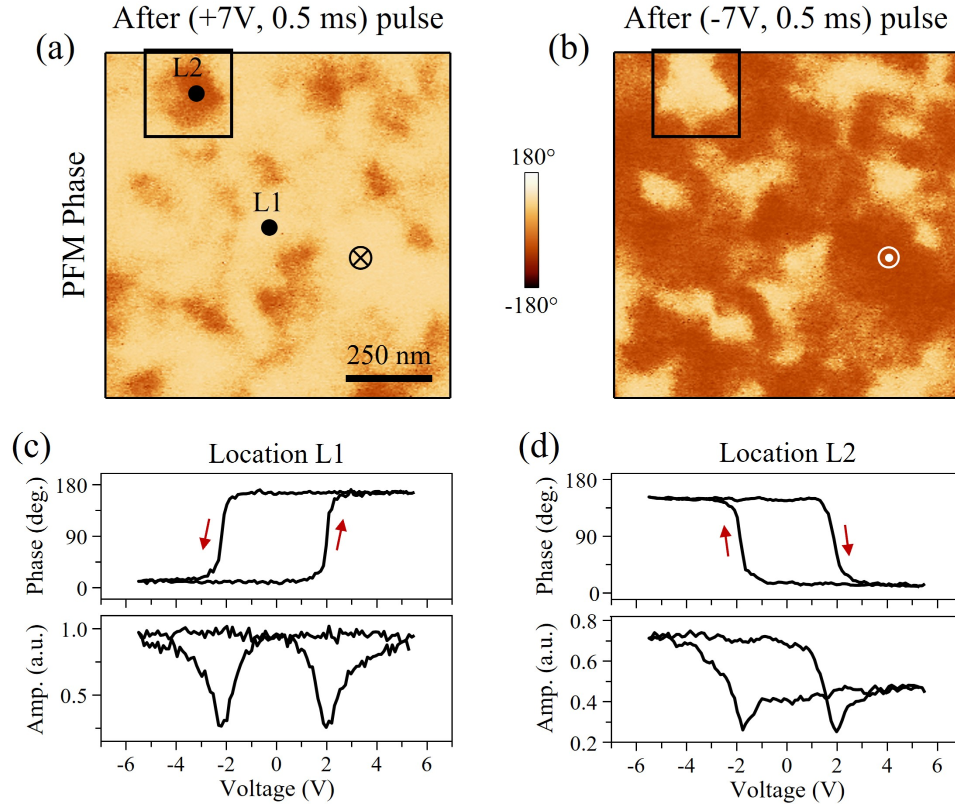

Figure 5.8. Coexistence of positive and negative d_{33} regions in IrO_x/La:HfO_2/IrO_x capacitors. (a,b) PFM phase images after application of (+7V, 0.5 ms) pulse (a), and (-7V. 0.5 ms) pulse (b). The square in (a,b) represents a region with positive d_{33}. (c,d) Representative bias off hysteresis loops obtained in location L1 (c) and in location L2 (d). From the sense of rotation of the PFM phase loops, location L1 is a negative d_{33} region while location L2 is a positive d_{33} region. All measurements were performed after wake-up.

behavior have been reported previously [64, 65] and was attributed to either charge injection/entrapment in the non-polar phases [65] or to a local oppositely oriented electric field of the oxygen vacancies [64]. However, switching of the polarization against the applied field when it is ramped below a certain threshold value, would result in the narrow anti-hysteretic bias-on PFM loops (see section B.7 in Appendix B). In our measurements, absence of the anti-hysteretic behavior in L2 region in the bias-on PFM mode (Fig. B.7 (f) in Appendix B) rules out the charge-related

mechanisms as a probable cause for its anomalous switching. Furthermore, robust switchability shown in Figs. 5.8 (c,d) rules out the possibility of a contribution from the non-ferroelectric phases. Hence, alternative mechanisms, such as those related to the ultra-high sensitivity of piezoelectricity in HfO_2-based films to local variations in structure or composition, need to be considered.

5.5 Conclusion

In conclusion, we have highlighted how a properly calibrated PFM phase signal can be useful for the identification of the local piezoelectric coefficient and outlined possible ways to calibrate the raw PFM phase signal. Typically, the raw PFM phase signal contains a parasitic phase offset related to the cantilever dynamics and the specific instrument, which can obscure the genuine sign of the piezoelectric coefficient. The parasitic phase offsets can be identified using standard reference samples with known sign of the piezoelectric coefficient or by using specific features of the cantilever-sample electrostatic interactions. The developed methodologies have been exploited to investigate the peculiarities of the piezoelectric behavior of hafnia-based ferroelectric capacitors. It was observed that depending on the film thickness, electrode materials, deposition method used or state of the capacitors, the sign of d_{33} could be either uniformly positive or negative, or there can be a mixture of both positive and negative d_{33} responses in the hafnia-based ferroelectric capacitors. Further structural studies are required to clarify the physical mechanism behind the observed variability. More importantly, these results highlight how a properly calibrated PFM phase signal can provide valuable nanoscopic insight into the spatial variations of the piezoelectric behavior that is not attainable by the macroscopic electromechanical measurements. This work provides clear guidelines

towards quantification of the PFM phase signal facilitating further studies into the piezoelectric behavior of hafnia and other emerging ferroelectrics.

References

[1] M. Alexe, and A. Gruverman (Eds.) *Ferroelectrics at Nanoscale: Scanning Probe Microscopy Approach* (Springer, New York, 2004).

[2] S. V. Kalinin, and A. Gruverman (Eds.) *Scanning Probe Microscopy: Electrical and Electromechanical Phenomena at the Nanoscale* (Springer, New York, 2006).

[3] S. V. Kalinin, A. Rar and S. Jesse, IEEE Transactions on Ultrasonics, Ferroelectrics, and Frequency Control **53**, 12 (2006).

[4] A. Gruverman, M. Alexe, and D. Meier, Nat. Commun. **10**, 1661 (2019).

[5] S. Hong, J. Appl. Phys. **129**, 051101 (2021).

[6] S. Kim, D. Seol, X. Lu, M. Alexe, and Y. Kim, Sci Rep **7**, 41657 (2017).

[7] D. Seol, B. Kim, and Y. Kim, Current Applied Physics **17**, 5, 661 (2017).

[8] C. W. Bark, P. Sharma, Y. Wang, S. H. Baek, S. Lee, S. Ryu, C. M. Folkman, T. R. Paudel, A. Kumar, S. V. Kalinin, A. Sokolov, E. Y. Tsymbal, M. S. Rzchowski, A. Gruverman, and C. B. Eom, Nano Lett. **12**, 4, 1765 (2012).

[9] A. S. Borowiak, N. Baboux, D. Albertini, B. Vilquin, G. S. Girons, S. Pelloquin, and B. Gautier, Appl. Phys. Lett. **105**, 012906 (2014).

[10] N. Balke, S. Jesse, Q. Li, P. Maksymovych, M. B. Okatan, E. Strelcov, A. Tselev, and S. V. Kalinin, J. Appl. Phys. **118**, 072013 (2015)

[11] S. Jesse, A. P. Baddorf, and S. V. Kalinin, Nanotechnology **17**, 1615 (2006).

[12] R. Proksch, J. App. Phy. **118**, 072011 (2015).

[13] R. K. Vasudevan, N. Balke, P. Maksymovych, S. Jesse, and S. V. Kalinin, Appl. Phys. Rev. **4**, 021302 (2017).

[14] N. Balke, P. Maksymovych, S. Jesse, A. Herklotz, A. Tselev, C.-B. Eom, I. I. Kravchenko, P. Yu, and S. V. Kalinin, ACS Nano **9**, 6, 6484 (2015).

[15] S. Jesse, A. P. Baddorf, and S. V. Kalinin, Appl. Phys. Lett. **88**, 062908 (2006).

[16] P. Paruch, T. Giamarchi, and J.-M. Triscone, Phys. Rev. Lett. **94**, 197601 (2005).

[17] T. Tybell, P. Paruch, T. Giamarchi, and J.-M. Triscone, Phys. Rev. Lett. **89**, 097601 (2002).

[18] A. Gruverman, D. Wu, and J. F. Scott, Phys. Rev. Lett. **100**, 097601 (2008).

[19] D. Wu, I. Vrejoiu, M. Alexe, and A. Gruverman, Appl. Phys. Lett. **96**, 112903 (2010).

[20] L. Collins, Y. Liu, O. S. Ovchinnikova, and R. Proksch, ACS Nano **13**, 8055 (2019).

[21] A. Chanthbouala, A. Crassous, V. Garcia, K. Bouzehouane, S. Fusil, X. Moya, J. Allibe, B. Dlubak, J. Grollier, A. Xavier, C. Deranlot, A. Moshar, R. Proksch, N. D. Mathur, M. Bibes, and A. Barthélémy, Nat. Nanotech. **7**, 101 (2012).

[22] Z. Wen, C. Li, D. Wu, A. Li, and N. Ming, Nat. Mater. **12**, 617 (2013).

[23] Z. Li, X. Guo, H.-B. Lu, Z. Zhang, D. Song, S. Cheng, M. Bosman, J. Zhu, Z. Dong, and W. Zhu, Adv.Mater. **26**, 7185 (2014).

[24] C. Ma, Z. Luo, W. Huang, L. Zhao, Q. Chen, Y. Lin, X. Liu, Z. Chen, C. Liu, H. Sun, X. Jin, Y. Yin, and X. Li, Nat. Commun. **11**, 1439 (2020).

[25] Y. Luo, X. Li, L. Chang, W. Gao, G. Yuan, J. Yin, and Z. Liu, AIP Adv. **3**, 122101 (2013).

[26] Z. Tan, L. Hong, Z. Fan, J. Tian, L. Zhang, Y. Jiang, Z. Hou, D. Chen, M. Qin, M. Zeng, J. Gao, X. Lu, G. Zhou, X. Gao, and J.-M. Liu, NPG Asia Mater. **11**, 20 (2019).

[27] A. Gruverman, B. J. Rodriguez, A. I. Kingon, R. J. Nemanich, A. K. Tagantsev, J. S. Cross, and M. Tsukada, Appl. Phys. Lett. **83**, 728 (2013).

[28] S. M. Neumayer, S. Saremi, L. W. Martin, L. Collins, A. Tselev, S. Jesse, S. V. Kalinin, and N. Balke, J. Appl. Phys. **128**, 171105 (2020).

[29] Y. Qi, and A. M. Rappe, Phys. Rev. Lett. **126**, 217601 (2021).

[30] L. You, Y. Zhang, S. Zhou, A. Chaturvedi, S. A. Morris, F. Liu, L. Chang, D. Ichinose, H. Funakubo, W. Hu, T. Wu, Z. Liu, S. Dong, and J. Wang, Sci. Rep. **5**, 4, eaav3780 (2019).

[31] S. M. Neumayer, L. Tao, A. O'Hara, J. Brehm, M. Si, P.-Y. Liao, T. Feng, S. V. Kalinin, P. D. Ye, S. T. Pantelides, P. Maksymovych, and N. Balke, Phys. Rev. Appl. **13**, 064063 (2020).

[32] N. Balke, S. Jesse, P. Yu, B. Carmichae, S. V. Kalinin, and A. Tselev, Nanotechnology 27, 425707 (2016).

[33] U. Schroeder, C. S. Hwang, and H. Funakubo (Eds.), *Ferroelectricity in Doped Hafnium Oxide: Materials, Properties and Devices*, Woodhead Publishing (2019).

[34] J. Liu, S. Liu, L. H. Liu, B. Hanrahan, and S. T. Pantelides, Phys. Rev. Applied **12**, 034032 (2019).

[35] J. Liu, S. Liu, J.-Y. Yang, and L. Liu, Phys. Rev. Lett. **125**, 197601, (2020).

[36] S. Dutta, P. Buragohain, S. Glinsek, C. Richter, H. Aramberri, H. Lu, U. Schroeder, E. Defay, A. Gruverman, and J. Íñiguez, Nat. Comms. **12**, 7301 (2021).

[37] A. L. Kholkin, E. K. Akdogan, A. Safari, P. F. Chauvy, and N. Setter, J. Appl. Phys. **89**, 8066 (2001).

[38] M. J. Haun, E. Furman, S. J. Jang, H. A. McKinstry, and L. E. Cross, J. Appl. Phys. **62**, 3331 (1987); Z. Kighelman, D. Damjanovic, M. Cantoni, and N. Setter, J. Appl. Phys. **91**, 1495 (2002).

[39] I. Katsouras, K. Asadi, M. Li, T. B. van Driel, K. S. Kjær, D. Zhao, T. Lenz, Y. Gu, P. W. M. Blom, D. Damjanovic, M. M. Nielsen, and D. M. de Leeuw, Nat. Mater. **15**, 78 (2016).

[40] U. Schroeder, C. Richter, M. H. Park, T. Schenk, M. Pešić, M. Hoffmann, F. Fengler, D. Pohl, B. Rellinghaus, C. Zhou, C.-C. Chung, J. Jones, and T. Mikolajick, Inorg. Chem. **57**(5), 2752 (2018).

[41] P. Buragohain, A. Erickson, P. Kariuki, T. Mittmann, C. Richter, P. D. Lomenzo, H. Lu, T. Schenk, T. Mikolajick, U. Schroeder, and A. Gruverman, ACS Appl. Mater. Interfaces **11**, 35115 (2019)..

[42] T. Mimura, T. Shimizu, H. Uchida, O. Sakata, and H. Funakubo, Appl. Phys. Lett. **113**, 102901 (2018).

[43] G. Meyer, and N. M. Amer, Appl. Phys. Lett. **53**, 1045 (1988).

[44] P. A. Yuya, D. C. Hurley, and J. A. Turner, J. Appl. Phys. **104**, 074916 (2008).

[45] A. Chouprik, R. Kirtaev, E. Korostylev, V. Mikheev, M. Spiridonov, and D. Negrov, Nanomaterials **12**, 1483 (2022).

[46] T. S. Böscke, J. Müller, D. Bräuhaus, U. Schröder, and U. Böttger, Appl. Phys. Lett. **99**, 102903 (2011).

[47] T. Schenk, N. Godard, A. Mahjoub, S. Girod, A. Matavz, V. Bobnar, E. Defay, and S. Glinsek, Phys. Status Solidi RRL **14**, 1900626 (2020).

[48] R. Shimura, T. Mimura, A. Tateyama, T. Shimizu, T. Yamada, Y. Tanaka, Y. Inoue, and H. Funakubo, Jpn. J. Appl. Phys. **60**, 031009 (2021).

[49] J. Muller, P. Polakowski, S. Mueller, and T. Mikolajick, ECS J. Solid State Sci. Technol. **4**, N30 (2015).

[50] F. Casset, A. Devos, S. Sadtler, A. Le Louarn, P. Emery, G. Le Rhun, P. Ancey, S. Fanget, and E. Defaÿ, 2012 IEEE International Ultrasonics Symposium **2180** (2012).

[51] H. Colder, B. Domengès, C. Jorel, P. Marie, M. Boisserie, S. Guillon, L. Nicu, A. Galdi, and L. Mechin, J. Appl. Phys. **115**, 053506 (2014).

[52] M. Berdova, X. Liu, C. Wiemer, A. Lamperti, G. Tallarida, E. Cianci, M. Faniculli, and S. Franssila, J. Vac. Sci. Technol. A **34**, 051510 (2016).

[53] L. Bolotov, S. Migita, R. Fujio, M. Ishimaru, S. Hatayama, and N. Uchida, Microelectron. Eng. **258**, 111770 (2022).

[54] M. Kopycinska-Müller, R. H. Geiss, and D. C. Hurley, Ultramicroscopy **106**, 466 (2006).

[55] B. J. Rodriguez, C. Callahan, S. V. Kalinin, and R. Proksch, Nanotechnology **18**, 475504, (2007).

[56] A. Labuda, and R. Proksch, Appl. Phys. Lett. **106**, 253103 (2015).

[57] L. Collins, and U. Celano, ACS Appl. Mater. Interfaces **12**, 37, 41659 (2020).

[58] H. Lu, S. Glinsek, P. Buragohain, E. Defay, J. Iñiguez, and A. Gruverman, Adv. Funct. Mater. **30**, 2003622 (2020).

[59] S. Jesse, H. N. Lee, and S. V. Kalinin, Rev. Sci. Instrum. **77**, 073702 (2006).

[60] D. Zhou, J. Xu, Q. Li, Y. Guan, F. Cao, X. Dong, J. Müller, T. Schenk, and U. Schröder Appl. Phys. Lett. **103**, 192904 (2013).

[61] T. Schenk, M. Hoffmann, J. Ocker, M. Pešić, T. Mikolajick, and U. Schroeder, ACS Appl. Mater. Interfaces **7**, 36, 20224 (2015).

[62] M. Lederer, R. Olivo, D. Lehninger, S. Abdulazhanov, T.s Kämpfe, S. Kirbach, C. Mart, K. Seidel, and L. M. Eng, Phys. Status Solidi RRL **15**, 2100086 (2021).

[63] E. D. Grimley, T. Schenk, X. Sang, M. Pešić, U. Schroeder, T. Mikolajick, and J. M. LeBeau, Adv. Electron. Mater. **2**, 1600173 (2016).

[64] A. Chouprik, M. Spiridonov, S. Zarubin, R. Kirtaev, V. Mikheev, Y. Lebedinskii, S. Zakharchenko, and D. Negrov., ACS Appl. Electron. Mater. **1**, 3, 275 (2019).

[65] I. Stolichnov M. Cavalieri, E. Colla, T. Schenk, T. Mittmann, T. Mikolajick, U. Schroeder, and A. M. Ionescu, ACS Appl. Mater. Interfaces **10**, 30514 (2018).

Chapter 6

Nanoscale probing of antiferroelectric-ferroelectric phase transitions

6.1 Introduction

Antiferroelectrics (AFEs) are a class of functional materials that are characterized by no net remanent polarization and have conventionally found applications in high energy storage devices [1, 2, 3, 4, 5], pyroelectric energy harvesting [3, 6, 7], electrocaloric cooling [3, 8, 9], transducers [10, 11], etc. A typical macroscopic signature of antiferroelectrics is the appearance of double polarization-voltage (P-V) hysteresis loops signifying the transition between the non-polar or the anti-polar AFE state to the polar ferroelectric (FE) state. Microscopically, the traditional description of antiferroelectrics involves an antipolar arrangement of dipoles in adjacent subcells resulting in zero net remanent polarization in the absence of an electric field [12]. Application of an electric field aligns the dipoles resulting in the polar state. This description has since been expanded to also include materials with a non-polar ground state that can be transformed to a polar state under the application of an electric field [13]. In the latter description, the energy barrier between the non-polar and the polar phases should be low enough such that an electric field can induce the transformation to the polar state. An example of a classical AFE is $PbZrO_3$ (PZO), characterized by an anti-polar ground state [14, 15], while an example of the latter description is ZrO_2 in which the ground state

is a non-polar phase [16, 17]. ZrO_2 is a sister compound of HfO_2 and is the current state-of-the-art gate dielectric in the dynamic random access memory (DRAM) industry [18]. Pure ZrO_2 thin films exist in a non-polar tetragonal ($P4_2/nmc$) structure which, under an applied electric field, undergoes a transformation to a polar orthorhombic phase ($Pca2_1$) [16].

The AFE $\rightarrow$FE phase transition is accompanied by a large volume change together with a large change in the electromechanical strain [11]. Although piezoresponse force microscopy (PFM) is an electromechanical strain-based technique, there have been hardly any reports on the investigation of the antiferroelectric properties using PFM [19]. In this chapter, PFM spectroscopy studies of the AFE $\leftrightarrow$ FE phase transitions in the model AFE material PZO is first shown. It was observed that the PFM amplitude loops exhibit four characteristic peaks corresponding to the AFE $\leftrightarrow$ FE phase transitions, which is drastically different from the butterfly-shaped hysteresis loops characterized by the polarization switching-related double minima observed in ferroelectrics. Analysis of the piezoelectric response within the framework of the phenomenological Landau theory showed that these peaks can be attributed to the sharp increase of the dielectric susceptibility at the phase transitions. The characteristic four peak-behavior can be considered as the microscopic electromechanical signature of AFE $\leftrightarrow$ FE phase transitions which can be used to verify if the macroscopic double or pinched P-V loops observed in a new material system is due to antiferroelectricity or can be attributed to other physical reasons such as domain pinning. This is particularly relevant to clarify the microscopic origins of the pinched P-V loops commonly observed in the family of HfO_2-based ferroelectrics. As an example, the PFM investigations were extended to ZrO_2-based thin film capacitors and compared with La:HfO_2 capacitors both of which display pinched P-V loops. It was confirmed that

the pinched P-V loops in the ZrO_2 capacitors were indeed due to the AFE $\leftrightarrow$ FE phase transition, while in the La:HfO_2 capacitors it could be attributed to domain pinning.

The results presented in this chapter have been published in Refs. [20, 21].

6.2 Materials and methods

The 60-nm-thick PZO films used in this study have been grown by chemical solution deposition (CSD) on Pt-coated SiO_2/Si substrates with a $PbTiO_3$ seed layer. 50-nm-thick Pt top electrodes were dc-sputtered with a surface area of 200x200 μm^2. The details of the deposition method can be found in Ref. [20]. A series of atomic layer deposition (ALD) grown ZrO_2 films with thicknesses of 4.3 nm, 5.3 nm, 10.6 nm, and 14.7 nm sandwiched between TiN top and bottom electrodes were used to investigate the electromechanical behavior in ZrO_2-system (Ref. [21]). Finally, as a reference ferroelectric, $IrO_2/Pb(Zr_{0.4}Ti_{0.6})O_3$ (PZT)/Pt capacitors were used with the 200 nm-thick (111)-oriented PZT films fabricated by magnetron sputtering on the Pt bottom electrode.

The PFM measurements have been carried out in the capacitor geometry, and the details of the measurement are discussed in section 2.3.1 in Chapter 2.

6.3 PFM spectroscopy measurements in antiferroelectrics

To highlight the essential differences in the electrical and electromechanical responses in ferroelectrics and antiferroelectrics, we perform a comparative study of ferroelectric IrO_2/PZT/Pt capacitors and antiferroelectric Pt/PZO/Pt capacitors. Figs. 6.1 (a,b) represent macroscopic P-V loops in the ferroelectric PZT capacitors and antiferroelectric PZO capacitors. The P-V loops measured in the ferroelectric

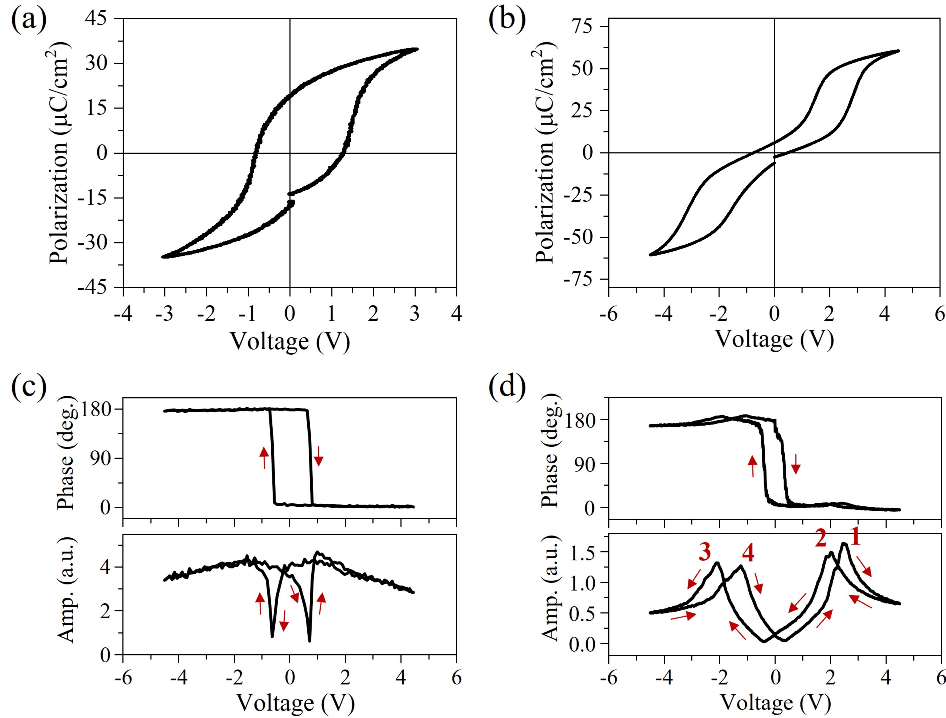

Figure 6.1. (a,c) P-V loop (a) and PFM phase (top panel) and amplitude (bottom panel) (c) in IrO_2/PZT/Pt capacitors. (b,d) P-V loop (b) and PFM phase (top panel) and amplitude (bottom panel) (d) in Pt/PZO/Pt capacitors. The numbers in (d) are labels for the four switching peaks. The arrows indicate the electric field sweeping directions. All PFM spectroscopy loops have been acquired in the bias-on mode.

PZT capacitors exhibit typical single hysteresis associated with polarization switching (Fig. 6.1 (a)), while the P-V loops in the antiferroelectric PZO capacitors exhibit characteristic double hysteresis loops (Fig. 6.1 (b)) associated with the field induced AFE $\leftrightarrow$ FE phase transitions.

We begin our discussion on the local PFM spectroscopy loops by highlighting differences in the testing methodology for ferroelectrics and antiferroelectrics. Conventional PFM spectroscopy loops are typically acquired in a pulsed dc mode where a small-signal sinusoidal ac driving voltage, V_{ac}, is superimposed onto dc pulses, V_{dc}, to measure the electromechanical response while the V_{dc} is used to

induce polarization switching underneath the tip. The PFM loops can be be measured either when the V_{dc} is on (bias-on mode) or when the V_{dc} is off (bias-off mode), with the choice of mode being dependent on the experimental conditions and research goals. For instance, the bias-on loops can be useful to prevent polarization relaxation between pulses in the absence of V_{dc} [22] while the bias-off mode is typically used for measurements on bare surface to minimize the electrostatic contributions. In the case of ferroelectrics, the PFM amplitude loops are butterfly-shaped in both the modes, with the finite PFM amplitude at zero bias signifying stable remanent polarization and the amplitude minima corresponding to the local coercive fields. A representative PFM spectroscopy loop acquired in the bias-on mode in ferroelectric PZT capacitors is shown in Fig. 6.1 (c). The minima coincide with the 180° phase reversal due to the field-induced polarization switching.

On the other hand, the PFM measurements should be performed only in the bias-on mode in antiferroelectrics due to no net remanent polarization and no piezoelectricity in the absence of an electric field. Testing the antiferroelectric Pt/PZO/Pt capacitors in the bias-on mode revealed dramatically different PFM amplitude loops with four maxima and negligible amplitude response at zero bias (bottom panel in Fig. 6.1 (d)). To understand the origin of the four maxima in the PFM amplitude, we turn to a theoretical description of the piezoelectric response in antiferroelectrics from the viewpoint of the phenomenological Landau model of phase transitions, which is discussed in the next section. The 180° phase difference at the far positive and far negative polarities correspond to the two oppositely oriented polarization states in the field-induced ferroelectric phase.

6.4 Theoretical description of the piezoelectric response in antiferroelectrics

The simplest Landau potential capturing the antiferroelectric behavior, first proposed by Kittel [12], can be written as:

$$F = F_0 + \frac{1}{2}\alpha A^2 + \frac{1}{4}\beta A^4 + \frac{1}{2}\alpha' P^2 + \frac{1}{4}\beta P^4 + \frac{3}{2}\beta A^2 P^2 + g\eta A^2 + g'\eta P^2 + \frac{1}{2}\gamma\eta^2 - EP \quad (6.1)$$

where A and P are the antiferroelectric (AFE) and ferroelectric (FE) order parameters, respectively, while η is the relevant out-of-plane strain. The parameters controlling the energy of the polar orders are $\alpha < \alpha' < 0$ and $\beta > 0$; also $\gamma > 0$ is the relevant elastic constant. The coupling with strain is given by $g' < g < 0$, so that the development of both A and P produces an elongation of the cell, the effect being stronger for the polarization. The strain dependence on A and P can be obtained by solving

$$\frac{\partial F}{\partial \eta} = 0 \quad (6.2)$$

which yields

$$\eta = -\frac{1}{\gamma}(gA^2 + g'P^2) \quad (6.3)$$

By inserting this expression into Eq. 6.1, it is possible to derive a strain-free potential with renormalized anharmonic couplings for A and P. The free energy expression then reduces to:

$$\tilde{F} = \tilde{F}_0 + \frac{1}{2}\alpha A^2 + \frac{1}{4}\beta A^4 + \frac{1}{2}\alpha' P^2 + \frac{1}{4}\beta P^4 + \frac{3}{2}\beta A^2 P^2 - EP \qquad (6.4)$$

noting that the strain η can be obtained via Eq. 6.2. This form of the potential is used in the following discussion.

Application of an electric field to the AFE sample will result in a linear increase of P and a quadratic reduction of A up to the point when the AFE state is no longer the minimum of the Landau potential, at which point the dielectric susceptibility will diverge. More specifically, the dielectric susceptibility which is given by

$$\chi = [6\alpha + 8\beta A^2]^{-1} \qquad (6.5)$$

will become infinite when

$$A^2 = -\frac{3\alpha}{4\beta} = \frac{3}{4}(A_0^2) \qquad (6.6)$$

where A_0 is the AFE order parameter at zero applied field. In other words, when the applied electric field reduces A to about 87% of its zero-field value, the system undergoes a transition to the polar FE state (AFE→FE). The piezoelectric response will be dominated by this singularity:

$$\frac{d\eta}{dE} \sim -\frac{2}{\gamma}(2gA_0\frac{dA}{dE} + g'\chi^2)E \sim -\frac{2}{\gamma}g'\chi^2 E \qquad (6.7)$$

such that the PFM amplitude is zero at zero field and diverges together with the dielectric susceptibility at the AFE→FE transition giving rise to peaks 1 and 3 in Fig. 6.1 (d) corresponding to the AFE→FE transitions for the positive and negative polarities, respectively. Please note that since $\gamma > 0$ and $g' < 0$, the piezoelectric response always remains positive.

The backward transition to the AFE state (FE→AFE) upon the reduction in the applied field occurs when the field is small enough such that the AFE state becomes a minimum of the Landau potential (hence the back-switching field must be smaller than the one at which the AFE→FE transition occurs). At the FE→AFE phase transition, the polarization P reduces sharply going from a value of about $\sqrt{\alpha'/\beta}$ (corresponding to the spontaneous polarization P_0 of the FE state) to nearly zero. The susceptibility of the FE state

$$\chi = \frac{1}{\alpha' + 3\beta P^2} \tag{6.8}$$

will diverge when

$$P^2 = \frac{1}{3}(P_0)^2 \tag{6.9}$$

or when P is reduced to about 58% of P_0 as the FE→AFE proceeds upon the field reduction. During this phase transition, the piezoelectric response is given by

$$\frac{d\eta}{dE} = -\frac{2}{\gamma} g' \chi P = -\frac{2}{\gamma} g' \chi (P_0 + \chi E) \tag{6.10}$$

which is always positive ($\gamma > 0$, $g' < 0$) and diverges with χ resulting in the peaks 2 and 4 in Fig. 6.1 (d) during the backward FE→AFE phase transition for the positive and negative polarities, respectively.

Hence, the specific shape of the PFM amplitude hysteresis loops in the PZO capacitors can be attributed to the sharp increase (in the ideal case, divergence) of the dielectric susceptibility at the AFE ↔ FE phase transitions. Since PZO is a model antiferroelectric material, the observed PFM characteristics in the PZO capacitors can be taken as the microscopic signature of the AFE ↔ FE phase transitions.

(This theoretical description of the piezoelectric response was formulated by Prof. Jorge Iniguez.)

6.5 Field induced AFE ↔ FE phase transitions in ZrO_2

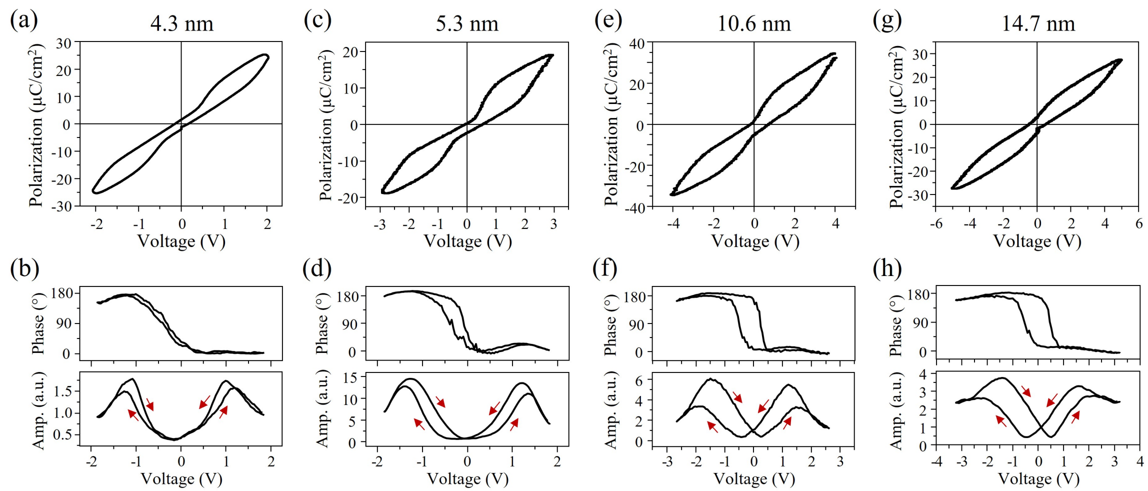

Figure 6.2. (a,c,e,g) P-V loops and (b,d,f,h) PFM phase (top panel) and PFM amplitude (bottom panel) in $TiN/ZrO_2/TiN$ capacitors with ZrO_2 thicknesses of 4.3 nm (a,b), 5.3 nm (c,d), 10.6 nm (e,f) and 14.7 nm (g,h). Figure adapted from Ref. [21].

Fig. 6.2 (a,c,e,g) shows macroscopic P-V loops in ZrO_2-based thin film capacitors which exhibit double-hysteresis behavior similar to that observed in antiferroelectrics (Fig. 6.1 (b)). Recent theoretical reports suggested that the antiferroelectricity in ZrO_2 is intrinsic with the energy of the non-polar tetragonal phase being $\sim$ 1 meV f.u.$^{-1}$ lower than that of the polar orthorhombic phase. The energy barriers between the two phases were found to be between 1-3 meV f.u.$^{-1}$ for the ZrO_2 films with thickness greater than 10 nm and increased to more than 7 meV f.u.$^{-1}$ for the 5.3 nm-thick-films [21]. A depolarization field model based on the macroscopic P-V measurements showed that the large depolarization fields in ZrO_2

can help stabilize the non-polar phase and makes the polar phase metastable [21]. However, microscopic verification of the genuine antiferroelectric nature in ZrO_2 was still lacking. In this context, we applied the previous methodology used in the testing of the PZO capacitors to elucidate the microscopic mechanism of the origin of the macroscopic double hysteresis behavior in the P-V loops.

Fig. 6.2 (b,d,f,h) shows the local PFM spectroscopy loops carried out in the bias-on mode in ZrO_2 capacitors of different thicknesses. The four maxima behavior in the amplitude loops is similar to that observed in the PZO capacitors previously (Fig. 6.1 (d)) and drastically different from the amplitude loops observed in ferroelectrics (Fig. 6.1 (c)). From the specific shape of the PFM amplitude loops, the macroscopic double hysteresis loops can be attributed to genuine field induced AFE $\leftrightarrow$ FE phase transitions as opposed to other microscopic mechanisms such as domain pinning. An example illustrating the PFM loops for pinned domains measured in pristine La:HfO_2 capacitors that also exhibit macroscopic pinched hysteresis loops (Fig. 3.1 (c) in Chapter 3) was shown in Fig. 3.3 in Chapter 3 where the PFM amplitude loops showed discrete levels associated with the pinning-depinning process due to interactions with defects but does not exhibit the four maxima behavior observed in the ZrO_2 capacitors. It is interesting to note that the PFM amplitude loops progressively acquire a ferroelectric-like shape manifested by an increase in the remanent amplitude at zero bias and the appearance of a double minima.

PFM imaging in the presence of a constant DC bias in TiN/ZrO_2 (5.3 nm)/TiN capacitors revealed a similar variation in the amplitude signal as that obtained from the spectroscopy loops (Fig. 6.3). Starting from a negligible amplitude at zero bias, which results in a noisy phase signal [23], the amplitude increases to a maximum at the phase transition. No domain-like features could be observed in the FE phase

which might be due to the domain features being smaller than the PFM resolution limit.

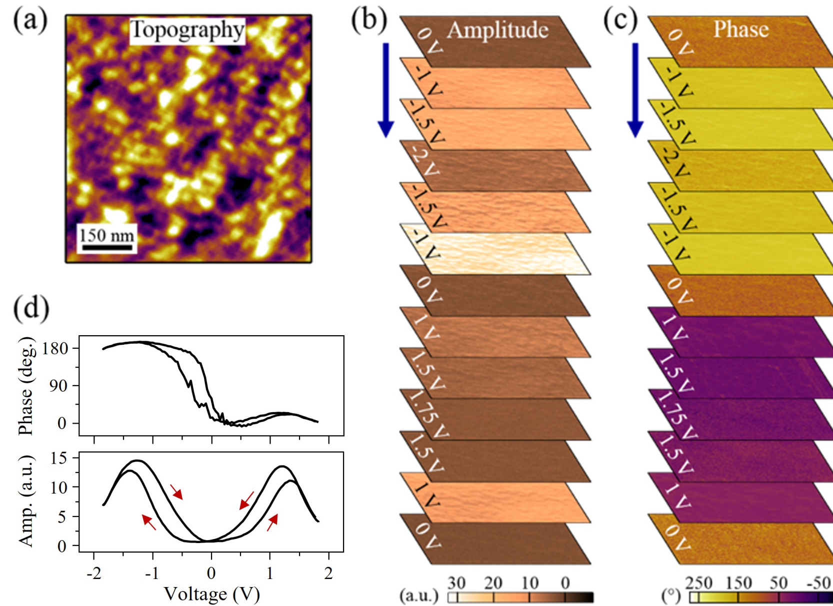

Figure 6.3. (a) Topographic image of the electrode surface in the TiN/ZrO_2 (5.3 nm)/TiN capacitor. (b,c) Evolution of the PFM amplitude (b) and PFM phase images as a function of constant DC bias applied during imaging which show a change of the electromechanical response due to the field-induced phase transitions. The blue arrows indicate the sequences in which the images were obtained. (d) PFM spectroscopy loops acquired on the TiN/ZrO_2 (5.3 nm)/TiN capacitor. Figure adapted from Ref. [21].

6.6 Conclusion

In conclusion, PFM spectroscopy loops measured in the bias-on regime display significantly different amplitude loops in antiferroelectrics compared to that in ferroelectric materials. The PFM amplitude loops in antiferroelectrics display characteristic four maxima behavior which can be attributed to the sharp increase of the dielectric susceptibility at the AFE $\leftrightarrow$ FE phase transitions. Extending the

PFM spectroscopy testing methodology to ZrO_2-based thin film capacitors also showed the four maxima behavior in the PFM amplitude loops, which proves that the macroscopic double hysteresis loops in ZrO_2 can be attributed to genuine AFE $\leftrightarrow$ FE phase transitions.

References

[1] B. Jaffe, Proceedings of the IRE **49**, 8, 1264 (1961).

[2] Z. Liu, T. Lu, J. Ye, G. Wang, X. Dong, R. Withers, and Y. Liu, Adv. Mater. Technol. **3**, 1800111 (2018).

[3] B. Xu, J. Íñiguez, and L. Bellaiche, Nat Commun **8**, 15682 (2017).

[4] M. H. Park, H. J. Kim, Y. J. Kim, T. Moon, K. D. Kim, and C. S. Hwang, Nano Energy **12**, 131 (2015).

[5] L. Yang, X. Kong, F. Li, H. Hao, Z. Cheng, H. Liu, J. Li, and S. Zhang, Progress in Materials Science **102**, 72 (2019).

[6] B. Hanrahan, Y. Espinal, S. Liu, Z. Zhang, A. Khaligh, A. Smith, and S. P. Alpayb, J. Mater. Chem. C **6**, 9828 (2018).

[7] X. Wang, X. Hao, Q. Zhang, S. An, and X. Chou, J Mater Sci: Mater Electron **28**, 1438 (2017).

[8] B. A. Tuttle, and D. A. Payne, Ferroelectrics **37**, 603 (1981).

[9] A. S. Mischenko, Q. Zhang, J. F. Scott, R. W. Whatmore, and N. D. Mathur, Science **311**, 1270 (2006).

[10] D. Berlincourt, IEEE Trans. Sonics Ultrason. **13**, 116 (1966).

[11] K. Uchino, Jpn. J. Appl. Phys. **24**, 460 (1985).

[12] C. Kittel, Phys. Rev. **82**, 729 (1951).

[13] K. M. Rabe, In Functional Metal Oxides (Eds: S. B. Ogale, T. V. Venkatesan, and M. G. Blamire), Wiley-VCH Verlag GmbH & Co. KGaA, Weinheim, Germany 2013, pp. 221–244.

[14] H. Maniwa, E. Sawaguchi, and S. Hoshino, Phys. Rev. **83**, 1078 (1951).

[15] G. Shirane, E. Sawaguchi, and Y. Takagi, Phys. Rev. **84**, 476 (1951).

[16] S. E. Reyes-Lillo, K. F. Garrity, and K. M. Rabe, Phys. Rev. B **90**, 140103(R) (2014).

[17] J. Müller, T. S. Böscke, U. Schröder, S. Mueller, D. Bräuhaus, U. Böttger, L. Frey, and T. Mikolajick, Nano Lett. **12**, 8, 4318 (2012).

[18] D.-S. Kil, H.-S. Song, K.-J. Lee, K. Hong, J.-H. Kim, K.-S. Park, S.-J. Yeom, J.-S. Roh, N.-J. Kwak, H.-C. Sohn, J.-W. Kim, and S.-W. Park, 2006 Symposium on VLSI Technology, 2006. Digest of Technical Papers, 38–39 (2006).

[19] K. Boldyreva, D. Bao, G. Le Rhun, L. Pintilie, M. Alexe, and D. Hesse, J. Appl. Phys. **102**, 044111 (2007).

[20] H. Lu, S. Glinsek, P. Buragohain, E. Defay, J. Iñiguez, and A. Gruverman, Adv. Funct. Mater. **30**, 2003622 (2020).

[21] P. D. Lomenzo, M. Materano, T. Mittmann, P. Buragohain, A. Gruverman, T. Kiguchi, T. Mikolajick, and U. Schroeder, Adv. Electron. Mater. **8**, 2100556 (2022).

[22] M. Alexe, and A. Gruverman (Eds.) *Ferroelectrics at Nanoscale: Scanning Probe Microscopy Approach* (Springer, New York, 2004).

[23] A. Labuda, and R. Proksch, Appl. Phys. Lett. **106**, 253103 (2015).

Chapter 7

Fluid imprint and inertial switching in ferroelectric HfO_2-based capacitors

7.1 Introduction

Imprint is one of the most serious degradation effects in ferroelectrics manifested by the shift of a hysteresis loop along the voltage axis resulting in effective asymmetry of the coercive field, destabilization of one of the polarization states and, as a consequence, retention or even write failure [1, 2, 3]. Imprint phenomenon has been widely investigated in perovskite ferroelectrics, such as $BaTiO_3$ (BTO) and $Pb(Zr,Ti)O_3$ (PZT) [1, 2, 3, 4, 5]. It is generally attributed to an internal bias that can have various origins including electrical charge injection, migration and trapping at the interface or grain boundaries, defect dipole alignment as well as stress gradients [4, 6, 7, 8].

Although HfO_2-based devices show a lot of promise, the integration of HfO_2-based films into electronic devices is hampered by serious performance instability associated with the profound wake-up effect, limited endurance and strong imprint effect [9, 10, 11, 12, 13, 14, 15, 16]. Comprehensive understanding of the microscopic mechanism behind the peculiar imprint behavior of the HfO_2-based films requires moving beyond the integral electrical testing methods, such as First Order Reversal Curve (FORC), used so far [9, 10, 12, 16]. In this chapter, we combine the pulse switching techniques with high-resolution domain imaging by

means of Piezoresponse Force Microscopy (PFM) to gain insight into the imprint effect in La-doped HfO_2 (La:HfO_2) capacitors by establishing a correlation between the macroscopic switching characteristics and the domain time-voltage-dependent behavior. It is shown that La:HfO_2 capacitors exhibit a much more pronounced imprint than their PZT counterparts. This can be explained by the different physical properties of the layers. Furthermore, in addition to conventional imprint developing with time in the capacitors set to a specific polarization state, an easily changeable imprint, termed as fluid imprint, with a strong dependence on the switching pre-history and pulse train sequence has been observed. In addition, domain structure visualization reveals an inertial switching effect, manifested by continued polarization switching in the direction of the applied electric field long after the termination of the external pulse. These observations highlight the critical role played by the injected charges and mobile charges/defects in the switching behavior of ferroelectric (FE) HfO_2-based devices.

The results presented in this chapter have been published in Ref. [17].

7.2 Materials and methods

The 20-nm-thick La:HfO_2 films were integrated in a capacitor structure with 25 nm thick iridium oxide (IrO_x) bottom and top electrodes sputtered in a BESTEC physical vapor deposition (PVD) tool at room temperature. IrO_x was deposited on silicon substrates with 200 nm thermally grown SiO_2. Electrodes were fabricated using the process at a pressure of 1 μbar, and 20:5 Ar/O_2 ratio to obtain a typical resistivity value of about 100 $\mu\omega/\mathrm{cm}^2$. The capacitor areas were defined by evaporating IrO_x through a shadow mask. Lanthanum-doped hafnium oxide films were deposited in an Oxford Instruments OpAL ALD tool by atomic layer deposition (ALD) as described

elsewhere [18]. The HfO_2 films were doped by replacing every tenth HfO_2 cycles by La_2O_3 cycles resulting in a La content of about 10 mol %. The IrO_x bottom electrode and the complete IrO_x/La:HfO_2/IrO_x was annealed in O_2 atmosphere at 600°C for 10 min to ensure high oxygen content in all layers. Grazing incidence X-ray diffraction (GI-XRD) was carried out to analyze the phases present in the polycrystalline La:HfO_2 films with IrO_x electrodes. The phases were deconvoluted by applying Gaussian fits and the areas under the individual Gaussians were integrated to extract the approximate HfO_2 phase percentage.

The PFM measurements have been carried out in the capacitor geometry using an AC modulation bias with amplitude 0.65V. The details of the PFM measurements are discussed in section 2.3.1 in chapter 2. The pulse switching measurements have been performed as described in section 2.3.3 in chapter 2. The capacitance-voltage ($C-V$) measurements were performed using a commercial Radiant Precision SC tester.

7.3 Wake-up effect

The pristine state is characterized by a typical pinched polarization-voltage ($P-V$) hysteresis loop (Fig. 7.1 (a), black curve) with very low remanent polarization (P_r). Structural characterization by GI-XRD (Fig. 7.1 (b)) shows a higher volume fraction of non-ferroelectric monoclinic and tetragonal phases compared to the previously published case with TiN electrodes [18]. Analysis of the phase fractions revealed a significant monoclinic phase fraction, constituting approximately 50 % of the film, which might be one of reasons for the low remanent polarization in the as-grown state. PFM imaging of the La:HfO_2 capacitors in the pristine state does not reveal any sign of the domain structure after application of ±6 V voltage pulses and yields a relatively weak PFM amplitude signal (Fig. 7.1 (c,d)). These PFM observations are

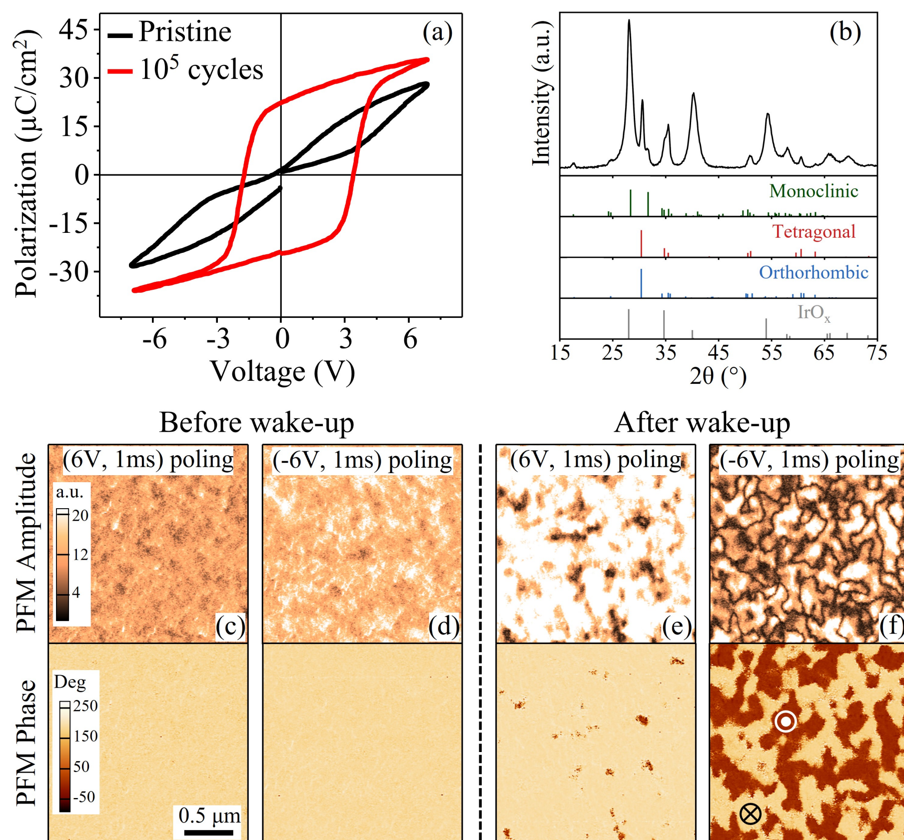

Figure 7.1. (a) $P - V$ loops for the La:HfO_2 capacitor in the pristine state (black) and after the wake-up process (red). (b) Grazing incidence X-ray diffraction of the 20-nm-thick La:HfO_2 capacitors with IrO_x electrodes. (c-f) PFM amplitude (top row) and PFM phase (bottom row) images of the La:HfO_2 capacitor in the pristine state (c,d) and after wake-up (e,f). The measurements were done on a 160-μm-diameter capacitor. Figure adapted from Ref. [17].

consistent with a low volume fraction of the ferroelectric phase in the pristine state and are in contrast with that of the pristine state in the La:HfO_2 capacitors with TiN electrodes, where a clear polydomain configuration could be observed in the pristine state (see Fig. 3.1 (e,f) in Chapter 3). After the capacitors were subjected to the wake-up process [9, 19, 20, 21, 22] (via application of 10^5 cycles of alternating square pulses of 7 V in amplitude at 10 kHz), the $P - V$ testing yielded a Pr value of $\sim$22 μC/cm^2 (Fig. 7.1 (a), red curve), which points to a field-cycling induced

phase transformation from a non-FE to the FE phase [16, 20, 22]. The increase in Pr is accompanied by the increased domain switchability as seen from PFM imaging (Fig. 7.1 (e,f)). A significant difference in the amount of the switched polarization by positive and negative pulses might be due to the asymmetric boundary conditions at the top and bottom interfaces resulting from the different growth conditions of the top and bottom electrodes or it could as well be due to the manifestation of the field-induced imprint as is discussed next.

7.4 Fluid and time-dependent imprint

Investigation of the imprint effect has been carried out using a pulse train sequence shown in Fig. 7.2 (a). Before each measurement, the capacitors were cycled 100 times using (± 7 V, 50 μs) pulses to erase the previous imprinted state (see Fig. 7.3). Then, the capacitor was poled to a certain state by application of a set pulse followed by a triangular waveform to measure the transient switching currents, which were subsequently integrated to obtain the $P-V$ hysteresis loops. Measurement of the $P-V$ loops as a function of the delay time $\mathrm{t_d}$ (Fig. 7.2 (a)) after the set pulse application allows testing of the conventional time-dependent imprint. On the other hand, acquisition of the hysteresis loops as a function of the set pulse parameters (duration and amplitude) provides information on the fluid imprint behavior, which is determined by sample switching pre-history. The term "fluid" is chosen to reflect the ease, with which the sign and magnitude of imprint changes in the La:HfO_2 capacitors upon switching. The proposed approach allows us to investigate the dynamic behavior of fluid imprint and to differentiate it from conventional imprint, which take place at different time scales.

A time-dependent shift of the $P-V$ loops observed during investigation of

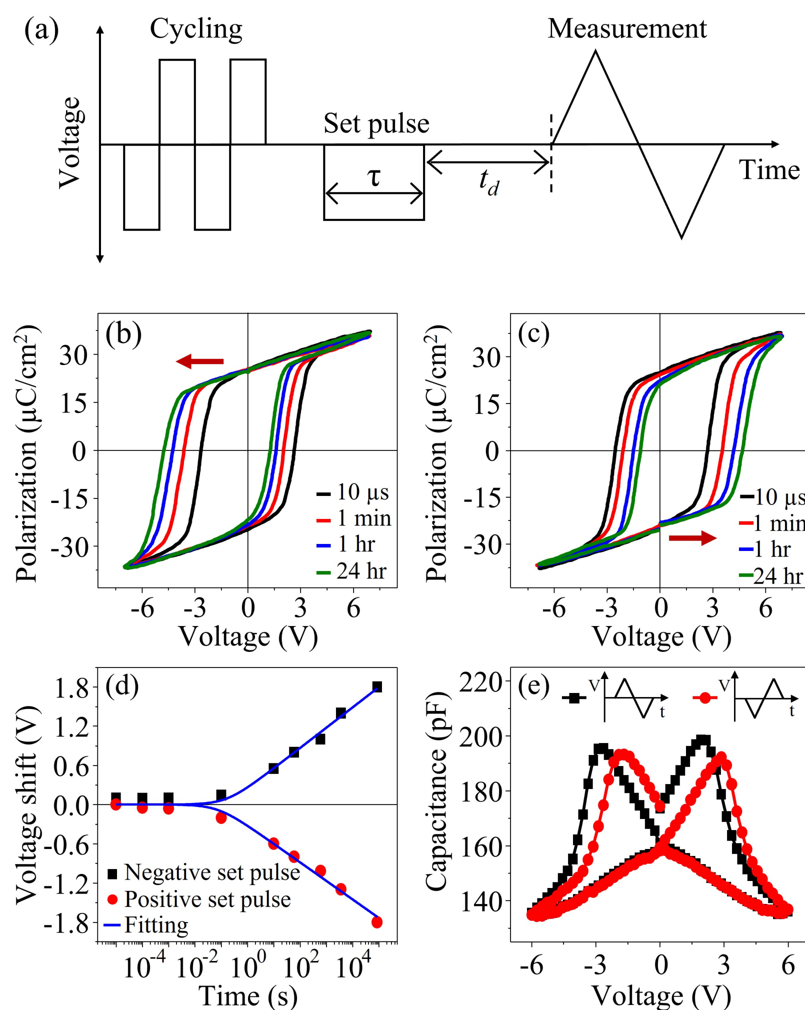

Figure 7.2. (a) A pulse train sequence used for investigation of the imprint behavior. τ denotes the duration of the set pulse while t_d denotes the time delay between the set pulse and the triangular waveform. (b-d) Development of static imprint in the La:HfO_2 capacitors as a function of the delay time t_d between the set pulse and the measurements. (b, c) $P-V$ loops after (+6 V, 5 ms) (b) and (-6 V, 5 ms) (c) set pulse application. The arrows indicate the direction of the voltage shift. (d) Voltage shift as a function of time (calculated from the loops in (b) and (c)) for both polarities. The blue curves represent fit of the experimental data by Equation 7.3. (e) Effect of the testing pulse sequence on the $C-V$ loops suggesting that the observed voltage shift can be a result of the measurement process itself. The measurements were performed on the 90-μm-diameter capacitors. Figure adapted from Ref. [17].

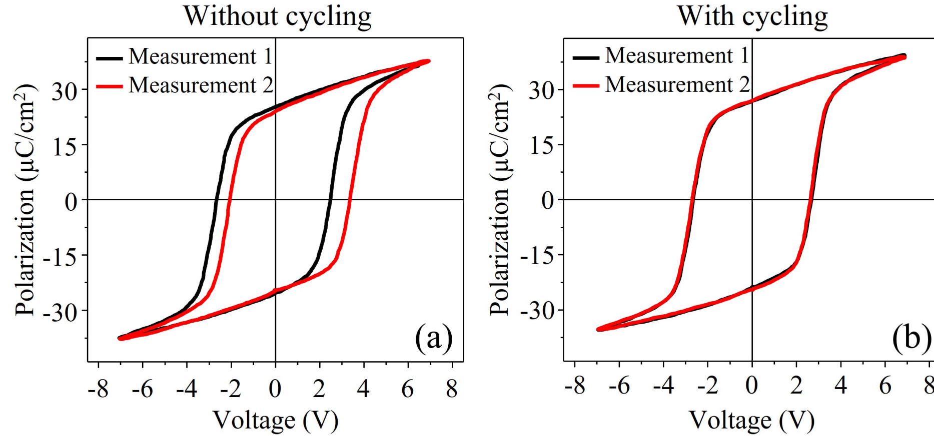

Figure 7.3. Two consecutive polarization-voltage ($P - V$) loops measured using identical testing parameters without cycling (a) and with cycling (b) between the two measurements. If the capacitors were not cycled between the measurements, there was a shift of the second loop with respect to the first one (a). On the other hand, electrical cycling of the capacitors between the measurements resulted in identical $P - V$ loops (b). A (-6 V, 5 ms) set pulse with a 10 μs delay between the set pulse and the P-V measurement was used. The capacitors were cycled 100 times using ($\pm$ 7 V, 50 μs) pulses. Figure adapted from Ref. [17].

conventional imprint is shown in Figs. 7.2 (b,c). The capacitor was switched to a specific polarization state by applying a set pulse with amplitude in the range from 4 V to 6 V with a duration of 5 ms. The set pulse parameters have been chosen to ensure complete poling of the capacitor, which was verified by PFM observation of the resulting single-domain structure. In 7.2 (b,c), it can be clearly seen that the polarity of the set pulse, which switches the polarization either to the downward (toward the bottom electrode) (P_{down}) or upward (P_{up}) direction, determines the sign of the voltage shift defined as

$$V_{shift} = \frac{V_{c+} + V_{c-}}{2} \tag{7.1}$$

where V_{c+} and V_{c-} represent the positive and negative coercive voltages,

respectively. A positive set pulse creates a preference for the P_{down} state leading to the $P - V$ loop shift to the left, while a negative set pulse, which induces the P_{up} state, causes the shift to the right.

Fig. 7.2(d) shows the highly non-linear time dependence of the voltage shift for both polarities of set pulses. Nearly symmetric $P - V$ loops have been observed right after the ac cycling. Subsequently, the imprint starts to evolve with V_{shift} reaching a value of 1.8 V (0.9 MV/cm) within 24 hours. This behavior is similar to that reported for PZT-based capacitors [2, 3] except that the magnitude of imprint, normalized to the coercive voltage, is nearly 3 to 4 times larger in the La:HfO_2 capacitors so that their total voltage shift could be as large as the coercive voltage. To understand the relatively large imprint value in La:HfO_2 capacitors, we have calculated the depolarization fields in HfO_2 and PZT capacitors as a function of the film thickness and the dielectric constants of the passive layers. A passive, non-switching dielectric layer at the interface, sometimes referred to as a dead layer [23, 24], can cause a significant depolarization field in the ferroelectric layer. The depolarization field across a ferroelectric with polarization P_s and an interfacial passive layer can be described as

$$E_{FE} = \frac{-P_s}{\epsilon_0(\epsilon_{FE} + \epsilon_{Int}\frac{d_{FE}}{d_{Int}})} \tag{7.2}$$

where ϵ_{FE} and ϵ_{Int} are the dielectric constants of the ferroelectric and passive layers, respectively, and d_{FE} and d_{Int} are their thicknesses, respectively. Assuming that on both interfaces HfO_2 and PZT have passive layers of only 1 or 2 lattice cells in thickness [22], i.e. roughly 1 nm in total, the depolarization fields in both materials are significant and increase substantially within the 5-20 nm thickness range (Fig. 7.4(a)). The large depolarization field across the ferroelectric can drive charge carriers to the

passive layer interface where they become trapped, producing pinned domains and a voltage offset. Such charge carriers may originate from injected charge and charge traps away from the interface, charge accumulated along grain boundaries, and/or defect dipole charges. The depolarization field in HfO_2 is significantly larger than in PZT. For the specific scenario shown in inset in Fig. 7.4(b), it can be anywhere from 5 to 30 times larger in HfO_2 than in PZT. The depolarization field difference can be primarily attributed to the different thickness ranges, which are typically used for the two materials that are discussed here, i.e. the 5-20 nm thickness range for HfO_2 films and the 70-300 nm range for PZT films. The larger depolarization field may be the reason for stronger imprint seen in HfO_2 capacitors when compared to PZT capacitors. It must be noted, however, that if PZT was scaled down to the 10-15 nm thickness range, the depolarization field in PZT would become comparable to the one in HfO_2.

Previously, to explain the time-dependent behavior of imprint in PZT, Grossmann *et al.* [2, 3] proposed an interface screening model (ISM), according to which the presence of an interfacial passive layer [5] between the ferroelectric thin film and the electrode results in incomplete screening of the polarization charges by the charges on the electrodes. When such a capacitor is poled, space separation between the bound polarization charges and the electrode charges leads to a strong electric field across the passive layer. This field promotes charge transport into the layer [25] and followed by charge accumulation and trapping at the ferroelectric/passive layer interface [26]. If the de-trapping time constant of the accumulated charges is much longer than the polarization switching time, an internal bias field due to these charges will manifest as a voltage shift in the P-V loop [27]. Tagantsev *et al.* then put forward an analytical treatment of the problem along the lines of the ISM based on charge injection into the passive layer from the electrode [5]. They found a universal logarithmic-type time

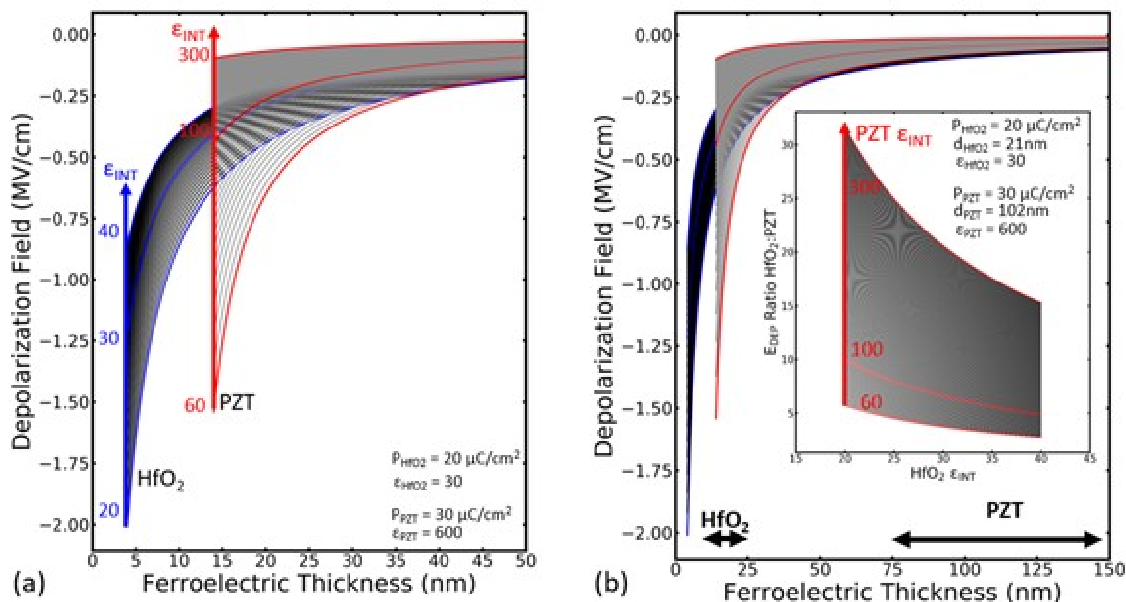

Figure 7.4. (a) Depolarization fields in HfO_2 and PZT capacitors calculated as a function of the ferroelectric layer thickness and the dielectric constant of the passive layer ϵ_{Int}. Parameters of the HfO_2 and PZT layers used in the calculations are shown in the lower right corner of the plot. (b) The same plot as in (a) shown for the larger thickness range of the HfO_2 and PZT layers. The inset in (b) shows the ratio of the depolarization field in HfO_2 and PZT as a function of the dielectric constant of the passive layer ϵ_{Int} in PZT. The passive layer thickness for both materials was assumed to be 1 nm. Figure courtesy of P. D. Lomenzo and adapted from Ref. [17].

dependence of the voltage shift for an exponential injection current into the passive layer and for weak polarization screening. This expression, given by

$$V_{shift} = V_0 ln(1 + t/\tau_0) \tag{7.3}$$

where V_0 and τ_0 are the logarithmic slope and the crossover time between the linear and logarithmic charge relaxation, respectively, gives an excellent fit to the non-linear time dependence of V_{shift} observed in La:HfO_2 capacitors (Fig. 7.2 (d)) highlighting a critical role played by the passive layer in development of imprint. It is interesting to note that the set pulse amplitude has only a slight impact on the

voltage shift as shown in Fig. C.1 in section C.1 in Appendix C. In addition, we note that imprint in the HfO_2-based capacitors could be reduced by replacing the IrO_x electrodes with the TiN ones as shown in Fig. C.2 in Appendix C.

The small signal $C-V$ measurements provided a first glimpse of the fluid imprint as explained below. Fig. 7.2(e) shows a horizontal shift of the $C-V$ loops, which depends on the sequence of the testing pulses, or switching prehistory. It can be seen that although the starting and the ending points of the loops at 0 V are the same for both pulse train sequences, the $C-V$ loop shifts to the left if the testing waveform ends with a negative bias and to the right if it ends with a positive bias. The former suggests that the capacitor structure is quite symmetric, while the latter is a strong indication that the voltage shift of the $C-V$ loops occurs only during testing, i.e., it is a result of the measurement process itself.

To gain a deeper insight into the dynamic behavior of the fluid imprint, the $I-V$ measurements have been carried out as a function of the set pulse duration τ (with the delay time t_d fixed at 10 μs). For these studies, the pulse train was slightly modified in comparison to the one shown in Fig. 7.2(a): after the ac cycling, a preset pulse of sufficiently high amplitude and duration is applied to induce complete poling of the capacitor followed by application of the set pulse (Fig. 7.5 (a)). Results of the fluid imprint testing are shown in Fig. 7.5 (b) (note that the triangular waveform starts with the negative bias). It can be seen that an increase in the positive set pulse duration results in the shift of the positive switching current peak to the left along with the appearance of a negative current peak, which is indicative of the gradual development of the preference for the P_{down} state.

For comparison, results of the $I-V$ measurements as a function of the delay time t_d between the set pulse and the triangular waveform, which tests the conventional imprint behavior, are shown in Fig. 7.5 (c) (the set pulse duration is fixed at 100

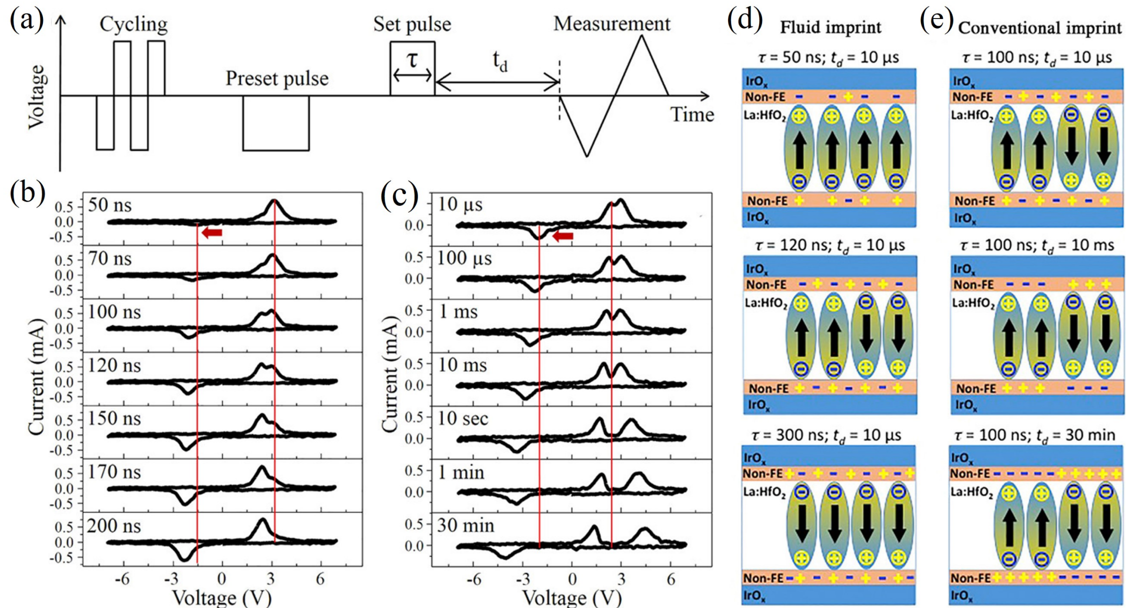

Figure 7.5. (a) Pulse train sequence used for investigation of the imprint effects. (b,c) Transient current-voltage ($I - V$) curves for increasing τ but fixed $t_d = 10\mu$s (b), and for fixed $\tau = 100$ ns but increasing t_d (c). The amplitude of the preset and the set pulses was 6 V. The preset pulse duration was 5 ms. For the triangular waveform the amplitude was 7 V with a 100 μs period. The arrows in (b,c) indicate the direction of the initial voltage change. The vertical red lines in (b,c) serve as a visual reference to compare the shift in the switching current peaks upon changing τ (b) and t_d (c). (d) Illustration of the fluid imprint mechanism depicting the charge distribution after application of the set pulses of different duration and constant 10 μs delay and showing the stabilization of the switched polarization due to the charge injection and entrapment at the dielectric/FE layer interface. (e) Illustration of the conventional imprint mechanism depicting the charge distribution at the interfaces after application of the set pulses of fixed 100 ns duration and different delay times and showing stabilization of opposite polarization state due to the redistribution of charges across the FE layer. The measurements were performed on the 90 μ m-diameter capacitors. Figure adapted from Ref. [17].

ns). It can be seen that, similar to the effect of the set pulse duration, increase in the delay time t_d shifts the negative current peak to the left. However, in addition to this, there is a split of the positive current peak into two peaks, which move further apart upon increase in the delay time. This behavior can be explained in the following way. First, application of the negative preset pulse switches the polarization to the upward

direction, which gets stabilized due to the injected charges, leading to an imprinted P_{up} state. This state is almost unperturbed by the shortest positive set pulse of 50 ns (Fig. 7.5 (d)) as is indicated by the asymmetric $I - V$ curve (Fig. 7.5 (b)) - there is only a positive current peak resulting from the switching of the P_{up} to P_{down} state under a positive half of the triangular waveform. Next, an increase in the set pulse duration to 120 ns leads to partial polarization reversal and formation of the polydomain structure (Fig. 7.5 (d)). As a result, the current peaks start to appear under a negative half of the triangular waveform due to the switching from the P_{down} to P_{up} state (Fig. 7.5 (b)). Charge injection during application of the positive set pulse creates an internal electric field pointing toward the bottom electrode thereby favoring the downward polarization. As a result, we observe a shift of the switching current peaks to the left (toward negative voltage). Note that if we use a delay time much longer than 10 μs used in Fig. 7.5 (b) to allow relaxation of the injected charge, then redistribution of the free charge carriers due to the induced polydomain state would screen and stabilize domains of both polarities (Fig. 7.5 (e)). Because charge redistribution/de-trapping is much slower than the duration of the triangular waveform, the $I - V$ testing itself does not disturb the screening field configuration of the polydomain state (Fig. 7.5 (e)). This means that the screening fields of alternating directions (oriented upward for the P_{up} domains and downward for the P_{down} domains in Fig. 7.5 (e)) should lead to the splitting of the positive current peak: the regions with the downward internal field will switch at lower bias than the regions with the upward field. This is exactly what is observed in Fig. 7.5 (c). The longer is the delay time the larger is the internal field, which implies that the two positive current peaks will move further apart. This split-up tendency is already visible in Fig. 7.5 (b) where the width of the set-pulse was varied at the lowest delay time. This proves that the charge injection effect is also impacted by the polarity of the domains. Note that the

current peak splitting is consistent with the observation of the multiple current peaks using field cycling with non-saturating pulse trains (sub-cycling) [9, 10]. If long set pulses were used so that all domains would be switched, then the internal field would be of the same direction and no current peak splitting would occur. This scenario is highlighted in Fig. C.3 in Appendix C, where the split up in the I-V curves disappear when the switching is complete.

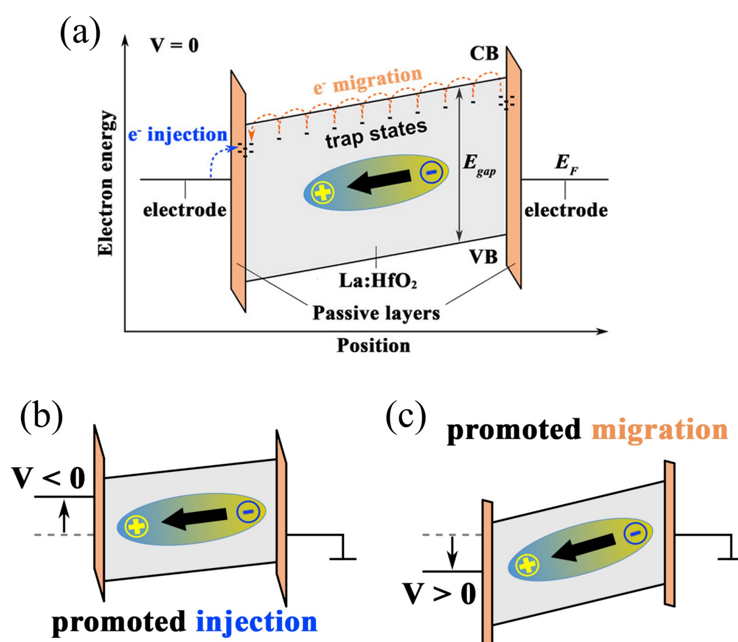

Figure 7.6. (a) Simplified band diagram illustrating mechanisms of fluid and conventional imprint. CB, VB, EF and Egap stand for the conduction band, valence band, Fermi level and bandgap energy, respectively. (b) Electron injection into the passive layer through Schottky emission or direct tunneling (in the upper panel, from the left electrode) and subsequent entrapment at the ferroelectric/passive layer interface accounts for fluid imprint and occurs during negative pulse application (V < 0). (c) Electron migration across the ferroelectric layer via Poole-Frenkel emission or trap-assisted tunneling accounts for static imprint, which can be accelerated if the opposite bias, V > 0, is applied to the capacitor as long it is lower than the threshold switching voltage. Figure courtesy of T. Schenk and adapted from Ref. [17].

Thus, the La:HfO_2 capacitors exhibit two distinctly different imprint effects in response to the change in the delay time t_d (conventional imprint) and in the set

pulse duration τ (fluid imprint). A simplified band diagram illustrating these two effects in the FE capacitor with the interface passive layers is shown in Fig. 7.6 (a). As explained above, separation between the bound polarization charges and the electrode charges leads to an electric field across the passive layer. At the same time, there is an oppositely aligned depolarizing field formed across the FE layer. At V = 0, both the interfaces and the FE therefore appear tilted. This can give rise to two different routes of imprint: (1) electron injection into the passive layer due to the interface potential barrier lowering during the electric field application and subsequent entrapment at the FE/passive layer interface. This process accounts for fluid imprint and could occur through Schottky emission or direct tunneling into the first trap state during pulse application [4]; (2) electron migration across the FE layer via Poole−Frenkel emission or trap-assisted tunneling [28] and entrapment near the FE/passive layer interface or at the defect sites within the interfacial layers or grain boundaries within the FE film causing conventional imprint. This effect can be accelerated if the opposite bias is applied to the capacitor as long it is lower than the threshold switching voltage (Figs. 7.6 (b,c)). This mechanism explains why the electric field cycling could give rise to the local imprint of different polarities [9].

7.5 Inertial switching

The soundness of the injected charge mechanism and its impact has been particularly evident when investigating the domain structure evolution as a function of time after pulse application, which reveals an interesting effect (Fig. 7.7). The capacitor was subjected to the same preliminary treatment as for the imprint measurements (Fig. 7.5). Then, the capacitor was imaged by PFM: first, after application of the positive preset pulse (6 V, 5 ms), which yielded complete poling into the P_{down} state (Figs.

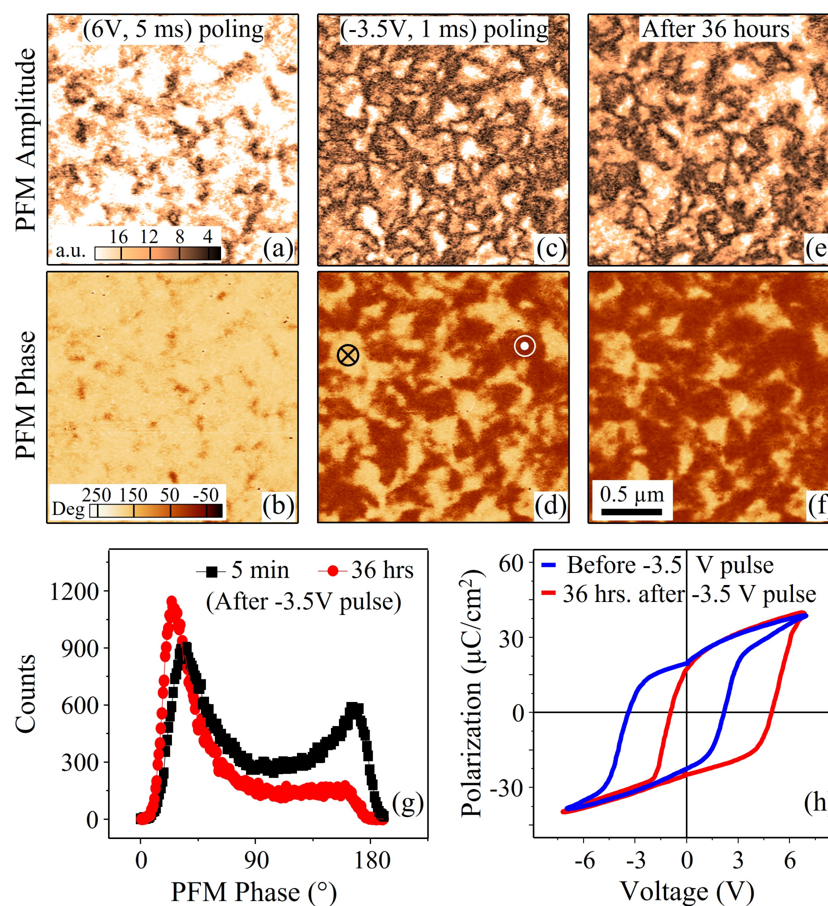

Figure 7.7. Observation of inertial switching in the La:HfO_2 capacitor. PFM amplitude (a,c,e) and phase (b,d,f) images after application of the (6 V, 5 ms) preset pulse (a,b), after application of the (−3.5 V, 1 ms) set pulse (c,d), and 36 hours later (e,f). It can be seen that the capacitor continues to switch even though there was no additional external bias applied after the set pulse. The dark (bright) regions correspond to P_{up} (P_{down}). (g) Histogram analysis of the phase images in (d,f) showing evolution of the polarization toward P_{up} after application of the set pulse. (h) $P-V$ loops acquired before application of the (−3.5 V, 1 ms) set pulse (blue) and 36 hours later (red), which show development of a strong preference for the P_{up} state. Figure adapted from Ref. [17].

7.7 (a,b)), and, next, after the negative set pulse (−3.5 V, 1 ms) application, which resulted in partial switching to the P_{up} state (Figs. 7.7 (c,d)). The capacitor was then left in this state for 36 h with no additional bias applied, while its polydomain structure was monitored by PFM. It was found that the domains continued to switch

to the P_{up} direction long after the set pulse was applied (Figs. 7.7 (e,f)). Histogram analysis of the PFM phase images (Fig. 7.7 (g)) shows that additional 20% of the polarization has switched to the P_{up} state during that period in the absence of the external field. This continuous switching in the same direction as the previously applied field is reminiscent of the inertial motion of domain walls and, hence, is termed as "inertial switching". The inertial switching has been also observed after the positive set pulse application; in this case, to the P_{down} state as shown in Fig. C.4 in Appendix C.

That this is indeed switching and not back-switching due to the pre-existing internal field is confirmed by the $P-V$ loop measurements performed right before and 36 hours after application of the negative set pulse (Fig. 7.7 (h)). The initial loop (blue curve in Fig. 7.7 (h)) is fairly centered (similar to the $P-V$ loops for short delay times in Fig. 7.2 (b,c)) indicating almost no imprint, while the loop acquired 36 hours after the negative set pulse is shifted to the right (red curve in Fig. 7.7 (h)) – a signature of the P_{up} imprint. Note that stabilization of the polydomain structure due to conventional imprint would typically lead to a pinched $P-V$ loop [29]. Finally, to make sure that the observed behavior is not an artifact due to the PFM imaging process, several continuous PFM scans have been taken. No significant change in the domain structure was detected, confirming that the data in Figs. 7.7 (c-f) obtained by a time-dependent process was not affected by PFM imaging. Based on the collection of these data, it can be concluded that the inertial switching is one of the manifestations of the injected charge entrapment. Additional instances of the inertial switching observed in 10-nm-thick $Hf_{0.5}Zr_{0.5}O_2$ (HZO)-based capacitors with TiN top and bottom electrodes highlights the possibility that this might be of a generic nature in hafnia-based systems with strong charge injection (Fig. C.5 in Appendix C).

7.6 Conclusion

In conclusion, a combination of the pulse switching technique and high-resolution domain imaging by means of PFM has been used to investigate the time−dependent and switching history−induced imprint in FE La:HfO_2 capacitors. This approach allowed us to establish correlation between development of imprint and domain switchability. It has been shown that the La:HfO_2 capacitors exhibit a much more pronounced imprint than the conventional PZT−based FE capacitors. Also, in addition to conventional time−dependent imprint occurring with time in the poled capacitors, an easily changeable fluid imprint with a strong dependence on the switching prehistory has been observed. Our studies suggest that while the redistribution of the mobile charges under the depolarizing field and subsequent entrapment at the film−electrode interface is the root cause of the conventional imprint, charge injection into and transport across the interface dielectric layer is the main mechanism for the fluid imprint, which occurs during the external voltage application. An interesting consequence of this effect is inertial switching − a very slow continuation of domain switching in the direction of the previously applied field even after the field was turned off. From an application point of view, imprint can be a serious limitation factor for the memory device performance. Thus, an optimization of the interface structural properties is required to minimize or eliminate its detrimental effect − similar to what is necessary for alleviation of the wake-up effect and retention loss.

References

[1] W. L. Warren, D. Dimos, G. E. Pike, B. A. Tuttle, M. V. Raymond, R. Ramesh, and J. T. Evans, Appl. Phys. Lett. **67**, 866 (1995).

[2] M. Grossmann, O. Lohse, D. Bolten, U. Boettger, T. Schneller, and R. Waser, J. Appl. Phys. **92**, 2680 (2002).

[3] M. Grossmann, O. Lohse, D. Bolten, U. Boettger, and R. Waser, J. Appl. Phys. **92**, 2688 (2002).

[4] A.K. Tagantsev, I. Stolichnov, N. Setter, and J. S. Cross, J. Appl. Phys. **96**, 11 (2004).

[5] A. K. Tagantsev, and G. Gerra, J. Appl. Phys. **100**, 051607 (2006).

[6] W. L. Warren, G. E. Pike, K. Vanheusden, D. Dimos, B. A. Tuttle, and J. Robertson, J. Appl. Phys. **79**, 9250 (1996).

[7] D. Dimos, W. L. Warren, M. B. Sinclair, B. A. Tuttle, and R. W. Schwartz, J. Appl. Phys. **76** (7), 4305 (1994).

[8] D. Lee, A. Yoon, S. Y. Jang, J.-G. Yoon, J.-S. Chung, M. Kim, J. F. Scott, and T. W. Noh, Phys. Rev. Lett. **107**, 057602 (2011).

[9] T. Schenk, U. Schroeder, M. Pešic, M. Popovici, Y. V. Pershin, and T. Mikolajick, ACS Appl. Mater. Interfaces **6**, 19744 (2014).

[10] T. Schenk, M. Hoffmann, J. Ocker, M. Pešic, T. Mikolajick, and U. Schroeder, ACS Appl. Mater. Interfaces **7**, 20224 (2015).

[11] F. P. G. Fengler, M. Pešic, S. Starschich, T. Schneller, C. Künneth, U. Böttger, H. Mulaosmanovic, T. Schenk, M. H. Park, R. Nigon, P. Muralt, T. Mikolajick, and U. Schroeder, Adv. Electron. Mater. **3**, 1600505 (2017).

[12] F. P. G. Fengler, M. Hoffmann, S. Slesazeck, T. Mikolajick, and U. Schroeder, J. Appl. Phys. **123**, 204101 (2018).

[13] K. Carl, and K. H. Härdtl, Ferroelectrics **17**, 473-486 (1978).

[14] G. Arlt, and H. Neumann, Ferroelectrics **87** (1), 109-120 (1988).

[15] R. Lohkämper, H. Neumann, and G. Arlt, J. Appl. Phys. **68**, 4220 (1990).

[16] M. Pešić, F. P. Fengler, L. Larcher, A. Padovani, T. Schenk, E. D. Grimley, X. Sang, J. M. LeBeau, S. Slesazeck, U. Schroeder, and T. Mikolajick, Adv. Funct. Mater. **26**, 4601-4612 (2016).

[17] P. Buragohain, A. Erickson, P. Kariuki, T. Mittmann, C. Richter, P. D. Lomenzo, H. Lu, T. Schenk, T. Mikolajick, U. Schroeder, and A. Gruverman, ACS Appl. Mater. Interfaces **11**, 35115 (2019).

[18] U. Schroeder, C. Richter, M. H. Park, T. Schenk, M. Pešić, M. Hoffmann, F. Fengler, D. Pohl, B. Rellinghaus, C. Zhou, C.-C. Chung, J. Jones, and T. Mikolajick, Inorg. Chem. **57**(5), 2752 (2018).

[19] S. Müller, C. Adelmann, A. Singh, S. Van Elshocht, U. Schroeder, and T. Mikolajick, ECS J. Solid State Sci. Technol. **1**, N123 (2012).

[20] D. Zhou, J. Xu, Q. Li, Y. Guan, F. Cao, X. Dong, J. Müller, T. Schenk, and U. Schroeder, Appl. Phys. Lett. **103**, 192904 (2013).

[21] M. H. Park, H. J. Kim, Y. J. Kim, Y. H. Lee, T. Moon, K. D. Kim, S. D. Hyun, and C. S. Hwang, Appl. Phys. Lett. **103**, 192907 (2015).

[22] E. D. Grimley, T. Schenk, X. Sang, M. Pešic, U. Schroeder, T. Mikolajick, and J. M. LeBeau, Adv. Electron. Mater. **2**, 1600173 (2016).

[23] M. Stengel, and N. A. Spaldin, Nature **443**, 679-682 (2006).

[24] A. K. Tagantsev, M. Landivar, E. Colla, and N. Setter, J. Appl. Phys. **78**, 2623 (1995).

[25] A. K. Tagantsev, and I. Stolichnov, Appl. Phys. Lett. **74**, 1326 (1999).

[26] P. Li, Z. Huang, Z. Fan, H. Fan, Q. Luo, C. Chen, D. Chen, M. Zeng, M. Qin, Z. Zhang, X. Lu, X. Gao, and J.-M. Liu, ACS Appl. Mater. Interfaces **9**, 27120 (2019).

[27] P. Schorn, U. Ellerkmann, D. Bolten, U. Boettger, and R. Waser, Integr. Ferroelectr. **53**, 361-369 (2003).

[28] Z. Fan, J. Xiao, J. Wang, L. Zhang, J. Deng, Z. Liu, Z. Dong, J. Wang, and J. Chen, Appl. Phys. Lett. **108**, 232905 (2016).

[29] T. Schenk, E. Yurchuk, S. Mueller, U. Schroeder, S. Starschich, U. Böttger, and T. Mikolajick, Appl. Phys. Rev. **1**, 041103 (2014).

[30] A. Chouprik, S. Zakharchenko, M. Spiridonov, S. Zarubin, A. Chernikova, R. Kirtaev, P. Buragohain, A. Gruverman, A. Zenkevich, and D. Negrov, ACS Appl. Mater. Interfaces **10**, 8818 (2018).

[31] Y. Matveyev, D. Negrov, A. Chernikova, Y. Lebedinskii, R. Kirtaev, S. Zarubin, E. Suvorova, A. Gloskovskii, and A. Zenkevich, ACS Appl. Mater. Interfaces **29**, 49, 43370 (2017).

Chapter 8

Summary and future directions

8.1 Summary

The work presented in this dissertation involved elucidation of the nanoscopic electrical and electromechanical behavior in ferroelectric HfO_2-based and antiferroelectric ZrO_2-based devices using piezoresponse force microscopy (PFM), and correlated the observed behavior with the macroscopic, integral measurements. More specifically, this dissertation involved nanoscale investigations of - (i) mechanism of polarization reversal process through the visualization of domain structures and comparison of the effect of film microstructure on domain nucleation behavior, (ii) piezoelectric properties in HfO_2 involving the sign of the longitudinal piezoelectric coefficient, d_{33}, and the nature of phase transitions in antiferroelectric ZrO_2, and (iii) imprint behavior in HfO_2-based capacitors.

Time-resolved domain imaging with macroscopic pulse switching current measurements demonstrated that the polarization reversal process occurred primarily through the nucleation of domains. Visualization of the domain switching process in epitaxial Y:HfO_2 capacitors, and polycrystalline La:HfO_2 and Y:HfO_2 capacitors revealed that the lateral domain wall velocity varied from being negligible in the epitaxial capacitors to differing by an order of magnitude in the La:HfO_2 and the Y:HfO_2 capacitors, highlighting the strong impact of the underlying grain sizes on the switching behavior. More importantly, for the applied fields close to the thermodynamic activation fields, convergence of the nucleation limited switching

(NLS) and the Komogorov-Avrami-Ishibashi (KAI) models was observed in both types of Y:HfO_2 capacitors. The convergence signifies that switching is governed by a homogeneous nucleation process characterized by a very narrow distribution of the nucleation times. For films with high nucleation density, the switching would be equivalent to a uniform domain-less polarization reversal. The obtained results highlight that the effect of film microstructure on the dynamic characteristics of the devices is not significant when operated close to the thermodynamic activation fields.

Next, a complex dependence of the sign of d_{33} on the electrical and mechanical boundary conditions was demonstrated in HfO_2-based devices. We have shown that depending on the film thickness, electrode materials or a deposition method used, the sign of d_{33} could be either uniformly positive or negative, or there can be a mixture of both positive and negative d_{33} responses in the hafnia-based ferroelectric capacitors. On the other hand, a transition of the sign of d_{33} from positive to negative was demonstrated with electrical field-cycling. In addition, we have demonstrated that the PFM amplitude loops in antiferroelectric ZrO_2-based devices displayed four characteristic peaks that could be attributed to the sharp increase in the dielectric susceptibility at the AFE $\leftrightarrow$ FE phase transitions. Such characteristic PFM amplitude loops provided a microscopic confirmation of the genuine AFE $\leftrightarrow$ FE phase transitions in ZrO_2.

Finally, we have demonstrated that HfO_2-based devices exhibit much more pronounced imprint than conventional PZT-based capacitors. We have highlighted the important role played by injected charges on the development of imprint behavior in HfO_2-based devices.

8.2 Future directions

During the course of this work, the sign of d_{33} was found to be strongly sample-dependent. We observed different possible combinations of the variation in the sign of d_{33} - from being uniformly negative or uniformly positive, a transition from an initial positive sign to a negative sign after field cycling, and even coexistence of regions with both positive and negative signs within the same film! This highlights that the sign of d_{33} is not trivial and has a complex dependence on different parameters. Delineation of the effect of different parameters such as strain, texture, dopant sizes, fraction of polar and non-polar phases present, deposition method, electrodes, etc. on the sign of d_{33} will be an important direction to pursue to better understand the piezoelectric behavior of hafnia. It is worth pointing out here that the majority of the theoretical reports have predicted a negative d_{33} so far [1, 2, 3] in the relaxed polar orthorhombic phase, although the possibility of a tunable piezoresponse in hafnia was predicted in Ref. [3] by controlling the local chemical environment of the chemically active oxygen atoms. The experimental factors that can impact this environment certainly requires a very detailed investigation involving structural measurements in addition to the PFM measurements.

Finally, during our PFM investigations in hafnia, highly non-conventional PFM spectroscopic loops were frequently encountered. A comprehensive interpretation of the loop shapes based on factors such as coexistence of non-polar phase fractions in a polar matrix, extrinsic contributions such as charge injection, etc. requires further work. Such a study can be helpful in pinpointing specific shapes observed in PFM spectroscopy to different contributing factors and can help increase the overall understanding of local variations in the underlying microstructure.

References

[1] J. Liu, S. Liu, L. H. Liu, B. Hanrahan, and S. T. Pantelides, Phys. Rev. Applied **12**, 034032 (2019).

[2] J. Liu, S. Liu, J.-Y. Yang, and L. Liu, Phys. Rev. Lett. **125**, 197601, (2020).

[3] S. Dutta, P. Buragohain, S. Glinsek, C. Richter, H. Aramberri, H. Lu, U. Schroeder, E. Defay, A. Gruverman, and J. Íñiguez, Nat. Comms. **12**, 7301 (2021).

Appendix A

Supplementary Information for Chapter 4

A.1 Calculation of intrinsic coercive field in Y:HfO_2 capacitors

The paraelectric-ferroelectric phase transition in HfO_2 has been reported to be of the first order due to the observation of thermal hysteresis [1] near the phase transition temperature. Hence, we can express the Gibbs free energy in the Landau-Ginzburg-Devonshire (LGD) formalism as:

$$g = g_0 + \frac{1}{2}\alpha P^2 + \frac{1}{4}\beta P^4 + \frac{1}{6}\gamma P^6 - EP \tag{A.1}$$

where $\alpha = \alpha_0(T - T_0)$, T is the measurement temperature and T_0 is the phase transition temperature, E is the electric field, P is the polarization, and g_0 is the free energy density of the paraelectric phase at zero electric field. Additionally, coefficients $\beta < 0$ and $\gamma > 0$.

Minimizing Eq. A.1 leads to:

$$E = \alpha P + \beta P^3 + \gamma P^5 \tag{A.2}$$

The intrinsic coercive field, $E_{c,i}$ can be obtained from Eq. A.2 as (from Ref. [2]):

$$E_{c,i} = \frac{6}{25}\sqrt{\frac{3}{5}}\frac{|\beta|^{\frac{5}{2}}}{\gamma^{\frac{3}{2}}}f(t) \tag{A.3}$$

$$f(t) = \left[\frac{1}{\sqrt{2}}\sqrt{1+\sqrt{1-\frac{5}{9}t}}\right]\left[\frac{1}{2}(1+\sqrt{1-\frac{5}{9}t}-\frac{5}{3}t)\right] \tag{A.4}$$

where $t = 4\alpha\gamma/\beta^2$. Hence, from Eqs. A.3 and A.4, the value of the $E_{c,i}$ can be estimated from the values of the LGD coefficients. However, in HfO_2 there are no reports so far that have performed detailed measurements to estimate the LGD coefficients. In the absence of reliable values of the LGD coefficients, it will be difficult to estimate the value of $E_{c,i}$ using Eqs. A.3 and A.4. However, we can approximate the value of $E_{c,i}$ from the depolarization field [3] as:

$$E_{c,i} = \frac{P}{\epsilon_0\epsilon_r} \tag{A.5}$$

where ϵ_0 and ϵ_r are the free space permittivity and the dielectric constant, respectively. In HfO_2 the dielectric constant has been reported to be around 30 [4]. Combined with the remanent polarization values of 20 μC/cm^2 and 12.5 μC/cm^2, obtained from the P-E loops as shown in 4.1, the obtained $E_{c,i}$ values for the polycrystalline and the epitaxial films are 7.5 MV/cm and 4.5 MV/cm respectively. These values are very close to the thermodynamic activation fields, E_a, of 5.8 MV/cm and 4.8 MV/cm for the polycrystalline and the epitaxial film respectively, obtained from Merz's empirical equation [5]:

$$t_{sw} = t_0 exp(E_a/E) \tag{A.6}$$

where t_0 is the field independent switching time factor, E is the applied electric field (see Fig. 4.1 (c)). The activation fields and the intrinsic coercive fields are remarkably close to each other with $E_{c,i}/E_a$ ratios of 1.3 and 0.9 for the polycrystalline and the epitaxial films, respectively. From these calculations, it is highly possible

that as the applied fields approach the thermodynamic activation fields the switching approaches the homogeneous switching limit.

References

[1] T. Mimura, T. Shimizu, O. Sakata, and H. Funakubo, Appl. Phys. Lett. **118**, 112903 (2021).

[2] S. Ducharme, V. M. Fridkin, A.V. Bune, S. P. Palto, L. M. Blinov, N. N. Petukhova, and S. G. Yudin, Phys. Rev. Lett. **84**, 1 (2000).

[3] E. Paramonova, V. Bystrov , X. Meng, H. Shen, J. Wang, and V. Fridkin, Nanomaterials **10**, 1841 (2020).

[4] E. D. Grimley, T. Schenk, X. Sang, M. Pešić, U. Schroeder, T. Mikolajick, and J. M. LeBeau, Adv. Elec. Mater. **2**, 1600173 (2016).

[5] W. Merz, Phys. Rev. **95**, 3 (1954).

Appendix B

Supplementary Information for Chapter 5

B.1 Relationship between vertical piezoresponse force microscopy (PFM) phase signal and sign of the longitudinal piezoelectric coefficient

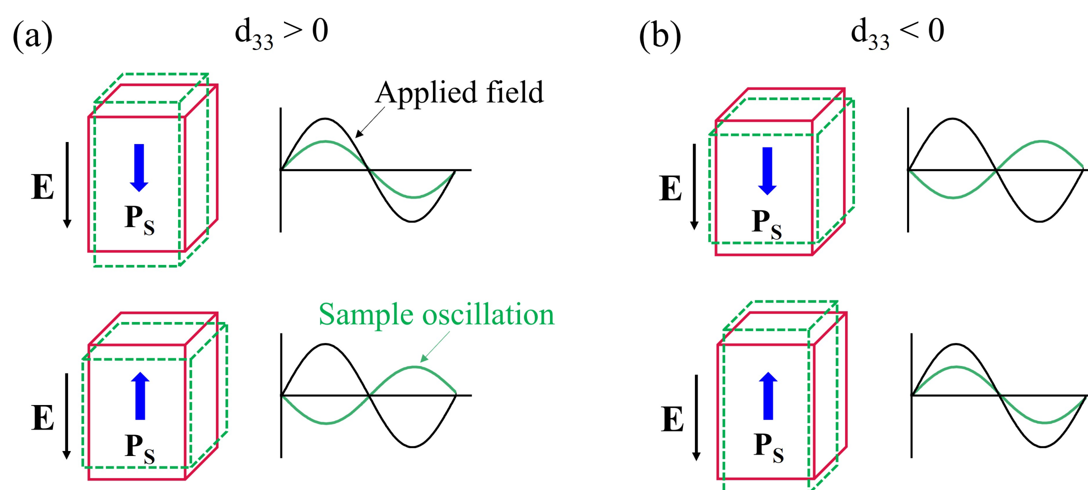

Figure B.1. Origin of PFM phase contrast for domains with opposite polarity in a material with positive (a) and negative (b) d_{33}. The solid red cuboids represent the undeformed state of the domains in the absence of an external electric field while the dashed green cuboids represent the deformed state in the presence of an external electric field. E and P_s stand for the applied electric field and the spontaneous polarization, respectively, with the corresponding black and blue arrows indicating their respective directions in the different configurations.

In PFM, a small signal AC driving voltage is used to induce sample oscillations due to the converse piezoelectric effect, and the sample response is then recorded using

lock-in techniques. The amplitude and phase of the sample response in the vertical PFM mode is related to the magnitude and the sign of the longitudinal piezoelectric coefficient, d_{33}. When operating in resonance enhanced mode, the amplitude, $A_{1\omega}$, of the PFM signal is related to the magnitude of $d_{33,eff}$ and the driving voltage, V_{AC}, as

$$A_{1\omega} = d_{33,eff} V_{AC} Q \tag{B.1}$$

where Q is the quality factor of the first tip-sample contact resonance. The origin of the PFM phase contrast is represented schematically in Fig. B.1. In a material with positive d_{33} (Fig. B.1 (a)), the sample will expand (contract) during the positive (negative) half cycle when the polarization is oriented downwards such that the sample deformation and the AC driving voltage will be in-phase. When the polarization is oriented upwards, the sample will contract (expand) during the positive (negative) half cycles resulting in a 180° out of phase signal between the sample deformation and the AC driving voltage. The scenario is reversed in a material with negative d_{33} – the sample deformation and the AC driving voltage will be in-phase (180° out of phase) when the polarization is pointing upward (downward) as shown in Fig. B.1 (b). From this physical principle, the PFM phase signal will have a clockwise sense of rotation for materials with positive d_{33} and counterclockwise rotation for materials with negative d_{33}.

B.2 Procedure for adjustment of initial phase offsets using reference samples

The procedure for the adjustment of initial phase offsets using a reference sample with well-known sign of d_{33} is demonstrated using IrO_2/PZT/Pt capacitors in Fig. B.2.

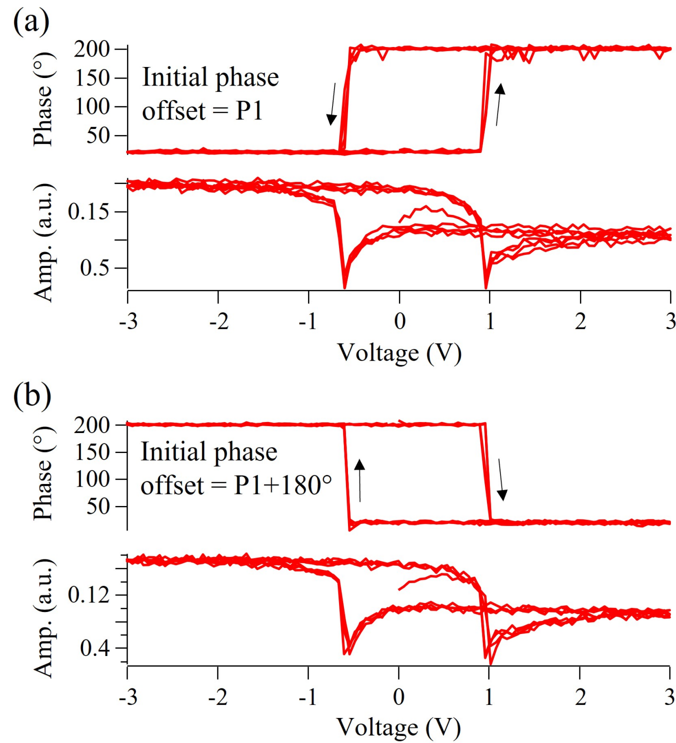

Figure B.2. Procedure for the adjustment of initial phase offsets demonstrated using IrO_2/PZT/Pt capacitors. (a) PFM spectroscopic loops acquired with an arbitrary initial phase offset, P1, resulted in counterclockwise phase loops (top panel). (b) Adding 180° to P1 resulted in a clockwise phase loop, which is the expected sense of rotation for a positive d_{33} material such as PZT. The bottom panels represent the PFM amplitude loops. All loops were acquired in the bias-off mode.

PZT is a well-known material with positive d_{33} [1]. When the PFM spectroscopic loops are acquired with an arbitrary initial phase offset, P1, the phase loop may exhibit a counterclockwise sense of rotation (Fig. B.2 (a)), top panel), which is mirror inverted with respect to the expected sense of rotation for a positive d_{33} material. In such a situation, adding 180° to P1 will result in a phase loop with the correct clockwise sense of rotation, as shown in the top panel in Fig. B.2 (b). This initial phase offset value (=180° + P1) should be maintained the same in all subsequent experiments with the same cantilever and same measurement parameters.

B.3 Comparison of arbitrary and properly adjusted initial phase offsets

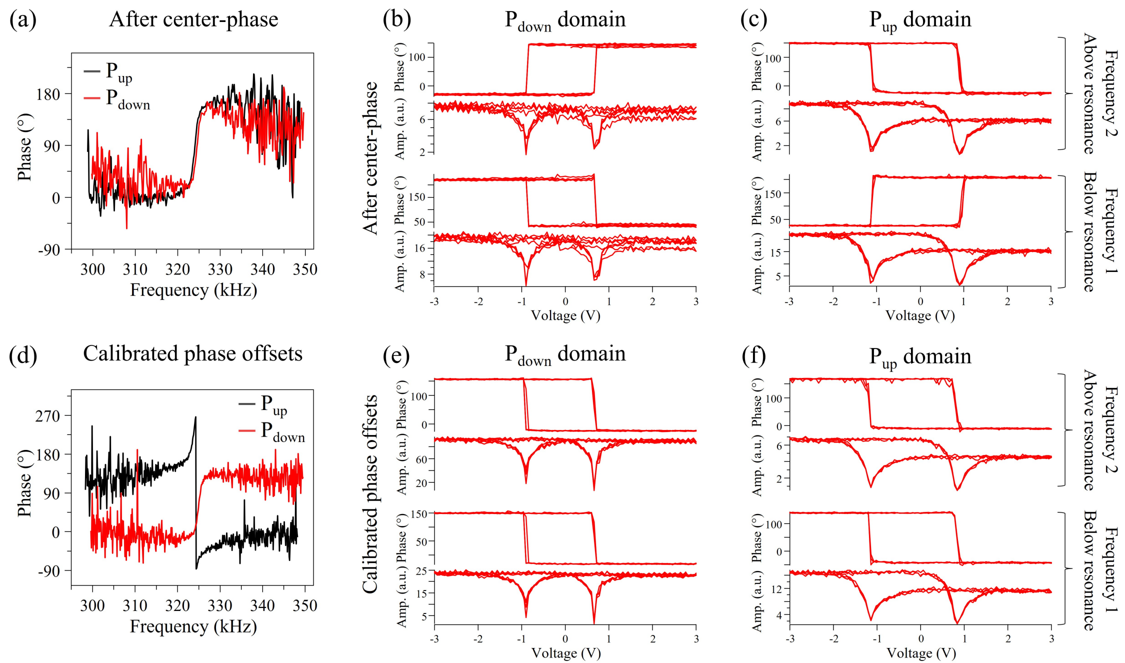

Figure B.3. Effect of center phase and after adjusting the initial phase offsets in IrO_2/PZT/Pt capacitors. The results were obtained in the resonance-enhanced dual AC resonance tracking (DART) mode. (a,d) Frequency spectrum corresponding to the upward and downward polarization states after performing center-phase (a) and after calibrating the initial phase offsets (d). (b,c) PFM spectroscopy loops obtained below and above the resonance frequency for downward polarization (b) and upward polarization (c) states after performing center phase. (e,f) PFM spectroscopy loops obtained below and above the resonance frequency for downward polarization (e) and upward polarization (f) states after calibrating the initial phase offsets. (b,c,e,f) The top and bottom panels for each frequency correspond to the PFM phase and PFM amplitude loops, respectively. All loops were acquired in the bias-off mode.

The effect of arbitrary and calibrated phase offsets on the PFM phase signal is highlighted in Fig. B.3. In the resonance-enhanced dual AC resonance tracking (DART) mode, the PFM signal is simultaneously acquired at two frequencies – below and above the first harmonic tip-sample contact resonance frequency [2]. It

was observed that a software-based adjustment of the initial phase offsets (such as performing 'center phase' in the Asylum Research AFM systems) leads to PFM phase loops whose sense of rotation strongly depends on the polarization direction of the domain underneath the tip, as well as the measurement frequency – i.e., above or below the resonance frequency (see phase loops in Fig. B.3 (b,c)). Software-based adjustments such as 'center phase' adjust the initial phase offsets such that the phase signal always has a low value below and a high value above the resonance frequency, with a value of 90° at the resonance frequency. As a result, software adjusted initial phase offsets have a phase difference of nearly 180° between the upward and downward polarization states, which results in the similar phase spectra near the resonance (Fig. B.3 (a)), but mirror inverted phase loops for the upward and downward polarization states as shown in Figs. B.3 (b,c). Additionally, the mirror inverted phase loops for the frequencies below and above the resonance can be understood from the fact that the phase difference is nearly 180° below and above the resonance and the software adjusted initial phase offsets are the same for both frequencies. Such a strong variation in the phase loops depending on the polarization direction and frequency leads to ambiguity in the determination of the true sign of d_{33}.

On the other hand, when properly calibrated initial phase offsets are used, the PFM phase loops exhibit the same sense of rotation irrespective of the polarization direction or the measurement frequency (Figs. B.3 (e,f)). A calibration procedure such as that outlined in section B.2 can be used for *both* frequencies below and above the resonance and once calibrated, the same initial phase offsets should be used in all subsequent measurements using the same cantilever.

B.4 Single frequency PFM spectroscopy loops with calibrated initial phase offsets

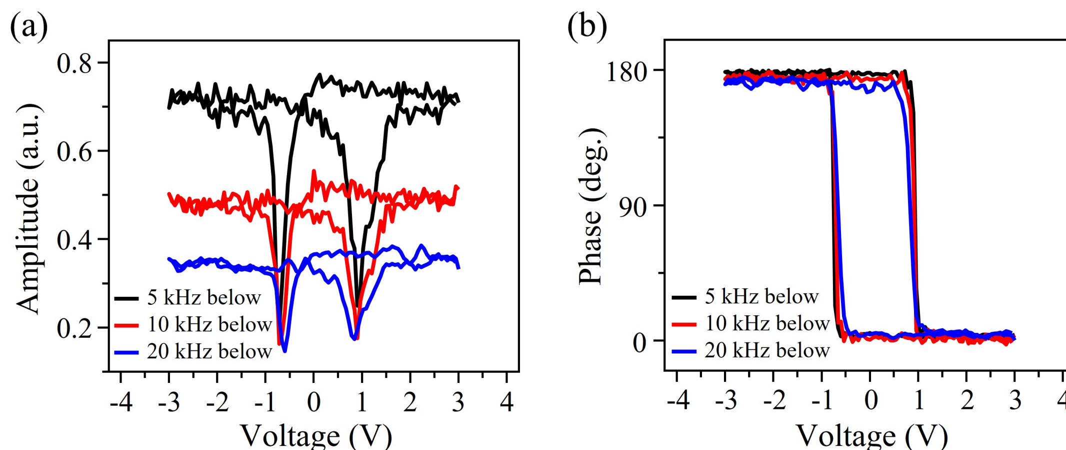

Figure B.4. Quantification of the PFM phase loops in single frequency PFM mode. (a,b) PFM amplitude (a) and PFM phase (b) loops at different frequencies below the first tip-sample contact resonance frequency. Measurements were performed on IrO_2/PZT/Pt capacitors. All loops were acquired in the bias-off mode.

The methodologies to quantify the PFM phase signal that were outlined in the main text can also be extended to single frequency PFM as shown in Fig. B.4. Please note that all the measurements in the main text were performed in the resonance enhanced DART PFM mode. Fig. B.4 (b) shows the calibrated phase loops obtained on IrO_2/PZT/Pt capacitors for different frequencies below the first tip-sample contact resonance frequency, highlighting the applicability of the proposed methodologies to single frequency PFM results as well. We also note that the PFM amplitude signal reduces farther away from the resonance due to reduction in the amplification of the PFM signal as the measurement frequencies move farther away from the resonance frequency (Fig. B.4 (a)).

B.5 Effect of cantilever stiffness on electrostatic contribution and removal of electrostatics in bias-on loops by linear slope correction

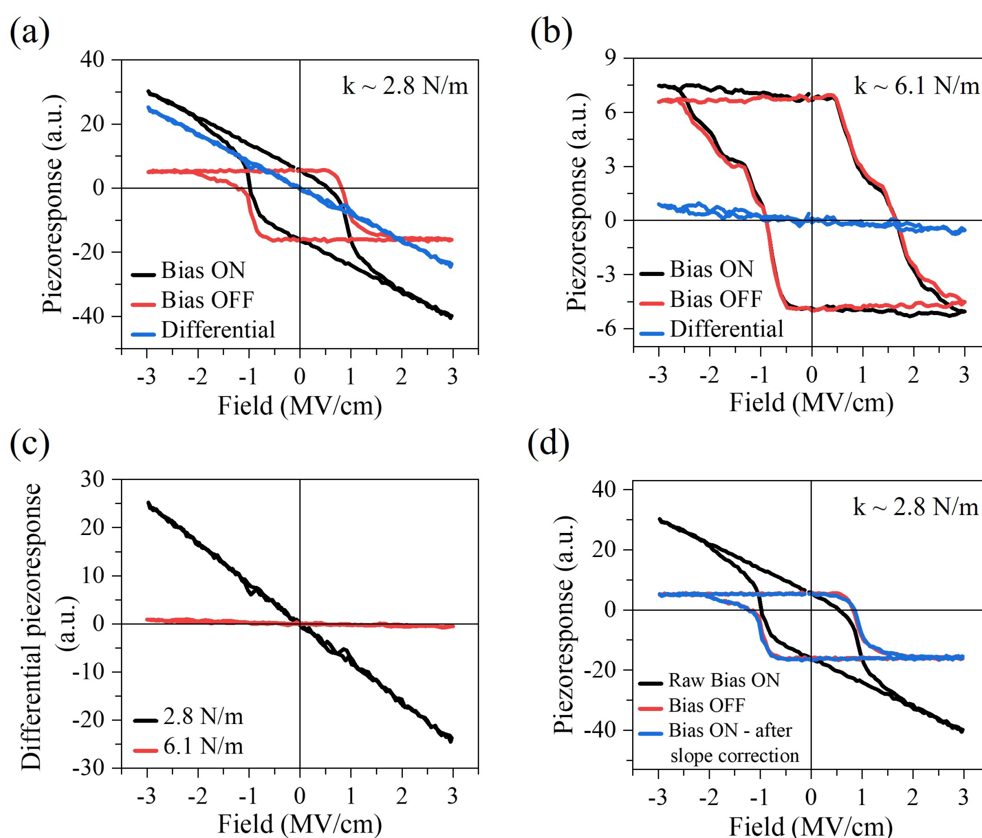

Figure B.5. Effect of cantilever stiffness on electrostatics. Results obtained in Ti/Pt/TiN/La:HfO$_2$/TiN capacitors after wake-up. (a,b) Bias on, bias off and differential piezoresponse signal obtained using cantilevers with stiffness ~2.8 N/m (a) and ~6.1 N/m (b). (c) Comparison of the differential piezoresponse containing only the linear contribution (electrostatics) for cantilevers with $k \sim 2.8$ N/m and ~6.1 N/m. (d) Overlap of the bias on piezoresponse loops with the bias-off piezoresponse loops after subtraction of the linear contribution from the total bias on piezoresponse signal for a cantilever with k ~2.8 N/m. The differential piezoresponse signals are obtained by subtracting the raw bias off piezoresponse loop from the raw bias on piezoresponse loop.

In PFM spectroscopic measurements, the total first harmonic piezoresponse signal, $PR_{1\omega}$, is given by the following equation:

$$PR_{1\omega} = d_{33,eff}V_{ac} + \frac{1}{k}\frac{dC}{dz}V_{ac}(V_{dc} - V_{sp}) \tag{B.2}$$

where k is the cantilever spring constant, $\frac{dC}{dz}$ is the cantilever-sample capacitance gradient and V_{sp} is the surface potential. The first term contains only the piezoelectric response and gives rise to the signal in the bias-off mode. The second term is the electrostatic term, which makes a linear contribution with a negative slope to the measured piezoresponse due to the capacitive coupling. The electrostatic term is inversely proportional to the cantilever stiffness, k. The effect of the cantilever stiffness is highlighted in Figs. B.5 (a-c). There is noticeable electrostatic contribution when using medium stiffness cantilevers (k ~2.8 N/m) as can be seen from the differential piezoresponse signal in Fig. B.5 (a). The electrostatics is significantly minimized upon using stiffer cantilevers with k ~6.1 N/m (Fig. B.5 (b)). Fig. B.5 (c) shows the comparison of the differential piezoresponse signals for the two cantilevers, clearly illustrating the lower electrostatics when using the stiffer cantilever. In addition, Fig. B.5 (d) shows that subtraction of the linear contribution from the bias on piezoresponse signal often results in a good overlap with the bias-off piezoresponse loops. Such slope correction from the bias-on loops provides a way to extract the genuine electromechanical response, which can be particularly useful when using PFM setups where the spectroscopic measurements can be performed only using a continuous triangular wave, i.e., in the bias-on mode only.

B.6 PFM phase images with calibrated initial phase offsets

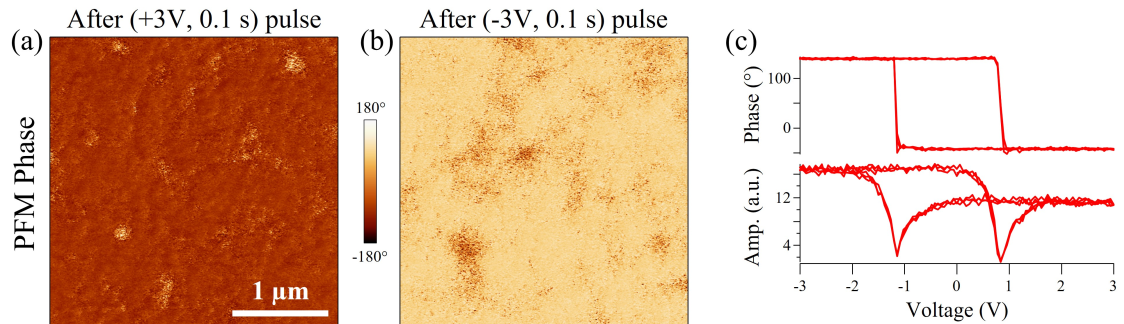

Figure B.6. (a,b) PFM phase images after application of (+3V, 0.1 s) pulse (a) and after application of (-3V, 0.1 s) pulse (b). The images were obtained using the same calibrated initial phase offsets. (c) Representative bias-off PFM spectroscopy loop. Top panel represents the PFM phase signal, and the bottom panel represents the PFM amplitude signal. Measurements were performed on IrO_2/PZT/Pt capacitors.

Figs. B.6 (a,b) shows representative PFM phase images obtained on a PZT capacitor after application of (±3V, 0.1 s) switching pulses. The images were obtained using the same initial phase offsets that were calibrated using the methods outlined in the main text. Since the calibrated initial phase offsets were used, the majority of the regions in Figs. B.6 (a,b) exhibited low (high) phase values after application of the positive (negative) switching pulses consistent with the response expected in a positive d33 material such as PZT. The spatial variations in the phase observed in Fig. B.6 (b) can be attributed to local inhomogeneities resulting in pinning of the downward polarization state. In addition, the use of the same calibrated initial phase offsets during imaging and during PFM spectroscopy measurements gives consistent phase information from both sets of measurements – such as a low phase value after application of a +3V switching pulse in the PFM phase image in Fig. B.6 (a) and the low phase value on the far positive side in the spectroscopy loop (Fig. B.6 (c), top panel).

B.7 Comparison of topography and PFM images, and transient switching currents in $IrO_x/La:HfO_2/IrO_x$ capacitors

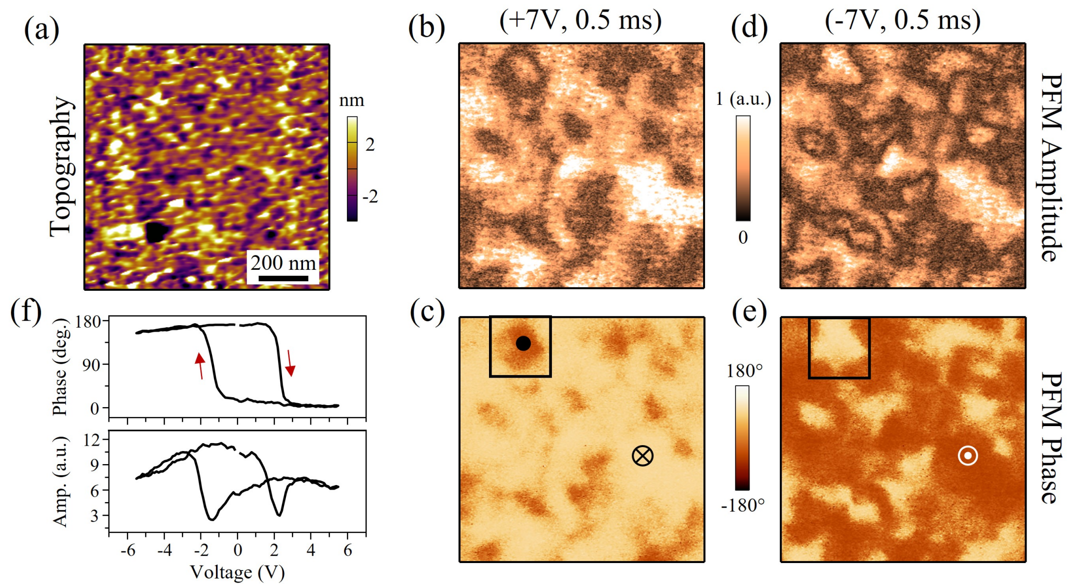

Figure B.7. (a) Topographic image of the top electrode surface. (b-e) PFM amplitude images (b,d) and PFM phase images (c,e) after application of (+7V, 0.5 ms) pulse (b,c) and after application of (-7V, 0.5 ms) pulse (d,e). The images were acquired in the same region as (a). The black square in (c) and (e) highlights a region with phase contrast opposite to the surrounding regions. (f) Bias-on PFM phase (top panel) and amplitude (bottom panel) loops obtained in the location marked with a black circle in (c), that switched with opposite phase contrast in comparison to its surrounding matrix. The red arrows indicate the measurement direction. All measurements were performed after wake-up.

Fig. B.7 (a) shows the topography of the region where the PFM phase images were obtained in Fig. 5.8 in the main text. The corresponding PFM amplitude images after the application of ±7V, 0.5 ms pulses are shown in Figs. B.7 (b,d). Comparison of the surface morphology and the observed features in the PFM images showed no correlation, highlighting that the features observed in the PFM images correspond to

the underlying domain structure.

Fig. B.7 (f) shows a representative bias-on hysteresis loop obtained in the location marked with a black circle in Fig. B.7 (c) that switched opposite to its surrounding matrix. One of the possible reasons for the appearance of such opposite phase contrast could be polarization reorientation due to a local oppositely aligned electric field of the charged oxygen vacancies, E_{vac} [3]. However, such reorientation at low applied fields would give rise to narrow anti-hysteretic bias-on PFM loops. The origin of such anti-hysteretic behavior can be understood as follows: at the far positive fields the polarization will be oriented downward, i.e., along the direction of E_{app} since E_{app} is larger than the oppositely oriented local E_{vac}. This will be manifested by a high value ($\sim 180°$) of the phase signal. As E_{app} is ramped down towards zero and becomes smaller than E_{vac}, the polarization can reorient upwards to align with the direction of the local E_{vac}, giving rise to a low value ($\sim 0°$) of the phase at the positive field value. The polarization will continue to remain in the upward state as the applied field is ramped towards the maximum negative value, and correspondingly the phase signal will remain at the low level. However, application of the negative field would change the polarity of E_{vac} such that the new preferential polarization direction due to E_{vac} is now downwards. As E_{app} is ramped down towards zero from the maximum negative value, there can be another polarization reorientation to now align along the downward direction, which will then change the phase to a high value ($\sim 180°$) again. Since the polarization reorientations occur before E_{app} changes polarity, an anti-hysteretic behavior can be expected in the corresponding bias-on PFM loops. (In contrast, typical ferroelectric PFM phase loops are hysteretic in nature because of the reversal of the polarization at the coercive fields, E_c, which occurs after E_{app} changes polarity. A schematic illustrating the differences between the hysteretic and anti-hysteretic loops are shown in Fig. B.8.) Although the above picture seems to be

consistent with the observed PFM phase contrast in region L2 in Figs. 5.8 (a,b) in Chapter 5 (Figs. B.7 (c,e) here), the absence of anti-hysteretic bias-on loops in Fig. B.7 (f) suggests that the opposite phase contrast in region L2 cannot be explained by the polarization reorientation against the applied field. Hence, we have to consider alternative mechanisms, such as positive d_{33} in these regions, which would result in the opposite changes in phase contrast in comparison to the surrounding regions with negative d_{33}.

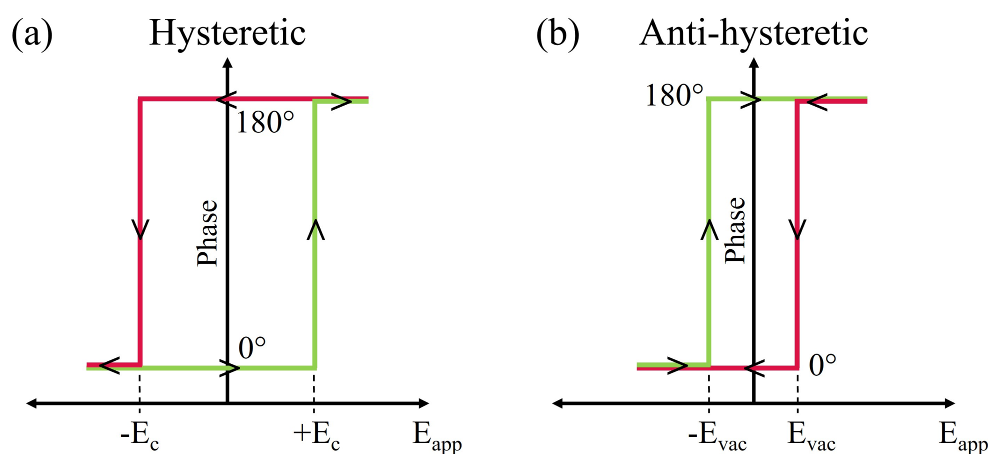

Figure B.8. Schematic of PFM phase loops for hysteretic (a) and anti-hysteretic behavior (b). The red lines indicate loop traversal from positive to negative fields while the green lines indicate loop traversal from negative to positive fields. Arrows are a visual guide to indicate the direction of loop traversal. E_{app}, E_c, E_{vac} represents the applied electric fields, coercive field and field due to oxygen vacancies, respectively.

References

[1] A. L. Kholkin, E. K. Akdogan, A. Safari, P. F. Chauvy, and N. Setter, J. Appl. Phys. **89**, 8066 (2001).

[2] B. J. Rodriguez, C. Callahan, S. V. Kalinin, and R. Proksch, Nanotechnology **18**, 475504, (2007).

[3] A. Chouprik, M. Spiridonov, S. Zarubin, R. Kirtaev, V. Mikheev, Y. Lebedinskii, S. Zakharchenko, and D. Negrov., ACS Appl. Electron. Mater. **1**, 3, 275 (2019).

Appendix C

Supplementary Information for Chapter 7

C.1 Effect of set pulse amplitude on conventional imprint

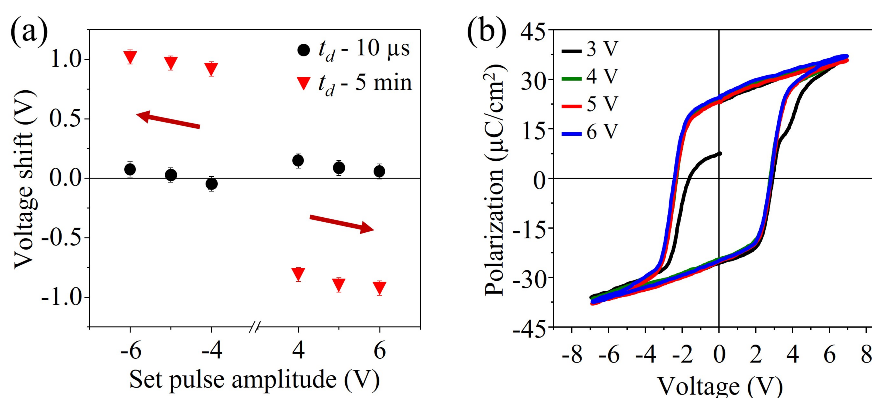

Figure C.1. Effect of the set pulse amplitude on conventional imprint. (a) Voltage shift as a function of the set pulse amplitude for two different delay times t_d (duration of the set pulse τ is fixed at 5 ms). (b) P−V loops obtained after application of the 5-ms-long set pulses of different amplitudes for a fixed delay time td of 10 μs. Figure taken from Ref. [17].

The effect of the set pulse amplitude on conventional imprint is illustrated in Fig. C.1 (a). It can be seen that for a fixed value of t_d an increase in the set pulse amplitude does not make a significant impact on imprint. However, increasing the delay time leads to a much larger imprint. The 5−ms−long set pulses with the amplitude of 4 V and above were sufficient to switch the polarization completely (Fig. C.1 (b)).

C.2 Comparison of the wake-up process and imprint behavior in La:HfO_2 capacitors with IrO_x and TiN electrodes

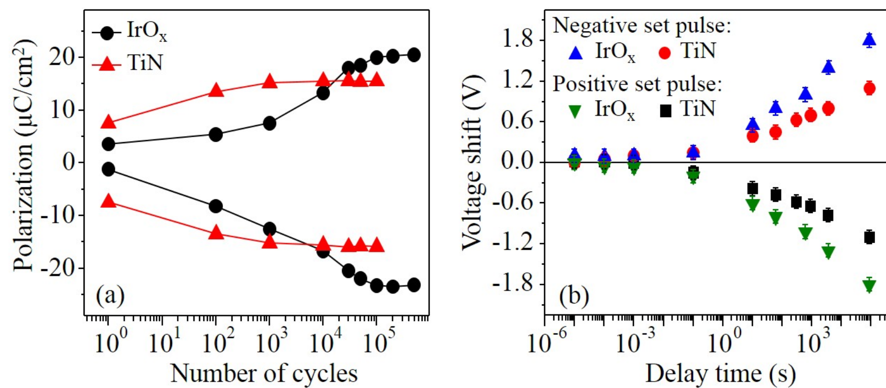

Figure C.2. (a) Polarization as a function of the number of pulse cycles during the wake-up process carried out using (± 7 V, 50 μs) pulses in La:HfO_2 capacitors with IrO_x and TiN electrodes. (b) A voltage shift as a function of the delay time (t_d) after application of (6 V, 5 ms) set pulses of both polarities in La:HfO_2 capacitors with IrO_x and TiN electrodes. Figure taken from Ref. [17].

The number of ac cycles (± 7 V, 50 μs) required to achieve the maximal polarization in La:HfO_2 capacitors with IrO_x electrodes is nearly two orders of magnitude higher than for the similar 20-nm-thick La:HfO_2 capacitors with TiN electrodes (Fig. C.2 (a)). Additionally, the higher as-grown remanent polarization in the capacitors with TiN electrodes as compared to the IrO_x electrodes is most likely due to the lower fraction of non-ferroelectric phase in the samples with the IrO_x electrodes. It was also found that the voltage shift developed as a function of the delay time (t_d) was larger for the IrO_x electrodes than for the TiN electrodes (Fig. C.2 (b)). According to the interface screening model, the depolarization field is directly proportional to the remanent polarization [1]. Capacitors with TiN

electrodes have a lower remanent polarization (15 μC/cm^2) as compared to those with IrO_x electrodes (23 µC/cm^2). This difference can qualitatively account for the lower conventional imprint in the sample with TiN electrodes. For the fluid imprint, which is attributed to electron injection, conclusions can only be drawn if the exact band alignment parameters (work function of IrO_x, conduction band offsets, trap levels) are known.

C.3 Correlation of split-up in I-V peaks and domain configuration

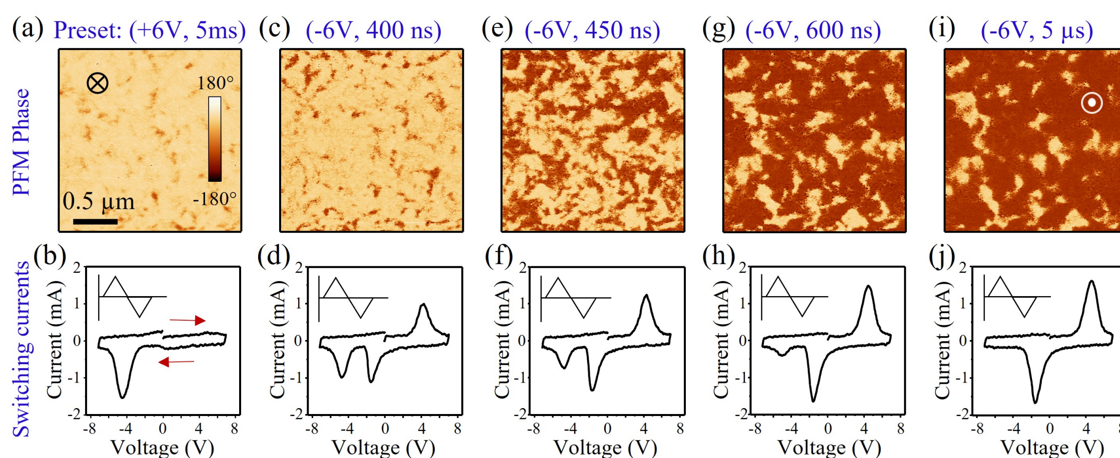

Figure C.3. (a,c,e,g,i) PFM phase images as a function of switching pulses of increasing duration showing the evolution of the domain configuration from downward polarization to upward polarization state. (b,d,f,h,j) Corresponding I-V curves obtained after the application of the switching pulses show split up in the I-V curves in the polydomain configuration. The insets show the triangular waveform used to measure the $I - V$ curves. Measurements were performed on a 160 μm diameter capacitor.

In Chapter 7, it was mentioned that the split in the I-V peaks disappear when the switching is complete. This scenario is illustrated in Fig. C.3 which shows the stroboscopic PFM phase images (top row) at different stages of the domain reversal

process and the corresponding I-V curves (bottom row) measured after the PFM images were collected. The capacitors were set to the downward polarized state by the application of a (+6V, 5ms) pulse, which resulted in the majority of the locations showing a bright phase contrast (Fig. C.3 (a)). The I-V curve taken after the application of this pulse does not show any switching current peak in the positive polarity which confirms that the polarization was completely switched downwards. Gradual increase in the switching pulse duration led to an increase in the fraction of regions with a darker phase contrast (or lower phase value) with a corresponding increase in the switching current peak in the positive polarity of the I-V curves. The intermediate polydomain configurations are characterized by the appearance of multiple switching peaks in the I-V curves. With an increase in the fraction of upward domains under application of negative pulses of increasing duration, there is a corresponding reduction in the amplitude of the second peak (Fig. C.3 (h)). When a sufficiently long pulse is applied to induce complete polarization switching (Fig. C.3 (i)), the split in the I-V curves also disappear. Please note that the switching time obtained independently from PUND measurements was $\sim 1\ \mu$s, which highlights that a 5 μs pulse was sufficiently long to induce complete polarization switching. The regions with bright phase contrast represent pinned or unswitchable regions.

C.4 Inertial switching to P_{down} state in IrO_x/La:HfO_2/IrO_x capacitors

Demonstration of inertial switching to the P_{down} state is shown in Fig. C.4. The capacitor was first switched mostly to the P_{up} state by applying a preset (−6V, 5 ms) pulse (Fig. C.4 (a,b)). A (+3.5 V, 1 ms) set pulse was then applied to partially

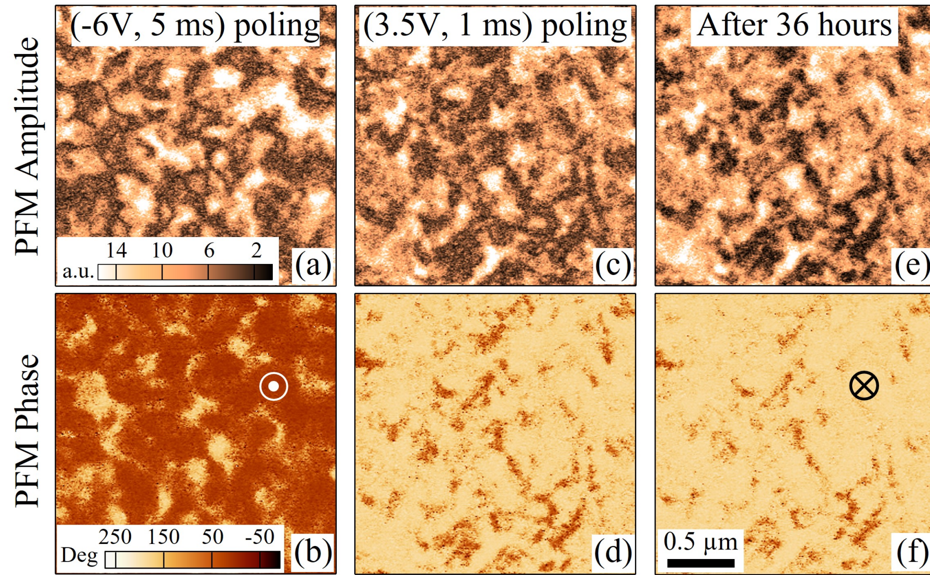

Figure C.4. PFM amplitude (a,c,e) and phase (b,d,f) images after application of the (−6 V, 5 ms) preset pulse (a,b), after application of the (3.5 V, 1 ms) set pulse (c,d), and 36 hours later (e,f). Figure taken from Ref. [17].

switch the polarization to P_{down} (Fig. C.4 (c,d)). The capacitor was then allowed to sit for 36 hours while the change in the domain configuration was monitored in periodic intervals by PFM. The capacitor continued to switch toward the P_{down} state even after the field was off as can be seen from the increase in the PFM amplitude (Fig. C.4 (e)) and the increase in the percentage of the bright color (corresponding to P_{down}) in the PFM phase image (Fig. C.4 (f)).

C.5 Inertial switching in TiN/$Hf_{0.5}Zr_{0.5}O_2$ (HZO)/TiN capacitors

Inertial switching for both polarization states was also observed in 10-nm-thick HZO films sandwiched between TiN top and bottom electrodes as shown in Fig. C.5. (Details about the growth procedure of these films can be found in Ref. [2]). The

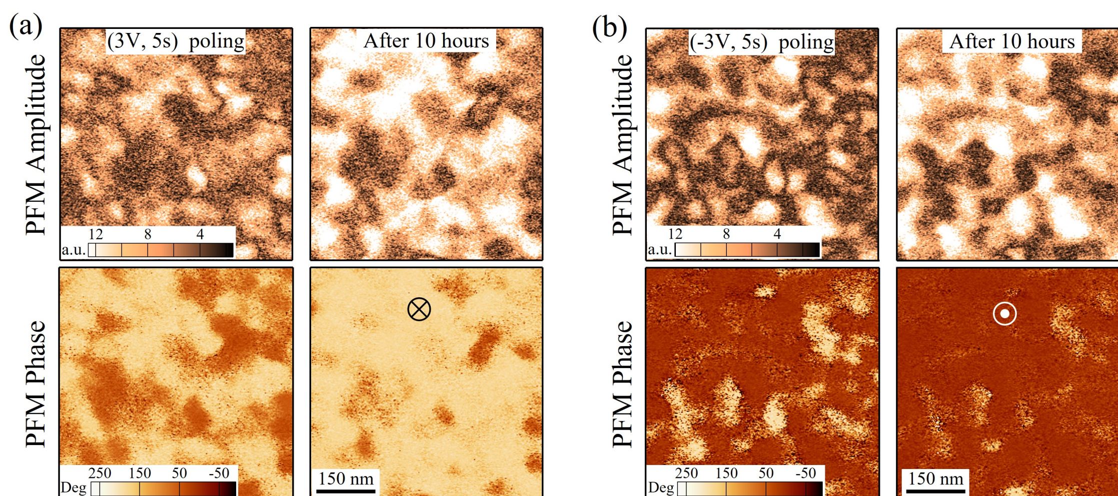

Figure C.5. (a,b) PFM amplitude (top panels) and PFM phase images (bottom panels) showing the inertial switching behavior in TiN/$Hf_{0.5}Zr_{0.5}O_2$/TiN capacitors after application of a positive switching pulse (a) and after a negative switching pulse (b). In both (a,b) the left column represents the images taken immediately after the application of the switching pulse, while the right column images were taken after 10 hours. In these 10-nm-thick HZO-based capacitors the coercive voltage was $\sim$ 1 V.

PFM phase images after waiting for 10 hours since the application of the switching pulses (both positive and negative) clearly reveal the increase in the fraction of switched domains along with a corresponding increase in the PFM amplitude signal. This signifies a time-dependent polarization switching process in the absence of an applied electric field, i.e., an inertial switching behavior. In operando hard X-ray photoemission spectroscopy measurements have shown that the TiN electrodes get oxidized at both the top and bottom interfaces at different steps of the growth processes resulting in the formation of a TiO_x/TiOn layer [3]. Charge injection into such an interfacial passive layer [4] can lead to an internal field that can result in the slow time-dependent inertial switching behavior as observed in Fig. C.5.

References

[1] M. Grossmann, O. Lohse, D. Bolten, U. Boettger, T. Schneller, and R. Waser, J. Appl. Phys. **92**, 2680 (2002).

[2] A. Chouprik, S. Zakharchenko, M. Spiridonov, S. Zarubin, A. Chernikova, R. Kirtaev, P. Buragohain, A. Gruverman, A. Zenkevich, and D. Negrov, ACS Appl. Mater. Interfaces **10**, 8818 (2018).

[3] Y. Matveyev, D. Negrov, A. Chernikova, Y. Lebedinskii, R. Kirtaev, S. Zarubin, E. Suvorova, A. Gloskovskii, and A. Zenkevich, ACS Appl. Mater. Interfaces **29**, 49, 43370 (2017).

[4] A. K. Tagantsev, and I. Stolichnov, Appl. Phys. Lett. **74**, 1326 (1999).